Synthetic Approaches Towards 3rd Generation, Light-Harvesting Metal-Organic Frameworks for Photo-Electrocatalytic Energy Conversions

A thesis submitted to the University of Dublin for the degree of Doctor of Philosophy

Muhamed Mulahmetović

School of Chemistry

University of Dublin

2023

I declare that this thesis has not been submitted as an exercise for a degree at this or any other university and it is entirely my own work.

I agree to deposit this thesis in the University's open access institutional repository or allow the library to do so on my behalf, subject to Irish Copyright Legislation and Trinity College Library conditions of use and acknowledgement.

_____

Muhamed Mulahmetovic

Acknowledgements

Firstly, I would like to thank and express my gratitude to Prof. Wolfgang Schmitt for his constant support, advice, patience, encouragement, and guidance throughout this project and the thesis. I would also like to thank him for giving me the opportunity to carry out my Ph.D. research in his group.

I would like to acknowledge and thank the staff in the School of Chemistry and School of Physics. In particular I would like to thank Prof. Louise Bradley and her research group for all their help with the photophysical measurements. Also, Dr. John O'Brien and Dr. Manuel Ruether for their tireless work and assistance with the analytical techniques, especially NMR. I want to express my gratitude to Dr. Brendan Twamley for his contribution to the crystallographic work and Dr. Gary Hessman, Peter Brien, Anne Marie Farrell, Patsy Greene, Dr. Noelle Scully and Ben Power for all their hard work.

I wish to express my utmost appreciation to the entire Schmitt group past and present for their moral support, friendliness, and good vibes inside and outside the lab. In particular I would like to thank Greg Byrne for all his contributions to the project especially for his work on the synthesis and crystallography of the metallo-ligands, Dr. Joaquin Soriano Lopez (Ximo) for his overall guidance and especially his help in electrochemistry, Dr. Mariah O'Doherty for EDX analysis, Dr. Nian-Yong Zhu (Jom), Dr. Friedrich Steuber and Éadaoin Whelan for their crystallographic work, Dr. Swetanshu Tandon for DFT measurements, Dr. Sebastien Vaesen for the RASPA simulations, Dr. Kevin Byrne and Dr. Rory Elliot for all their advice and support. I also wish to thank Joe, Dean, Gearoid and Aviral for all the banter and encouragement. I would like to acknowledge my great summer students Aobh, Breno, and Mary for all their outstanding hard work and positive attitude which they brought to this project. A special shoutout to my brothers from Grg cnt spl, even with everyone spread across the globe we always support and have each others backs.

I would like to take this opportunity to emphasise my gratitude and appreciation to my parents for everything they have provided me with and for all their love and support throughout my life and especially for their encouragement which I badly needed sometimes. Finally, I owe a massive thanks to my wife Emina without who I wouldn't have been able to do any of this. Thank you for all the moral support, comfort, kind words, encouragement and love you unconditionally give me day in and day out.

Summary

Society's increasing energy requirements as well as evident climate change problems present humanity with significant scientific challenges. Switching to more renewable energies sources such as the high density, carbon-free energy carrier H_2 offers society with a viable alternative and a way to address the issues associated by the usage of fossil fuels. However, existing H_2 manufacturing technologies are unfortunately both costly and unviable. Solar H_2O splitting is a promising method for producing abundant H_2 in a sustainable manner. Nevertheless, the absence of effective, low-cost catalysts for the endergonic, proton-coupled 4 electron oxygen evolution half-reaction (OER) is impeding progress in the field of solar H_2O splitting. Therefore, to fulfil society's energy demands in an environmentally responsible way, it is critical to develop efficient H_2O oxidation catalysts (WOCs).

Current WOCs generally demonstrate low activity or instability. While many advanced catalysts depend on expensive rare-earth elements. Metal-organic frameworks (MOFs) are metallo-supramolecular materials that are composed of metal-containing units linked by organic ligands. This emerging class of materials features well-defined cavities and remarkable surface areas. Additionally, they possess the ability to incorporate photoactive and redox-active components within their frameworks. As a result, MOFs provide promising platforms for the development of advanced materials that may be used in a wide range of applications. Thus, MOFs are regarded as potentially efficient WOCs. Similarly, MOFs for light-driven transformations and energy technologies such as photocatalytic converters and fuel cells, have particularly received a lot of research attention.

This thesis aims to prepare and synthesise a variety of novel photoactive metallo-ligands and subsequently novel MOFs with photoactive capabilities that can be exploited in light-driven chemical transformations and related applications. The results presented in this thesis include the synthesis and structural, photophysical and photochemical characterisations of several novel photoactive materials. Additionally, an alternative synthetic strategy was developed, in which electrochemical techniques were utilised to produce thin films of photoactive MOFs on conductive surfaces. Furthermore, the investigation of these hybrid organic-inorganic systems as photoactive catalysts for artificial photosynthetic applications is outlined.

Chapter 1 provides an overview on the historical context of this work as well as an introduction to the topics in this thesis. A summary of the literature on the relevant materials in this thesis and their potential application is discussed. The chapter concludes with a description of the aims and objectives of this research project.

Chapter 2 contains an optimised synthetic pathway towards five novel Ru^{II}-based metallo-ligands which would have the potential to be used for the synthesis of MOFs. These extended linear metallo-ligands are designed upon a rigid, photoactive $[Ru(bpy)_3]^{2+}$ (bpy = bis-2,2'-bipyridine) skeleton; [bis-(2,2'-bipyridine)-ruthenium(II)(5,5'-(bis-4-ethynylbenzoic acid)-2,2'-bipyridine)]$^{2+}$, $\mathbf{H_2[L_{bpy}\text{-}R_1]^{2+}}$, [bis-(2,2'-bipyridine)-ruthenium(II)(5,5'-(bis-3-ethynylbenzoic acid)-2,2'-bipyridine)]$^{2+}$, $\mathbf{H_2[L_{bpy}\text{-}R_2]^{2+}}$, [bis-(2,2'-bipyridine)-ruthenium(II)(5,5'-(bis-5-ethynylisophthalic acid)-2,2'-bipyridine)]$^{2+}$, $\mathbf{H_4[L_{bpy}\text{-}R_3]^{2+}}$, [bis-(2,2'-bipyridine)-ruthenium(II)(3,8'-(bis-5-ethynylisophthalic acid)-1,10'-phenanthroline)]$^{2+}$, $\mathbf{H_4[L_{phen}\text{-}R_3]^{2+}}$, and [tris-(5,5'-(bis-5-ethynylisophthalic acid)-2,2'-bipyridine)-ruthenium(II)]$^{2+}$, $\mathbf{H_{12}[L_{tris}\text{-}R_3]^{2+}}$. Their purity and structures were elucidated and confirmed using various spectroscopic techniques such as NMR spectroscopy, mass spectrometry and single-crystal X-ray diffraction. The packing of the complexes in their 3D structures illustrated the intermolecular forces present within the crystal structures and the importance of $\pi - \pi$ stacking interactions for stabilising the structures. Physicochemical characterisation defined the physical and chemical properties, composition, identification, and thermal stabilities of the novel Ru-based metallo-ligands.

Chapter 3 evaluates the role of the Ru^{II} centre as a chromophore by investigating the photochemical, photophysical and electrochemical properties of the novel metallo-ligands; $\mathbf{H_2[L_{bpy}\text{-}R_1]^{2+}}$, $\mathbf{H_2[L_{bpy}\text{-}R_2]^{2+}}$, $\mathbf{H_4[L_{bpy}\text{-}R_3]^{2+}}$, and $\mathbf{H_4[L_{phen}\text{-}R_3]^{2+}}$. A comparative analysis with the parent core complex $[Ru(bpy)_3]^{2+}$ revealed that the metallo-ligands maintained the characteristic photophysical properties of $[Ru(bpy)_3]^{2+}$, demonstrating closely matching UV-Vis absorption and steady-state emission spectra. A retention in the electrochemical properties along with a reduction in the optical band gap energies and an increase in fluorescent lifetimes of the metallo-ligands when compared to $[Ru(bpy)_3]^{2+}$ highlighted the applicability of the metallo-ligands for the synthesis of photoactive MOFs for photo-electrocatalytic applications.

Chapter 4 looks at the synthesis of three highly augmented isostructural MOFs; **Ni-MOF** [Ni(**L$_{bpy}$-R$_3$**)($H_2O)_2$], **Co-MOF** [Co(**L$_{bpy}$-R$_3$**)($H_2O)_2$] and **Zn-MOF** [Zn(**L$_{bpy}$-R$_3$**)($H_2O)_2$] using the novel acetylene-extended, light-harvesting Ru^{II}-bipyridyl metallo-ligand, **H_4[L$_{bpy}$-R$_3$]$^{2+}$**. The MOFs were found to crystallise in the cubic space group $Fm\bar{3}m$ and consist of 12-connected cubohemioctahedral cages which form face-centred cubic networks. Additionally, the MOFs were found to consist of exceptionally large cage-type cavities with truncated tetrahedral and octahedral geometries which were subsequently estimated using RASPA. Analysis of the packing arrangement of the MOFs shows a series of channels which are lined with photoactive ruthenium centres and are expected to play a vital role in photocatalysis. Photophysical characterisation showed that the optical properties of the free metallo-ligand is maintained in the framework of the MOFs. Additionally, the incorporation of **H_4[L$_{bpy}$-R$_3$]$^{2+}$** into the MOF network was found to allow for the rapid shuttling or redistribution of excited electrons from the photosensitiser *via* the conjugated ligand backbone towards the metal nodes. Physicochemical characterisation highlighted the identity, purity and thermal stability of the novel MOFs. Further, it was demonstrated that the **Ni-MOF** and **Co-MOF** could be synthesised under electrochemical conditions on the conductive surface of fluorine doped tin oxide (FTO) glass electrodes. The **Ni-MOF/FTO** and **Co-MOF/FTO** electrodes in both CV and LSV experiments demonstrated improved catalytic activity in relation to photo-electrocatalytic water oxidation upon visible light irradiation. Post-catalytic characterisation experiments support the assignment of both **Ni-MOF/FTO** and **Co-MOF/FT**O as genuine photoactive WOCs. Preliminary studies on the encapsulation of guest species in the pores of the **Ni-MOF** and **Ni-MOF/FTO** are also investigated in this chapter.

Chapter 5 describes the experimental materials and methods along with a detailed experimental procedure for each compound mentioned in this thesis.

Chapter 6 concludes on the work carried in this thesis and outlines some possible areas that could be investigated in future studies.

Table of Contents

Abbreviations

BET	Brunauer-Emmet-Teller
Bpy	2,2-bipyridine
d	Doublet
CB	Conduction band
$CDCl_3$	Deuterated chloroform
DCM	Dichloromethane
DEF	Diethylformamide
DIPA	Diisopropylamine
DMF	Dimethylformamide
DMSO	Dimethylsulfoxide
DSSC	Dye-sensitised solar cell
Et_2O	Diethylether
EtOH	Ethanol
ESI-MS	Electrospray ionisation mass spectroscopy
Fig.	Figure
FLIM	Fluorescence lifetime imaging
FT-IR	Fourier-transform infrared spectroscopy
FTO	Fluorine-doped tin oxide
IRMOF	Iso-Reticular metal-organic framework
HEC	Hydrogen evolution catalyst
HER	Hydrogen evolution reaction
HKUST	Hong Kong University of Science and Technology

HOMO	Highest occupied molecular orbital
J	Coupling constant
LUMO	Lowest unoccupied molecular orbital
LSV	Linear sweep voltammetry
m/z	Mass/charge ratio
m	Multiplet
MeCN	Acetonitrile
MeOH	Methanol
MIL	Matérial Institut Lavoisier
MLCT	Metal-to-ligand charge transfer
MOF	Metal-organic framework
MOP	Metal-organic polyhedra
NHE	Normal hydrogen electrode
OEC	Oxygen evolution complex
OER	Oxygen evolving reaction
NMR	Nuclear magnetic resonance
PEC	Photo-electrochemical cell
PL	Photoluminescence
POM	Polyoxometalate
POMOF	Polyoxometalate-based metal-organic framework
PS	Photosensitiser
PS I	Photosystem I
PS II	Photosystem II
PSM	Post-synthetic modification

PPM	Parts per million
P-XRD	Powder X-Ray Diffraction
Q_A	Bound plastoquinone electron carrier of PS II
Q_B	Mobile plastoquinone electron carrier of PS II
SBU	Secondary building unit
SC 1	Anodic semiconductor electrode of PEC
SC 2	Cathodic semiconductor electrode of PEC
SEA	Sacrificial electron acceptor
SED	Sacrificial electron donor
s	Singlet
t	Triplet
TEA	Triethylamine
TGA	Thermogravimetric analysis
THF	Tetrahydrofuran
TOF	Turn Over Frequency
TON	Turn Over Number
UV-vis	Ultraviolet-visible
UiO	Universitetet i Oslo
VB	Valence band
WOC	Water Oxidation Catalyst
XRD	X-ray diffraction
Y_Z	A redox-active tyrosine residue on the D1 subunit
ZIF	Zeolitic imidazolate framework

Chapter 1

Introduction

1. Introduction

1.1 Global Outlook and Motivation

Humanity is confronted with numerous economic and environmental challenges. These challenges are predicted to exacerbate with the expected increase in the global population. The beginning of the industrial revolution in the 18th century has forever altered humanity's regard for nature. For centuries, exploiting the energy contained in fossil fuels has had an influence on every element of humankind where with respect to the world's population, this has particularly been the case. Within only a few decades, the population surged from around 750 million in 1750 to nearly 8 billion in 2022. According to the United Nations, it is estimated that by the year 2050 the world's population will have passed 9 billion people and reached over 11 billion by 2100. This rapid population increase was followed by a significant surge in energy usage, which is expected to surpass 27 TW by 2050.[1]

The combustion of fuels with low (coal), medium (oil), or high (natural gas) hydrogen concentrations accounts for more than 80% of today's global energy production.[2] The chemical energy of C–C and C–H bonds is transformed into heat during the combustion of carbonaceous fuels, while simultaneously producing H_2O and CO_2. Excess CO_2 emissions into the atmosphere contribute to heat-trapping and this anthropogenic emission significantly surpasses the rate at which it is separated into the biosphere and oceans. Many people today are switching to more energy-intensive forms of transportation as a result of economic development. As a result, the transportation industry is regarded as Europe's greatest CO_2 emitter and an increasing source of emissions worldwide.[3] Thus, CO_2 concentrations in the atmosphere have reached all-time highs in the last 650,000 to 20,000,000 years.[4–7] The accumulation of CO_2 in our atmosphere is recognised as having the potential to dramatically destabilise the earth's climate system and lead to an increase in extreme weather events.[8] The rise in temperatures and sea levels, ocean acidification and intensification of tropical cyclones, all have major implications for biodiversity.[9–14]

As a result, new and innovative solutions coupled with the harnessing of energy sources that are both renewable and carbon-neutral must be developed to overcome the vast number of problems that all these challenges will bring.[15,16] Solar, wind, tidal,

hydrothermal, and geothermal power are all examples of ecologically beneficial and renewable energy sources that are currently being researched.[17]

Solar energy is a highly attractive as it is both clean and indefinite. It is estimated that the total amount of energy reaching the surface of the earth is greater than 100,000 TW which is several orders of magnitude more than the world's current consumption of 15 TW per year.[18] Therefore, the energy provided by the sun every hour equates to as much energy as humankind consumes in a year.[19]

The development of specific coordination compounds, consisting of a variety of organic and inorganic units with distinct topologies, are recognised as conceivably effective in overcoming these challenges. This chapter will initially introduce an overview of solar energy storage and modern sustainable energy technologies. It will subsequently introduce and examine an associated class of coordination compounds, known as metal organic frameworks (MOFs). The chapter will give an overview of appropriate literature references, while focusing on the components that come together to form these polymeric structures. The materials' essential characteristics, as well as their use in various applications, will be explored.

1.2 Solar Energy Storage and Modern Technologies

Photosynthesis can be seen as the process of capturing and storing sunlight as solar fuels through the splitting of H_2O. It potentially offers a way to meet society's energy demands in a sustainable way. Nature's method of storing and utilising solar energy could be used to design artificial photosynthetic devices.[15] Such technologies would provide an opportunity to substitute fossil fuels with environmentally friendly carbon-free fuel sources. Moreover, utilising the two virtually limitless resources, water and sunlight, photosynthetic fuels can be generated.[20] Currently, technologies that adopt this process, unfortunately, are hampered by significant costs, low stability, and sluggish reaction rates, deeming them unfeasible for solar fuel generation.[21]

Photovoltaic systems are to date the most extensively used technology for utilising solar energy.[22] Exploitation of the photovoltaic effect, photovoltaic cells harvest solar energy to produce an electrical current.[23] Although this technology has come a long way since its inception and despite constant advances in performance, it is not without its drawbacks.[24,25] High manufacturing costs and the fact that a number of devices depend on the mining of rare-earth elements such as In and Te, are just two disadvantages.[26,27] Hence, in the vast majority of places solar energy continues to be more costly than grid power.[28] It has been found that even with a decrease in manufacturing costs[29] a major challenge of these systems is their ability to produce electricity only during the day, while energy is required constantly. Besides this, only a small proportion of global energy usage is in the form of electricity whereas, liquid fuels utilised for many other purposes such as transportation account for the majority of global energy consumption. As a result, an effective mechanism for storing, transferring, and rapidly releasing solar energy is necessary.[30] H_2 has been proposed as a highly promising energy carrier. In addition to H_2 being carbon-free, it also boasts a significantly high gravimetric energy density (142 MJ kg^{-1}) in comparison to petrol (46 MJ kg^{-1}). The existing commercial techniques for producing H_2, however, are both expensive and non-renewable.[31,32] A promising solution to overcome these issues is the utilisation of solar energy to split H_2O into H_2 and O_2. Therefore, in order to achieve technological advancements in artificial photosynthesis, understanding the fundamental mechanical principles of how Nature accomplishes H_2O splitting is essential.

1.3 Natural Photosynthesis

Approximately 2.5 billion years ago, oxygenic photosynthesis initially appeared instigating one of the most momentous events in evolutionary history.[33] Cyanobacteria were the first species to use sunlight to convert H_2O and CO_2 into energy-dense carbohydrates while producing O_2 as a waste product (Eq. 1.3.1).[34,35] The success of these prokaryotic photoautotrophs which subsequently evolved into chloroplasts through endosymbiosis led to the build-up of O_2 in the atmosphere and the creation of the ozone layer.[36] This 'Great Oxidation Event' prompted the world's greatest extinction event while also laying the foundations for the evolution of intricate multicellular aerobic species.[37]

$$6CO_2 + 6H_2O \xrightarrow{h\nu} C_6H_{12}O_6 + 6O_2 \qquad (1.3.1)$$

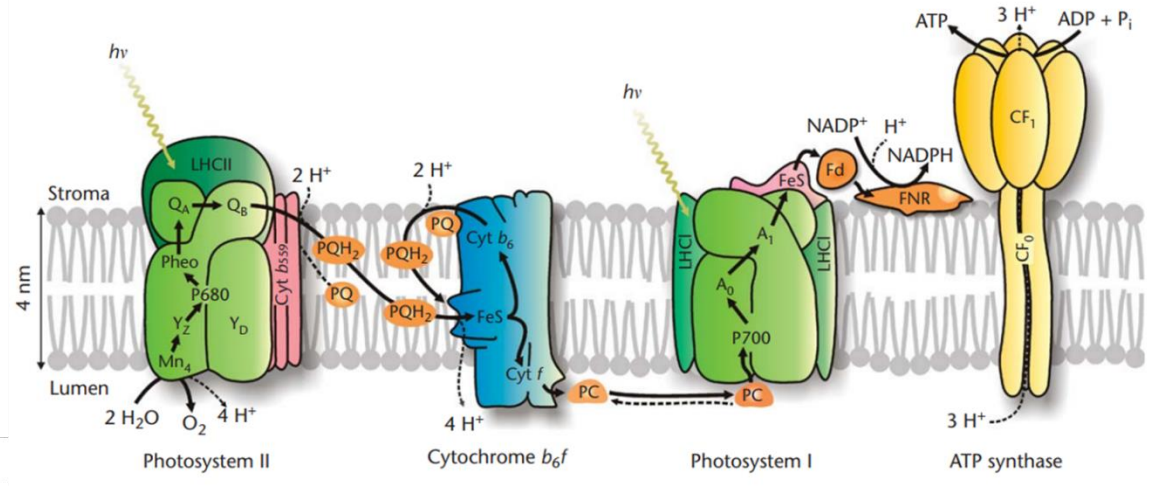

Figure 1.1: Representation of the light-driven electron-proton transport processes that takes place between the membrane-bound proteins and cofactors in the thylakoid membrane of photosynthetic organisms. Reproduced from reference 39.

Photosynthesis produces carbohydrates, which serve as the basic components of all living organisms as well as fossil fuels.[38] By developing and utilising a sophisticated electron-proton transport mechanism facilitated by highly complex thylakoid membrane-bound protein complexes and cofactors, cyanobacteria and eukaryotic photosynthetic organisms have managed to perfect the utilisation of solar energy (Fig. 1.1).[39]

Natural photosynthesis encompasses the absorption of sunlight and the conversion of its solar energy into electrical energy. The converted energy subsequently moves to nearby catalytic centres. At these sites it is further transformed into chemical energy while undergoing the catalytic splitting of H_2O and photoreduction of CO_2. More accurately, the process involves two units photosystem II and photosystem I. These units are connected by cytochrome b_6f and other electron carriers. These reaction centres shuttle electrons from H_2O to nicotinamide–adenine dinucleotide phosphate ($NADP^+$).

The process is initiated through the absorption of photons by porphyrin pigments chlorophyll *a* and chlorophyll *b* in the LHCII and LHCI units. This in turn produces a photoinduced charge separation.[40,41] The electron-hole pairs created in LHCII are subsequently channelled to P_{680}, primary electron donor of PS II.[40,41] Upon the excitation of P_{680}, P_{680}* subsequently transfers electrons to the pheophytin (Pheo) which shuttles the electrons to plastoquinone electron pairs Q_A and Q_B, creating $P_{680}^{\bullet+}$, $Q_A^{\bullet-}$ and $Q_B^{\bullet-}$. Regeneration of the P_{680} occurs through the transferal of electrons derived from H_2O by an $\{Mn_4\}$ cluster which is known as the oxygen-evolving complex (OEC) *via* the redox-active tyrosine residue (Y_z) to the excitonic dimer.[42] The reduction of $Q_B^{\bullet-}$ leads to the formation of plastoquinol (PQH_2). This PQH_2 passes through the thylakoid membrane and is oxidised by cytochrome b_6f and subsequently reduces plastocyanin (PC).

A second light-driven process takes place at P_{700} and functions as the primary electron donor of PS I. In PS I, the P_{700} oxidises PC, while in turn reducing the electron carrier protein ferredoxin (Fd) through the transfer of electrons from chlorophyll *a* (A_0) to the cofactor vitamin K (A_1) and subsequently to an iron-sulfur protein (FeS). Finally, electron transfer from the reduced Fd to $NADP^+$ is accomplished by the flavoenzyme ferredoxin-$NADP^+$ oxidoreductase (FNR) to generate NADPH. Figure 1.2 demonstrates the energy of the electrons involved in the process.[43] Nature's entirely sustainable energy storage approach is built on the foundation of this sequence of redox reactions.[44]

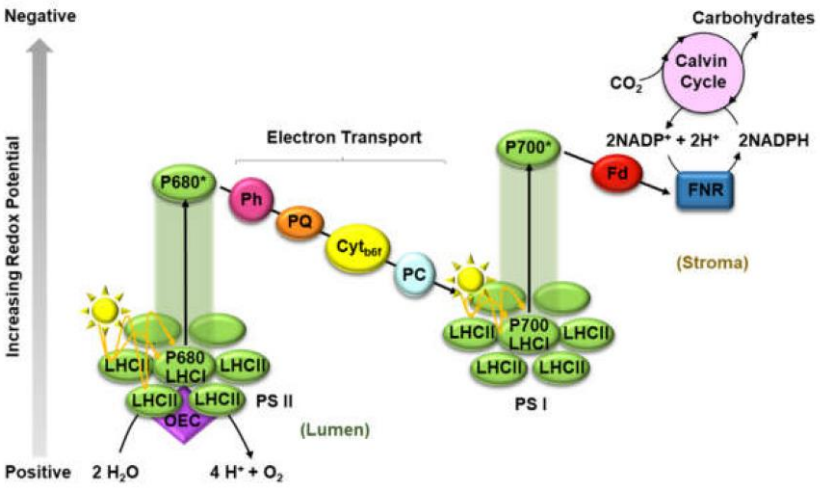

Figure 1.2: Schematic representation of natural photosynthesis with light-absorbing units PS I and PS II, electron transport chain, Oxygen-Evolving-Complex (OEC), $NADP^+$ reductase and the Calvin cycle in a "Z-scheme". Light-Harvesting-Complex (LHC), Pheophytin (Ph) Plastocyanin (PC), Plasmoquin (PQ), Ferredoxin-$NADP^+$ oxidoreductase (FNR), Ferredoxin (Fd). Reproduced from reference 43.

The proton gradient along the thylakoid membrane is ultimately formed through the oxidation of H_2O by the OEC, the sequential reduction of Q_A and Q_B, the oxidation of PQH_2 by cytochrome b_6f and the conversion of $NADP^+$ to NADPH by FNR. The mitochondrial enzyme, ATP synthase, localised in the inner thylakoid membrane, uses the energy stored within the proton gradient to convert adenosine diphosphate (ADP) to adenosine triphosphate (ATP). Finally, the Calvin-Benson cycle occurs which consumes the energy carriers ATP and NADH in order to drive the conversion of atmospheric CO_2 into carbohydrates.[45]

The photoexcitation of the P_{680} is a one-photon / one-electron process. Whereas, PQ reduction and H_2O oxidation are two- and four-electron processes, respectively. As a result, there is a requirement for a charge build-up coupled with protonation reactions involving intermediates. Furthermore, the highly endergonic process that is light-driven H_2O splitting has been calculated to have a Gibbs free energy of $\Delta G° = +237$ kJ per mole of decomposed H_2O.[46] By utilising photosystem II, a highly specialised, dimeric thylakoid membrane-bound protein complex with unmatched light-driven H_2O oxidation capabilities, nature overcomes energy challenges.[47]

1.4 Artificial Photosynthesis

1.4.1 H_2O Splitting Reaction

$$2H_2O \longrightarrow O_2 + 4H^+ + 4e^- \qquad E^\circ = 1.23\ V\ vs\ NHE \qquad (1.4.1)$$

$$4H^+ + 4e^- \longrightarrow 2H_2 \qquad E^\circ = 0\ V\ vs\ NHE \qquad (1.4.2)$$

$$2H_2O \longrightarrow O_2 + 2H_2 \qquad E^\circ = 1.23\ V\ vs\ NHE \qquad (1.4.3)$$

The abundance of H_2O throughout the world's seas, lakes, and rivers implies that the solvent of life possesses a virtually infinite supply of redox equivalents. Nature's approach to synthesising complex carbohydrates that perform a variety of functions is through the utilisation of high-energy protons and electrons that are extracted from H_2O by photosystem II.[48] Using this strategy, a more practical method for obtaining H_2, which could for instance be used for carbon-free fuel and chemical feedstock, could be accomplished through the recombination of reducing equivalents released during the decomposition of H_2O.[49,50] Thus, this method is possible by coupling H_2O oxidation (Eq. 1.4.1) with proton reduction (Eq. 1.4.2) to subsequently yield H_2 and O_2 (Eq. 1.4.3).

1.4.2 Electrolytic H_2O Splitting

In 1789, water electrolysis was first demonstrated by Jan Rudolph Deiman and Adriaan Paets van Troojstwijk.[51] It was discovered that applying an electrical potential to H_2O leads to its decomposition into its elemental constituents H_2 and O_2.[52] In their experiment, a strong electrostatic generator was used to deliver a voltage across two gold electrodes immersed in water, triggering the formation of H_2 at the cathode and O_2 at the anode. This significant discovery influenced the development of chemical theory. However, the process of generating H_2 using H_2O electrolysis is currently highly expensive.[53] The reason for this is that due to H_2O's intrinsic stability, substantial quantities of energy are required to bring about its decomposition into its elemental constituents. The free energy necessary to convert one mole of H_2O into H_2 and ½O_2 under standard conditions is ΔG° = 237.2 kJ. According to the Nernst equation, this equates to an electric potential of E° = +1.23 V per electron transferred.[54] In order to overcome the constraints involved with the breakdown and formation of novel chemical bonds, extra energy beyond this theoretical minimal potential (overpotential (η)), must be applied in reality.[55] This is especially the case for the oxygen-evolving reaction (OER), which necessitates the

transfer of four electrons and four protons, several bond rearrangements, and the creation of an O=O bond.[56,57] Using a water oxidation catalyst (WOC) or an H_2 evolution catalyst (HEC) in conjunction with an anode or cathode, respectively, the overpotentials of water splitting can be decreased.[58] Electrocatalysts help accelerate water splitting by providing alternate and lower-energy pathways, lowering the OER or hydrogen evolving reaction (HER) kinetic constraints and thus reducing the amount of energy needed to split water. The required overpotential needed to induce a catalytic reaction determines the efficiency of the electrocatalyst used in the experiment. Therefore, electrocatalysts performing at potentials near to $E°$ = 1.23 V vs NHE for the OER and $E°$ = 0.00 V vs NHE for the HER, are greatly desired.[59] Ultimately, ideal electrocatalysts present low overpotentials, high catalytic stability, and are made of inexpensive, non-toxic earth-abundant materials capable of large-scale commercialisation.[60–62]

Standard electrolysers, despite using effective catalysts, still require a considerable amount of energy and unless they are coupled with renewable energy sources, this method will not provide a long-term solution to the energy emergency.[63] Hence, solar energy may be used to power this operation in a sustainable manner. Thus, allowing H_2 to be produced without the need for fossil fuels. Even though such artificial photosynthetic devices have significant potential benefits, they also pose substantial technological difficulties.

1.4.3 Photo-Electrochemical Cell (PEC)

In 1972, the first significant step forward in the development of light-driven water splitting was reported by Fujishima and Honda.[64,65] In their setup, a titanium dioxide (TiO_2) semiconducting photoanode was exposed to UV light, generating oxygen at the anode and hydrogen at a nonirradiated platinum cathode. Additionally, the development of the photo-electrochemical cell (PEC) led to the enhancement of this significant technological breakthrough.[64] Using a PEC, solar energy may be converted into energy stored in chemical bonds and as a result, this discovery offered the first concrete evidence that artificial photosynthesis may be feasible. A conventional PEC is made up of two semiconductor electrodes submerged in an aqueous electrolyte solution and linked through an exterior circuit (Fig. 1.3).[66]

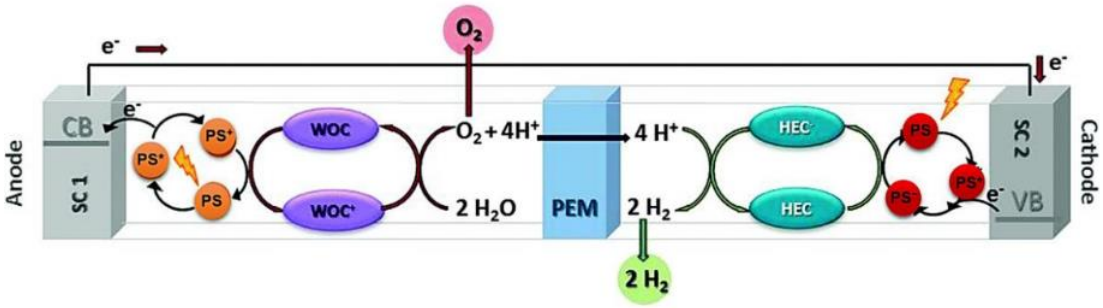

Figure 1.3: Photo-Electrochemical Cell for light-driven H_2O splitting. Photosensitiser (PS), Proton Exchange Membrane (PEM), Semiconducting photoelectrodes (SC 1 or SC 2), Hydrogen evolution catalyst (HEC) and Water Oxidation Catalyst (WOC). Adapted from reference 15.

A proton exchange membrane (PEM) separates a PEC into two segments. The first is the anodic section for OER and the second is the cathodic section for HER. Physical segregation is beneficial since an effective WOC could be inactive towards the HER, while an efficient HEC could be unsuitable for facilitating the OER. Furthermore, having two separate sections for H_2 and O_2 production is advantageous because it enables the generation of highly pure H_2 in a secure environment since it inhibits the explosive mixing of the two gases. Photons absorbed by semiconducting photoelectrodes (SC 1 or SC 2) with adequate band gaps or by an accompanying photosensitiser (PS) supplies the driving power for water splitting. Utilising either a WOC, a HEC or even both can enhance the system's performance by reducing the amount of energy necessary to produce O_2 and H_2.[67] PECs have been widely investigated for water splitting since Fujishima and Honda's first development.[68,69] Despite major technological advancements, these systems are still presented with challenges such as attaining a solar-to-hydrogen conversion rate of more than 10% along with the long-term stability of the devices.[70,71] Additionally, the semiconductors used in PECs generally consist of wide band gaps meaning significant portions of the solar spectrum cannot be used. For instance, the PEC system Fujishima and Honda used employed an n-type TiO_2 photoanode semiconductor which could only absorb UV-light as it consisted of a ~3.2 eV band gap.[72,73] As a result, PEC systems are not currently a commercially feasible method of producing H_2.[74] In order to economically improve PECs for water splitting, a considerable amount of research is being conducted to increase the efficiency of these technologies.[66,67,75] An example of this is through the development and use of viable WOCs and HECs to reduce the overpotentials for water splitting. The employment of homogeneous catalysts by their dissolution in the

electrolyte or heterogeneous catalysts through their anchoring to electrodes can be used to improve the formation of both O_2 and H_2.[15] Similarly, the development of semiconductors with narrower band gaps or the incorporation of a light-absorbing PS may enable the use of larger sections of the solar spectrum.[76]

1.4.4 Photocatalytic H_2O Splitting

At present, solar water splitting is a popular topic in materials and catalysis research.[77] Investigating and optimising catalysts individually for each half-reaction is a common approach. This can be accomplished by the utilisation of homogeneously dispersed PSs and sacrificial reagents, where the latter enables independent research and optimisation of OER and HER catalysts. Thus, in these systems, electrons travel through the WOC or HEC, replicating what occurs in a PEC. However, compared to a complete water splitting cell, fewer parameters must be controlled, and detrimental charge-carrier recombination events are avoided. Hence, studying the OER and HER individually, the evolved gases in the respective reactions do not need to be isolated. Upon optimisation of the WOC and HEC, the catalysts can be integrated into a functioning PEC.[78]

1.4.5 Photosensitisers for H_2O Splitting

In every photocatalytic water splitting system, a light-harvesting PS is essential.[79] Photoinduced charge separation is achieved when a photon is absorbed by a PS, resulting in the oxidation or reduction of a WOC or a HEC, respectively. Therefore, PS are crucial drivers for photocatalytic OER and HER.[78] In addition to being constructed from inexpensive and abundant, non-toxic materials, a PS in order to be viable for photocatalytic water splitting must satisfy numerous demanding requirements. These prerequisites include having the ability to absorb a wide range of visible light and possess a redox potential large enough to accommodate electron transfer from a WOC or a HEC. Additionally, the PS must boast long-lived excited states and demonstrate photostability.[80,81] It is also essential that suitable anchoring groups such as carboxylate anchors are present in the structure of the PS to ensure successful binding to semiconductor surfaces.[82] In the literature, chromophores such as Ru- and Ir-based polypyridyl complexes and porphyrins amongst others have been employed as PSs for

photocatalytic water splitting.[83–87] Figure 1.4 below illustrates the structures of some of the most commonly used PSs.

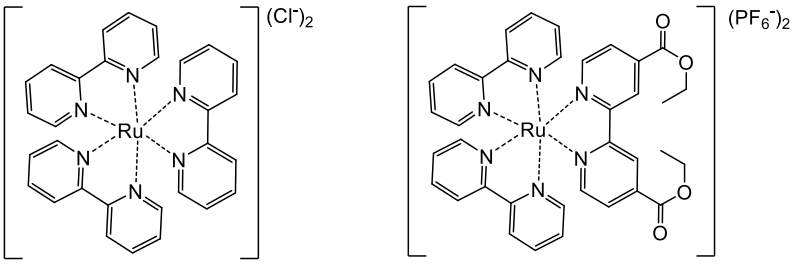

Figure 1.4: Common PSs used in photocatalytic water splitting. $[Ru(bpy)_3]Cl_2$ (left) and $[Ru(bpy)_2(deeb)](PF_6)_2$ (right).

Ruthenium polypyridyl complexes are highly attractive photosensitisers for water splitting due to their broad coverage and high molar absorptivity in the visible region, along with their acceptable redox potentials.[88–90] Similarly, ruthenium-polypyridyl complexes exhibit broad absorption spectra, extended excited-state lifetimes, and excellent electrochemical stability. The ancillary ligands, which are commonly bipyridines or terpyridines, can be substituted with other functional groups to enhance spectroscopic and electrochemical characteristics. Furthermore, $[Ru(bpy)_3]Cl_2$ (bpy = 2,2'-bipyridine) is one of the most investigated PS for molecular catalytic water splitting experiments.[91,92] This homoleptic polypyridyl Ru^{II} complex is commonly used since it fulfils the majority of the criteria discussed previously. However, there are certain drawbacks of using $[Ru(bpy)_3]Cl_2$ as the photosensitiser for such catalytic experiments, such as its susceptibility to decomposition under working conditions of the OER, as well as high costs, due to its rare-earth element (ruthenium) content.[93]

Another series of ruthenium complexes of the form $[Ru(4,4'\text{-}(COOH)_2bpy)_2(X)_2]^{2+}$, where X=Cl, Br, I, CN, or SCN were reported by Gratzel *et al.*.[94] These complexes showed to be efficient photosensitisers, especially the thiocyanato complex $(NBu_4)_2[Ru(4,4'\text{-}(COOH)(COO)bpy)_2(NCS)_2]$ which is often known as N719 or "red dye". Between 480 nm and 600 nm, this Ru complex demonstrated an extinction coefficient of 14,000 M^{-1} cm^{-1} and an incident photon-to-current conversion efficiency (IPCE) of over 80%.[94] Thiocyanate ligands are believed to enhance visible light absorption and charge transfer between the photoexcited chromophore and the iodide/triiodide redox mediator, resulting in increased dye-sensitised solar cell (DSSC) efficiency.[95,96] Similarly, ruthenium complexes which absorb incident light more

efficiently due to their larger extinction coefficients in the visible region have also been reported in the literature. Examples of these include a series of heteroleptic ruthenium sensitisers with the formula $[Ru(4,4'\text{-}(COOH)_2bpy)(4,4'\text{-}(R)_2bpy)(NCS)_2]$, where R is an electron-rich substituent such as alkyl thiophene,[97,98] alkyl furan,[98] phenylene vinylene[99,100] or 2-thiophene-2-yl-vinyl[101]. These ruthenium photosensitisers demonstrated extinction coefficients of up to 24,200 M^{-1} cm^{-1} at 554 nm.[97]

Similarly, the heteroleptic ester functionalised photosensitiser, $[Ru^{II}(bpy)_2(deeb)](PF_6)_2$ (deeb = diethyl 2,2'-bipyridine-4,4'-dicarboxylate) is a further promising chromophore for sensitising water splitting catalysts. This complex is highly comparable to the previously mentioned $[Ru(bpy)_3]Cl_2$. However, in its one-electron oxidised form, it exhibits a higher redox potential. The redox potential of the homoleptic $[Ru(bpy)_3]Cl_2$ is $E_{1/2}$ $[Ru^{III}(bpy)_3]^{3+}/[Ru^{II}(bpy)_3]^{2+}$ = 1.26 V vs. NHE, while the heteroleptic $[Ru^{II}(bpy)_2(deeb)](PF_6)_2$ exhibits a redox potential of $E_{1/2}$ $[Ru^{III}(bpy)_2(deeb)]^{3+}/[Ru^{II}(bpy)_2(deeb)]^{2+}$ = 1.40 V vs. NHE. Hence, due to the higher redox potential of $[Ru^{II}(bpy)_2(deeb)](PF_6)_2$ it is predicted that this photosensitiser produces a greater driving force for water splitting reactions.[91]

In addition to ruthenium polypyridyl chromophores, porphyrins have been extensively explored in artificial photosynthesis as biomimetic light harvesters.[102] Lifetimes and charge recombination of photoinduced charge-separated states have been vastly investigated using porphyrin-based donor-acceptor dyads.[103,104] Similarly, photoinduced electron transfer to catalytic electron mediators through non-covalent bonds has also been studied using these systems.[105,106] Furthermore, aside from not being made of rare-earth metals, porphyrins have an advantage over ruthenium complexes as their absorption spectra expand further into the near-IR region, while in the visible region of the spectrum, they frequently have high molar extinction coefficients and a good IPCE.[65,80,107] Porphyrin sensitisers have also been employed in DSSCs exhibiting total power conversion efficiency upwards of 10%.[108–110] However, a major disadvantage of utilising porphyrins as photosensitisers is their inherent tendency to aggregate. This leads to interactions between photoexcited and ground-state species, lowering the porphyrins' overall efficiency as photosensitisers. Nevertheless, high-potential porphyrins have indeed been considered efficient light harvesters for light-driven water splitting reactions.[111,112]

As previously mentioned, one of the key disadvantages of Fujishima and Honda's water oxidation system is that it required UV irradiation with wavelengths below 385 nm in order to drive electrons over TiO_2's 3.2 eV band gap.[64] Therefore, shifting the absorption towards the visible region has been the subject of much investigation. Many methods for this have been investigated in the literature, including the development of non-oxide semiconductors,[113] doping of wide band gap semiconductors,[114] the addition of secondary nanoparticles,[115–117] or sensitisation of the semiconductor surface with materials that absorb photons over the entire solar spectrum.[94,109,118–123] A significant approach within the literature has been the utilisation of nanoporous thin films to bind and employ materials that enable the absorption of photons across a greater portion of the solar spectrum.[124] Therefore, the most commonly employed PSs for light-harvesting water-oxidation photoanodes are ruthenium-based polypyridyl complexes, porphyrins, and organic dyes.[88–90,111]

1.5 Catalysts for H_2O Oxidation

The major bottleneck process in light-driven water splitting is the OER.[15,125] While there are several efficient catalysts for the HER, catalysing the thermodynamically demanding OER is considerably problematic.[126–128] The main reason for this is the OERs endergonic and intricate character, as significant overpotentials are required for the reaction to proceed successfully.[56,57,129] Furthermore, for a WOC to be efficient in OERs it must be able to sustain strongly oxidising settings, generate four oxidising equivalents, and be stable to various intermediates.[78,130,131] Therefore, stable, low-cost WOCs that fulfil the above requirements have the capacity to change societies approach toward renewable energy production.[132–135]

To quantitively compare catalysts in the literature, two main metrics are used; Turn-Over-Number (TON) and Turn-Over-Frequency (TOF). The term TON is related to the robustness of the catalyst i.e. the maximum use of a catalyst under defined reaction conditions (Eq. 1.5.1).[136,137] Whereas the TOF is associated with a catalyst's activity and can be calculated as the derivative of the number of turnovers of the catalytic cycle with respect of the time per active site (Eq. 1.5.2).[136,137]

$$TON = \frac{Moles\ of\ O_2\ Evolved}{Moles\ of\ WOC\ Employed} \quad (1.5.1)$$

$$TOF = \frac{Moles\ of\ O_2\ Evolved}{Moles\ of\ WOC\ Employed\ x\ Time\ Elapsed} \quad (1.5.2)$$

1.5.1 Molecular WOCs

Much research has been carried out on the synthesis of highly active and sufficiently stable molecular WOCs that mimic the OEC for large scale and low-cost H_2 generation.[131,138] It has been identified that redox-active metal centres and stabilising organic ligands are often the main components of these systems.[15] The advantages of utilising molecular WOCs come from their optimisable electronic characteristics and their potential to be attached to the surface of anodes of advanced water splitting technologies.[139,140] In 1982, Meyer *et al.* reported the first molecular WOC, a dinuclear ruthenium complex (cis,cis-$[(bpy)_2(H_2O)Ru^{III}ORu^{III}(H_2O)(bpy)_2]^{4+}$) (Fig. 1.5).[141,142] This molecular WOC displays a turnover frequency (TOF) of 4.2×10^{-3} s^{-1} and a turnover number (TON) of 13.2 and is given the name 'blue dimer' due to its distinct colour in solution.[143–145]

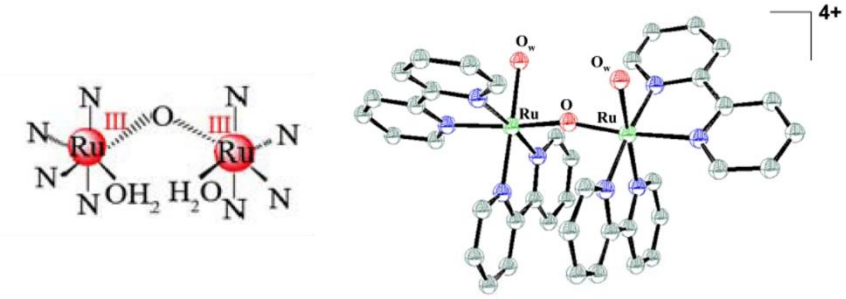

Figure 1.5: Structure of the ruthenium 'blue dimer' cation, cis,cis-$[(bpy)_2(H_2O)Ru^{III}ORu^{III}(OH_2)(bpy)_2]^{4+}$. The first molecular WOC. Colour scheme: C grey, N blue, O red, Ru lime green. Reproduced from reference 144.

A multitude of mono- and polynuclear WOCs exhibiting over five orders of magnitude higher TOFs and TONs have been synthesised since the discovery of the 'blue dimer'.[146] Catalysts composed of non-toxic and earth-abundant elements are important and highly relevant in the goal of reaching a compromise between high performance and cost-effectiveness.[68] Therefore, several first-row transition metals, such as Co,[147–150] Ni,[151] Cu,[152,153] Cr,[154] Mn,[89,155–159] and Fe,[160,161] have indeed been utilised to construct OER catalysts.

Moreover, Co-based WOCs in the literature have in recent years demonstrated remarkable O_2 evolution activity.[162–166] In 2017, a noble metal-free polyoxometalate (POM) ($Ba_8[Co_9(H_2O)_6(OH)_3(HPO_4)_2(PW_9O_{34})_3]\cdot 55H_2O$) reported by Galán-Mascarós *et al.* (Fig. 1.6) exhibited significant electrocatalytic OER activity when coupled with

carbon paste.[167] The OER activity obtained using this POM when compared to that of cutting-edge catalysts such as IrO_2 is exceptional as it achieves a high current density of 1 mA cm^{-1} at an overpotential of 189 mV in acidic conditions.

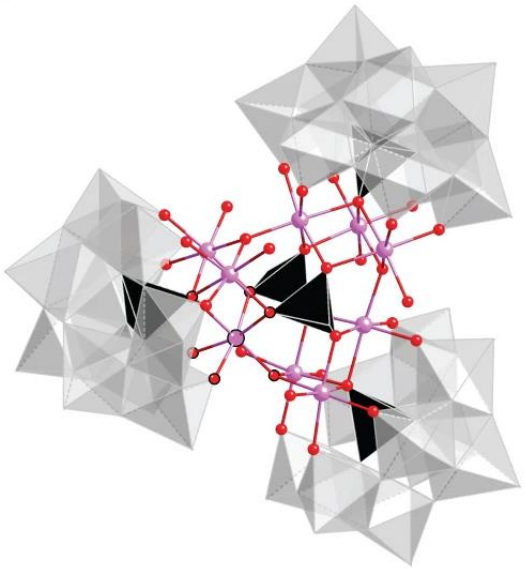

Figure 1.6: Molecular structure of the Co-based POM WOC $[Co_9(H_2O)_6(OH)_3(HPO_4)_2(PW_9O_{34})_3]^{16-}$ cluster. Colour scheme: Co pink, O red, WO_6 grey octahedra; PO_4, black tetrahedra. Reproduced from reference 167.

1.5.2 Photosensitiser – Catalyst Dyad Complexes

As mentioned previously, the major bottleneck to light-driven water splitting is the OER however, this bottleneck to O_2 production is made up of many processes. Research by Limburg *et al.* revealed that the rate-limiting step for particularly active WOCs involves the oxidation of the WOC by the PS^+.[93] This research demonstrated that the overall stability of the photocatalytic system is reduced due to the build-up and swift decay of the PS^+. This build-up is a result of the sluggish rate of electron transfer between the WOC and the PS^+. Thus, it is believed that the performance of the OER can be improved by enhancing the electronic communication between the two moieties.

A possible method to overcome these issues and improve electronic communication is by directly tethering a PS to a WOC *via* coordination or covalent bonds.[15] Numerous investigations have indicated that supramolecular structures composed of PSs that are chemically bonded to WOCs display higher performances compared to their intermolecular counterparts.[168–171] One of these promising supramolecular assemblies is a diruthenium PS – WOC dyad photocatalyst reported by Thummel *et al.*. Over six hours this complex demonstrated a TON of 134, which is twenty times higher than that obtained for a similar multicomponent system operating under identical conditions.[172] Therefore, efficient PS – WOC dyad photocatalysts may be utilised to generate H_2 and O_2 from solar energy and H_2O *via* their incorporation into dye-sensitised photoelectrochemical cells (DSPEC).[173,174]

Tuneable hybrid organic-inorganic materials such as metal-organic frameworks (MOFs) have the ability to incorporate PSs and WOCs within their well organised supramolecular structures.[175] The following section will introduce and provide an overview of the synthesis and the various applications of these promising and multifunctional materials.

1.6 Porous Inorganic and Hybrid Materials

Coordination compounds obtain their name from the presence of coordination bonds within their structures.[176] These coordination bonds are believed to form as a result of the donation of electron pairs from the ligands to the metal ions. Compounds that comprise of coordination bonds are commonly termed as 'complexes'. These compounds have been utilised since earlier civilisations and are commonly found in dyes and pigments due to their vibrant colours.[177] The range of colours and vibrancy of these compounds arises from the presence of transition metals in their structure. These transition metals give rise to the absorption of light within the visible region through a variety of mechanisms, including metal to ligand charge transfer, ligand to metal charge transfer and d-d transitions. Among the most well-known examples of these compounds are Prussian blue ($Fe_7(CN)_{18}$) a dark blue pigment and aureolin ($K_3[Co(NO_2)_6]$) a yellow pigment.

In 1756, Swedish mineralogist Axel Fredrik Cronstendt first identified an interesting group of compounds which today is one of industries most widely used porous materials. Upon heating a material known as stilbite, Axel Fredrik Cronstendt observed the production of steam which as a result lead to the discovery of the materials porous nature. He created the term 'Zeolite' from the Greek words 'zeo' meaning to boil and 'lithos' meaning stone to characterise this class of porous aluminosilicates, which is still used today.[178] One of the appealing aspects of these materials is that they may be extracted from the ground or synthesised at a low cost for industrial processes.[179] Many of them have broad industrial applications due to their series of properties such as their unique structures and particularly high porosities. Examples of industrial applications include the utilisation of these materials as absorbents, removal of Ca^{2+} from water and petrochemical 'cracking' and reforming. These aluminosilicates are comprised of AlO_4^{5-} and SiO_4^{4-} building units which give rise to a near-endless family of 3-dimensional inorganic highly porous structures that reveal surface areas on the order of hundreds of m^2/g (Fig. 1.7).[180–182] SBA-15 and MCM-41 are structurally similar mesoporous silicas that comprise of larger nanoscopic pores and surface areas of 900 and 2400 m^2/g, respectively.[183,184]

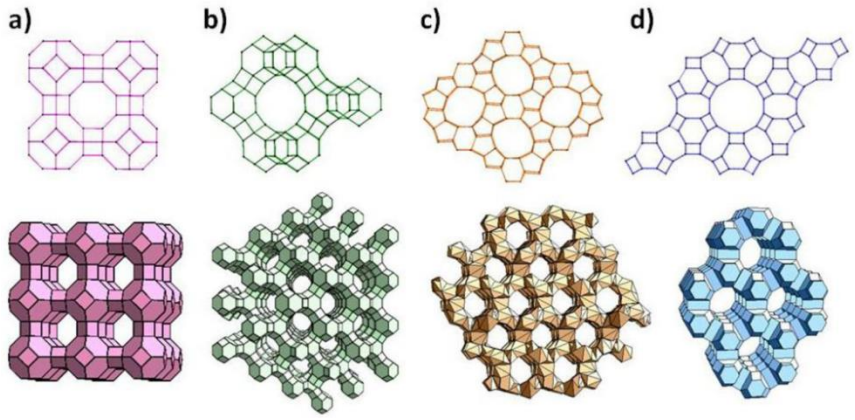

Figure 1.7: Various zeolite frameworks. a) Zeolite A (3D, 4.2 Å pores), b) Zeolite Y (3D, 7.4 Å pores), c) Zeolite L (1D, 7.1 Å pores) and d) ZSM-5 (silicalite) (2D, 5.3 × 5.6 Å and 5.1 × 5.5 Å pores). Reproduced from reference 181.

1.7 Metal-Organic Frameworks

1.7.1 Definition and Overview

MOFs are thought to be highly promising materials of the 21st century.[185,186] They are an important class of crystalline coordination polymers typically characterised by large surface areas and permanent porosity.[187,188] MOF chemistry, which is founded on both organic and inorganic chemistry has attracted widespread scientific attention in recent years since the early pioneering work of Hoskins and Robson in the 1990s.[187,189–191] These modular, metallo-supramolecular polymeric materials are formed through the repeating series of inorganic secondary building units (SBUs or 'nodes') such as metal ions or clusters that are linked by multitopic organic ligands (or 'linkers') *via* coordination bonds.[192,193] A wide range of inorganic SBUs consisting of main group metals,[194,195] transition metals,[196,197] lanthanides[198–202] and actinides[203,204] in combination with an almost endless number of organic ligands have been used to produce a variety of infinitely extended 1D, 2D or 3D networks with high crystallinity and long-range order (Fig. 1.8).[205,206] The various exciting properties of MOFs such as their high surface areas and their ability to be easily modified, enable these materials to be employed in a large range of novel technologies to address a diverse set of scientific challenges.[207–210]

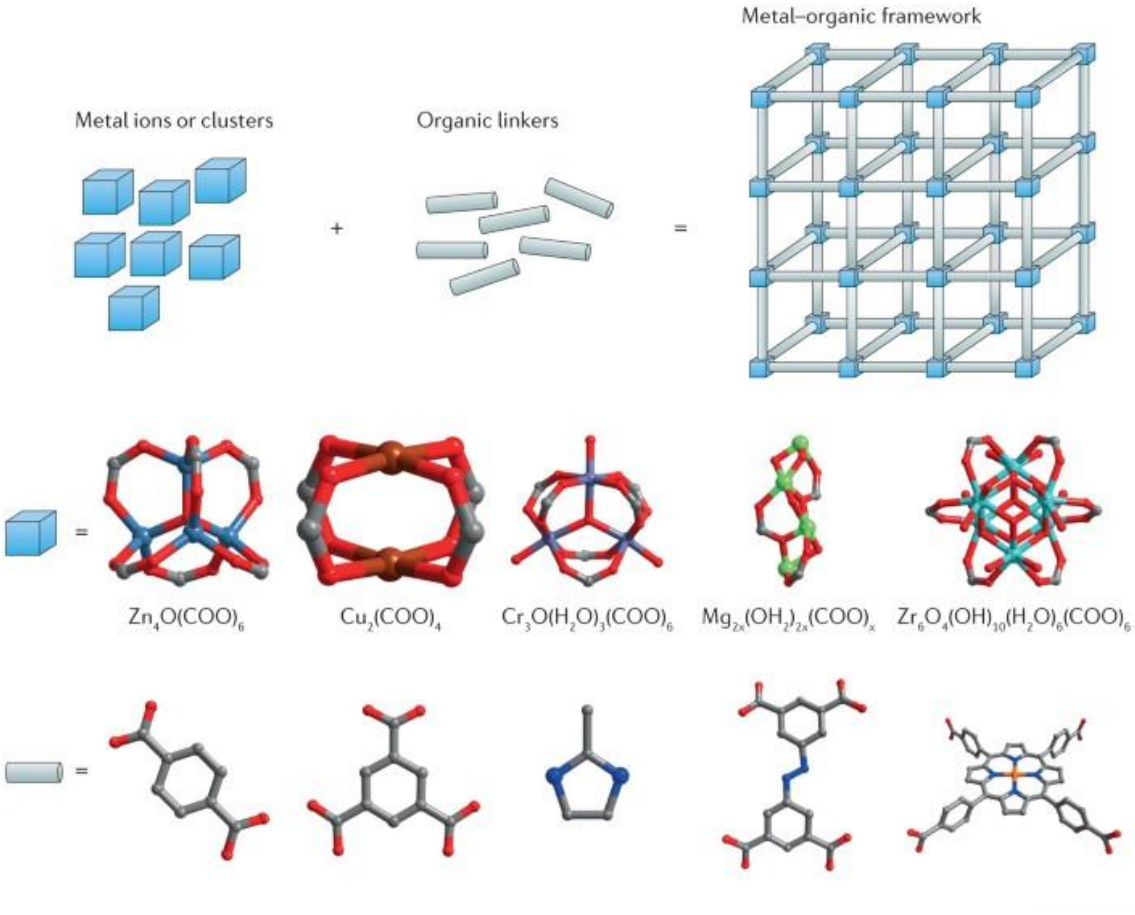

Figure 1.8: Illustration showing the assembling of inorganic and organic materials to produce a MOF network (top). Examples of SBU clusters featuring Zn^{II}, Cu^{II}, Mg^{II}, Cr^{III} and Zr^{IV} metal ions (middle). A series of typical ligands containing carboxylate, imidazolate, azolate or porphyrin functional groups (bottom). Colour scheme: C grey, O red, N blue, Zn^{II} light blue, Cu^{II} orange, Cr^{III} purple, Mg^{II} green and Zr^{IV} cyan. Reproduced from reference 205.

Briefly looking back at the history of these materials, in 1995 Yaghi *et al.* first introduced the name "metal-organic framework" when reporting a porous 3D interpenetrated network which was composed of Cu^{I} SBU nodes and bipyridine ligands $Cu(bpy)_{1.5}{\cdot}NO_3(H_2O)_{1.25}$.[211] Subsequently, in 2003 O'Keeffe *et al.* proposed that MOF structures may be controlled by carefully selecting the building blocks required, a technique that is known as "reticular synthesis".[188] The term reticular synthesis has been defined as "the process of assembling judiciously designed rigid molecular building blocks into predetermined ordered structures (networks), which are held together by strong bonding".[188] Hence, this building block approach enables the systematic

preparation of several isoreticular ('iso-reticular' = same net) MOFs with similar topologies by simply varying different parameters, such as the geometry of the organic linkers.[212–214] This concept is demonstrated by the isoreticular series of MOF-5 ($[Zn^{II}_4O(BDC)_3]$, BDC = 1,4-benzenedicarboxylate) analogues (IRMOFs) (Fig. 1.9).[215] MOF-5 was first discovered in 1999 and is a 3D porous MOF with a primitive cubic (**pcu**) topology, consisting of octahedral $\{Zn^{II}_4O\}$ SBUs linked by ditopic BDC ligands.[216]

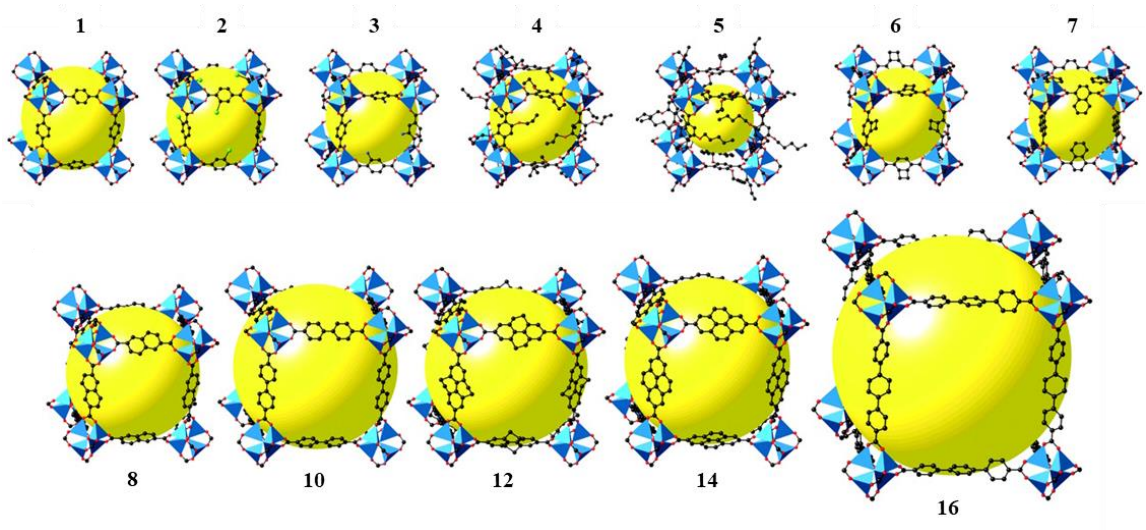

Figure 1.9: Crystal structures of MOF-5 (1) and IRMOF-n (n = 2 – 7, 8, 10, 12, 14, and 16), labeled respectively. Hydrogen atoms have been omitted for clarity. Colour scheme: C black, O red, Br green (in 2), amino-groups blue (in 3), Zn^{II} centres blue polyhedra. The void space is represented by yellow spheres. Adapted from reference 192.

In addition to the permanent porosity of MOFs demonstrated by Kitagawa *et al.*, the potential to construct these materials with predefined topologies and voids prompted a significant surge of interest in the field.[217] Following the evolutionary research by Hoskins and Robson,[189,193] O'Keeffe,[187] Fujita,[218] Kitagawa,[219] Zaworotko,[220] and Yaghi,[221] more than 99,000 unique MOFs have been deposited into the Cambridge Structural Database (CSD).[222] While, only in the last two decades there have been over 20,000 publications in the field alone.[223]

1.7.2 Synthesis of Metal-Organic Frameworks

The synthesis of MOFs can be problematic and the optimal reaction conditions for various metal-ligand combinations in each specific reaction must be identified. Additionally, MOF single crystals typically need to be obtained as to elucidate their specific unique structures. Furthermore, MOF synthesis does not necessarily always result in the formation of the desired product or default structure.

In most cases, MOFs are synthesised in the liquid phase through the combination of a metal salt with an organic ligand in an appropriate solvent mixture inside a sealed vessel. Two methods are predominantly used, the classical method or the solvothermal method. In the classical method, the reaction solution is maintained at a temperature that is less than the solvent's boiling point.[224] While, in the case of the solvothermal method, the reaction solution is heated to temperatures above the boiling point of the solvent.[225] Therefore, under appropriate conditions, a self-assembly process will result in the formation of crystalline MOF.[226,227] Moreover, the synthetic process generally used to synthesise MOFs is solvothermal synthesis. This process requires the use of a sealed Teflon-lined stainless-steel vessel containing the reaction solution which is heated for extended periods of time at high temperatures typically over the solvents boiling point (Fig. 1.10).[228] This approach provides the necessary energy to meet the thermodynamic requirements for the formation of MOF networks while also overcoming possible reactant solubility issues.[229–231] Utilisation of this method provides an effective means of obtaining desirable single crystals suitable for single-crystal X-ray diffraction studies.

However, if the crystallised material obtained is not of adequate quality for single-crystal X-ray diffraction experiments, the structure with sufficient certainty can thus be exceedingly challenging or impossible to elucidate. Hence, crystallisation is a delicate process that is frequently only achieved after much trial and error. Therefore, this ‘trial and error’ process can be seen as a limiting factor in the synthesis of MOFs. In addition, the exclusive formation of the desired material is not guaranteed during crystallisation as the target crystals must frequently be separated from other products.

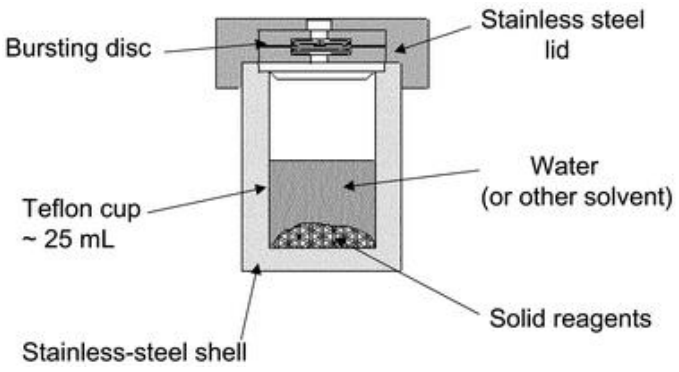

Figure 1.10: A schematic representation of a Teflon-lined stainless-steel autoclave generally used to perform solvothermal synthesis. Reproduced from reference 228.

Solvothermal techniques offer the ability to control and vary a wide range of synthetic factors, such as reactant concentrations, reaction time, temperature, pressure and pH. These variations can lead to an endless series of unique compounds or alterations to the size and morphology of the previously obtained crystals. Therefore, this approach has proven highly effective for the formation of hybrid inorganic-organic materials, such as MOFs. Further, dialkylformamide-type solvents are frequently chosen as the medium for solvothermal synthesis as the slow decomposition of this solvent results in the formation of dialkyamines which subsequently leads to the deprotonation of carboxylic acid-based ligands. This approach thus aids SBU and crystal formation of the MOF (Fig 1.11 (a)).[232] The reaction temperature should by definition, surpass the boiling point of the solvent,[233] however, this term is frequently used in the literature to classify reactions in sealed containers at high temperatures below the solvents boiling point.[234–236]

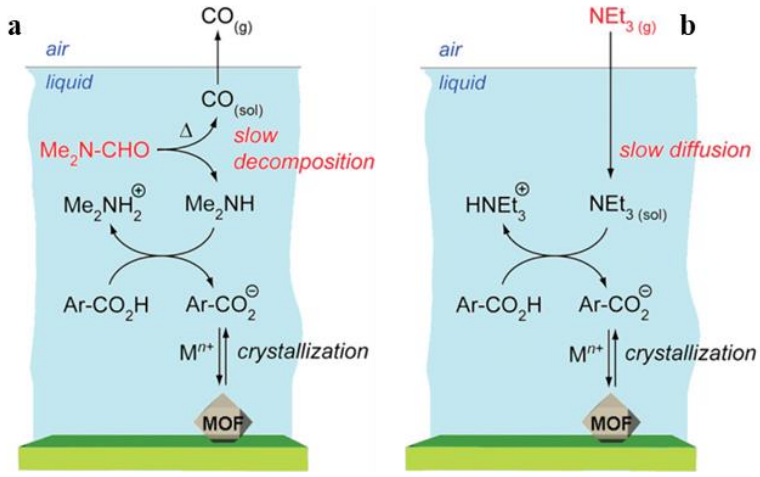

Figure 1.11: Typical crystallisation routes for the synthesis of MOFs. Slow thermal decomposition of N,N-dimethylformamide (a) and slow vapor diffusion of a base, triethylamine (b). Reproduced from reference 232.

Different synthetic strategies also employed for the formation of MOFs include electrochemical,[232,237–240] microwave-assisted,[241–243] mechanochemical,[244,245] sonochemical[246,247] and vapour diffusion[248] methods (Fig 1.12). The latter technique, for example, was initially used for the synthesis of the previously mentioned MOF, MOF-5.[216] This strategy involves the gradual diffusion of a base into its respective reaction system, resulting in carboxylate-based ligand deprotonation and slow crystallisation (Fig. 1.11 (b)). Furthermore, depending on the desired properties, morphology and target application of a MOF, the appropriate synthetic technique is selected. Once the structure of a MOF has been determined, techniques such as microwave-assisted, mechanochemical and sonochemical synthesis are frequently utilised to scale up manufacturing.

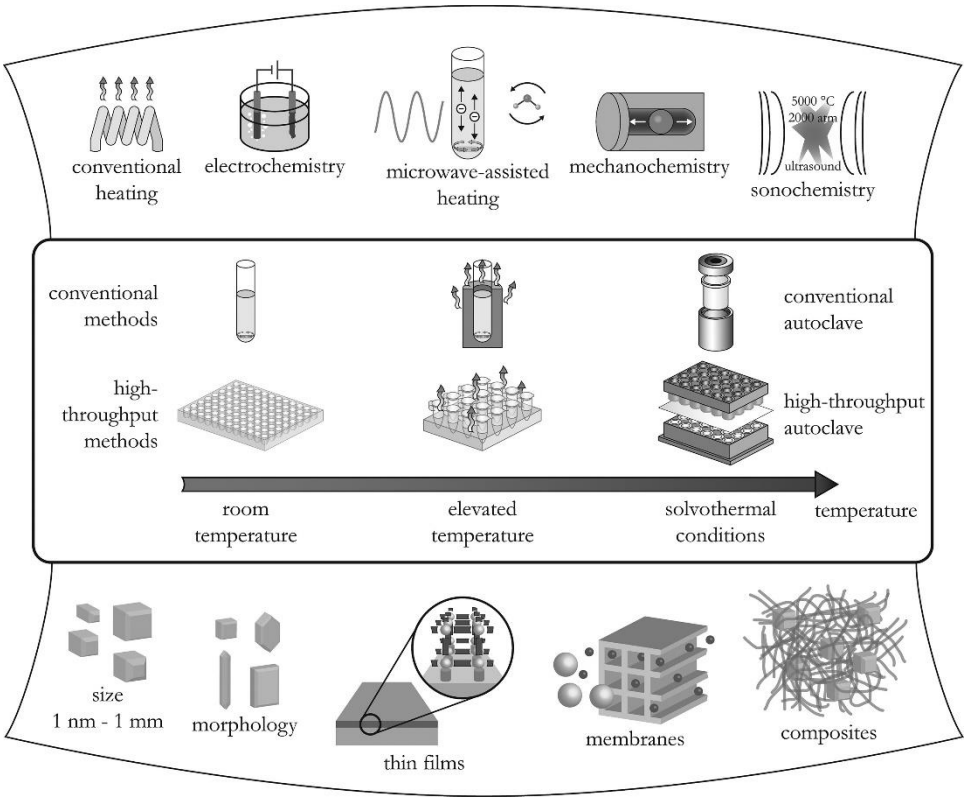

Figure 1.12: Illustrative overview of a series of synthetic techniques, various reaction temperatures, and final products in MOF synthesis. Reproduced from reference 189.

1.7.3 Electrochemical Synthesis and MOF deposition

Electrochemical deposition methods may be used to synthesise MOFs on conductive surfaces.[249] These approaches enable the production of MOFs on conductive surfaces, as thin films, in a fraction of the time necessary when compared to solvothermal synthesis. Additionally, the ambient conditions of temperature and pressure used, make electrochemical techniques both highly appealing and cost-effective.

For electrochemical deposition, two methods, anodic or cathodic deposition are typically used. However other methods such as charge driving,[250] dip-coating[251] and layer-by-layer[252] methods are also used for the fabrication of thin films. For the cathodic deposition approach, the reaction system contains both the inorganic and organic components required for the synthesis of the respective MOF. The synthetic mechanism is believed to be accredited to a change in the pH value of the reaction mixture at the electrode surface. The process begins with the production of a 'pro-base' at the cathode. The 'pro-bases' typically produced are oxoanions, such as nitrite ions, which are formed through the reduction of nitrate ions. These oxoanions have the ability to form oxide or hydroxide ions through the reduction of water in the reaction mixture. The hydroxide ions generated, subsequently deprotonate the carboxylic acid ligands in addition to possibly being required for the formation of certain SBUs.[232] Furthermore, the applied negative potential at the conductive surface attracts solvated metal ions which in combination with the deprotonated ligands in the solution induce the self-assembly, growth and electrodeposition of the respective MOF crystals on to the conductive substrate surface (Fig. 1.13). It is worth noting that this approach enables facile surface functionalisation, as well as being a highly effective approach to producing MOF electrodes for photo/electro-catalytic experiments.[250]

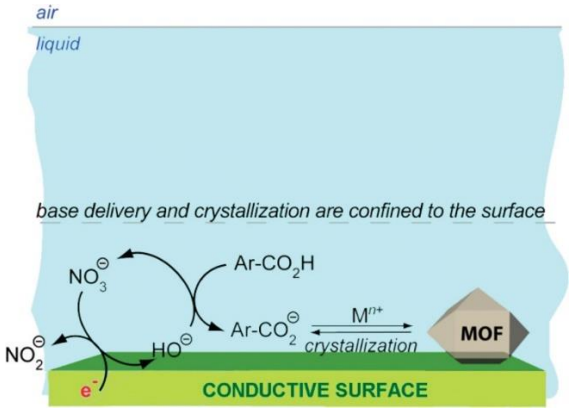

Figure 1.12: Mechanism of cathodic electrodeposition of crystalline MOFs at the conductive surface. Reproduced from reference 232.

The anodic deposition approach involves a reaction medium that at first only contains the ligand necessary for producing the MOF. The necessary metal ions are subsequently formed through anode oxidation. The structure and composition of the synthesised MOF is determined by the nature of the anode used.[253] Furthermore, the general mechanism of anodic electrodeposition may be separated into four stages; nucleation, growth of islands, intergrowth and detachment.[237]

Firstly, an applied oxidising potential results in the release of metal ions from the anode into the reaction mixture. When a sufficient metal-ligand concentration is achieved, MOF nuclei begin to develop both in the reaction mixture and on the surface of the anode.

Secondly, it has been found that following the formation of the initial nuclei, additional crystals tend to accumulate next to these existing ones, generating the growth of islands. The reason for this type of growth can be associated with the high current densities in the regions surrounding the crystals as a result of MOFs high resistance to current flow. Therefore, the high current density along with increased concentrations of metal ions in the region of existing crystals lead to the formation of additional nuclei and subsequently the growth of islands.

The highly important third phase of anodic electrodeposition is intergrowth. Compact intergrown layers of MOF formed from the growth and accumulation of nuclei, cover the surface of the anode. In addition, the ability of metal ions to diffuse through the pores, further promotes the production of MOF on the coated anode. However, further development of the MOF below a MOF layer may not occur due to the inability of large ligands to permeate through to the anode surface.

Finally, in order to obtain high quality electrodeposition of the MOF material, the last phase, detachment, must be avoided. Here, single crystals or most often larger MOF layer coatings detach from the anode and disperse into the reaction mixture. This phase typically arises from the breakdown of the anode material forming voids underneath the MOF layer, subsequently causing the layer to bulk and detach. Additionally, internal structural constraints from within the MOF layer may contribute to this deposition phase occurring.

It is important to note that the formation and development of MOF thin films is heavily influenced by the innate characteristics of the conductive surface, temperature, pressure, applied potentials and additives.[240,254–256]

1.7.4 Post-Synthetic Modification

Modification of existing frameworks has become a highly studied area of MOF chemistry in recent years, with the use of post-synthetic modifications (PSM) techniques to obtain MOFs with additional functionalities.[257–260] The three main methods of PSM are dative PSM, covalent PSM and post-synthetic deprotection (PSD) (Fig.1.13).[261,262]

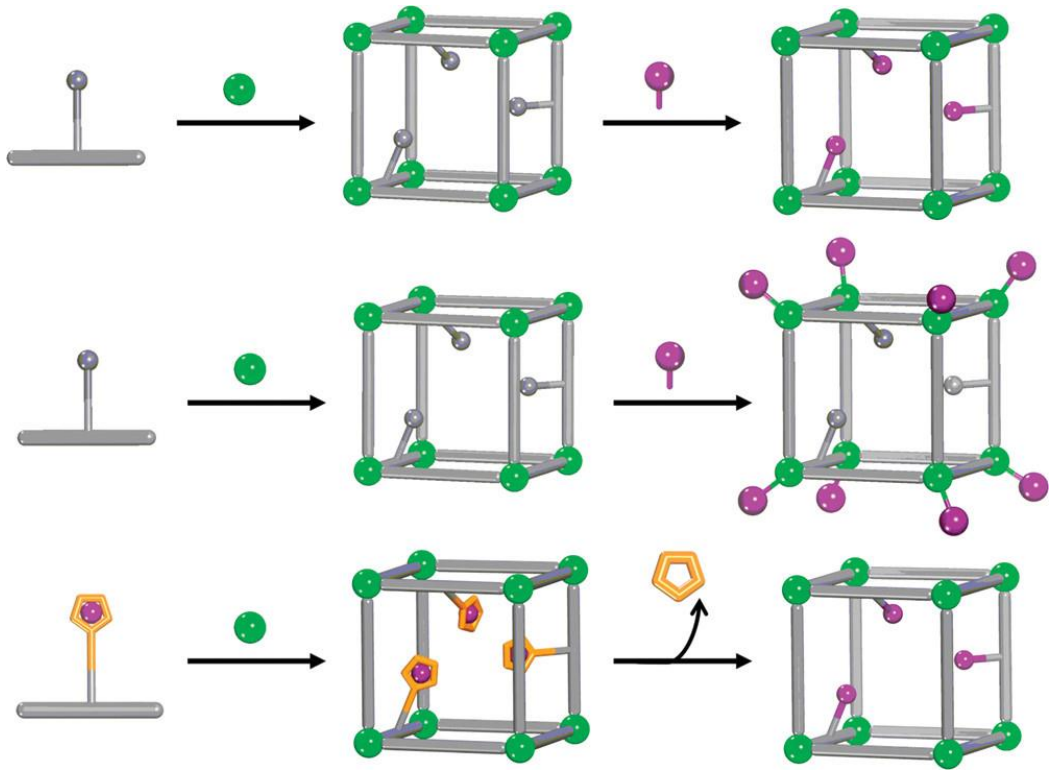

Figure 1.13: Generic schemes for covalent PSM (top), dative PSM (middle), and PSD (bottom). Reproduced from reference 262.

Covalent PSM is the most well-established, effective and versatile approach of introducing a wide range of chemical groups into a MOF.[258] It involves a covalent modification of the organic linker ligand or SBU, leading to the addition of the desired functional groups.[263] Research has shown that depending on the required outcome, this approach can either maintain the crystalline or molecular structure and porosity of the MOF[260,264,265] or modify it.[266] Furthermore, the approach utilises mild conditions whereby, the MOF is dispersed in a concentrated solution of, for example, a desired organic ligand, for a number of days at room temperature. The rate of exchange varies depending on the solvent system chosen as the medium, while the addition of heat may improve the rate. Dative PSM involves the addition of a desired metal or ligand component to a pre-formed MOF through the formation of a new metal-ligand bond with

either the organic linker ligand or SBU of the MOF, respectively. While PSD involves the post-synthetic deprotection of protected organic linker ligand components or cleavage of chemical bonds within the MOF framework to reveal new functional groups within the MOF and subsequently give new and different properties to the material.

The capability to modify already existing frameworks *via* PSM, enables the enhancement of countless MOFs. A prime example is the incorporation of light-harvesting functionalities into an existing framework through the addition of a chromophore by PSM.[267] Additionally, Long *et al.* were one of the first to report such experiments where they utilised PSM to immensely improve gas adsorption capacities of MOF-5.[268] The phenyl rings present in the framework of MOF-5 make up the majority of the internal surface. These terephthalate aromatic rings were speculated to be η^6 binding sites for metal centres and alteration of the structure with chromium hexacarbonyl by PSM yielded a modified piano stool complex, (η^6-arene)$Cr(CO)_3$ which brings about photoinduced CO dissociation in the presence of N_2 and H_2.[267]

Additionally, it has been demonstrated that Zr-based MOFs, which have been recognised for their high stabilities, are particularly tolerant to PSM and in certain situations specific SBUs can experience structural changes.[258,269] Therefore, by utilisation of PSM methods, multi-component heterometallic MOFs comprising of several different inorganic and organic SBUs can be produced from previously formed monometallic MOFs.[270,271] Furthermore, various network topologies can be post-synthetically modified using these methods (Fig. 1.14).[272,273]

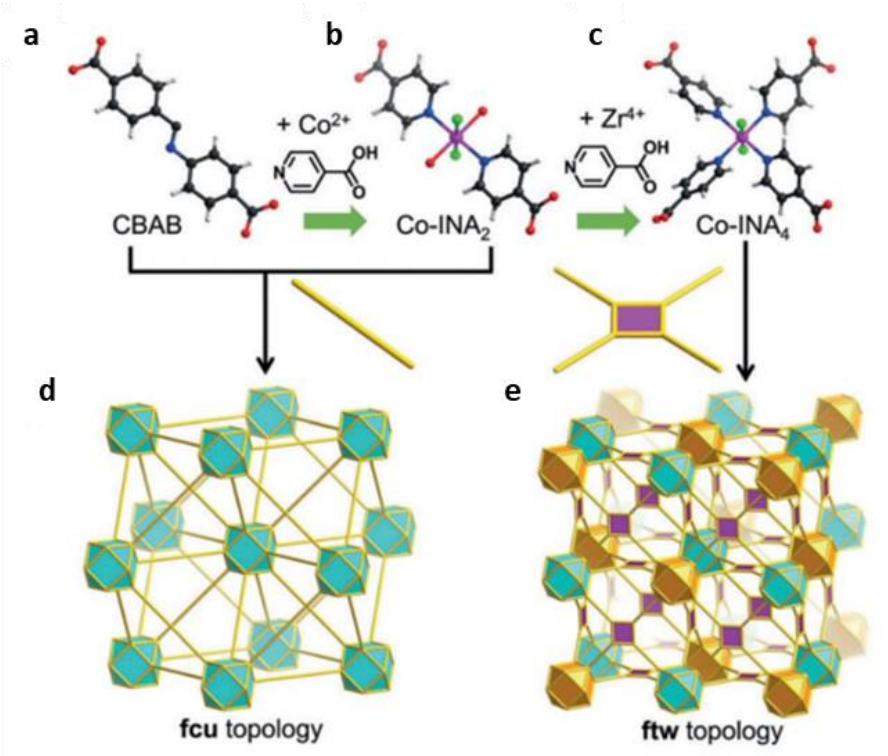

Figure 1.14: PSM topological transformation involving ligands and nodes. Linkers and their topological representations (a), (b), (c). Initial MOF with face-centered cubic (fcu) topology (d), new MOF structure with ftw topology (e). The Zr-SBUs are represented as teal cuboctahedrons and the additional Zr-SBUs are represented as orange cuboctahedrons. CBAB (4-carboxybenzylidene-4-aminobenzate) and INA (isonicotinate). Adapted from reference 272.

1.8 Structural Features of Metal-Organic Frameworks

1.8.1 Hydrolytic Stability

MOFs differ from one another owing to the many components from which they are constructed. Hence, their stabilities can vary significantly, while certain characteristics can frequently contribute to higher stabilities. MOF stability is currently being studied extensively due to its critical requirement when evaluating the possible efficiency of a MOF in a variety of applications.[274]

Numerous typical MOFs that are made of Cu^{II} and Zn^{II} ions have been found to be unviable for a variety of applications as a result of their poor hydrolytic, thermal or oxidative stabilities under the required conditions. The Zn-based MOF, MOF-5, which demonstrated remarkable gas absorption qualities but progressively degrades when exposed to moisture, is a notable example of a MOFs poor hydrolytic stability. Hydrolytic stability can be a significant problem for many MOFs as contact to certain quantities of water is inevitable. The reaction mechanism for hydrolytic degradation of MOFs, such as MOF-5, consists of a sequence of substitution reactions in which H_2O molecules displace organic ligands in the framework (Fig. 1.15).[275,276]

The strength of the bonds that constitute the framework may be used to estimate the hydrolytic stability of MOFs. The coordination bonds strength is associated with both the electronic configuration and the overlap of metal and ligand orbitals. Compounds with unfilled anti-bonding molecular orbitals are more hydrolytically stable and resistant to ligand exchange reactions. In general, both the charge and radii of the metal ions exhibit a direct relationship with the strength of a coordination bond, with strongly charged small metal ions leading to higher stabilities. Therefore, developing compounds with strong coordination bonds among the SBUs and ligands can lead to hydrolytic stability.

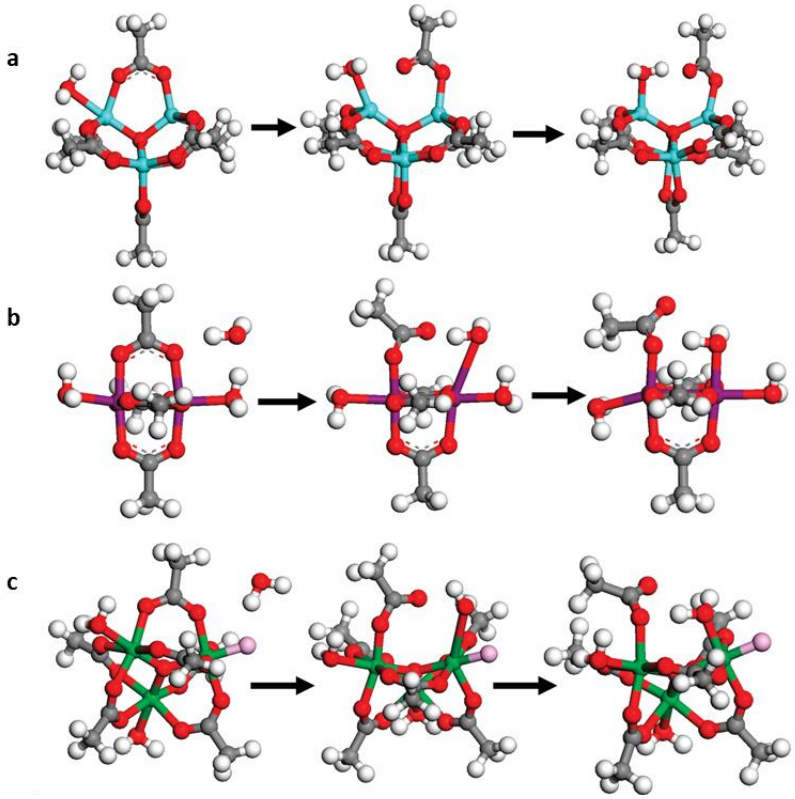

Figure 1.15: Mechanisms for hydrolytic degradation of MOFs involving ligand displacement reaction for MOF-5 (a), HKUST-1 (b), and MIL-101 (c). Structures represent reactant, transition state, and hydrolysis product clusters for each MOF. Mechanisms were derived from computational simulations using simplified clusters. Colour scheme: C grey, O red, H white, Zn light blue, Cu purple, Cr dark green, and F pink. Adapted from reference 275.

Furthermore, the hard and soft Lewis acid and base (HSAB) theory may be used to evaluate the anticipated stabilities. The theory suggests that hard Lewis bases, for example, carboxylates, establish strong interactions with hard Lewis acids like K^{I}, Zr^{IV} Al^{III}, and In^{III} while, soft Lewis acids, such as Cu^{I}, Pd^{II}, Cd^{II}, and Te^{IV}, create strong bonds with soft Lewis bases, such as imidazole. The University of Oslo, UiO-66[277] (Zr^{IV}) MOF and the Beijing University of Technology, BUT-70[278] (In^{III}) MOF, are examples of water-stable MOFs made of hard acids and hard bases. While several various coordination cages, such as [Pd(Me_4en)$_2$(1,3,5-tris(isonicotinoyloxyethyl)cyanurate)$_2$], incorporate soft Lewis bases and soft Lewis acids like Pd^{II}, to produce water-stable materials.[279] MOFs, such as the UiO Zr-based MOFs and PCN-601, where the latter is comprised of 8-connected {Ni_8} SBUs and 4-connected porphyrin ligands, possess well-connected SBUs, which typically provide stability by limiting SBU dissociation.[280,281] Many MOFs

possess coordinatively unsaturated sites (CUS) which are highly important for catalytic activity. These sites are located on the metal nodes of MOFs and are occupied by labile solvent molecules, such as H_2O. Therefore utilisation of these sites through the addition of ligands can both alter the properties of a MOF and improve its hydrolytic stability.[282,283]

Furthermore, the thermal stability of a MOF is inherently confined by the decomposition of the organic ligands that make up the framework. Rigid ligands and well-connected nodes are key components necessary in a framework in order to obtain MOFs that preserve their structures upon the removal of constitutional solvent molecules.

1.8.2 Catenation

Framework catenation is a common occurrence in MOFs and can be used as a synthetic method to control certain pore sizes. It is defined as the self-assembly of multiple separate frameworks within one another, all of which are comprised of the same or different components.[284] Catenation occurs due to the availability of vacant voids in the framework of MOFs, which allow the formation of additional nets inside the MOF. Supramolecular interactions including hydrogen bonding, $\pi - \pi$ interactions, and van der Waals forces facilitate the creation of interpenetrated species, which subsequently increase the stability of the material considerably.[285–289] Therefore, without causing any chemical bonds to break, an individual net in a catenated MOF may not be isolated from the remainder of the framework.

There are two types of catenation: interpenetration and interweaving (Fig. 1.16).[290] Where interpenetration is the ingrowth of two co-ordination networks within one another, where the frameworks are said to be maximally displaced from one another by the shifting of the second framework precisely one half of the pore size in the x, y and z directions.[291] This form of catenation can subsequently lead to undesirable effects on the porosity of a MOF. The second type of catenation known as interweaving is found to be similar to interpenetration, however, here the overall distance between the nets is minimised without the complete atomic overlap.[291]

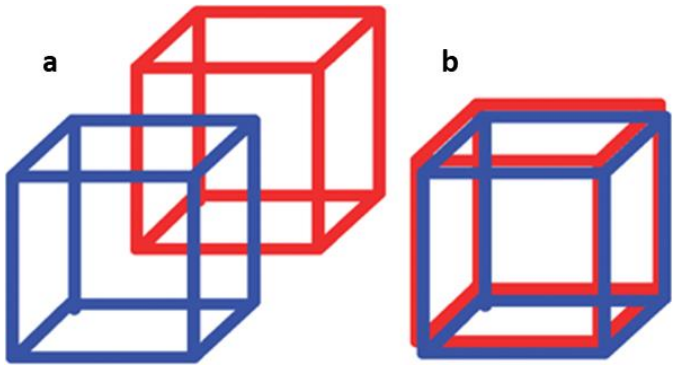

Figure 1.16: Illustration of the two types of catenation in two MOFs; Interpenetration (a) and Interweaving (b). Reproduced from reference 291.

Several reviews on the subject of network interpenetration have been published to date.[291–293] Reports published by Eddaoudi *et al.* highlighted the various challenges resulting from interpenetration within MOF networks alongside solutions to these problems.[192] Hence, it was identified that a possible remedy is to conduct synthetic procedures in dilute reaction conditions in order to prevent interpenetration of MOF networks. Recent studies have suggested additional alternative approaches to prevent interpenetration. These approaches include oxalate-based templates for MOF growth,[294] as well as the rational design of the organic linker units involved in the synthetic reactions, for example, the addition of sterically bulky groups to the organic linker as to prevent interpenetration.[293]

Despite the fact that interpenetration has been identified as a significant issue in MOF growth, research by Ma *et al.* demonstrated improved gas-storage properties of an interpenetrated network compared to an identical non-interpenetrated MOF.[294] One reason for the success of the improved gas storage capabilities can be attributed to the reduced effective pore-size. This reduction allowed for improved contiguity of gas molecules with pore walls, resulting in weak physical interactions. This has been recognised as a relatively unique occurrence, as many reports suggest negative impacts on MOFs gas-sorption properties due to catenation.[295]

Overall, it is clear that MOF growth is far from trivial, but rather a challenging and interesting area of chemistry and that due to their complex design and countless properties, MOFs have the potential to be used in a wide range of applications.

1.9 Potential Applications of Metal-Organic Frameworks

While it is crucial for researchers to develop new materials, it is also essential to look at potential applications for such materials. MOFs are incredibly complex, structurally flexible, low cost, high porosity and in most cases high yielding materials. They not only consist of high surface areas and low densities but are also highly attractive for a wide range of applications. In the literature, MOFs have proved to be effective in various applications such as gas storage,[215,296,297] drug delivery,[298–300] sensing,[301–304] light-harvesting,[305–309] and heterogeneous catalysis,[310,311] amongst others.[312–314] The vast diversity of MOFs and the various topics which arise from such an interesting field of chemistry can be seen in Figure 1.17, which illustrates the number of research publications on specific applications for MOFs for the period of 1990 to present.[223]

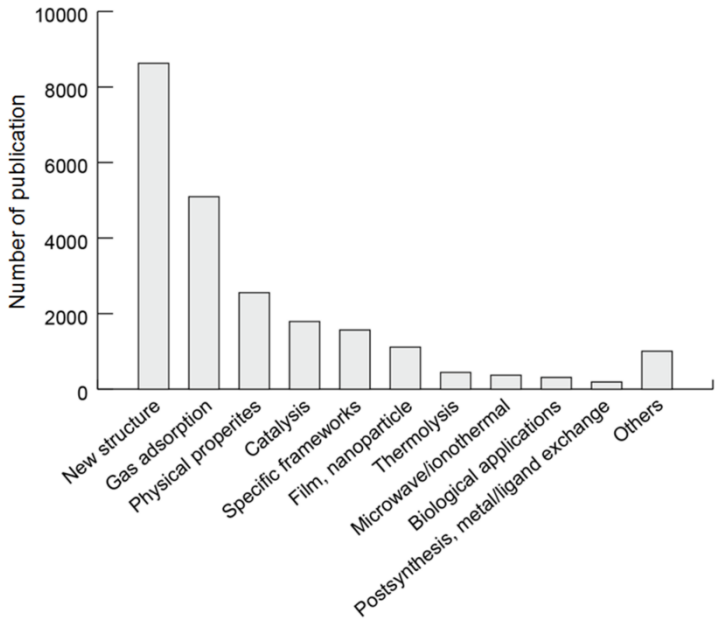

Figure 1.17: Cluster analysis of the number of publications in various research areas for MOFs from citation network analysis. Reproduced from reference 223.

1.9.1 Gas Storage and Absorption of Guest Molecules

Porous materials are essential in chemistry and engineering for a variety of reasons.[315] Thus, complex MOF networks exhibiting high surface areas and significant desired porosities are ideal candidates for applications such as gas adsorption. Additionally, due to their selective affinities between adsorbates, they are optimal materials for CO_2 capture,[316] energy storage of H_2 and CH_4,[317,318] and industrial synthesis of NH_3 and CO.[319,320]

The primary reason for utilising MOFs for hydrogen storage is that hydrogen is an ideal substituent for fossil fuels. This is demonstrated by the fact that hydrogen has a threefold higher heat of combustion (120 MJ/kg) than gasoline (44 MJ/kg), while also, the production of water as a by-product of combustion is more environmentally friendly.[321] MOF-5 was the first MOF to be identified to have significant hydrogen storage capabilities. In 2003, Rosi *et al.* investigated the adsorption of molecular hydrogen in MOF-5.[215] Utilising Brunauer-Emmett-Teller (BET) measurements, their research demonstrated that MOF-5 could adsorb up to 4.5 wt% of molecular hydrogen at a temperature and pressure of 78 K and 1 bar and 1 wt% at 298 K and 20 bar. As a result, this discovery sparked research into the novel synthesis and modification of MOFs in order to improve their hydrogen adsorption, particularly at ambient temperatures and pressures, so that they could be employed in fuel storage applications. Approaches such as the introduction of coordinatively unsaturated metal centres into the networks of MOFs have been attempted in order to improve the affinity for H_2 through strong metal−hydrogen interactions.[322–324] Similarly, efforts have been made to modify MOFs in order to adapt their pore sizes as to allow for more ideal van der Waal interactions with adsorbed gases.[325,326] Research carried out by Long *et al.* revealed that even though gravimetric storage capacities have a linear relationship with surface area, the pore sizes of MOFs play a vital role in gas storage. Thus, MOFs must be devised in such a way that maximum volumetric capacities are achieved, as it has been identified that using organic linker units that permit the adsorption enthalpy of hydrogen with the MOFs pore walls is more important than simply using longer linkers.[326,327] Both theoretically and experimentally, the optimal pore size has been determined to be 6 Å which is twice the kinetic diameter of a hydrogen molecule.[328]

Due to the potential to recycle captured CO_2, the gas adsorption properties of MOFs for CO_2 capture have become a highly researched topic.[316] Thus, these materials have been regarded as having great potential along with being both a cost-effective and environmentally friendly technique for storing captured CO_2.[329–332] Recent research indicates the physical and chemical interactions between the MOF framework and CO_2 molecules to be highly important.[333] As a result, three experimental approaches have been discovered to date to promote these interactions; i) generation of vacant sites for the coordination of CO_2 through MOF activation,[334] ii) functionalisation of the organic linker units with polar groups, as to improve affinity for CO_2,[335] and iii) functionalisation of the pores with nitrogen-containing triazoles[336] and amines.[337]

SIFSIX are a class of MOFs that have demonstrated exceptional selective CO_2 adsorption properties. SIFSIX MOFs containing pyrazine linkers[338] (Fig. 1. 18), which are structurally modified forms of the MOFs discovered by Zaworotko in 1995,[220] have shown selective CO_2 uptake at incredibly low CO_2 pressures of approximately 40 Pa.[339] The 3.5 Å pore size of the MOF is seen to be one of the key factors contributing to its selective CO_2 sorption properties. The selectivity is due to the pore size being significantly close to the 3.30 Å kinetic diameter of CO_2 molecules while remaining smaller than that required for N_2 sorption. The CO_2 molecules interact significantly with the surfaces of the MOFs channels and pores. This results in moderately high sorption enthalpies and subsequently permits the efficient isolation of CO_2 from dry air, even at low concentrations. As a result, these and various other MOFs are being utilised for the adsorption of CO_2 from the atmosphere.[297,340–342]

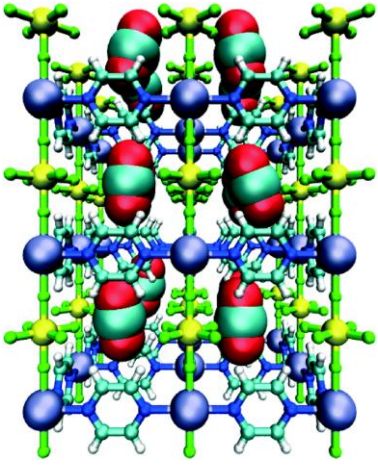

Figure 1.17: Molecular representation of the pyrazine-based SIFSIX-3-Zn framework at CO_2 saturation. Colour scheme: C cyan, H white, N blue, O red, F green, Zn violet, and Si yellow. Reproduced from reference 338.

In addition to gas sorption and separation, MOFs are also being widely investigated for the absorption and release of various guest molecules due to their unique host properties and customisable vacant pore sizes. These features have been the subject of much investigation, demonstrating the enormous potential of MOFs for the absorption of guest molecules.[343–345] However, the exorbitant cost of these host materials makes commercialisation in fields such as drug delivery difficult.[346,347]

Research demonstrates that guest molecules may be introduced into these materials to achieve initial or additional electrical conductivity functionalities within the framework, whilst also maintaining the initial porosity of the MOF.[348] Likewise, it has been identified that these guests bridge between SBUs and produce alternative pathways for charges to flow, and as a result provide or increase the overall conductivity of the framework.[349] This method has been utilised extensively by MOF chemists, with examples demonstrating the absorption of the electron acceptors, buckminsterfullerene (C_{60})[348] and tetracyanoquinodimethane (TCNQ),[349] into the vacant cavities of MUV-2 (Fig 1.18) and HKUST-1 MOFs, respectively. The respective absorption of these molecules demonstrated improved conductivity by two orders of magnitude in the MUV-2 MOF and from 10^{-8} to 0.07 S/cm in the HKUST-1 MOF.

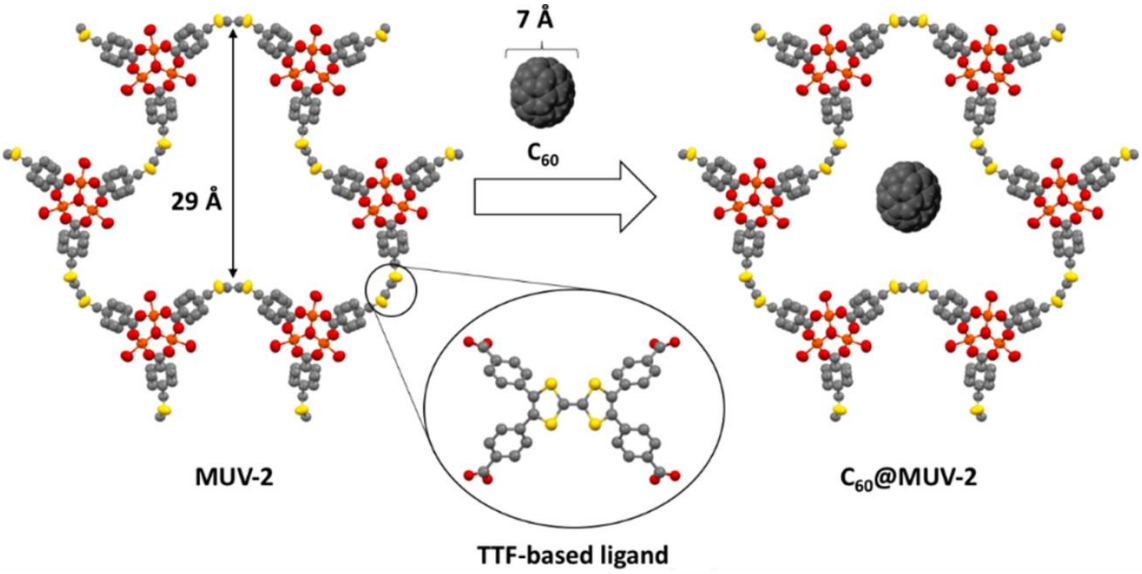

Figure 1.18: Schematic representation of the encapsulation of C_{60} inside the electron-donor TTF-based MUV-2 MOF cavities. Colour scheme: C grey, S yellow, Fe orange, O red. Adapted from reference 348.

1.9.2 Catalysis

Global energy demand has risen dramatically in recent decades, and global energy demand projections show an upward trend, with annual consumption expected to reach around 778 Etta Joule by 2035.[350] This is predicted to pose significant challenges to the oil and gas industry, which is a major producer and consumer of energy. Thus, the increased use of fossil fuels will have severe negative consequences for both human health and the environment. As a result, scientists from various disciplines have been working to develop alternative energy sources, with solar energy being one of the most promising renewable energy technologies.[351]

Catalysts are essential in reducing the activation energy of a reaction and the employment of MOFs in catalysis has been an area of high interest in recent times. Catalysts are divided into two categories: homogeneous and heterogeneous. Homogeneous catalysis refers to a reaction where the substrates and the catalyst are in the same phase. Homogenous catalysts are mainly organic or organometallic compounds with either open metal sites or coordination sites on the metal that are either unoccupied or bound by relatively weak coordinating molecules. Typically, homogeneous catalysis occurs in solution, with the components of the reaction being dissolved in the desired solvent to constitute the reaction system. Homogeneous catalysts can be quite effective in ambient conditions since all of their catalytic sites are accessible to the reactants in the reaction system. They are, however, frequently unstable, particularly at elevated temperatures, and are highly challenging to recycle. Heterogeneous catalysis involves systems where the catalyst is in a different phase from that of the reactants or products. Heterogeneous catalysts are often solid metals, metal salts, metal oxides or organic materials such as enzymes. They are generally the preferred forms of catalysts due to their lower operational costs and durability even at high temperatures.[352] Additionally, heterogeneous catalysts are usually easily recovered and recycled, however, their activity is reduced due to their low selectivity and poor exposure to reactants in the system.

MOFs are employed as heterogeneous catalysts, however, they likewise exhibit many characteristics of homogeneous catalysts. As a result, MOFs demonstrate the combined properties of both types of catalysts, such as selectivity and large surface areas of homogeneous catalysts and robustness, recoverability and recyclability of heterogeneous catalysts. MOFs can undergo catalysis in numerous ways such as the utilisation of their

pores to bring and maintain reactants in close proximity to one another.[353,354] They can also catalyse a reaction by exploiting their potential 'open' metal sites located within their framework.[355,356] These catalytic sites are located either on the SBU, as a component of the linkers that make up the framework or on possible guest complexes encapsulated in the MOF.[357] However, even though MOFs possess great potential for catalysis they also have their limitations such as lower chemical and thermal stability when compared to efficient alternative porous inorganic catalysts.

MOFs have demonstrated their effectiveness in catalysing various types of reactions such as multi-component coupling reactions,[358] amidation reactions,[359] bromination reactions,[360] Diels−Alder cyclisation reactions,[361] allylic oxidation reactions,[361] alkane and alkene oxidation reactions,[362,363] sulfide oxidation reactions,[356] oxidative dehydrogenation reactions,[258,364] oxidative coupling reactions,[365] and acetylenic acid cyclisation reactions,[366] amongst several others. Interestingly, MOFs have also demonstrated their applicability in both catalytic and photocatalytic water splitting reactions,[367–370] CO_2 photoreduction reactions,[371,372] and photodegradation of organic molecules.[373,374]

Similarly, the employment of stable MOFs which encapsulate catalytically active guest species is another approach to utilising inactive MOFs for catalysis. In 2015, Zhou *et al.* effectively utilised the pores of the stable aluminium-based PCN-333 MOF for the encapsulation of three separate enzymes. It was identified that strong MOF-enzyme interactions yielded significant enzyme loadings. A much-improved catalytic activity was observed for the MOF-enzyme composite when compared to that of the individual enzymes. It was also identified that each void present within the MOF encapsulated a single enzyme, thus preventing enzyme agglomeration and increasing activity.[375] A further example was reported in 2018 by Farha *et al.*. They demonstrated the encapsulation of platinum nanoparticles during the synthesis of a Zr_6-based MOF, in a one-pot synthesis and encapsulation approach. The synthesised MOF-nanoparticle composite was efficiently employed in alkene hydrogenation reactions demonstrating relatively high activity while additionally, preventing the frequent occurrence of nanoparticle agglomeration.[376]

1.9.3 MOFs for HER and OER

At present, numerous MOFs have been employed as catalysts for water splitting due to their structural diversity, porosity, and robustness.[175] MOFs and various composites have displayed great potential as catalysts for hydrogen evolution.[244,249,377,378] Typically, HER studies utilising MOFs are carried out in acidic media due to reduced energy demands and enhanced catalytic capabilities.

Examples of MOFs used in HER catalysis include MOS 1 and MOS 2, reported in 2015. These cobalt-based MOFs consisting of conjugated benzenehexathiol and triphenylene-2,3,6,7,10,11-hexathiolate ligands have demonstrated considerable HER activities at a variety of pHs. At a pH of 1.3, MOS 1 demonstrated significant HER activity, revealing an onset potential of 280 mV (vs SHE) and a Tafel slope of 149 mV/dec.[379] Similarly, a 2 dimensional Co^{II}-based MOF with a pentanuclear $\{Co_5\}$ SBU was utilised to produce a MOF composite with graphene. In a 0.5M sulfuric acid solution, this material was revealed to be highly active in the HER and remarkably stable following 1000 catalytic cycles. It exhibited an onset overpotential of 125 mV along with a Tafel slope of 91 mV/dec.[380]

In 2011, Lin *et al*. were one of the first to utilise a MOF as a WOC. They reported successful OEC with a TOF of 4.8 h^{-1} by exchanging several linkers that make up the framework of UiO-67 with iridium-based WOCs.[381,382] Furthermore, since the initial discovery by Lin *et al.* several other MOFs have been reported as WOCs. One of these examples is MAF-X27-OH, a Co^{II}-based azolate MOF, that was synthesised from MAF-X27-Cl by post-synthetic ion-exchange methods. At a pH of 14, this MOF demonstrated significant improvements in catalytic activity when compared to the parent MOF, revealing a reduction in the electrochemical water oxidation onset overpotential by 95 mV at 10 mA/cm^2.[383] The reduction in the onset overpotential alongside the improved catalytic activity was attributed to an alteration in the reaction mechanism upon the exchange of Cl with OH groups. This change allowed the reaction to occur intramolecularly via an intraframework coupling pathway. (Fig. 1.19).

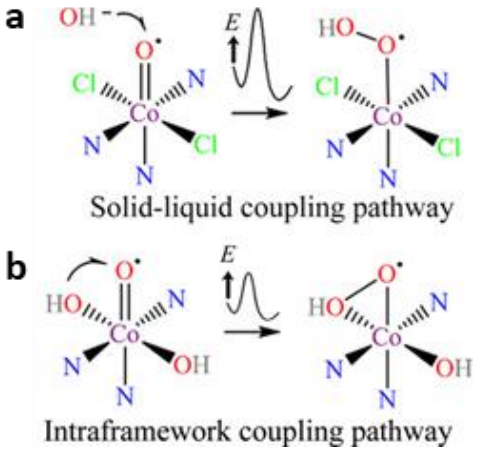

Figure 1.19: Solid−liquid coupling pathway for MAF-X27-Cl (a). Intraframework coupling pathway for MAF-X27-OH (b). Adapted from reference 383.

MOFs are viable materials for constructing OER or HER photocatalysts due to their large surface areas, which permit rapid catalytic kinetics, and their optimisable light absorption and redox characteristics.[384–386] As mentioned previously, the flexibility of MOFs allows the components necessary for light-induced water splitting to be integrated into a single heterogeneous supramolecular system.[387,388] In addition to these MOF-chromophore dyads, the porosity of MOFs permits them to encapsulate HEC and WOC within their frameworks for the HER and OER, respectively.[389,390]

In 2015, Lin *et al.* demonstrated the incorporation of a photocatalytic metal centre ($Ru(bpy)_3^{2+}$ moiety) into the structure of the organic linker of UiO-66 MOF. UiO-66 comprises of dicarboxylate terminated ligands and $\{Zr_6(\mu_3\text{-}O)_4(\mu_3\text{-}OH)_4\}$ SBUs.[391] It was further demonstrated that a noble-metal-free polyoxometalate (POM) could be encapsulated within the MOFs vacant cavities *via* a 'one-pot' synthetic approach, in which the MOF, during its formation, self-assembled around the catalytically active POM (Fig 1.20). As a result, this enabled light-induced electron transfer between the modified UiO-66 MOF and the POM *via* the incorporated photoactive moiety, promoting photocatalytic proton reduction.[391]

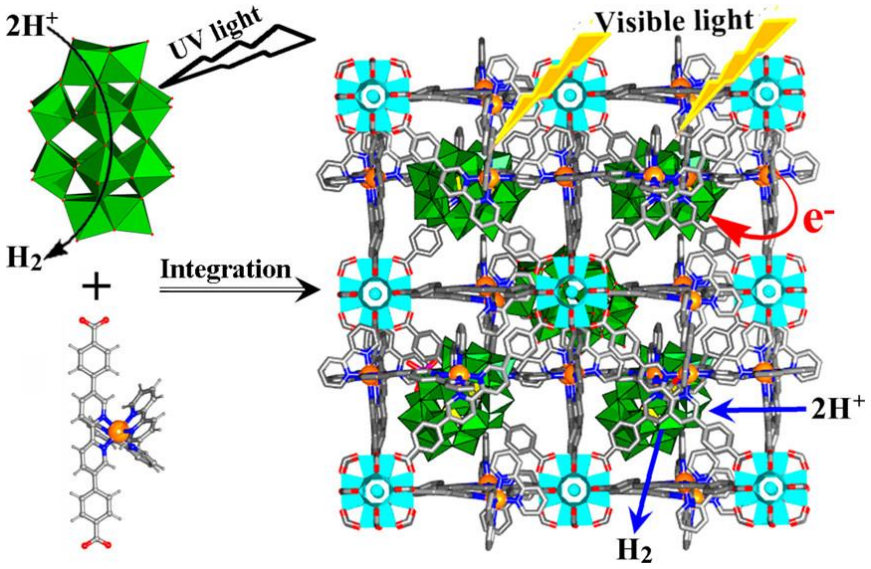

Figure 1.20: Incorporation of a POM into the framework of UiO-66 MOF by charge assisted self-assembly. Colour scheme: $[P_2W_{18}O_{62}]^{6-}$ green polyhedral, Zr turquoise polyhedral, Ru orange, N blue, O red, C grey. Reproduced from reference 391.

In 2016, Chi *et al.* demonstrated the photocatalytic water oxidation activity of MIL-101(Fe).[392] A TON of 27.3 and a TOF of 0.1 s^{-1} were reported upon light irradiation of the MOF in the presence of a $[Ru(bpy)_3](ClO_4)^2$ photosensitiser and $Na_2S_2O_8$ sacrificial electron acceptor. While in 2019, Huang *et al.* reported on the remarkable catalytic water oxidation activity of a Co^{II}-based MOF consisting of triazolate linker ligands and $\{Co^{II}_8OH_6\}$ SBUs $[Co_8(OH)_6(bdt)_4(Hbdt)_2]$.[170] The MOF was believed to be a potential candidate for OER due to its robustness, large surface area and availability of open metal sites.[383] Light irradiation of the MOF in presence of a $[Ru(bpy)_3]SO_4$ photosensitiser and a $Na_2S_2O_8$ sacrificial electron acceptor, revealed a rapid generation of O_2 along with an outstanding TOF (3.05 s^{-1}) and TON (1.2×10^6). Furthermore, the MOFs TON was two orders of magnitude higher than that of any prior reported WOCs.

To date, numerous reports have been published on the use of MOFs as catalysts and photocatalysts for various applications, such as water splitting. As a result, demonstrating the sheer scale of interest and versatility of MOFs.[393–395]

1.10 Aims and Objectives

The general aim of this research project was to design and synthesise Ru^{II}-based metallo-ligands to use in the preparation of novel MOFs in which photoactive moieties are incorporated in their frameworks. Thus, the ultimate aim of this investigation was to synthesise novel, porous, photoactive 3rd generation MOFs that could potentially promote light-driven chemical transformations and hence be utilised for 'solar-fuel'-related applications. A further aim was to design and develop novel photoactive MOF thin films *via* bulk electrochemical deposition and to exploit their photoactive capabilities in photo- and electro-catalytic H_2O oxidation studies. The synthetic techniques were aimed at obtaining crystalline materials as to allow for detailed structural analysis of metallo-ligands and MOFs. Additionally, the photophysical properties of the synthesised novel materials investigated.

The specific objectives of this research project can be summarised as follows:

I. To develop synthetic strategies to produce novel photoactive homoleptic and heteroleptic extended linear linker moieties which encompass a ruthenium-tris-bipyridyl core $\mathbf{H_2[L_{bpy}\text{-}R_1]^{2+}}$, $\mathbf{H_2[L_{bpy}\text{-}R_2]^{2+}}$, $\mathbf{H_4[L_{bpy}\text{-}R_3]^{2+}}$, $\mathbf{H_4[L_{phen}\text{-}R_3]^{2+}}$ and $\mathbf{H_{12}[L_{tris}\text{-}R_3]^{2+}}$.
II. To use appropriate analytical techniques and to investigate their physicochemical and photophysical properties of the metallo-ligands.
III. To synthesise a variety of photoactive MOFs *via* solvothermal synthesis using the developed metallo-ligands and to prepare phase pure MOF single-crystals suitable for X-ray diffraction for structural identification.
IV. To investigate the photophysical properties of the synthesised photoactive MOFs and to compare and contrast their attributes with their respective uncoordinated metallo-ligand precursor.
V. To design and develop MOF thin films *via* cathodic electrochemical synthesis and *in-situ* film deposition and to fully characterise the produced films *via* various spectroscopic techniques.
VI. To investigate the potential photo-electrocatalytic activities of the synthesised MOF thin films for photo-electrocatalytic H_2O oxidation. To identify possible guest encapsulation capacities of the MOFs and MOF thin films.

For these purposes the following metallo-ligands were targeted:

$H_2[L_{bpy}\text{-}R_1]^{2+}$ = [bis-(2,2'-bipyridine)-ruthenium(II)(5,5'-(bis-4-ethynylbenzoic acid)-2,2'-bipyridine)]$^{2+}$

$H_2[L_{bpy}\text{-}R_2]^{2+}$ = [bis-(2,2'-bipyridine)-ruthenium(II)(5,5'-(bis-3-ethynylbenzoic acid)-2,2'-bipyridine)]$^{2+}$

$H_4[L_{bpy}\text{-}R_3]^{2+}$ = [bis-(2,2'-bipyridine)-ruthenium(II)(5,5'-(bis-5-ethynylisophthalic acid)-2,2'-bipyridine)]$^{2+}$

$H_4[L_{phen}\text{-}R_3]^{2+}$ = [bis-(2,2'-bipyridine)-ruthenium(II)(3,8'-(bis-5-ethynylisophthalic acid)-1,10'-phenanthroline)]$^{2+}$

$H_{12}[L_{tris}\text{-}R_3]^{2+}$ = [tris-(5,5'-(bis-5-ethynylisophthalic acid)-2,2'-bipyridine)-ruthenium(II)]$^{2+}$

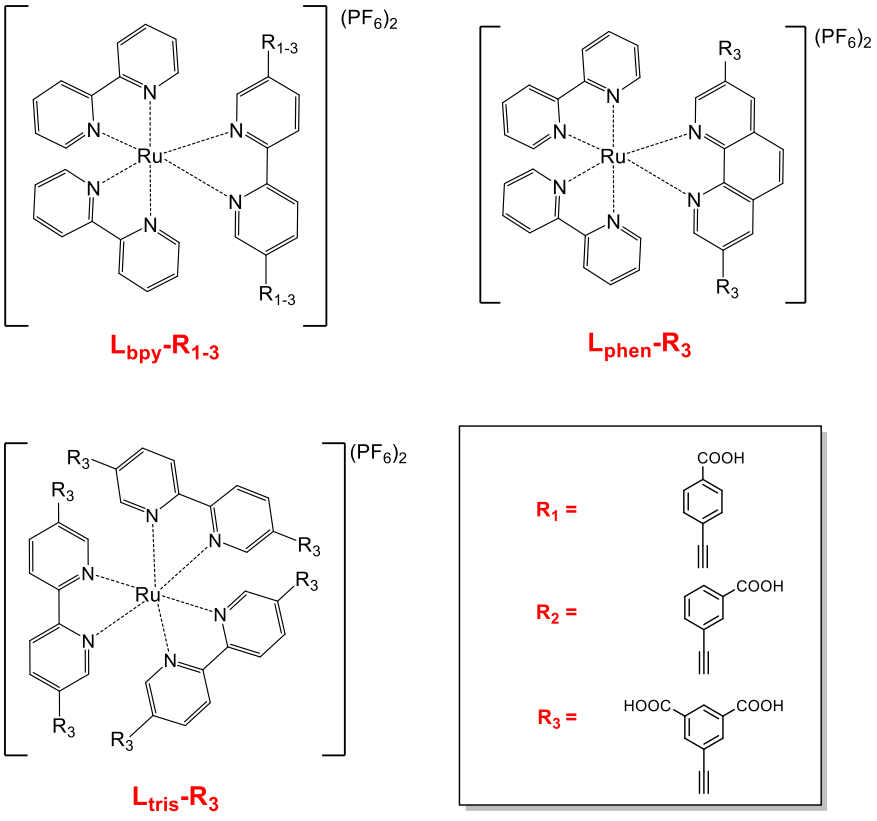

Figure 1.21: Structures of the novel photoactive metallo-ligands designed and synthesised.

Chapter 2 describes the synthetic approach employed for the synthesis of novel Ru^{II} polypyridine metallo-ligands $\mathbf{H_2[L_{bpy}\text{-}R_1]^{2+}}$, $\mathbf{H_2[L_{bpy}\text{-}R_2]^{2+}}$, $\mathbf{H_4[L_{bpy}\text{-}R_3]^{2+}}$, $\mathbf{H_4[L_{phen}\text{-}R_3]^{2+}}$ and $\mathbf{H_{12}[L_{tris}\text{-}R_3]^{2+}}$ which incorporate carboxylate functionalities and relate to the vastly studied $[Ru(bpy)_3]^{2+}$. The identity and purity of the metallo-ligands were analysed using NMR spectroscopy. Single crystals X-ray structures of the metallo-ligands are discussed. Finally, additional physicochemical characterisations were conducted confirming the successful synthesis of the desired complexes.

Chapter 3 explores the photochemical, photophysical and electrochemical properties of the metallo-ligands $\mathbf{H_2[L_{bpy}\text{-}R_1]^{2+}}$, $\mathbf{H_2[L_{bpy}\text{-}R_2]^{2+}}$, $\mathbf{H_4[L_{bpy}\text{-}R_3]^{2+}}$, and $\mathbf{H_4[L_{phen}\text{-}R_3]^{2+}}$. The photophysical behaviour of the metallo-ligands aimed to indicate how effective the chromophore moiety is within each of the structures. Additionally, analyses utilising various spectroscopic and characterisation techniques were carried out to compare the synthesised metallo-ligands with the archetype, complex $[Ru(bpy)_3]^{2+}$ **($\mathbf{[L6]^{2+}}$)**.

Chapter 4 describes three highly augmented MOFs, that are composed of acetylene-extended, light-harvesting Ru^{II}-bipyridyl metallo-ligands ($\mathbf{H_4[L_{bpy}\text{-}R_3]^{2+}}$) and 12-connected cubohemioctahedral cages forming a face-centered cubic network. The synthesis, crystal structures, physicochemical and photophysical properties of the novel MOFs are investigated. Electrochemical *in-situ* film deposition on conductive substrates of the novel synthesised photoactive MOFs are also demonstrated and examined. The chapter concludes with an investigation on the applicability of the novel systems. The produced electrodes were applied as photoanodes in preliminary photo-electrochemical H_2O oxidation studies in organic media and subsequent characterisation experiments demonstrated purity of the materials post-catalysis. Additionally, spectroscopic characterisation demonstrated successful utilisation of the synthesised MOFs and MOF electrodes vacant cavities in preliminary guest encapsulation experiments.

1.11 References

1 N. S. Lewis and D. G. Nocera, *Proc. Natl. Acad. Sci.*, 2006, **103**, 15729–15735.

2 R. J. Detz, J. N. H. Reek and B. C. C. van der Zwaan, *Energy Environ. Sci.*, 2018, **11**, 1653–1669.

3 G. Archer, T. Earl, E. Bannon, J. Poliscanova, N. Muzi and S. Alexandridou, *CO2 EMMISIONS FROM CARS*: the facts, European Federation for Transport and Environment AISBL, Brussels, 2018.

4 H. Hellevang and P. Aagaard, *Sci. Rep.*, 2015, **5**, 17352.

5 U. Siegenthaler, T. F. Stocker, E. Monnin, D. Lüthi, J. Schwander, B. Stauffer, D. Raynaud, J.-M. Barnola, H. Fischer, V. Masson-Delmotte and J. Jouzel, *Science*, 2005, **310**, 1313–1317.

6 R. Heede, *Clim. Change*, 2014, **122**, 229–241.

7 D. Schimel, B. B. Stephens and J. B. Fisher, *Proc. Natl. Acad. Sci.*, 2015, **112**, 436–441.

8 M.S.L.J., *The Economist explains: The 2°C limit on global warming*, https://www.economist.com/the-economist-explains/2015/12/06/the-2degc-limit-on-global-warming, (accessed 27 May 2022).

9 J. Huang, X. Zhang, Q. Zhang, Y. Lin, M. Hao, Y. Luo, Z. Zhao, Y. Yao, X. Chen, L. Wang, S. Nie, Y. Yin, Y. Xu and J. Zhang, *Nat. Clim. Chang.*, 2017, **7**, 875–879.

10 C. C. Hay, E. Morrow, R. E. Kopp and J. X. Mitrovica, *Nature*, 2015, **517**, 481–484.

11 G. A. Meehl, W. M. Washington, W. D. Collins, J. M. Arblaster, A. Hu, L. E. Buja, W. G. Strand and H. Teng, *Science*, 2005, **307**, 1769–1772.

12 S. Solomon, G.-K. Plattner, R. Knutti and P. Friedlingstein, *Proc. Natl. Acad. Sci.*, 2009, **106**, 1704–1709.

13 V. Ramanathan and Y. Feng, *Proc. Natl. Acad. Sci.*, 2008, **105**, 14245–14250.

14 J. Hansen, M. Sato, R. Ruedy, P. Kharecha, A. Lacis, R. Miller, L. Nazarenko, K. Lo, G. A. Schmidt, G. Russell, I. Aleinov, S. Bauer, E. Baum, B. Cairns, V. Canuto, M. Chandler, Y. Cheng, A. Cohen, A. Del Genio, G. Faluvegi, E. Fleming, A. Friend, T. Hall, C. Jackman, J. Jonas, M. Kelley, N. Y. Kiang, D. Koch, G. Labow, J. Lerner, S. Menon, T. Novakov, V. Oinas, J. Perlwitz, J. Perlwitz, D. Rind, A. Romanou, R. Schmunk, D. Shindell, P. Stone, S. Sun, D. Streets, N. Tausnev, D. Thresher, N. Unger, M. Yao and S. Zhang, *Atmos. Chem. Phys.*, 2007, **7**, 2287–2312.

15 S. Berardi, S. Drouet, L. Francàs, C. Gimbert-Suriñach, M. Guttentag, C. Richmond, T. Stoll and A. Llobet, *Chem. Soc. Rev.*, 2014, **43**, 7501–7519.

16 S. C. Anenberg, P. Achakulwisut, M. Brauer, D. Moran, J. S. Apte and D. K. Henze, *Sci. Rep.*, 2019, **9**, 11552.

17 R. Eisenberg, H. B. Gray and G. W. Crabtree, *Proc. Natl. Acad. Sci.*, 2020, **117**, 12543–12549.

18 A. Cho, *Science*, 2010, **329**, 786–787.

19 T. Grewe, M. Meggouh and H. Tüysüz, *Chem. - An Asian J.*, 2016, **11**, 22–42.

20 D. Narzi, D. Bovi and L. Guidoni, *Proc. Natl. Acad. Sci.*, 2014, **111**, 8723–8728.

21 A. Harriman, *Philos. Trans. R. Soc. A Math. Phys. Eng. Sci.*, 2013, **371**, 20110415.

22 M. Kumar, A. Dubey, N. Adhikari, S. Venkatesan and Q. Qiao, *Energy Environ. Sci.*, 2015, **8**, 3134–3159.

23 B. Parida, S. Iniyan and R. Goic, *Renew. Sustain. Energy Rev.*, 2011, **15**, 1625–1636.

24 W. L. Waltz, *Radiat. Phys. Chem.*, 1984, **23**, 491.

25 R. R. King, D. C. Law, K. M. Edmondson, C. M. Fetzer, G. S. Kinsey, H. Yoon, R. A. Sherif and N. H. Karam, *Appl. Phys. Lett.*, 2007, **90**, 183516.

26 A. M. Alfantazi and R. R. Moskalyk, *Miner. Eng.*, 2003, **16**, 687–694.

27 Z. He, Y. Yang, J.-W. Liu and S.-H. Yu, *Chem. Soc. Rev.*, 2017, **46**, 2732–2753.

28 K. Branker, M. J. M. Pathak and J. M. Pearce, *Renew. Sustain. Energy Rev.*, 2011, **15**, 4470–4482.

29 H. Apostoleris, S. Sgouridis, M. Stefancich and M. Chiesa, *Nat. Energy*, 2019, **4**, 833–834.

30 N. Cox, D. A. Pantazis, F. Neese and W. Lubitz, *Interface Focus*, 2015, **5**, 20150009.

31 I. Staffell, D. Scamman, A. Velazquez Abad, P. Balcombe, P. E. Dodds, P. Ekins, N. Shah and K. R. Ward, *Energy Environ. Sci.*, 2019, **12**, 463–491.

32 M. A. Rosen and S. Koohi-Fayegh, *Energy, Ecol. Environ.*, 2016, **1**, 10–29.

33 P. M. Shih, J. Hemp, L. M. Ward, N. J. Matzke and W. W. Fischer, *Geobiology*, 2017, **15**, 19–29.

34 R. M. Soo, J. Hemp, D. H. Parks, W. W. Fischer and P. Hugenholtz, *Science*, 2017, **355**, 1436–1440.

35 R. Buick, *Philos. Trans. R. Soc. B Biol. Sci.*, 2008, **363**, 2731–2743.

36 J. F. Allen, W. B. M. de Paula, S. Puthiyaveetil and J. Nield, *Trends Plant Sci.*, 2011, **16**, 645–655.

37 M. S. W. Hodgskiss, P. W. Crockford, Y. Peng, B. A. Wing and T. J. Horner, *Proc. Natl. Acad. Sci.*, 2019, **116**, 17207–17212.

38 J. Barber and P. D. Tran, *J. R. Soc. Interface*, 2013, **10**, 20120984.

39 Govindjee, J. F. Kern, J. Messinger and J. Whitmarsh, in *eLS*, Wiley, 2010, vol. 1, p. 2010.

40 J. Barber and M. D. Archer, *J. Photochem. Photobiol. A Chem.*, 2001, **142**, 97–106.

41 T. Renger, V. May and O. Kühn, *Phys. Rep.*, 2001, **343**, 137–254.

42 M. Grabolle and H. Dau, *Biochim. Biophys. Acta - Bioenerg.*, 2005, **1708**, 209–218.

43 C. Casadevall, *Water*, 2022, **14**, 371.

44 H. Inoue, T. Shimada, Y. Kou, Y. Nabetani, D. Masui, S. Takagi and H. Tachibana, *ChemSusChem*, 2011, **4**, 173-179.

45 M. P. Johnson, *Essays Biochem.*, 2016, **60**, 255–273.

46 U. Ulmer, T. Dingle, P. N. Duchesne, R. H. Morris, A. Tavasoli, T. Wood and G. A. Ozin, *Nat. Commun.*, 2019, **10**, 3169.

47 G. Renger and T. Renger, *Photosynth. Res.*, 2008, **98**, 53–80.

48 S. Trouvelot, M.-C. Héloir, B. Poinssot, A. Gauthier, F. Paris, C. Guillier, M. Combier, L. Trdá, X. Daire and M. Adrian, *Front. Plant Sci.*, 2014, **5**, 1–14.

49 D. Zhao, D. Yuan and H.-C. Zhou, *Energy Environ. Sci.*, 2008, **1**, 222.

50 F. Ausfelder and A. Bazzanella, in *Hydrogen Science and Engineering : Materials, Processes, Systems and Technology*, Wiley-VCH Verlag GmbH & Co. KGaA, Weinheim, Germany, 2016, vol. 1, pp. 19–40.

51 G. Chisholm and L. Cronin, in *Storing Energy*, Elsevier, 2016, pp. 315–343.

52 R. de Levie, *J. Electroanal. Chem.*, 1999, **476**, 92–93.

53 H. A. M. Snelders, *Ambix*, 1979, **26**, 116–133.

54 P. Tang and J. Arbiol, *Nanoscale Horizons*, 2019, **4**, 1256–1276.

55 C. Xiang, K. M. Papadantonakis and N. S. Lewis, *Mater. Horizons*, 2016, **3**, 169–173.

56 H. Tributsch, in *RSC Energy and Environment Series*, eds. S. D. Tilley, S. Lany and R. van de Krol, Royal Society of Chemistry, Cambridge, 2018, pp. 1–28.

57 J. H. Kim, D. Hansora, P. Sharma, J.-W. Jang and J. S. Lee, *Chem. Soc. Rev.*, 2019, **48**, 1908–1971.

58 N.-T. Suen, S.-F. Hung, Q. Quan, N. Zhang, Y.-J. Xu and H. M. Chen, *Chem. Soc. Rev.*, 2017, **46**, 337–365.

59 B. You and Y. Sun, *Acc. Chem. Res.*, 2018, **51**, 1571–1580.

60 R. Paul, D. Zemlyanov, A. K. Roy and A. A. Voevodin, in *Carbon Based Nanomaterials for Advanced Thermal and Electrochemical Energy Storage and Conversion*, Elsevier, 2019, pp. 63–88.

61 Z. Li, W. Luo, M. Zhang, J. Feng and Z. Zou, *Energy Environ. Sci.*, 2013, **6**, 347–370.

62 C. Jiang, S. J. A. Moniz, A. Wang, T. Zhang and J. Tang, *Chem. Soc. Rev.*, 2017, **46**, 4645–4660.

63 S. Chu, Y. Cui and N. Liu, *Nat. Mater.*, 2017, **16**, 16–22.

64 A. Fujishima and K. Honda, *Nature*, 1972, **238**, 37–38.

65 K. J. Young, L. A. Martini, R. L. Milot, R. C. Snoeberger, V. S. Batista, C. A. Schmuttenmaer, R. H. Crabtree and G. W. Brudvig, *Coord. Chem. Rev.*, 2012, **256**, 2503–2520.

66 B. Zhang and L. Sun, *Chem. Soc. Rev.*, 2019, **48**, 2216–2264.

67 I. Roger, M. A. Shipman and M. D. Symes, *Nat. Rev. Chem.*, 2017, **1**, 0003.

68 K. Park, Y. J. Kim, T. Yoon, S. David and Y. M. Song, *RSC Adv.*, 2019, **9**, 30112–30124.

69 C. S. Tan, K. W. Kemp, M. R. Braun, A. C. Meng, W. Tan, C. E. D. Chidsey, W. Ma, F. Moghadam and P. C. McIntyre, *Sustain. Energy Fuels*, 2019, **3**, 1490–1500.

70 X. Shi, H. Jeong, S. J. Oh, M. Ma, K. Zhang, J. Kwon, I. T. Choi, I. Y. Choi, H. K. Kim, J. K. Kim and J. H. Park, *Nat. Commun.*, 2016, **7**, 11943.

71 R. Fan, S. Cheng, G. Huang, Y. Wang, Y. Zhang, S. Vanka, G. A. Botton, Z. Mi and M. Shen, *J. Mater. Chem. A*, 2019, **7**, 2200–2209.

72 X. Chen and S. S. Mao, *Chem. Rev.*, 2007, **107**, 2891–2959.

73 S. Hoang, S. Guo, N. T. Hahn, A. J. Bard and C. B. Mullins, *Nano Lett.*, 2012, **12**, 26–32.

74 B. A. Pinaud, J. D. Benck, L. C. Seitz, A. J. Forman, Z. Chen, T. G. Deutsch, B. D. James, K. N. Baum, G. N. Baum, S. Ardo, H. Wang, E. Miller and T. F. Jaramillo, *Energy Environ. Sci.*, 2013, **6**, 1983.

75 A. Hossain, K. Sakthipandi, A. K. M. Atique Ullah and S. Roy, *Nano-Micro Lett.*, 2019, **11**, 103.

76 J. Luo, S. K. Karuturi, L. Liu, L. T. Su, A. I. Y. Tok and H. J. Fan, *Sci. Rep.*, 2012, **2**, 451.

77 Y. Wang, A. Vogel, M. Sachs, R. S. Sprick, L. Wilbraham, S. J. A. Moniz, R. Godin, M. A. Zwijnenburg, J. R. Durrant, A. I. Cooper and J. Tang, *Nat. Energy*, 2019, **4**, 746–760.

78 M. D. Kärkäs, O. Verho, E. V. Johnston and B. Åkermark, *Chem. Rev.*, 2014, **114**, 11863–12001.

79 S. T. Kochuveedu, *J. Nanomater.*, 2016, **2016**, 1–12.

80 M. Natali, E. Deponti, D. Vilona, A. Sartorel, M. Bonchio and F. Scandola, *Eur. J. Inorg. Chem.*, 2015, **2015**, 3467–3477.

81 J. Corredor, M. J. Rivero, C. M. Rangel, F. Gloaguen and I. Ortiz, *J. Chem. Technol. Biotechnol.*, 2019, **94**, 3049–3063.

82 K. J. Young, L. A. Martini, R. L. Milot, R. C. Snoeberger, V. S. Batista, C. A. Schmuttenmaer, R. H. Crabtree and G. W. Brudvig, *Coord. Chem. Rev.*, 2012, **256**, 2503–2520.

83 H. Junge, N. Rockstroh, S. Fischer, A. Brückner, R. Ludwig, S. Lochbrunner, O. Kühn and M. Beller, *Inorganics*, 2017, **5**, 14.

84 H.-C. Chen, J. N. H. Reek, R. M. Williams and A. M. Brouwer, *Phys. Chem. Chem. Phys.*, 2016, **18**, 15191–15198.

85 H.-C. Chen, D. G. H. Hetterscheid, R. M. Williams, J. I. van der Vlugt, J. N. H. Reek and A. M. Brouwer, *Energy Environ. Sci.*, 2015, **8**, 975–982.

86 G. Landrou, A. A. Panagiotopoulos, K. Ladomenou and A. G. Coutsolelos, *J. Porphyr. Phthalocyanines*, 2016, **20**, 534–541.

87 B. C. M. Martindale, G. A. M. Hutton, C. A. Caputo and E. Reisner, *J. Am. Chem. Soc.*, 2015, **137**, 6018–6025.

88 W. J. Youngblood, S.-H. A. Lee, Y. Kobayashi, E. A. Hernandez-Pagan, P. G. Hoertz, T. A. Moore, A. L. Moore, D. Gust and T. E. Mallouk, *J. Am. Chem. Soc.*, 2009, **131**, 926–927.

89 R. Brimblecombe, A. Koo, G. C. Dismukes, G. F. Swiegers and L. Spiccia, *J. Am. Chem. Soc.*, 2010, **132**, 2892–2894.

90 L. Li, L. Duan, Y. Xu, M. Gorlov, A. Hagfeldt and L. Sun, *Chem. Commun.*, 2010, **46**, 7307.

91 M. D. Kärkäs, T. M. Laine, E. V. Johnston and B. Akermark, in *Applied Photosynthesis - New Progress*, InTech, 2016, vol. 306, pp. 129–132.

92 E. Deponti and M. Natali, *Dalton Trans.*, 2016, **45**, 9136–9147.

93 B. Limburg, E. Bouwman and S. Bonnet, *ACS Catal.*, 2016, **6**, 5273–5284.

94 M. K. Nazeeruddin, A. Kay, I. Rodicio, R. Humphry-Baker, E. Mueller, P. Liska, N. Vlachopoulos and M. Graetzel, *J. Am. Chem. Soc.*, 1993, **115**, 6382–6390.

95 T. W. Hamann and J. W. Ondersma, *Energy Environ. Sci.*, 2011, **4**, 370–381.

96 M. Tuikka, P. Hirva, K. Rissanen, J. Korppi-Tommola and M. Haukka, *Chem. Commun.*, 2011, **47**, 4499.

97 C. Chen, M. Wang, J. Li, N. Pootrakulchote, L. Alibabaei, C. Ngoc-le, J. Decoppet, J. Tsai, C. Grätzel, C. Wu, S. M. Zakeeruddin and M. Grätzel, *ACS Nano*, 2009, **3**, 3103–3109.

98 F. Gao, Y. Wang, D. Shi, J. Zhang, M. Wang, X. Jing, R. Humphry-Baker, P. Wang, S. M. Zakeeruddin and M. Grätzel, *J. Am. Chem. Soc.*, 2008, **130**, 10720–10728.

99 D. Kuang, C. Klein, S. Ito, J.-E. Moser, R. Humphry-Baker, N. Evans, F. Duriaux, C. Grätzel, S. M. Zakeeruddin and M. Grätzel, *Adv. Mater.*, 2007, **19**, 1133–1137.

100 P. Wang, C. Klein, R. Humphry-Baker, S. M. Zakeeruddin and M. Grätzel, *J. Am. Chem. Soc.*, 2005, **127**, 808–809.

101 K.-J. Jiang, N. Masaki, J. Xia, S. Noda and S. Yanagida, *Chem. Commun.*, 2006, 2460.

102 M. R. Wasielewski, *Chem. Rev.*, 1992, **92**, 435–461.

103 S. L. Gould, G. Kodis, R. E. Palacios, L. de la Garza, A. Brune, D. Gust, T. A. Moore and A. L. Moore, *J. Phys. Chem. B*, 2004, **108**, 10566–10580.

104 P. A. Liddell, D. Kuciauskas, J. P. Sumida, B. Nash, D. Nguyen, A. L. Moore, T. A. Moore and D. Gust, *J. Am. Chem. Soc.*, 1997, **119**, 1400–1405.

105 J. H. Kim, S. H. Lee, J. S. Lee, M. Lee and C. B. Park, *Chem. Commun.*, 2011, **47**, 10227.

106 P. Zhang, M. Wang, C. Li, X. Li, J. Dong and L. Sun, *Chem. Commun.*, 2010, **46**, 8806.

107 A. Hagfeldt, G. Boschloo, L. Sun, L. Kloo and H. Pettersson, *Chem. Rev.*, 2010, **110**, 6595–6663.

108 A. Yella, H.-W. Lee, H. N. Tsao, C. Yi, A. K. Chandiran, M. K. Nazeeruddin, E. W.-G. Diau, C.-Y. Yeh, S. M. Zakeeruddin and M. Grätzel, *Science.*, 2011, **334**, 629–634.

109 T. Bessho, S. M. Zakeeruddin, C.-Y. Yeh, E. W.-G. Diau and M. Grätzel, *Angew. Chem. Int. Ed.*, 2010, **49**, 6646–6649.

110 Y.-C. Chang, C.-L. Wang, T.-Y. Pan, S.-H. Hong, C.-M. Lan, H.-H. Kuo, C.-F. Lo, H.-Y. Hsu, C.-Y. Lin and E. W.-G. Diau, *Chem. Commun.*, 2011, **47**, 8910.

111 G. F. Moore, J. D. Blakemore, R. L. Milot, J. F. Hull, H. Song, L. Cai, C. A. Schmuttenmaer, R. H. Crabtree and G. W. Brudvig, *Energy Environ. Sci.*, 2011, **4**, 2389.

112 G. F. Moore, S. J. Konezny, H. E. Song, R. L. Milot, J. D. Blakemore, M. L. Lee, V. S. Batista, C. A. Schmuttenmaer, R. H. Crabtree and G. W. Brudvig, *J. Phys. Chem. C*, 2012, **116**, 4892–4902.

113 K. Maeda and K. Domen, *J. Phys. Chem. C*, 2007, **111**, 7851–7861.

114 H. Kato and A. Kudo, *J. Phys. Chem. B*, 2002, **106**, 5029–5034.

115 K. Awazu, M. Fujimaki, C. Rockstuhl, J. Tominaga, H. Murakami, Y. Ohki, N. Yoshida and T. Watanabe, *J. Am. Chem. Soc.*, 2008, **130**, 1676–1680.

116 K. Tvrdy, P. A. Frantsuzov and P. V. Kamat, *Proc. Natl. Acad. Sci.*, 2011, **108**, 29–34.

117 J. Yu, G. Dai and B. Huang, *J. Phys. Chem. C*, 2009, **113**, 16394–16401.

118 W. M. Campbell, A. K. Burrell, D. L. Officer and K. W. Jolley, *Coord. Chem. Rev.*, 2004, **248**, 1363–1379.

119 M. K. Nazeeruddin, P. Péchy, T. Renouard, S. M. Zakeeruddin, R. Humphry-Baker, P. Comte, P. Liska, L. Cevey, E. Costa, V. Shklover, L. Spiccia, G. B. Deacon, C. A. Bignozzi and M. Grätzel, *J. Am. Chem. Soc.*, 2001, **123**, 1613–1624.

120 R. Argazzi, N. Y. Murakami Iha, H. Zabri, F. Odobel and C. A. Bignozzi, *Coord. Chem. Rev.*, 2004, **248**, 1299–1316.

121 N. Robertson, *Angew. Chem. Int. Ed.*, 2006, **45**, 2338–2345.

122 Y. Ooyama and Y. Harima, *Eur. J. Org. Chem.*, 2009, **2009**, 2903–2934.

123 A. S. Polo, M. K. Itokazu and N. Y. Murakami Iha, *Coord. Chem. Rev.*, 2004, **248**, 1343–1361.

124 M. K. Nazeeruddin, P. Liska, J. Moser, N. Vlachopoulos and M. Grätzel, *Helv. Chim. Acta*, 1990, **73**, 1788–1803.

125 A. Izgorodin, O. Winther-Jensen and D. R. MacFarlane, *Aust. J. Chem.*, 2012, **65**, 638.

126 M. Nippe, R. S. Khnayzer, J. A. Panetier, D. Z. Zee, B. S. Olaiya, M. Head-Gordon, C. J. Chang, F. N. Castellano and J. R. Long, *Chem. Sci.*, 2013, **4**, 3934.

127 W. Liu, E. Hu, H. Jiang, Y. Xiang, Z. Weng, M. Li, Q. Fan, X. Yu, E. I. Altman and H. Wang, *Nat. Commun.*, 2016, **7**, 10771.

128 J. Deng, P. Ren, D. Deng, L. Yu, F. Yang and X. Bao, *Energy Environ. Sci.*, 2014, **7**, 1919–1923.

129 H. Dau and I. Zaharieva, *Acc. Chem. Res.*, 2009, **42**, 1861–1870.

130 C. Mavrokefalos and G. Patzke, *Inorganics*, 2019, **7**, 29.

131 J. D. Blakemore, R. H. Crabtree and G. W. Brudvig, *Chem. Rev.*, 2015, **115**, 12974–13005.

132 T. R. Cook, D. K. Dogutan, S. Y. Reece, Y. Surendranath, T. S. Teets and D. G. Nocera, *Chem. Rev.*, 2010, **110**, 6474–6502.

133 M. G. Walter, E. L. Warren, J. R. McKone, S. W. Boettcher, Q. Mi, E. A. Santori and N. S. Lewis, *Chem. Rev.*, 2010, **110**, 6446–6473.

134 J. H. Montoya, L. C. Seitz, P. Chakthranont, A. Vojvodic, T. F. Jaramillo and J. K. Nørskov, *Nat. Mater.*, 2017, **16**, 70–81.

135 Z. W. She, J. Kibsgaard, C. F. Dickens, I. Chorkendorff, J. K. Nørskov and T. F. Jaramillo, *Science*, 2017, **355**, eaad4998.

136 S. Kozuch and J. M. L. Martin, *ACS Catal.*, 2012, **2**, 2787–2794.

137 C. Costentin, G. Passard and J.-M. Savéant, *J. Am. Chem. Soc.*, 2015, **137**, 5461–5467.

138 M. Schulze, V. Kunz, P. D. Frischmann and F. Würthner, *Nat. Chem.*, 2016, **8**, 576–583.

139 B. Wurster, D. Grumelli, D. Hötger, R. Gutzler and K. Kern, *J. Am. Chem. Soc.*, 2016, **138**, 3623–3626.

140 S. W. Sheehan, J. M. Thomsen, U. Hintermair, R. H. Crabtree, G. W. Brudvig and C. A. Schmuttenmaer, *Nat. Commun.*, 2015, **6**, 6469.

141 J. A. Gilbert, D. S. Eggleston, W. R. Murphy, D. A. Geselowitz, S. W. Gersten, D. J. Hodgson and T. J. Meyer, *J. Am. Chem. Soc.*, 1985, **107**, 3855–3864.

142 S. W. Gersten, G. J. Samuels and T. J. Meyer, *J. Am. Chem. Soc.*, 1982, **104**, 4029–4030.

143 J. P. Collin and J. P. Sauvage, *Inorg. Chem.*, 1986, **25**, 135–141.

144 J. J. Concepcion, J. W. Jurss, J. L. Templeton and T. J. Meyer, *Proc. Natl. Acad. Sci.*, 2008, **105**, 17632–17635.

145 D. Moonshiram, V. Purohit, J. Concepcion, T. Meyer and Y. Pushkar, *Materials*, 2013, **6**, 392–409.

146 B. Limburg, E. Bouwman and S. Bonnet, *Coord. Chem. Rev.*, 2012, **256**, 1451–1467.

147 Q. Yin, J. M. Tan, C. Besson, Y. V Geletii, D. G. Musaev, A. E. Kuznetsov, Z. Luo, K. I. Hardcastle and C. L. Hill, *Science*, 2010, **328**, 342–345.

148 D. K. Dogutan, R. McGuire and D. G. Nocera, *J. Am. Chem. Soc.*, 2011, **133**, 9178–9180.

149 D. Wang and J. T. Groves, *Proc. Natl. Acad. Sci.*, 2013, **110**, 15579–15584.

150 A. J. Esswein, Y. Surendranath, S. Y. Reece and D. G. Nocera, *Energy Environ. Sci.*, 2011, **4**, 499–504.

151 X.-B. Han, Y.-G. Li, Z.-M. Zhang, H.-Q. Tan, Y. Lu and E.-B. Wang, *J. Am. Chem. Soc.*, 2015, **137**, 5486–5493.

152 P. Garrido-Barros, I. Funes-Ardoiz, S. Drouet, J. Benet-Buchholz, F. Maseras and A. Llobet, *J. Am. Chem. Soc.*, 2015, **137**, 6758–6761.

153 S. M. Barnett, K. I. Goldberg and J. M. Mayer, *Nat. Chem.*, 2012, **4**, 498–502.

154 M. Shamsipur, A. (Arman) Taherpour, H. Sharghi, V. Lippolis and A. Pashabadi, *Electrochim. Acta*, 2018, **265**, 316–325.

155 E. A. Karlsson, B.-L. Lee, T. Åkermark, E. V. Johnston, M. D. Kärkäs, J. Sun, Ö. Hansson, J.-E. Bäckvall and B. Åkermark, *Angew. Chem. Int. Ed.*, 2011, **50**, 11715–11718.

156 K. J. Young, M. K. Takase and G. W. Brudvig, *Inorg. Chem.*, 2013, **52**, 7615–7622.

157 P. D. Frischmann, K. Mahata and F. Würthner, *Chem. Soc. Rev.*, 2013, **42**, 1847–1870.

158 B. Schwarz, J. Forster, M. K. Goetz, D. Yücel, C. Berger, T. Jacob and C. Streb, *Angew. Chem. Int. Ed.*, 2016, **55**, 6329–6333.

159 J. Limburg, J. S. Vrettos, L. M. Liable-Sands, A. L. Rheingold, R. H. Crabtree and G. W. Brudvig, *Science*, 1999, **283**, 1524–1527.

160 J. L. Fillol, Z. Codolà, I. Garcia-Bosch, L. Gómez, J. J. Pla and M. Costas, *Nat. Chem.*, 2011, **3**, 807–813.

161 M. Okamura, M. Kondo, R. Kuga, Y. Kurashige, T. Yanai, S. Hayami, V. K. K. Praneeth, M. Yoshida, K. Yoneda, S. Kawata and S. Masaoka, *Nature*, 2016, **530**, 465–468.

162 F. Evangelisti, R. Güttinger, R. Moré, S. Luber and G. R. Patzke, *J. Am. Chem. Soc.*, 2013, **135**, 18734–18737.

163 N. S. McCool, D. M. Robinson, J. E. Sheats and G. C. Dismukes, *J. Am. Chem. Soc.*, 2011, **133**, 11446–11449.

164 C.-F. Leung, S.-M. Ng, C.-C. Ko, W.-L. Man, J. Wu, L. Chen and T.-C. Lau, *Energy Environ. Sci.*, 2012, **5**, 7903.

165 T. Ishizuka, A. Watanabe, H. Kotani, D. Hong, K. Satonaka, T. Wada, Y. Shiota, K. Yoshizawa, K. Ohara, K. Yamaguchi, S. Kato, S. Fukuzumi and T. Kojima, *Inorg. Chem.*, 2016, **55**, 1154–1164.

166 A. I. Nguyen, M. S. Ziegler, P. Oña-Burgos, M. Sturzbecher-Hohne, W. Kim, D. E. Bellone and T. D. Tilley, *J. Am. Chem. Soc.*, 2015, **137**, 12865–12872.

167 M. Blasco-Ahicart, J. Soriano-López, J. J. Carbó, J. M. Poblet and J. R. Galan-Mascaros, *Nat. Chem.*, 2018, **10**, 24–30.

168 F. Li, Y. Jiang, B. Zhang, F. Huang, Y. Gao and L. Sun, *Angew. Chem. Int. Ed.*, 2012, **51**, 2417–2420.

169 Q. Chen, Q. Zhou, T.-T. Li, R. Liu, H. Li, F. Guo and Y.-Q. Zheng, *Transit. Met. Chem.*, 2019, **44**, 349–354.

170 D. L. Ashford, D. J. Stewart, C. R. Glasson, R. A. Binstead, D. P. Harrison, M. R. Norris, J. J. Concepcion, Z. Fang, J. L. Templeton and T. J. Meyer, *Inorg. Chem.*, 2012, **51**, 6428–6430.

171 M. R. Norris, J. J. Concepcion, D. P. Harrison, R. A. Binstead, D. L. Ashford, Z. Fang, J. L. Templeton and T. J. Meyer, *J. Am. Chem. Soc.*, 2013, **135**, 2080–2083.

172 N. Kaveevivitchai, R. Chitta, R. Zong, M. El Ojaimi and R. P. Thummel, *J. Am. Chem. Soc.*, 2012, **134**, 10721–10724.

173 B. D. Sherman, D. L. Ashford, A. M. Lapides, M. V. Sheridan, K.-R. Wee and T. J. Meyer, *J. Phys. Chem. Lett.*, 2015, **6**, 3213–3217.

174 B. D. Sherman, M. V. Sheridan, K.-R. Wee, S. L. Marquard, D. Wang, L. Alibabaei, D. L. Ashford and T. J. Meyer, *J. Am. Chem. Soc.*, 2016, **138**, 16745–16753.

175 K. Meyer, M. Ranocchiari and J. A. van Bokhoven, *Energy Environ. Sci.*, 2015, **8**, 1923–1937.

176 A. McNaught and A. Wilkinson, *The IUPAC Compendium of Chemical Terminology*, International Union of Pure and Applied Chemistry (IUPAC), Research Triangle Park, NC, 2014.

177 M. V. Orna, A. W. Kozlowski, A. Baskinger and T. Adams, 1994, pp. 165–176.

178 C. Colella and A. F. Gualtieri, *Microporous Mesoporous Mater.*, 2007, **105**, 213–221.

179 R. Virta, Mineral resource of the month: natural and synthetic zeolites, http://www.geotimes.org/june08/article.html?id=nn_zeolites.html, (accessed 31 May 2022).

180 R. Virta, Mineral Resource of the Month: Zeolites, https://www.earthmagazine.org/article/mineral-resource-month-zeolites/, (accessed 31 May 2022).

181 M. Pérez-Page, J. Makel, K. Guan, S. Zhang, J. Tringe, R. H. R. Castro and P. Stroeve, *Ceram. Int.*, 2016, **42**, 15423–15431.

182 Y. Zheng, X. Li and P. K. Dutta, *Sensors*, 2012, **12**, 5170–5194.

183 N. Thanabodeekij, S. Sadthayanon, E. Gulari and S. Wongkasemjit, *Mater. Chem. Phys.*, 2006, **98**, 131–137.

184 V. Chaudhary and S. Sharma, *J. Porous Mater.*, 2017, **24**, 741–749.

185 C.-Y. Su and Y.-B. Dong, *J. Solid State Chem.*, 2015, **223**, 1.

186 F.S. Ke, Y.S. Wu and H. Deng, J. Solid State Chem., 2015, **223**, 109-121.

187 H. Furukawa, K. E. Cordova, M. O'Keeffe and O. M. Yaghi, *Science*, 2013, **341**, 1230444-1230444.

188 O. M. Yaghi, M. O'Keeffe, N. W. Ockwig, H. K. Chae, M. Eddaoudi and J. Kim, *Nature*, 2003, **423**, 705–714.

189 N. Stock and S. Biswas, *Chem. Rev.*, 2012, **112**, 933–969.

190 C. M. MacGillivray, Leonard R. Lukehart, *Metal-Organic Framework Materials*, Wiley, New Jersey, 2014.

191 V. F. Cheong and P. Y. Moh, *Mater. Sci. Technol.*, 2018, **34**, 1025–1045.

192 M. Eddaoudi, J. Kim, N. Rosi, D. Vodak, J. Wachter, M. O'Keeffe and O. M. Yaghi, *Science*, 2002, **295**, 469–472.

193 B. F. Hoskins and R. Robson, *J. Am. Chem. Soc.*, 1990, **112**, 1546–1554.

194 K. M. Fromm, *Coord. Chem. Rev.*, 2008, **252**, 856–885.

195 M. Servati Gargari, V. Stilinović, A. Bauzá, A. Frontera, P. McArdle, D. Van Derveer, S. W. Ng and G. Mahmoudi, *Chem. - A Eur. J.*, 2015, **21**, 17951–17958.

196 L. K. Macreadie, E. J. Mensforth, R. Babarao, K. Konstas, S. G. Telfer, C. M. Doherty, J. Tsanaktsidis, S. R. Batten and M. R. Hill, *J. Am. Chem. Soc.*, 2019, **141**, 3828–3832.

197 X. Wei, S. Wang, Z. Hua, L. Chen and J. Shi, *ACS Appl. Mater. Interfaces*, 2018, **10**, 25422–25428.

198 Z.-H. Yan, M.-H. Du, J. Liu, S. Jin, C. Wang, G.-L. Zhuang, X.-J. Kong, L.-S. Long and L.-S. Zheng, *Nat. Commun.*, 2018, **9**, 3353.

199 Q. Yao, A. Bermejo Gómez, J. Su, V. Pascanu, Y. Yun, H. Zheng, H. Chen, L. Liu, H. N. Abdelhamid, B. Martín-Matute and X. Zou, *Chem. Mater.*, 2015, **27**, 5332–5339.

200 X. Guo, G. Zhu, Z. Li, F. Sun, Z. Yang and S. Qiu, *Chem. Commun.*, 2006, **1**, 3172–3174.

201 W. Yang, Z. Q. Bai, W. Q. Shi, L. Y. Yuan, T. Tian, Z. F. Chai, H. Wang and Z. M. Sun, *Chem. Commun.*, 2013, **49**, 10415–10417.

202 G. Tobin, S. Comby, N. Zhu, R. Clérac, T. Gunnlaugsson and W. Schmitt, *Chem. Commun.*, 2015, **51**, 13313–13316.

203 J. Andreo, E. Priola, G. Alberto, P. Benzi, D. Marabello, D. M. Proserpio, C. Lamberti and E. Diana, *J. Am. Chem. Soc.*, 2018, **140**, 14144–14149.

204 E. A. Dolgopolova, A. M. Rice and N. B. Shustova, *Chem. Commun.*, 2018, **54**, 6472–6483.

205 M. Eddaoudi, D. B. Moler, H. Li, B. Chen, T. M. Reineke, M. O'Keeffe and O. M. Yaghi, *Acc. Chem. Res.*, 2001, **34**, 319–330.

206 A. J. Howarth, Y. Liu, P. Li, Z. Li, T. C. Wang, J. T. Hupp and O. K. Farha, *Nat. Rev. Mater.*, 2016, **1**, 15018.

207 A. E. Baumann, D. A. Burns, B. Liu and V. S. Thoi, *Commun. Chem.*, 2019, **2**, 86.

208 P. Silva, S. M. F. Vilela, J. P. C. Tomé and F. A. Almeida Paz, *Chem. Soc. Rev.*, 2015, **44**, 6774–6803.

209 M. Bilal, M. Adeel, T. Rasheed and H. M. N. Iqbal, *J. Mater. Res. Technol.*, 2019, **8**, 2359–2371.

210 H.-C. Zhou, J. R. Long and O. M. Yaghi, *Chem. Rev.*, 2012, **112**, 673–674.

211 O. M. Yaghi and H. Li, *J. Am. Chem. Soc.*, 1995, **117**, 10401–10402.

212 R. J. Kuppler, D. J. Timmons, Q.-R. Fang, J.-R. Li, T. A. Makal, M. D. Young, D. Yuan, D. Zhao, W. Zhuang and H.-C. Zhou, *Coord. Chem. Rev.*, 2009, **253**, 3042–3066.

213 R. L. Martin, L.-C. Lin, K. Jariwala, B. Smit and M. Haranczyk, *J. Phys. Chem. C*, 2013, **117**, 12159–12167.

214 H. Furukawa, Y. B. Go, N. Ko, Y. K. Park, F. J. Uribe-Romo, J. Kim, M. O'Keeffe and O. M. Yaghi, *Inorg. Chem.*, 2011, **50**, 9147–9152.

215 N. L. Rosi, J. Eckert, M. Eddaoudi, D. T. Vodak, J. Kim, M. O'Keeffe and O. M. Yaghi, *Science*, 2003, **300**, 1127–1129.

216 H. Li, M. Eddaoudi, M. O'Keeffe and O. M. Yaghi, *Nature*, 1999, **402**, 276–279.

217 M. Kondo, T. Yoshitomi, H. Matsuzaka, S. Kitagawa and K. Seki, *Angew. Chem. Int. Ed. Eng.*, 1997, **36**, 1725–1727.

218 M. Fujita, D. Oguro, M. Miyazawa, H. Oka, K. Yamaguchi and K. Ogura, *Nature*, 1995, **378**, 469–471.

219 H.-C. "Joe" Zhou and S. Kitagawa, *Chem. Soc. Rev.*, 2014, **43**, 5415–5418.

220 S. Subramanian and M. J. Zaworotko, *Angew. Chem. Int. Ed. Eng.*, 1995, **34**, 2127–2129.

221 M. Li, D. Li, M. O'Keeffe and O. M. Yaghi, *Chem. Rev.*, 2014, **114**, 1343–1370.

222 H. Daglar and S. Keskin, *Coord. Chem. Rev.*, 2020, **422**, 213470.

223 T. Ogawa, K. Iyoki, T. Fukushima and Y. Kajikawa, *Materials*, 2017, **10**, 1428.

224 G. Férey, *Chem. Soc. Rev.*, 2008, **37**, 191–214.

225 A. Rabenau, *Angew. Chem Int. Ed. Eng.*, 1985, **24**, 1026–1040.

226 T. R. Cook, Y.-R. Zheng and P. J. Stang, *Chem. Rev.*, 2013, **113**, 734–777.

227 H. Vardhan, M. Yusubov and F. Verpoort, *Coord. Chem. Rev.*, 2016, **306**, 171–194.

228 R. I. Walton, *Chem. Soc. Rev.*, 2002, **31**, 230–238.

229 J. Li, Y. Peng, H. Liang, Y. Yu, B. Xin, G. Li, Z. Shi and S. Feng, *Eur. J. Inorg. Chem.*, 2011, **2011**, 2712–2719.

230 C. McKinstry, R. J. Cathcart, E. J. Cussen, A. J. Fletcher, S. V. Patwardhan and J. Sefcik, *Chem. Eng. J.*, 2016, **285**, 718–725.

231 P. Pachfule, R. Das, P. Poddar and R. Banerjee, *Cryst. Growth Des.*, 2011, **11**, 1215–1222.

232 M. Li and M. Dincă, *J. Am. Chem. Soc.*, 2011, **133**, 12926–12929.

233 S.-H. Feng and G.-H. Li, in *Modern Inorganic Synthetic Chemistry*, Elsevier, 2017, pp. 73–104.

234 I. M. Hauptvogel, V. Bon, R. Grünker, I. A. Baburin, I. Senkovska, U. Mueller and S. Kaskel, *Dalton Trans.*, 2012, **41**, 4172.

235 D. Saha, R. Zacharia, L. Lafi, D. Cossement and R. Chahine, *Chem. Eng. J.*, 2011, **171**, 517–525.

236 M. Almáši, V. Zeleňák, R. Gyepes, A. Zukal and J. Čejka, *Colloids Surfaces A Physicochem. Eng. Asp.*, 2013, **437**, 101–107.

237 N. Campagnol, T. R. C. Van Assche, M. Li, L. Stappers, M. Dincă, J. F. M. Denayer, K. Binnemans, D. E. De Vos and J. Fransaer, *J. Mater. Chem. A*, 2016, **4**, 3914–3925.

238 A. Martinez Joaristi, J. Juan-Alcañiz, P. Serra-Crespo, F. Kapteijn and J. Gascon, *Cryst. Growth Des.*, 2012, **12**, 3489–3498.

239 M. Li and M. Dincă, *Chem. Mater.*, 2015, **27**, 3203–3206.

240 N. Campagnol, T. Van Assche, T. Boudewijns, J. Denayer, K. Binnemans, D. De Vos and J. Fransaer, *J. Mater. Chem. A*, 2013, **1**, 5827.

241 Z. Ni and R. I. Masel, *J. Am. Chem. Soc.*, 2006, **128**, 12394–12395.

242 G. H. Albuquerque and G. S. Herman, *Cryst. Growth Des.*, 2017, **17**, 156–162.

243 J. Klinowski, F. A. Almeida Paz, P. Silva and J. Rocha, *Dalton Trans.*, 2011, **40**, 321–330.

244 M. Klimakow, P. Klobes, A. F. Thünemann, K. Rademann and F. Emmerling, *Chem. Mater.*, 2010, **22**, 5216–5221.

245 A. Pichon and S. L. James, *CrystEngComm*, 2008, **10**, 1839.

246 W.-J. Son, J. Kim, J. Kim and W.-S. Ahn, *Chem. Commun.*, 2008, 6336.

247 M. Bigdeli and A. Morsali, *Ultrason. Sonochem.*, 2015, **27**, 416–422.

248 J. Kim, B. Chen, T. M. Reineke, H. Li, M. Eddaoudi, D. B. Moler, M. O'Keeffe and O. M. Yaghi, *J. Am. Chem. Soc.*, 2001, **123**, 8239–8247.

249 G. Genesio, J. Maynadié, M. Carboni and D. Meyer, *New J. Chem.*, 2018, **42**, 2351–2363.

250 W.-J. Li, M. Tu, R. Cao and R. A. Fischer, *J. Mater. Chem. A*, 2016, **4**, 12356–12369.

251 D. Grosso, *J. Mater. Chem.*, 2011, **21**, 17033–17038.

252 G. Xu, T. Yamada, K. Otsubo, S. Sakaida and H. Kitagawa, *J. Am. Chem. Soc.*, 2012, **134**, 16524–16527.

253 R. Ameloot, L. Stappers, J. Fransaer, L. Alaerts, B. F. Sels and D. E. De Vos, *Chem. Mater.*, 2009, **21**, 2580–2582.

254 T. Mitra, F. Moreau, A. Nevin, C. U. Perotto, A. Summerfield, E. S. Davies, E. A. Gibson, T. L. Easun and M. Schröder, *Chem. Sci.*, 2018, **9**, 6572–6579.

255 S. D. Worrall, H. Mann, A. Rogers, M. A. Bissett, M. P. Attfield and R. A. W. Dryfe, *Electrochim. Acta*, 2016, **197**, 228–240.

256 H. Zhu, H. Liu, I. Zhitomirsky and S. Zhu, *Mater. Lett.*, 2015, **142**, 19–22.

257 S. J. D. Smith, B. P. Ladewig, A. J. Hill, C. H. Lau and M. R. Hill, *Sci. Rep.*, 2015, **5**, 7823.

258 H. G. T. Nguyen, N. M. Schweitzer, C.-Y. Chang, T. L. Drake, M. C. So, P. C. Stair, O. K. Farha, J. T. Hupp and S. T. Nguyen, *ACS Catal.*, 2014, **4**, 2496–2500.

259 M. Kim, J. F. Cahill, Y. Su, K. A. Prather and S. M. Cohen, *Chem. Sci.*, 2012, **3**, 126–130.

260 H. J. Park, Y. E. Cheon and M. P. Suh, *Chem. - A Eur. J.*, 2010, **16**, 11662–11669.

261 S. M. Cohen, *Chem. Rev.*, 2012, **112**, 970–1000.

262 J. Lei, R. Qian, P. Ling, L. Cui and H. Ju, *TrAC Trends Anal. Chem.*, 2014, **58**, 71–78.

263 A. D. Burrows, in *Encyclopedia of Inorganic and Bioinorganic Chemistry*, John Wiley & Sons, Ltd, Chichester, UK, 2014, pp. 1–24.

264 Z. Yin, S. Wan, J. Yang, M. Kurmoo and M. H. Zeng, *Coord. Chem. Rev.*, 2019, **378**, 500–512.

265 J. Seo, C. Bonneau, R. Matsuda, M. Takata and S. Kitagawa, *J. Am. Chem. Soc.*, 2011, **133**, 9005–9013.

266 T. Li, M. T. Kozlowski, E. A. Doud, M. N. Blakely and N. L. Rosi, *J. Am. Chem. Soc.*, 2013, **135**, 11688–11691.

267 C. L. Jones, A. J. Tansell and T. L. Easun, *J. Mater. Chem. A*, 2016, **4**, 6714–6723.

268 S. S. Kaye, A. Dailly, O. M. Yaghi and J. R. Long, *J. Am. Chem. Soc.*, 2007, **129**, 14176–14177.

269 S. Yuan, Y. Chen, J. Qin, W. Lu, X. Wang, Q. Zhang, M. Bosch, T. Liu, X. Lian and H. Zhou, *Angew. Chem. Int. Ed.*, 2015, **54**, 14696–14700.

270 S. Yuan, Y.-P. Chen, J.-S. Qin, W. Lu, L. Zou, Q. Zhang, X. Wang, X. Sun and H.-C. Zhou, *J. Am. Chem. Soc.*, 2016, **138**, 8912–8919.

271 S. Yuan, J.-S. Qin, J. Li, L. Huang, L. Feng, Y. Fang, C. Lollar, J. Pang, L. Zhang, D. Sun, A. Alsalme, T. Cagin and H.-C. Zhou, *Nat. Commun.*, 2018, **9**, 808.

272 S. Yuan, J. Qin, J. Su, B. Li, J. Li, W. Chen, H. F. Drake, P. Zhang, D. Yuan, J. Zuo and H. Zhou, *Angew. Chem. Int. Ed.*, 2018, **57**, 12578–12583.

273 G. González Miera, A. Bermejo Gómez, P. J. Chupas, B. Martín-Matute, K. W. Chapman and A. E. Platero-Prats, *Inorg. Chem.*, 2017, **56**, 4576–4583.

274 S. Yuan, L. Feng, K. Wang, J. Pang, M. Bosch, C. Lollar, Y. Sun, J. Qin, X. Yang, P. Zhang, Q. Wang, L. Zou, Y. Zhang, L. Zhang, Y. Fang, J. Li and H. Zhou, *Adv. Mater.*, 2018, **30**, 1704303.

275 J. J. Low, A. I. Benin, P. Jakubczak, J. F. Abrahamian, S. A. Faheem and R. R. Willis, *J. Am. Chem. Soc.*, 2009, **131**, 15834–15842.

276 H. Furukawa, F. Gándara, Y. B. Zhang, J. Jiang, W. L. Queen, M. R. Hudson and O. M. Yaghi, *J. Am. Chem. Soc.*, 2014, **136**, 4369–4381.

277 X. Liu, N. K. Demir, Z. Wu and K. Li, *J. Am. Chem. Soc.*, 2015, **137**, 6999–7002.

278 Z.-J. Guo, J. Yu, Y.-Z. Zhang, J. Zhang, Y. Chen, Y. Wu, L.-H. Xie and J.-R. Li, *Inorg. Chem.*, 2017, **56**, 2188–2197.

279 T. H. Noh, E. Heo, K. H. Park and O.-S. Jung, *J. Am. Chem. Soc.*, 2011, **133**, 1236–1239.

280 T.-F. Liu, D. Feng, Y.-P. Chen, L. Zou, M. Bosch, S. Yuan, Z. Wei, S. Fordham, K. Wang and H.-C. Zhou, *J. Am. Chem. Soc.*, 2015, **137**, 413–419.

281 K. Wang, X.-L. Lv, D. Feng, J. Li, S. Chen, J. Sun, L. Song, Y. Xie, J.-R. Li and H.-C. Zhou, *J. Am. Chem. Soc.*, 2016, **138**, 914–919.

282 Z. Chang, D.-S. Zhang, Q. Chen, R.-F. Li, T.-L. Hu and X.-H. Bu, *Inorg. Chem.*, 2011, **50**, 7555–7562.

283 N. Zhu, M. J. Lennox, G. Tobin, L. Goodman, T. Düren and W. Schmitt, *Chem. - A Eur. J.*, 2014, **20**, 3595–3599.

284 J. Kim, S. T. Yang, S. B. Choi, J. Sim, J. Kim and W. S. Ahn, *J. Mater. Chem.*, 2011, **21**, 3070–3076.

285 J. L. C. Rowsell and O. M. Yaghi, *J. Am. Chem. Soc.*, 2006, **128**, 1304–1315.

286 D. Sun, S. Ma, Y. Ke, T. M. Petersen and H.-C. Zhou, *Chem. Commun.*, 2005, 2663.

287 H. Kim, S. Das, M. G. Kim, D. N. Dybtsev, Y. Kim and K. Kim, *Inorg. Chem.*, 2011, **50**, 3691–3696.

288 M. Dincă, A. Dailly, C. Tsay and J. R. Long, *Inorg. Chem.*, 2008, **47**, 11–13.

289 S. Ma, X.-S. Wang, D. Yuan and H.-C. Zhou, *Angew. Chem.* 2008, **120**, 4198–4201.

290 J. L. C. Rowsell and O. M. Yaghi, *Angew. Chem. Int. Ed.*, 2005, **44**, 4670–4679.

291 S. S. Han, J. L. Mendoza-Cortés and W. A. Goddard, *Chem. Soc. Rev.*, 2009, **38**, 1460–1476.

292 S. R. Batten and R. Robson, *Angew. Chemie Int. Ed.*, 1998, **37**, 1460–1494.

293 O. K. Farha, C. D. Malliakas, M. G. Kanatzidis and J. T. Hupp, *J. Am. Chem. Soc.*, 2010, **132**, 950–952.

294 S. Ma, D. Sun, M. Ambrogio, J. A. Fillinger, S. Parkin and H.-C. Zhou, *J. Am. Chem. Soc.*, 2007, **129**, 1858–1859.

295 P. Ryan, L. J. Broadbelt and R. Q. Snurr, *Chem. Commun.*, 2008, 4132–4134.

296 C. Song, Y. Ling, Y. Feng, W. Zhou, T. Yildirim and Y. He, *Chem. Commun.*, 2015, **51**, 8508–8511.

297 B. Zheng, R. Yun, J. Bai, Z. Lu, L. Du and Y. Li, *Inorg. Chem.*, 2013, **52**, 2823–2829.

298 R. C. Huxford, J. Della Rocca and W. Lin, *Curr. Opin. Chem. Biol.*, 2010, **14**, 262–268.

299 P. Horcajada, C. Serre, G. Maurin, N. A. Ramsahye, F. Balas, M. Vallet-Regí, M. Sebban, F. Taulelle and G. Férey, *J. Am. Chem. Soc.*, 2008, **130**, 6774–6780.

300 M. Zulfiqar, Y. Zhao, G. Li, Z. Li and J. Ni, *Sci. Rep.*, 2019, **9**, 4571.

301 S. Carrasco, *Biosensors*, 2018, **8**, 92.

302 F.-Y. Yi, D. Chen, M.-K. Wu, L. Han and H.-L. Jiang, *ChemPlusChem*, 2016, **81**, 675–690.

303 W. P. Lustig, S. Mukherjee, N. D. Rudd, A. V. Desai, J. Li and S. K. Ghosh, *Chem. Soc. Rev.*, 2017, **46**, 3242–3285.

304 Y. Liu, X.-Y. Xie, C. Cheng, Z.-S. Shao and H.-S. Wang, *J. Mater. Chem. C*, 2019, **7**, 10743–10763.

305 J. Yu, X. Li and P. Deria, *ACS Sustain. Chem. Eng.*, 2019, **7**, 1841–1854.

306 L. Martins, L. K. Macreadie, D. Sensharma, S. Vaesen, X. Zhang, J. J. Gough, M. O'Doherty, N.-Y. Zhu, M. Rüther, J. E. O'Brien, A. L. Bradley and W. Schmitt, *Chem. Commun.*, 2019, **55**, 5013–5016.

307 J. L. White, M. F. Baruch, J. E. Pander, Y. Hu, I. C. Fortmeyer, J. E. Park, T. Zhang, K. Liao, J. Gu, Y. Yan, T. W. Shaw, E. Abelev and A. B. Bocarsly, *Chem. Rev.*, 2015, **115**, 12888–12935.

308 J.-J. Du, Y.-P. Yuan, J.-X. Sun, F.-M. Peng, X. Jiang, L.-G. Qiu, A.-J. Xie, Y.-H. Shen and J.-F. Zhu, *J. Hazard. Mater.*, 2011, **190**, 945–951.

309 C. Y. Lee, O. K. Farha, B. J. Hong, A. A. Sarjeant, S. T. Nguyen and J. T. Hupp, *J. Am. Chem. Soc.*, 2011, **133**, 15858–15861.

310 Z. Lei, Y. Xue, W. Chen, W. Qiu, Y. Zhang, S. Horike and L. Tang, *Adv. Energy Mater.*, 2018, **8**, 1801587.

311 S. K. Bharti and R. Roy, *TrAC Trends Anal. Chem.*, 2012, **35**, 5–26.

312 C. Pettinari, F. Marchetti, N. Mosca, G. Tosi and A. Drozdov, *Polym. Int.*, 2017, **66**, 731–744.

313 M. Ding, X. Cai and H.-L. Jiang, *Chem. Sci.*, 2019, **10**, 10209–10230.

314 J.-R. Li, R. J. Kuppler and H.-C. Zhou, *Chem. Soc. Rev.*, 2009, **38**, 1477.

315 A. G. Slater and A. I. Cooper, *Science*, 2015, **348**, aaa8075.

316 M. Ding, R. W. Flaig, H.-L. Jiang and O. M. Yaghi, *Chem. Soc. Rev.*, 2019, **48**, 2783–2828.

317 A. Ahmed, S. Seth, J. Purewal, A. G. Wong-Foy, M. Veenstra, A. J. Matzger and D. J. Siegel, *Nat. Commun.*, 2019, **10**, 1568.

318 Y. He, W. Zhou, G. Qian and B. Chen, *Chem. Soc. Rev.*, 2014, **43**, 5657–5678.

319 A. Evans, R. Luebke and C. Petit, *J. Mater. Chem. A*, 2018, **6**, 10570–10594.

320 S. Moribe, Z. Chen, S. Alayoglu, Z. H. Syed, T. Islamoglu and O. K. Farha, *ACS Mater. Lett.*, 2019, **1**, 476–480.

321 A. W. C. van den Berg and C. O. Areán, *Chem. Commun.*, 2008, 668–681.

322 M. Dincă, A. Dailly, Y. Liu, C. M. Brown, D. A. Neumann and J. R. Long, *J. Am. Chem. Soc.*, 2006, **128**, 16876–16883.

323 Y. Liu, H. Kabbour, C. M. Brown, D. A. Neumann and C. C. Ahn, *Langmuir*, 2008, **24**, 4772–4777.

324 N. Nijem, J.-F. Veyan, L. Kong, K. Li, S. Pramanik, Y. Zhao, J. Li, D. Langreth and Y. J. Chabal, *J. Am. Chem. Soc.*, 2010, **132**, 1654–1664.

325 N. Nijem, J.-F. Veyan, L. Kong, H. Wu, Y. Zhao, J. Li, D. C. Langreth and Y. J. Chabal, *J. Am. Chem. Soc.*, 2010, **132**, 14834–14848.

326 D. Gygi, E. D. Bloch, J. A. Mason, M. R. Hudson, M. I. Gonzalez, R. L. Siegelman, T. A. Darwish, W. L. Queen, C. M. Brown and J. R. Long, *Chem. Mater.*, 2016, **28**, 1128–1138.

327 J. L. C. Rowsell and O. M. Yaghi, *Angew. Chem. Int. Ed.*, 2005, **44**, 4670–4679.

328 Q. Wang and J. K. Johnson, *J. Chem. Phys.*, 1999, **110**, 577–586.

329 J. Liu, P. K. Thallapally, B. P. McGrail, D. R. Brown and J. Liu, *Chem. Soc. Rev.*, 2012, **41**, 2308–2322.

330 J. Yu, L.-H. Xie, J.-R. Li, Y. Ma, J. M. Seminario and P. B. Balbuena, *Chem. Rev.*, 2017, **117**, 9674–9754.

331 S. E. M. Elhenawy, M. Khraisheh, F. AlMomani and G. Walker, *Catalysts*, 2020, **10**, 1293.

332 Y. Lin, C. Kong, Q. Zhang and L. Chen, *Adv. Energy Mater.*, 2017, **7**, 1601296.

333 E. González-Zamora and I. A. Ibarra, *Mater. Chem. Front.*, 2017, **1**, 1471–1484.

334 M. P. Suh, H. J. Park, T. K. Prasad and D.-W. Lim, *Chem. Rev.*, 2012, **112**, 782–835.

335 Z. Zhang, Z.-Z. Yao, S. Xiang and B. Chen, *Energy Environ. Sci.*, 2014, **7**, 2868.

336 A. Demessence, D. M. D'Alessandro, M. L. Foo and J. R. Long, *J. Am. Chem. Soc.*, 2009, **131**, 8784–8786.

337 R. Vaidhyanathan, S. S. Iremonger, G. K. H. Shimizu, P. G. Boyd, S. Alavi and T. K. Woo, *Science*, 2010, **330**, 650–653.

338 K. A. Forrest, T. Pham and B. Space, *CrystEngComm*, 2017, **19**, 3338–3347.

339 P. Nugent, Y. Belmabkhout, S. D. Burd, A. J. Cairns, R. Luebke, K. Forrest, T. Pham, S. Ma, B. Space, L. Wojtas, M. Eddaoudi and M. J. Zaworotko, *Nature*, 2013, **495**, 80–84.

340 C. A. Trickett, A. Helal, B. A. Al-Maythalony, Z. H. Yamani, K. E. Cordova and O. M. Yaghi, *Nat. Rev. Mater.*, 2017, **2**, 17045.

341 O. Shekhah, Y. Belmabkhout, Z. Chen, V. Guillerm, A. Cairns, K. Adil and M. Eddaoudi, *Nat. Commun.*, 2014, **5**, 4228.

342 Q. Yang, V. Guillerm, F. Ragon, A. D. Wiersum, P. L. Llewellyn, C. Zhong, T. Devic, C. Serre and G. Maurin, *Chem. Commun.*, 2012, **48**, 9831.

343 E. Kolodzeiski and S. Amirjalayer, *Chem. – A Eur. J.*, 2020, **26**, 1263–1268.

344 S. Amirjalayer and R. Schmid, *J. Phys. Chem. C*, 2016, **120**, 27319–27327.

345 T. Wittmann, C. B. L. Tschense, L. Zappe, C. Koschnick, R. Siegel, R. Stäglich, B. V. Lotsch and J. Senker, *J. Mater. Chem. A*, 2019, **7**, 10379–10388.

346 P. Horcajada, T. Chalati, C. Serre, B. Gillet, C. Sebrie, T. Baati, J. F. Eubank, D. Heurtaux, P. Clayette, C. Kreuz, J. S. Chang, Y. K. Hwang, V. Marsaud, P. N. Bories, L. Cynober, S. Gil, G. Férey, P. Couvreur and R. Gref, *Nat. Mater.*, 2010, **9**, 172–178.

347 P. Horcajada, R. Gref, T. Baati, P. K. Allan, G. Maurin, P. Couvreur, G. Férey, R. E. Morris and C. Serre, *Chem. Rev.*, 2012, **112**, 1232–1268.

348 M. Souto, J. Calbo, S. Mañas-Valero, A. Walsh and G. Mínguez Espallargas, *Beilstein J. Nanotechnol.*, 2019, **10**, 1883–1893.

349 A. A. Talin, A. Centrone, A. C. Ford, M. E. Foster, V. Stavila, P. Haney, R. A. Kinney, V. Szalai, F. El Gabaly, H. P. Yoon, F. Léonard and M. D. Allendorf, *Science*, 2014, **343**, 66–69.

350 A. Rafiee and K. R. Khalilpour, in *Polygeneration with Polystorage for Chemical and Energy Hubs*, Elsevier, 2019, pp. 331–372.

351 A Promising Future: Solar Energy to Become Cheapest Power Source in 10 Years HeroX, https://www.herox.com/blog/222-a-promising-future-solar-energy-to-become-cheapest, (accessed 10 May 2022).

352 T.-C. Ong, R. Verel and C. Copéret, in *Encyclopedia of Spectroscopy and Spectrometry*, Elsevier, 2017, pp. 121–127.

353 T. Y. Zhou, B. Auer, S. J. Lee and S. G. Telfer, *J. Am. Chem. Soc.*, 2019, **141**, 1577–1582.

354 X. Li, J. Wu, C. He, Q. Meng and C. Duan, *Small*, 2019, **15**, 1804770.

355 J. Ye, L. Gagliardi, C. J. Cramer and D. G. Truhlar, *J. Catal.*, 2018, **360**, 160–167.

356 R. Limvorapitux, H. Chen, M. L. Mendonca, M. Liu, R. Q. Snurr and S. T. Nguyen, *Catal. Sci. Technol.*, 2019, **9**, 327–335.

357 J.-S. Qin, S. Yuan, C. Lollar, J. Pang, A. Alsalme and H.-C. Zhou, *Chem. Commun.*, 2018, **54**, 4231–4249.

358 G.-J. Chen, C.-Q. Chen, X.-T. Li, H.-C. Ma and Y.-B. Dong, *Chem. Commun.*, 2018, **54**, 11550–11553.

359 L. T. M. Hoang, L. H. Ngo, H. L. Nguyen, H. T. H. Nguyen, C. K. D. Nguyen, B. T. Nguyen, Q. T. Ton, H. K. D. Nguyen, K. E. Cordova and T. Truong, *Chem. Commun.*, 2015, **51**, 17132–17135.

360 J. Pang, S. Yuan, D. Du, C. Lollar, L. Zhang, M. Wu, D. Yuan, H.-C. Zhou and M. Hong, *Angew. Chem. Int. Ed.*, 2017, **129**, 14814–14818.

361 Y. Ueda, H. Ito, D. Fujita and M. Fujita, *J. Am. Chem. Soc.*, 2017, **139**, 6090–6093.

362 M. Tonigold, Y. Lu, B. Bredenkötter, B. Rieger, S. Bahnmüller, J. Hitzbleck, G. Langstein and D. Volkmer, *Angew. Chem. Int. Ed.*, 2009, **48**, 7546–7550.

363 L. Hamidipour and F. Farzaneh, *React. Kinet. Mech. Catal.*, 2013, **109**, 67–75.

364 Z. Li, A. W. Peters, V. Bernales, M. A. Ortuño, N. M. Schweitzer, M. R. DeStefano, L. C. Gallington, A. E. Platero-Prats, K. W. Chapman, C. J. Cramer, L. Gagliardi, J. T. Hupp and O. K. Farha, *ACS Cent. Sci.*, 2017, **3**, 31–38.

365 N. Van Velthoven, S. Waitschat, S. M. Chavan, P. Liu, S. Smolders, J. Vercammen, B. Bueken, S. Bals, K. P. Lillerud, N. Stock and D. E. De Vos, *Chem. Sci.*, 2019, **10**, 3616–3622.

366 Q.-Q. Wang, S. Gonell, S. H. A. M. Leenders, M. Dürr, I. Ivanović-Burmazović and J. N. H. Reek, *Nat. Chem.*, 2016, **8**, 225–230.

367 A. Kudo and Y. Miseki, *Chem. Soc. Rev.*, 2009, **38**, 253–278.

368 S. Ouyang, H. Tong, N. Umezawa, J. Cao, P. Li, Y. Bi, Y. Zhang and J. Ye, *J. Am. Chem. Soc.*, 2012, **134**, 1974–1977.

369 C. Wang, Z. Xie, K. E. DeKrafft and W. Lin, *J. Am. Chem. Soc.*, 2011, **133**, 13445–13454.

370 S. Lin, Y. Pineda-Galvan, W. A. Maza, C. C. Epley, J. Zhu, M. C. Kessinger, Y. Pushkar and A. J. Morris, *ChemSusChem*, 2017, **10**, 514–522.

371 H.-Q. Xu, J. Hu, D. Wang, Z. Li, Q. Zhang, Y. Luo, S.-H. Yu and H.-L. Jiang, *J. Am. Chem. Soc.*, 2015, **137**, 13440–13443.

372 S. Guo, H. Zhang, Y. Chen, Z. Liu, B. Yu, Y. Zhao, Z. Yang, B. Han and Z. Liu, *ACS Catal.*, 2018, **8**, 4576–4581.

373 E.-H. Zhou, B.-H. Li, W.-X. Chen, Z. Luo, J. Liu, A. Singh, A. Kumar and J.-C. Jin, *J. Mol. Struct.*, 2017, **1149**, 352–356.

374 Y. Pan, Q. Ding, H. Xu, C. Shi, A. Singh, A. Kumar and J. Liu, *CrystEngComm*, 2019, **21**, 4578–4585.

375 D. Feng, T.-F. Liu, J. Su, M. Bosch, Z. Wei, W. Wan, D. Yuan, Y.-P. Chen, X. Wang, K. Wang, X. Lian, Z.-Y. Gu, J. Park, X. Zou and H.-C. Zhou, *Nat. Commun.*, 2015, **6**, 5979.

376 H. Noh, C.-W. Kung, T. Islamoglu, A. W. Peters, Y. Liao, P. Li, S. J. Garibay, X. Zhang, M. R. DeStefano, J. T. Hupp and O. K. Farha, *Chem. Mater.*, 2018, **30**, 2193–2197.

377 Y. Bai, Y. Dou, L.-H. Xie, W. Rutledge, J.-R. Li and H.-C. Zhou, *Chem. Soc. Rev.*, 2016, **45**, 2327–2367.

378 N. Getachew, Y. Chebude, I. Diaz and M. Sanchez-Sanchez, *J. Porous Mater.*, 2014, **21**, 769–773.

379 A. J. Clough, J. W. Yoo, M. H. Mecklenburg and S. C. Marinescu, *J. Am. Chem. Soc.*, 2015, **137**, 118–121.

380 J.-W. Tian, M.-X. Fu, D.-D. Huang, X.-K. Wang, Y.-P. Wu, J. Y. Lu and D.-S. Li, *Inorg. Chem. Commun.*, 2018, **95**, 73–77.

381 J. H. Cavka, S. Jakobsen, U. Olsbye, N. Guillou, C. Lamberti, S. Bordiga and K. P. Lillerud, *J. Am. Chem. Soc.*, 2008, **130**, 13850–13851.

382 M. J. Katz, Z. J. Brown, Y. J. Colón, P. W. Siu, K. A. Scheidt, R. Q. Snurr, J. T. Hupp and O. K. Farha, *Chem. Commun.*, 2013, **49**, 9449–51.

383 X.-F. Lu, P.-Q. Liao, J.-W. Wang, J.-X. Wu, X.-W. Chen, C.-T. He, J.-P. Zhang, G.-R. Li and X.-M. Chen, *J. Am. Chem. Soc.*, 2016, **138**, 8336–8339.

384 A. Fateeva, P. A. Chater, C. P. Ireland, A. A. Tahir, Y. Z. Khimyak, P. V. Wiper, J. R. Darwent and M. J. Rosseinsky, *Angew. Chem. Int. Ed.*, 2012, **51**, 7440–7444.

385 M. Fuentes-Cabrera, D. M. Nicholson, B. G. Sumpter and M. Widom, *J. Chem. Phys.*, 2005, **123**, 124713.

386 Z. Jin and H. Yang, *Nanoscale Res. Lett.*, 2017, **12**, 539.

387 M. A. Nasalevich, M. van der Veen, F. Kapteijn and J. Gascon, *CrystEngComm*, 2014, **16**, 4919–4926.

388 D. Kim, D. R. Whang and S. Y. Park, *J. Am. Chem. Soc.*, 2016, **138**, 8698–8701.

389 B. Nohra, H. El Moll, L. M. Rodriguez Albelo, P. Mialane, J. Marrot, C. Mellot-Draznieks, M. O'Keeffe, R. Ngo Biboum, J. Lemaire, B. Keita, L. Nadjo and A. Dolbecq, *J. Am. Chem. Soc.*, 2011, **133**, 13363–13374.

390 J.-S. Qin, D.-Y. Du, W. Guan, X.-J. Bo, Y.-F. Li, L.-P. Guo, Z.-M. Su, Y.-Y. Wang, Y.-Q. Lan and H.-C. Zhou, *J. Am. Chem. Soc.*, 2015, **137**, 7169–7177.

391 Z.-M. Zhang, T. Zhang, C. Wang, Z. Lin, L.-S. Long and W. Lin, *J. Am. Chem. Soc.*, 2015, **137**, 3197–3200.

392 L. Chi, Q. Xu, X. Liang, J. Wang and X. Su, *Small*, 2016, **12**, 1351–1358.

393 J.-Q. Shen, P.-Q. Liao, D.-D. Zhou, C.-T. He, J.-X. Wu, W.-X. Zhang, J.-P. Zhang and X.-M. Chen, *J. Am. Chem. Soc.*, 2017, **139**, 1778–1781.

394 Y. An, Y. Liu, P. An, J. Dong, B. Xu, Y. Dai, X. Qin, X. Zhang, M.-H. Whangbo and B. Huang, *Angew. Chem. Int. Ed.*, 2017, **129**, 3082–3086.

395 X.-L. Wang, L.-Z. Dong, M. Qiao, Y.-J. Tang, J. Liu, Y. Li, S.-L. Li, J.-X. Su and Y.-Q. Lan, *Angew. Chemie Int. Ed.*, 2018, **57**, 9660–9664.

Chapter 2

Synthesis of Ru^{II}-Based Polypyridyl Complexes

2. Synthesis of Ru^{II}-Based Polypyridyl Complexes

2.1. Introduction

The tunability of MOFs arises due to the ability to vary the metal SBU, organic ligand, and synthetic conditions used in their preparation. Judicious selections of organic ligands in combination with various metal nodes are critical in MOF design and synthesis. Size, shape and rigidity of the organic ligands play a significant role in the structure and properties of MOFs.[1–3] Rigid extended linear ligands are highly advantageous for preparing MOFs, as the size of the ligand used may influence the pore size and functionality of the synthesised MOF.[4] In addition to ligand size, binding sites on the ligand are similarly important, as multidentate linkers containing O- and N- donors provide a diverse variety of coordination modes resulting in MOFs with myriad topologies.[5]

Similarly, incorporating photoactive moieties within a rigid ligand can provide unique photoactive attributes. In turn, this can engender a MOF with photoactive properties upon incorporating a photoactive ligand into the framework of the MOF. This functionalisation method is believed to be more efficient than post-synthetic modifications, such as guest loading of photoactive species, as it ensures guaranteed integration of the photoactive moiety within the framework while also increasing energy transfer propensity and stabilisation of the complex excited-state.[6–9] Furthermore, incorporating well-studied metal ions such as ruthenium(II) ions into the rigid backbone can facilitate ligand electron transfer characteristics. This approach can enable a MOF to possess photophysical and photochemical characteristics that can be utilised in various applications such as sensing and photocatalysis.[10–18]

This chapter describes the syntheses, crystal structures, and physicochemical characterisations of a variety of novel rigid photoactive ligands containing ruthenium(II) polypyridine moieties (Fig. 2.1) which was carried out in collaboration with Greg Byrne.

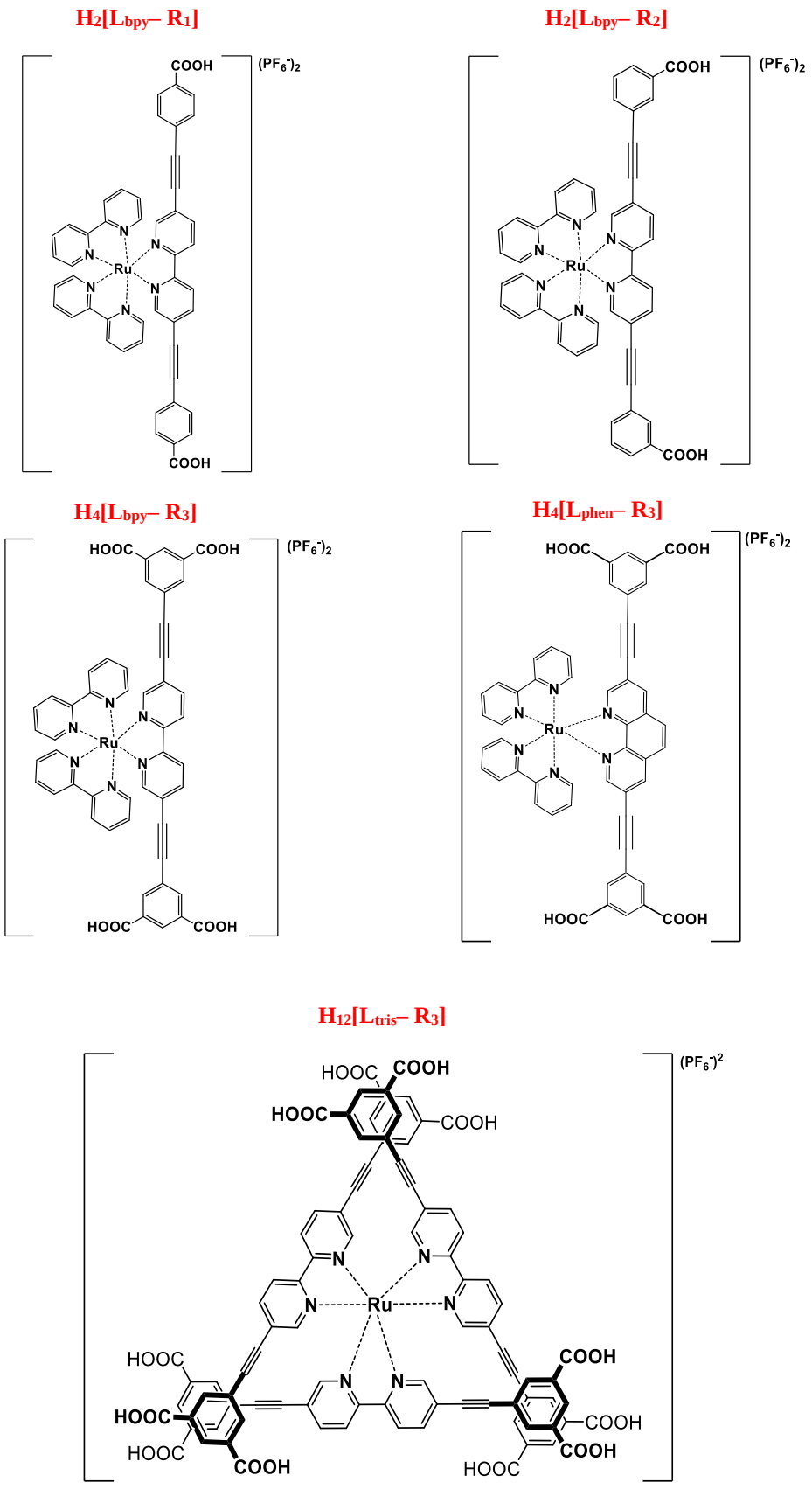

Figure 2.1: Novel rigid metallo-ligands containing ruthenium(II) polypyridine moieties.

2.2. Synthesis and Characterisation of Ru^{II} Polypyridyl Complexes

Polypyridine ligands are highly attractive multidentate ligands due to their ability to stabilise metal ions in low oxidation states, forming stable complexes with advantageous photochemical and electrochemical properties. They form chelates with η^2-coordination and influence the properties of the metal complexes they create.[19] Moreover, modifying polypyridine ligands by adding various substituents enables diverse chemical properties of a coordination complex to be tuned. These modifications can be beneficial in crystallisation processes depending on the substituent used. The addition of aromatic rings to polypyridine ligands improves their ability to form noncovalent bonds due to the increased capacity to exhibit $\pi - \pi$ stacking interactions. These interactions are essential adhesive and cohesive forces that promote crystallisation.[20] Additionally, extending polypyridine ligands with aromatic carboxylic acid substituents influences the pore sizes of the final desired MOF. Thus, with the aim of synthesising MOFs with applicable photochemical activity and large porosity, five novel extended ruthenium(II) polypyridyl complexes were initially synthesised *via* multistep palladium-catalysed Sonogashira cross-coupling reactions.

The full synthetic pathway for the novel metallo-ligands [bis-(2,2'-bipyridine)-ruthenium(II)(5,5'-(bis-4-ethynylbenzoic acid)-2,2'-bipyridine)]$^{2+}$, $\mathbf{H_2[L_{bpy}\text{-}R_1]^{2+}}$, [bis-(2,2'-bipyridine)-ruthenium(II)(5,5'-(bis-3-ethynylbenzoic acid)-2,2'-bipyridine)]$^{2+}$, $\mathbf{H_2[L_{bpy}\text{-}R_2]^{2+}}$, [bis-(2,2'-bipyridine)-ruthenium(II)(5,5'-(bis-5-ethynylisophthalic acid)-2,2'-bipyridine)]$^{2+}$, $\mathbf{H_4[L_{bpy}\text{-}R_3]^{2+}}$, [bis-(2,2'-bipyridine)-ruthenium(II)(3,8'-(bis-5-ethynylisophthalic acid)-1,10'-phenanthroline)]$^{2+}$, $\mathbf{H_4[L_{phen}\text{-}R_3]^{2+}}$, and [tris-(5,5'-(bis-5-ethynylisophthalic acid)-2,2'-bipyridine)-ruthenium(II)]$^{2+}$, $\mathbf{H_{12}[L_{tris}\text{-}R_3]^{2+}}$, are summarised in *Scheme 2.1*.

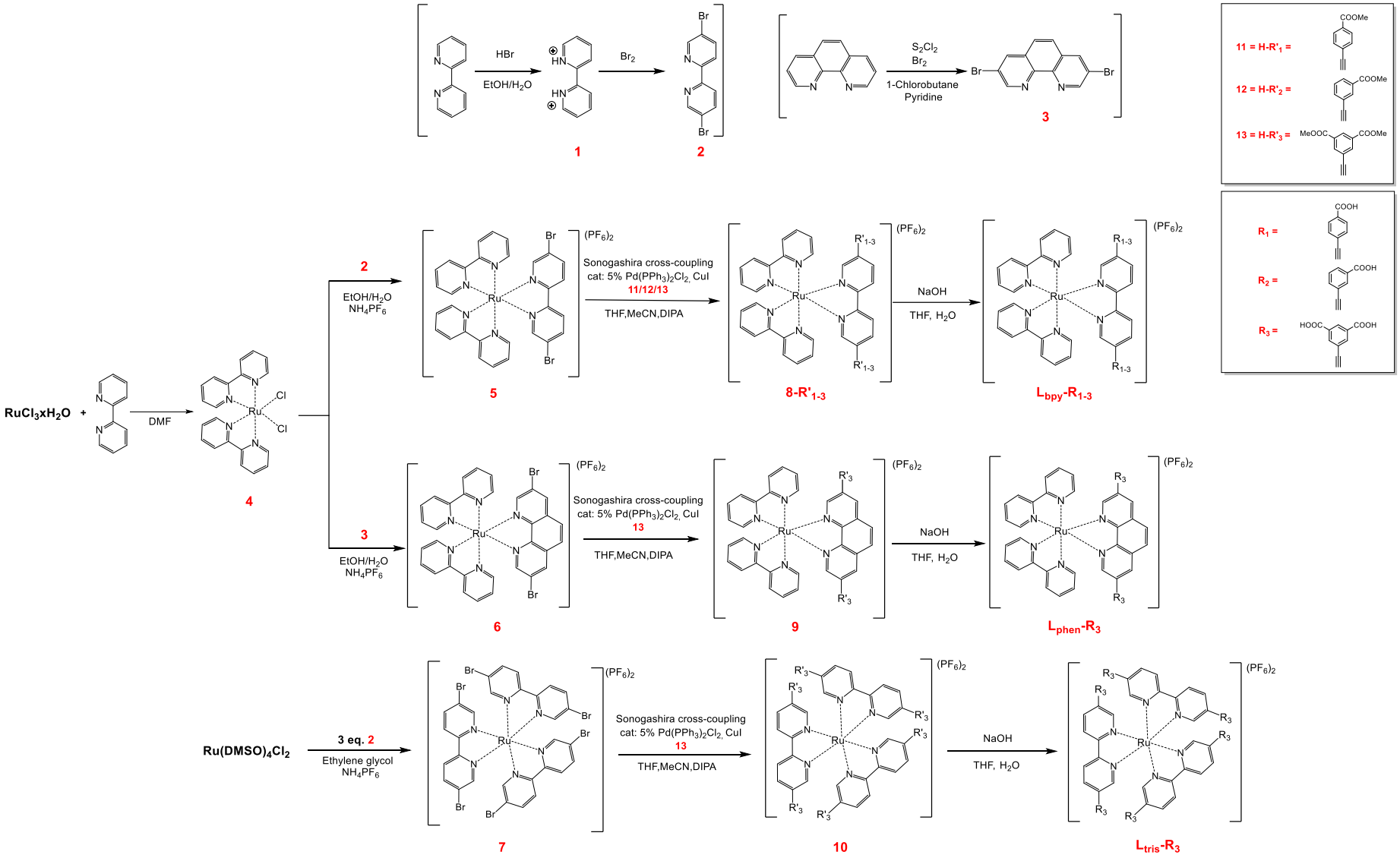

Scheme 2.1: Synthetic strategy for obtaining five novel ruthenium(II) polypyridyl complexes.

2.3. Synthesis of $H_2[L_{bpy}\text{-}R_1]^{2+}$, $H_2[L_{bpy}\text{-}R_2]^{2+}$ and $H_4[L_{bpy}\text{-}R_3]^{2+}$

$H_2[L_{bpy}\text{-}R_1]^{2+}$, **$H_2[L_{bpy}\text{-}R_2]^{2+}$** and **$H_4[L_{bpy}\text{-}R_3]^{2+}$** were synthesised *via* a multistep reaction procedure. The initial reaction involved the two-step synthesis of 5,5'-dibromo-2,2'-bipyridine (**2**) according to an adapted procedure by Woltering *et al.*[21] Firstly, 2,2'-bipyridine dihydrobromide (**1**) was synthesised and used as the precursor for the electrophilic aromatic bromination of 2,2'-bipyridine to produce 5,5'-dibromo-2,2'-bipyridine (**2**) in yields of over 60%. The dihydrobromide salt (**1**) was used to increase selectivity for the 5,5' positions, as direct bromination of the neutral bipyridine ligand is poor yielding and unselective (Scheme 2.2).[22]

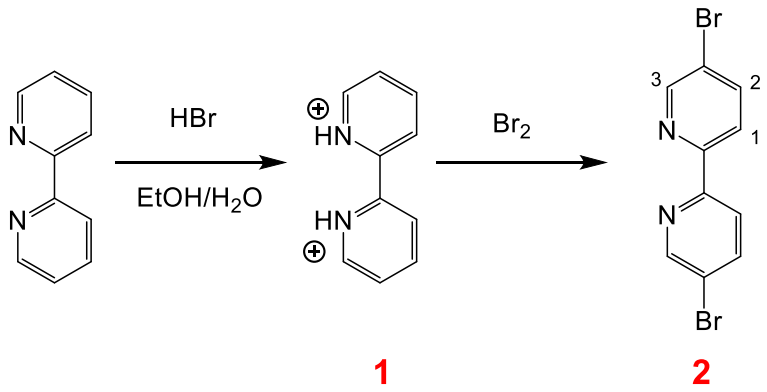

Scheme 2.2: Synthetic approach for the synthesis of 2,2'-bipyridine dihydrobromide and 5,5'-dibromo-2,2'-bipyridine.

Further, Romero *et al.* observed that variation of the bromine quantity and the reaction time greatly influences both the formation of the desired brominated product (mono-brominated bipyridine versus the dibrominated bipyridine (**2**)) and its yield (Fig. 2.2).[23] Thus, longer reaction times and larger quantities of bromine ensure bromination at the 5,5' positions while increasing the yield significantly.[24]

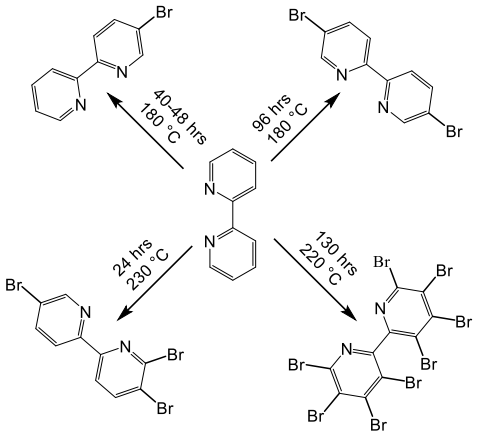

Figure 2.2: Reaction conditions for the synthesis of various bromo-substituted 2,2'-bipyridine moieties (adapted from Khimich *et al.*).[23]

Following completion of the reaction, analysis *via* ^{1}H-NMR spectroscopy (Fig. 2.3) and ESI mass spectrometry demonstrated that the precipitated product contained virtually no mono-brominated by-product. ^{1}H-NMR and mass spectra indicate a high degree of purity, with no detectable by-products, after washing the precipitate in hot ethanol, thus eliminating the need for purifying *via* column chromatography. The obtained dibromo-bipyridine 2 displayed significant lyophobic and hydrophobic properties, resulting in low solubility only in chloroform and DMF.

The ^{1}H-NMR spectrum of **2** reveals signals at 8.72 ppm, 8.30 ppm and 7.95 ppm, which are attributed to the H-atoms of the aromatic ring of the bipyridine moiety of **2**.[21]

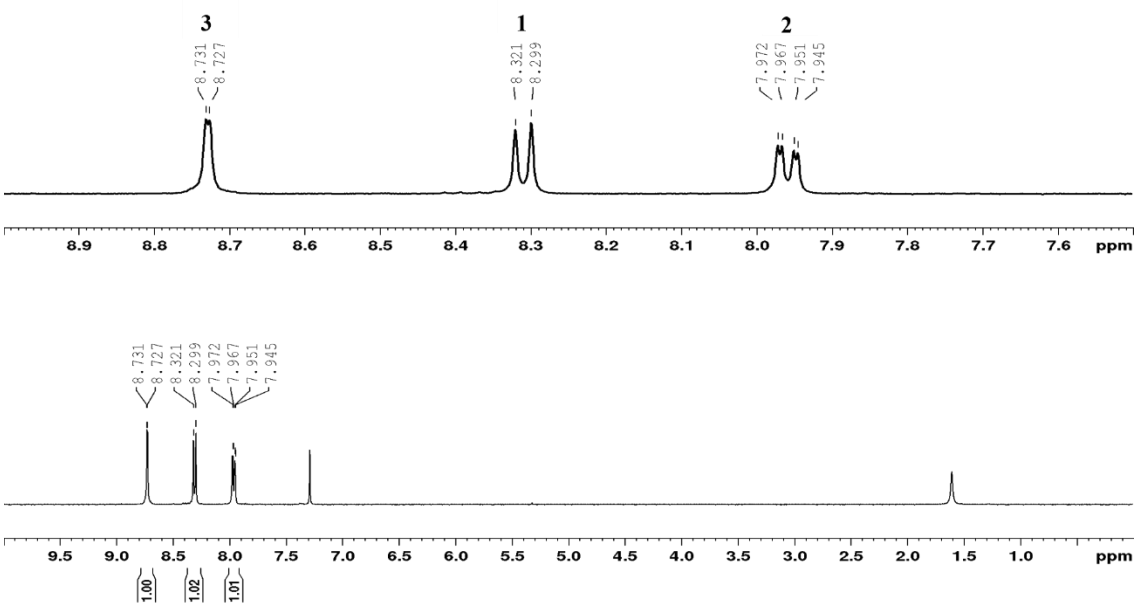

Figure 2.3: ^{1}H-NMR spectrum of 5,5'-dibromo-2,2'-bipyridine (2) in $CDCl_3$. Full spectrum of 2 (bottom), aromatic region of 2 (top).

It was envisaged that the use of alkyne-benzoic acid methyl ester groups would provide a means for linear extension of 2,2'-bipyridine moieties while also providing essential O-donors required for the subsequent coordination in MOF structures. Therefore, a two-step reaction was carried out for the synthesis of alkyne-benzoic acid methyl ester compounds, methyl 4-ethynylbenzoate (**11**), methyl 3-ethynylbenzoate (**12**), and dimethyl 5-ethynylisophthalate (**13**) that constitute the substituent head groups in the final target metallo-ligands.

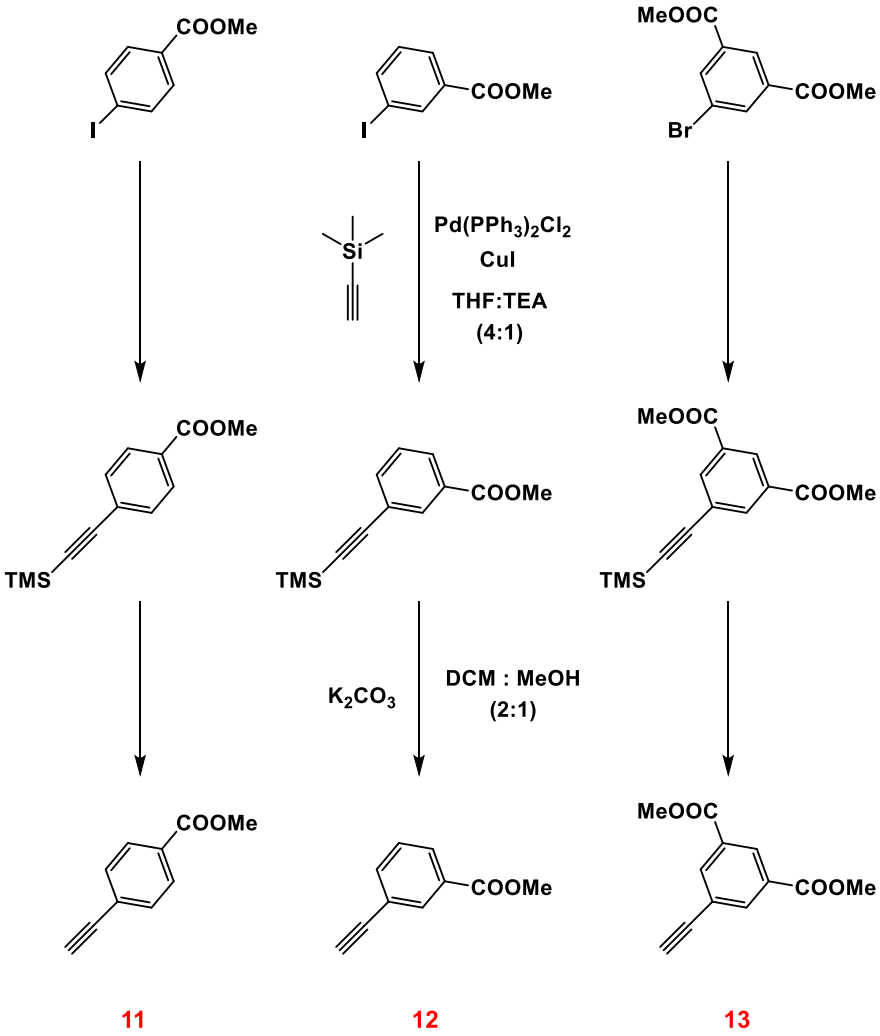

Scheme 2.3: Reaction pathway for the two-step synthesis of 11, 12 and 13.

The first step for the synthesis of alkyne-benzoic acid methyl ester compounds, **11**, **12** and **13** involved a Sonogashira cross-coupling reaction between the corresponding aryl halide and trimethylsilylacetylene under inert conditions, leading to the formation of a new carbon-carbon bond between the corresponding benzoate moieties and the TMS-protected ethynyl groups (Scheme 2.3). Catalyst loadings of 5% of $Pd(PPh_3)_2Cl_2$ and CuI in the presence of triethylamine (TEA) were required for the synthesis of TMS-protected

11-13 at satisfactory yields. However, shorter reaction times but higher temperatures were required to synthesise both TMS-protected **11** and **12** in contrast to TMS-protected **13** due to the increased reactivity of aryl iodide precursors in comparison to the bromo analogues.[25] The second step for the synthesis of **11, 12** and **13** involved the base-catalysed cleavage of the trimethylsilyl (TMS) groups resulting in the deprotection of the ethynyl groups. This reaction was identical for all three species involving potassium carbonate as the mild base (Scheme 2.3).

All three alkyne-benzoic acid methyl ester compounds were obtained as white crystalline powders in high yields (70% - 79%). Compounds **11**, **12** and **13** were subjected to purification by column chromatography and washing with aqueous NH_4Cl and brine. Analysis of the products *via* ^{1}H-NMR spectroscopy demonstrated the absence of starting materials and of other impurities in the samples (Fig. 2.4).

The ^{1}H-NMR spectra of **11**, **12** and **13** all exhibit signals at *ca.* 3.95 ppm and 3.20 ppm. These signals are attributed to the H-atoms of the methyl esters and ethynyl groups, respectively. The ^{1}H-NMR spectrum of **11** reveals an additional two signals at 8.02 ppm, and 7.57 ppm. Both signals integrate to two separate H-atoms and are attributed to the H-atoms of the aromatic ring. While the ^{1}H-NMR spectrum of **12** shows four additional signals that are attributed to individual H-atoms of the aromatic ring at 8.18 ppm, 8.03 ppm, 7.68 ppm and 7.42 ppm. The ^{1}H-NMR spectrum of **13** reveals signals at 8.66 ppm and 8.34 ppm which are attributed to one and two H-atoms respectively, of the aromatic ring. All H-atom signals in the ^{1}H-NMR spectra of **11**, **12** and **13** are in agreement with the literature.[26,27]

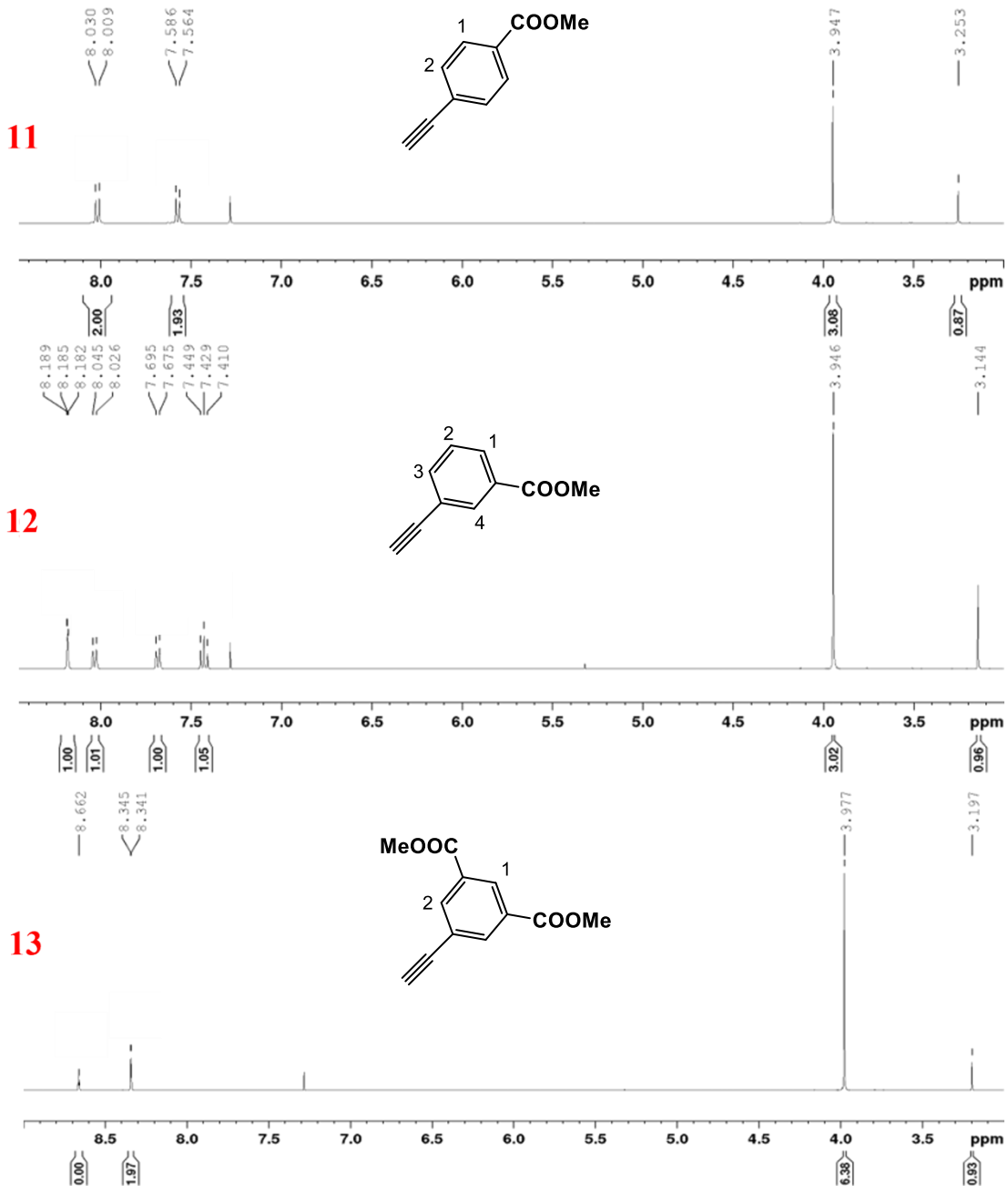

Figure 2.4: ^{1}H-NMR spectra of alkyne-benzoic acid methyl ester species 11, 12 and 13 in $CDCl_3$.

The initial approach for the synthesis of $\mathbf{H_2[L_{bpy}\text{-}R_1]^{2+}}$, $\mathbf{H_2[L_{bpy}\text{-}R_2]^{2+}}$, and $\mathbf{H_4[L_{bpy}\text{-}R_3]^{2+}}$, involved a Sonogashira cross-coupling reaction between the alkyne-benzoic acid methyl ester groups (**11-13**) and the brominated 2,2'-bipyridine **2** (Scheme 2.4). It was envisaged that this approach would yield extended 2,2'-bipyridine compounds **2-R'$_{1\text{-}3}$** which would subsequently be used for the synthesis of **8-R'$_{1\text{-}3}$** through their complexation with a bis-(2,2'-bipyridine)-ruthenium(II) dichloride precursor.

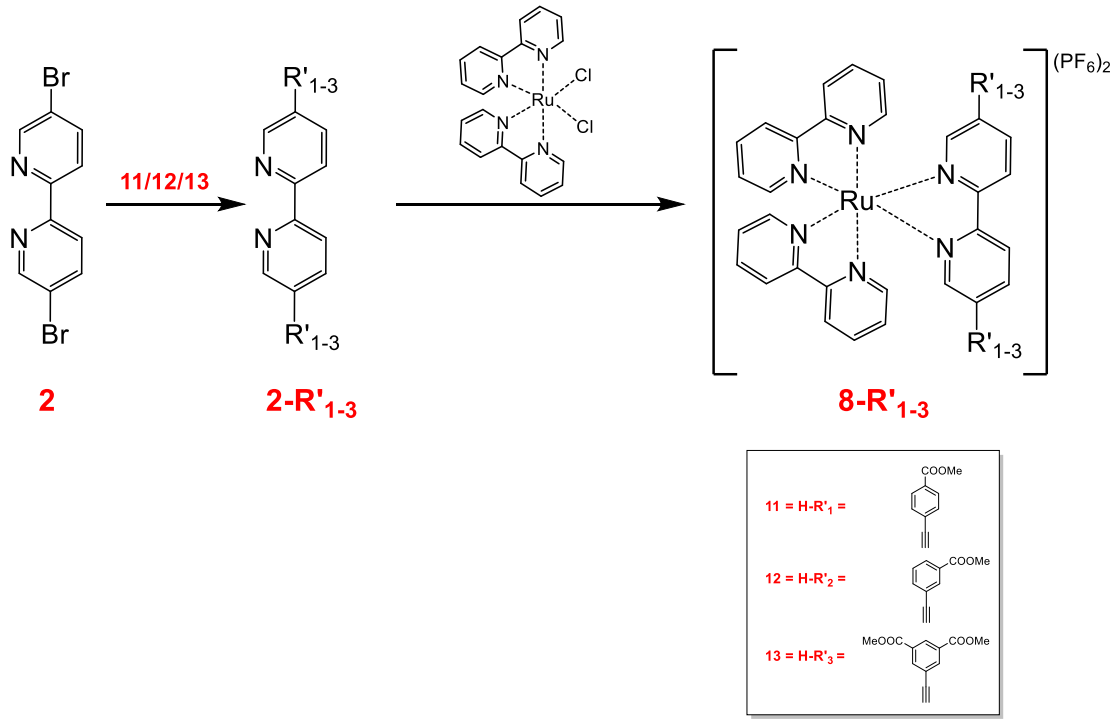

Scheme 2.4: Initial synthetic strategy for the synthesis of 8-R'$_{1\text{-}3}$.

However, this proved to be an unviable route for several reasons. Firstly, solubility tests demonstrated that **2** was only sparingly soluble in a wide range of solvents providing only low yields in Sonogashira cross-coupling reactions. Secondly, purification of the low-yielding products **2-R'$_{1\text{-}3}$** was also found to be highly problematic due to their difficulty in separation from starting materials and side products *via* column chromatography. Owing to these difficulties, only negligible yields of the desired **2-R'$_{1\text{-}3}$** compounds were obtained, and the approach was deemed impracticable.

A new synthetic approach was identified involving a Sonogashira cross-coupling reaction between the alkyne-benzoic acid methyl esters (**11-13**) and a brominated polypyridyl ruthenium(II) complex **5** (Scheme 2.5). This route was believed to be more viable as Sonogashira cross-coupling reactions are highly tolerable to various reaction conditions. Reactions can be carried out using certain metal complexes bearing a brominated

ligand.[28] Research by Tor and Tzalis indicated high reactivity for cross-coupling reactions at the 5,5' positions of 2,2'-bipyridine moieties of Ru^{II} complexes owing to the activating role of the coordinated Ru^{II} ion.[29] Therefore, utilising this high reactivity allowed an alternative synthetic strategy for obtaining the target ruthenium(II) polypyridine complexes.

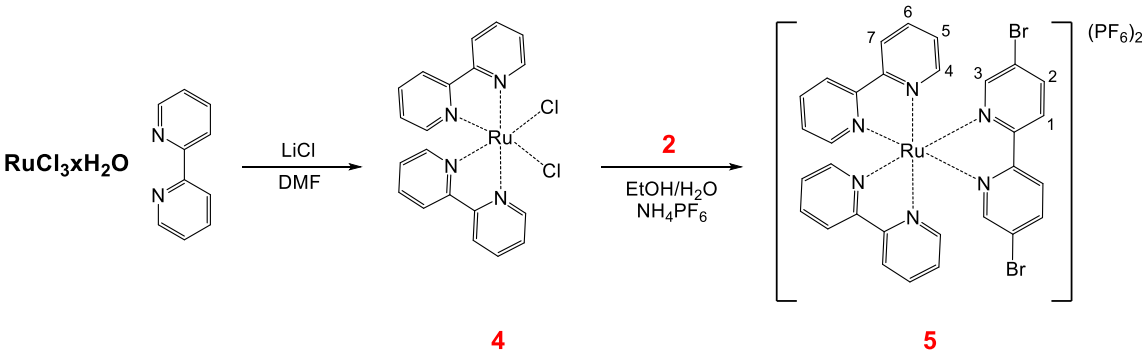

Scheme 2.5: Synthesis of bis-(2,2'-bipyridine)-ruthenium(II) dichloride (4), and bis-(2,2'-bipyridine)-ruthenium(II)(5,5'-dibromo-2,2'-bipyridine)]$(PF_6)_2$ (5).

The heteroleptic complex [bis-(2,2'-bipyridine)-ruthenium(II)(5,5'-dibromo-2,2'-bipyridine)]$(PF_6)_2$ (**5**) was therefore synthesised. To obtain **5**, bis-(2,2'-bipyridine)-ruthenium(II) dichloride (**4**) was initially synthesised according to an adapted procedure reported by Sullivan *et al.*[30] (Scheme 2.5). A purple microcrystalline material was obtained through the reaction of ruthenium(III) chloride hydrate, two equivalents of 2,2'-bipyridine and lithium chloride under an N_2 atmosphere. Analysis *via* ^{1}H-NMR spectroscopy and ESI mass spectrometry confirmed the purity of complex **4**.

One equivalent of the dibrominated 2,2'-bipyridine **2** was complexed to **4** in a solvent mixture of EtOH/H_2O (Scheme 2.5). The formation of the brominated complex **5** was evident from the distinct colour change from purple to deep red. The product was isolated through the addition of an excess amount of a saturated aqueous NH_4PF_6 solution which provided the necessary hexafluorophosphate counter-ions to precipitate the complex. The precipitate was recrystallised, resulting in the formation of red needle-like crystals of **5** in a high yield (80%). Interestingly, the hydrophobic character of the dibromo-bipyridine moiety **2** was retained in the synthesised ruthenium complex, **5**. However, **5** did show good solubility in acetonitrile and DMSO in contrast to **2**. The approach allowed a means to overcome solubility issues associated with the initially applied route. The compound was subsequently characterised by ^{1}H-NMR spectroscopy (Fig. 2.5) and ESI-mass

spectrometry. The ^{1}H-NMR spectrum of complex **5** reveals signals at 8.83 ppm, 8.49 ppm, 8.18 ppm, 7.85 ppm, 7.70 ppm, 7.67 and 7.55 ppm. The signal at 8.83 ppm is attributed to H-atoms of both the unsubstituted 2,2'-bipyridines and 5,5'-dibromo-2,2'-bipyridine moieties in complex **5**. The two signals at 8.49 ppm and 7.67 ppm are attributed to the remaining H-atoms of 5,5'-dibromo-2,2'-bipyridine in **5**. The signals at 8.18 ppm, 7.85 ppm, 7.70 and 7.55 ppm derive from the H-atoms of the unsubstituted 2,2'-bipyridine moieties. The ^{1}H-NMR spectrum and H-atom signals are in agreement with the literature.[31–33]

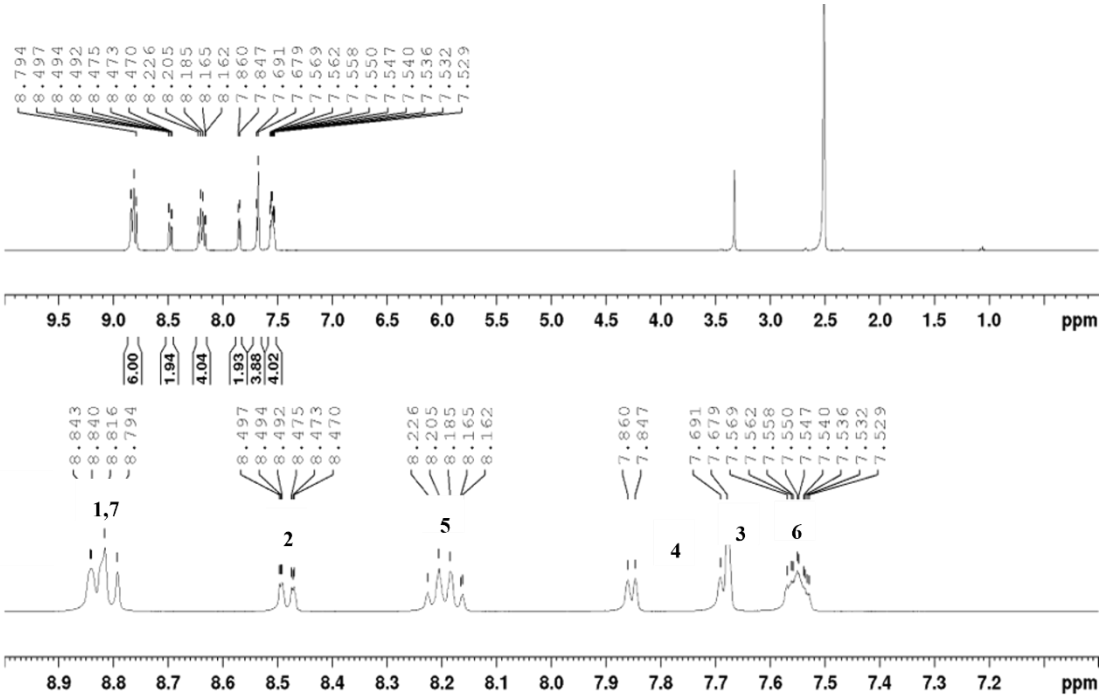

Figure 2.5: ^{1}H-NMR spectrum of [bis-(2,2'-bipyridine)-ruthenium(II)(5,5'-dibromo-2,2'-bipyridine)]$(PF_6)_2$ (5) in d_6-DMSO. Full spectrum of 5 (top), aromatic region of 5 (bottom).

The final reaction for the synthesis of the Ru^{II} polypyridyl complexes $\mathbf{H_2[L_{bpy}\text{-}R_1]^{2+}}$, $\mathbf{H_2[L_{bpy}\text{-}R_2]^{2+}}$, and $\mathbf{H_4[L_{bpy}\text{-}R_3]^{2+}}$ involved two steps. The initial step was a Sonogashira cross-coupling reaction between the alkyne-benzoic acid methyl ester compounds (**11-13**) and the heteroleptic ruthenium(II) complex **5**. Subsequently, the second step involved the base-catalysed ester hydrolysis of the methyl esters in $\mathbf{[8\text{-}R'_{1\text{-}3}]^{2+}}$ to yield the final Ru^{II} polypyridyl complexes $\mathbf{H_2[L_{bpy}\text{-}R_1]^{2+}}$, $\mathbf{H_2[L_{bpy}\text{-}R_2]^{2+}}$, and $\mathbf{H_4[L_{bpy}\text{-}R_3]^{2+}}$ (Scheme 2.6).

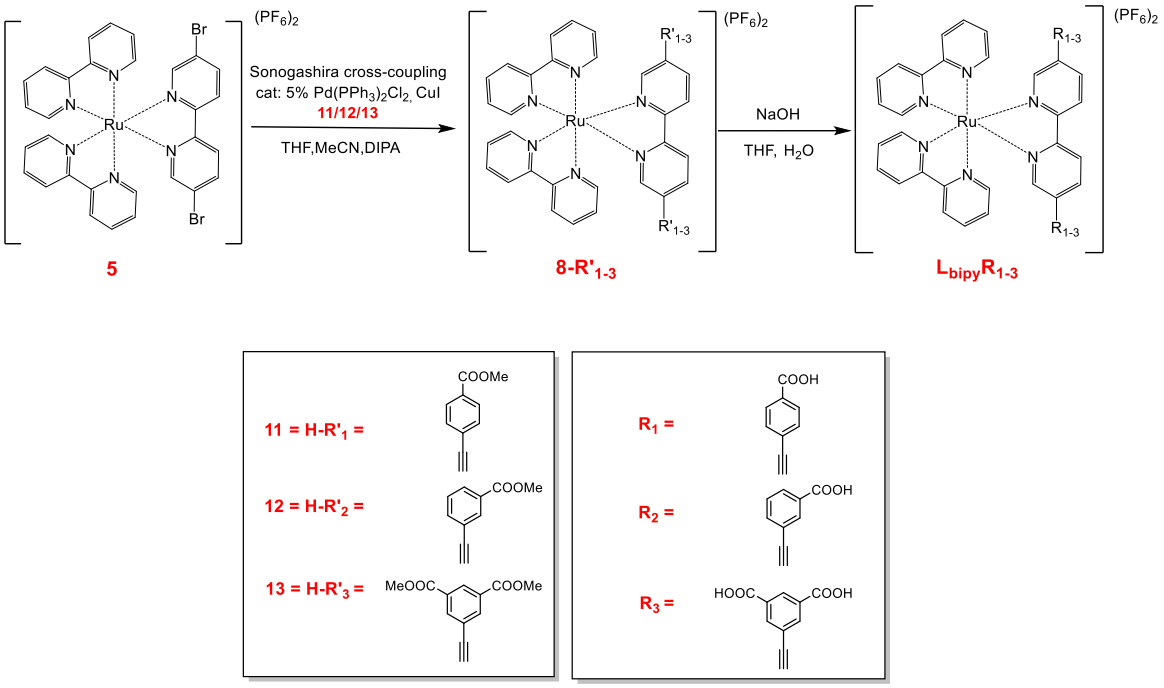

Scheme 2.6: Synthetic approaches to $\mathbf{[8\text{-}R'_{1\text{-}3}]^{2+}}$ and subsequently to $\mathbf{H_2[L_{bpy}\text{-}R_1]^{2+}}$, $\mathbf{H_2[L_{bpy}\text{-}R_2]^{2+}}$, and $\mathbf{H_4[L_{bpy}\text{-}R_3]^{2+}}$.

Following a modification of a procedure reported by Klemm *et al.*,[28] a Sonogashira cross-coupling reaction with catalyst loadings of 5 % of $Pd(PPh_3)_2Cl_2$ and CuI was carried out between two equivalents of the respective alkyne-benzoic acid methyl ester species (**11-13**) and complex **5**.

The modified procedure was identified to be highly practical in the high yielding synthesis of complexes $\mathbf{[8\text{-}R'_{1\text{-}3}]^{2+}}$. It was observed that the starting materials dissolved readily in MeCN and THF solvent mixtures. While upon completion of the reaction, it was identified that the final products $\mathbf{[8\text{-}R'_{1\text{-}3}]^{2+}}$ were insoluble in THF and thus precipitated out of their respective reaction mixtures. Therefore, allowing $\mathbf{[8\text{-}R'_{1\text{-}3}]^{2+}}$ to be isolated by simple gravity filtration and purified by washing with THF and water.

Analysis *via* ^{1}H-NMR spectroscopy and ESI mass spectrometry demonstrated the identity and purity of complexes **[8-R'$_{1\text{-}3}$]$^{2+}$**; the precipitates did not contain any residual starting materials or by-products of the Sonogashira cross-coupling reactions. Thus, this very efficient methodology of adding THF to the reaction mixture greatly simplified the synthesis of the target complexes while also bypassing any yield-reducing purification steps.

The final step for the synthesis of **H$_2$[L$_{bpy}$-R$_1$]$^{2+}$**, **H$_2$[L$_{bpy}$-R$_2$]$^{2+}$**, and **H$_4$[L$_{bpy}$-R$_3$]$^{2+}$**, was the base-catalysed ester hydrolysis of the respective methyl ester moieties present in complexes **[8-R'$_{1\text{-}3}$]$^{2+}$**. The reaction proceeded *via* an SN2 pathway, utilising sodium hydroxide as the base-catalyst in a solvent mixture of THF/H_2O (2:1) at room temperature under atmospheric conditions (Scheme 2.6). Upon completion of the reaction and removal of the organic solvent under reduced pressure, the remaining aqueous reaction solution was added to an excess amount of a strong acid (HPF_6 or $HClO_4$) to ensure complete protonation of the carboxylate ions and yield the respective desired metallo-ligand as a pure dicationic brick red precipitate in a high yield. The desired **H$_2$[L$_{bpy}$-R$_1$]$^{2+}$**, **H$_2$[L$_{bpy}$-R$_2$]$^{2+}$**, and **H$_4$[L$_{bpy}$-R$_3$]$^{2+}$** products obtained demonstrated high solubility in a variety of solvents (Fig. 2.6 (A)) which would prove to be highly beneficial in subsequent MOF synthesis. The highly hydrophobic products were purified by washing with water prior to drying at room temperature for three days. It was identified that the use of mild acids during the workup process would yield insoluble charge neutral Ru^{II} polypyridyl complexes (Fig. 2.6 (B)). Analysis *via* ^{1}H-NMR spectroscopy showed high purity along with the loss of the methyl ester H-atom signals for all three novel Ru^{II} polypyridyl complexes.

Figure 2.6: Solubility in d_6-DMSO of a synthesised Ru^{II} complex using a strong acid (A), and a weak acid (B) in the acidification workup during the base-catalysed ester hydrolysis reaction.

The desired metallo-ligands $\mathbf{H_2[L_{bpy}\text{-}R_1]^{2+}}$, $\mathbf{H_2[L_{bpy}\text{-}R_2]^{2+}}$, and $\mathbf{H_4[L_{bpy}\text{-}R_3]^{2+}}$ were characterised *via* ^{1}H, ^{13}C, ^{13}C^{1}H-COSY and HMBC-NMR. Comparison of the ^{1}H-NMR spectra of $\mathbf{H_2[L_{bpy}\text{-}R_1]^{2+}}$, $\mathbf{H_2[L_{bpy}\text{-}R_2]^{2+}}$, and $\mathbf{H_4[L_{bpy}\text{-}R_3]^{2+}}$ (Fig. 2.7 – 2.9) with the ^{1}H-NMR spectra of the respective alkyne-benzoic acid methyl ester group (**11-13**) and complex **5**, aided the complete assignment of the ^{1}H-NMR spectrum of each metallo-ligand.

The ^{1}H-NMR spectra of $\mathbf{H_2[L_{bpy}\text{-}R_1]^{2+}}$, $\mathbf{H_2[L_{bpy}\text{-}R_2]^{2+}}$, and $\mathbf{H_4[L_{bpy}\text{-}R_3]^{2+}}$ show similar chemical shifts for their respected H-atoms. The spectra also reveal intense signals attributed to residual solvents, water and dimethyl sulfoxide at chemical shifts of *ca.* 3.35 ppm and 2.50 ppm, respectively. Furthermore, the ^{1}H-NMR spectrum of $\mathbf{H_2[L_{bpy}\text{-}R_1]^{2+}}$ shows two doublets at 7.98 ppm and 7.62 ppm each integrating to two H-atoms and are attributed to the alkyne-benzoic acid methyl ester $\mathbf{R_1}$ moieties. The H-atoms of the extended 2,2'-bipyridine moiety of $\mathbf{H_2[L_{bpy}\text{-}R_1]^{2+}}$ give rise to three individual signals at 8.96 ppm, 8.42 ppm and 7.84 ppm with each integrating to two H-atoms. The remaining H-atoms that are attributed to the two unsubstituted bipyridine moieties of $\mathbf{H_2[L_{bpy}\text{-}R_1]^{2+}}$ give rise to signals at 8.85 ppm, 8.19 ppm, 7.86 ppm, 7.71 ppm and 7.57 ppm.

In the ^{1}H-NMR spectrum of $\mathbf{H_2[L_{bpy}\text{-}R_2]^{2+}}$ three signals located at 8.02 ppm, 7.75 ppm and 7.60 ppm can be attributed to the H-atoms of the alkyne-benzoic acid methyl ester moieties $\mathbf{R_2}$. Three signals with chemical shifts of 8.96 ppm, 8.43 ppm and 7.84 ppm with each integrating to two H-atoms are attributed to the H-atoms in the extended

2,2'-bipyridine moiety of $\mathbf{H_2[L_{bpy}\text{-}R_2]^{2+}}$. Signals at 8.84 ppm, 8.20 ppm, 7.87 ppm, 7.73 ppm and 7.57 ppm are attributed to the H-atoms of the two unsubstituted 2,2'-bipyridine moieties. The ^{1}H-NMR spectrum of $\mathbf{H_4[L_{bpy}\text{-}R_3]^{2+}}$ displays overlapping signals for the H-atom of different moieties in $\mathbf{H_4[L_{bpy}\text{-}R_3]^{2+}}$. The signals at 8.98 ppm, 8.48 ppm and 7.90 ppm derive from H-atoms in the extended bipyridine moiety. The alkyne-benzoic acid methyl ester groups $\mathbf{R_3}$ exhibit signals at chemical shifts of 8.48 ppm and 8.21 ppm, while the H-atoms attributed to the unsubstituted 2,2'-bipyridine moieties reveal signals at 8.85 ppm, 8.21 ppm, 7.90 ppm, 7.71 ppm and 7.56 ppm.

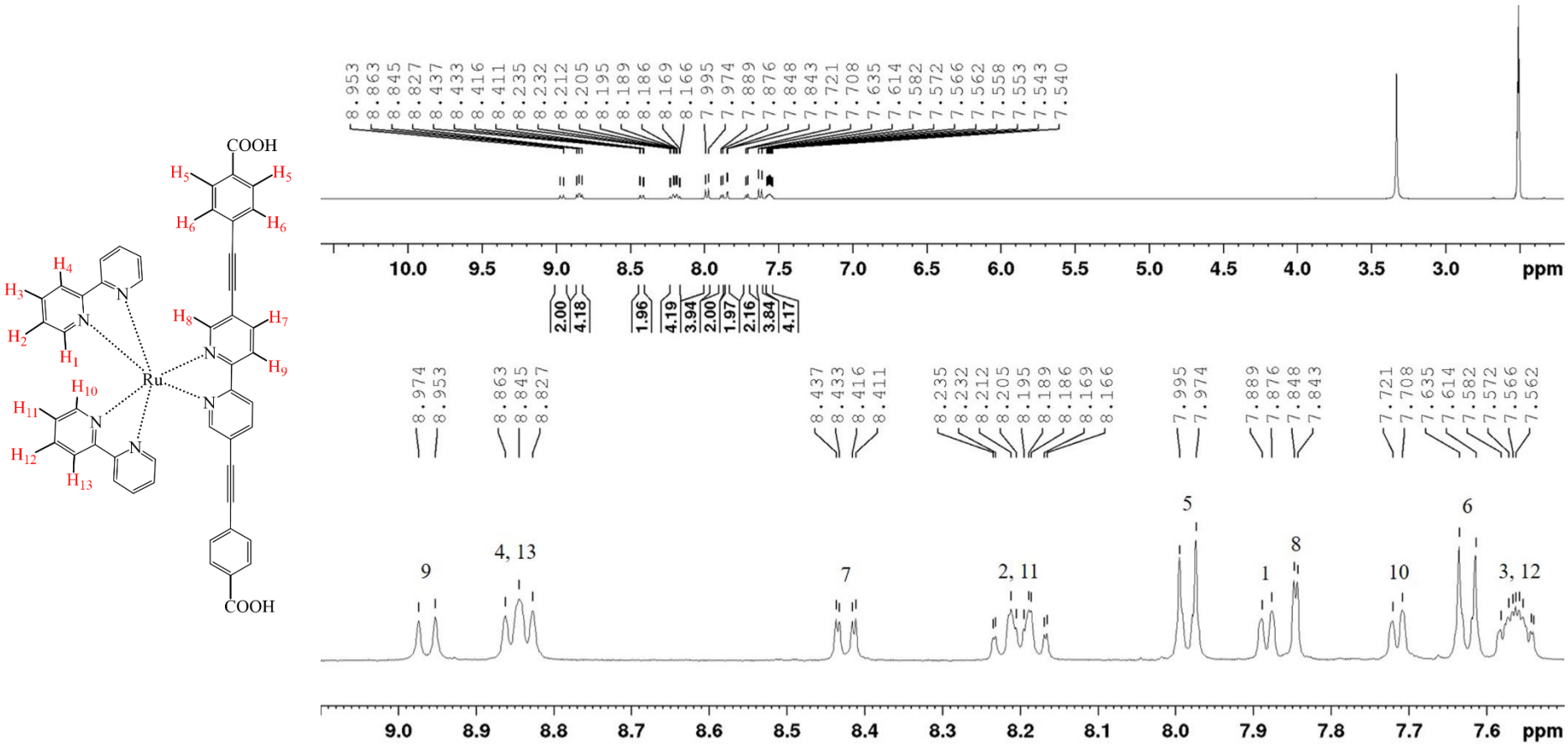

Figure 2.7: Labelled ^{1}H-NMR spectrum of $H_2[L_{bpy}\text{-}R_1]^{2+}$ in d_6-DMSO. Full spectrum of $H_2[L_{bpy}\text{-}R_1]^{2+}$ (top), aromatic region of $H_2[L_{bpy}\text{-}R_1]^{2+}$ (bottom).

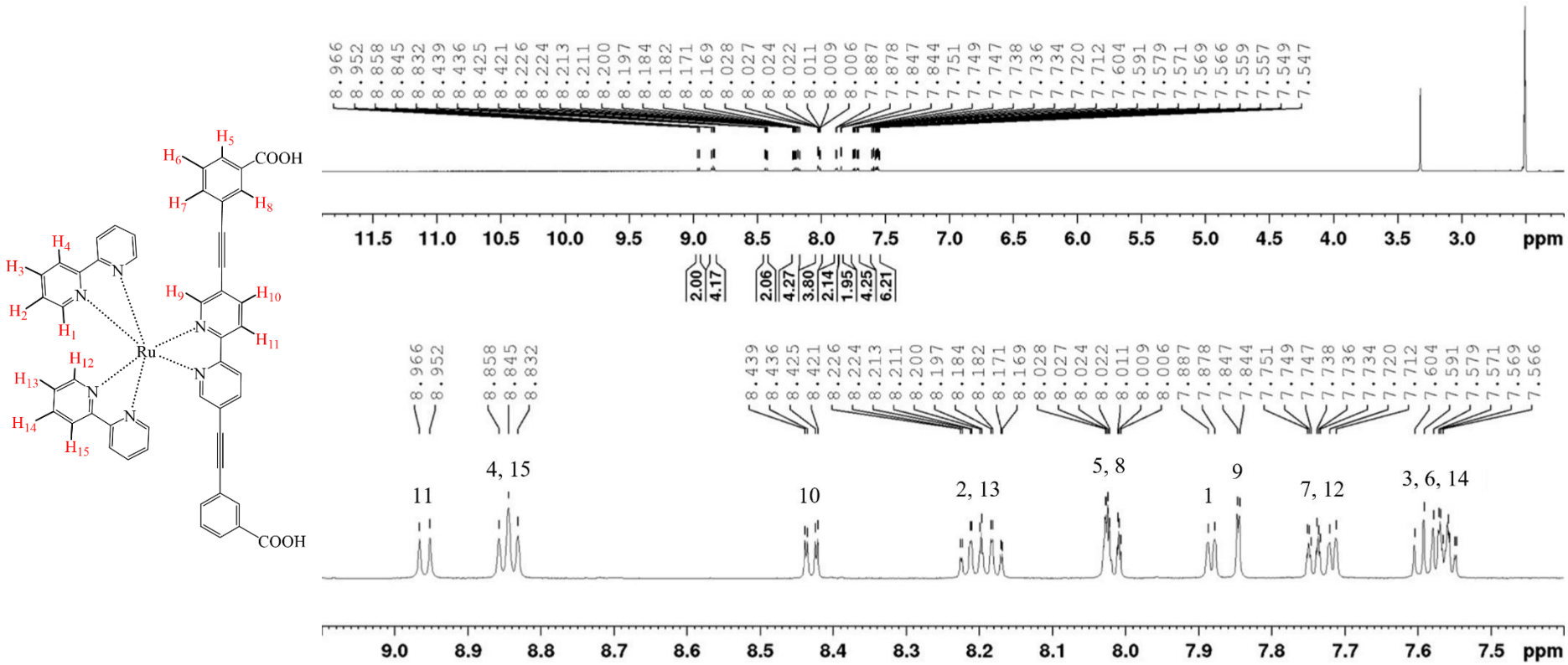

Figure 2.8: Labelled ^{1}H-NMR spectrum of $H_2[L_{bpy}\text{-}R_2]^{2+}$ in d_6-DMSO. Full spectrum of $H_2[L_{bpy}\text{-}R_2]^{2+}$ (top), aromatic region of $H_2[L_{bpy}\text{-}R_2]^{2+}$ (bottom).

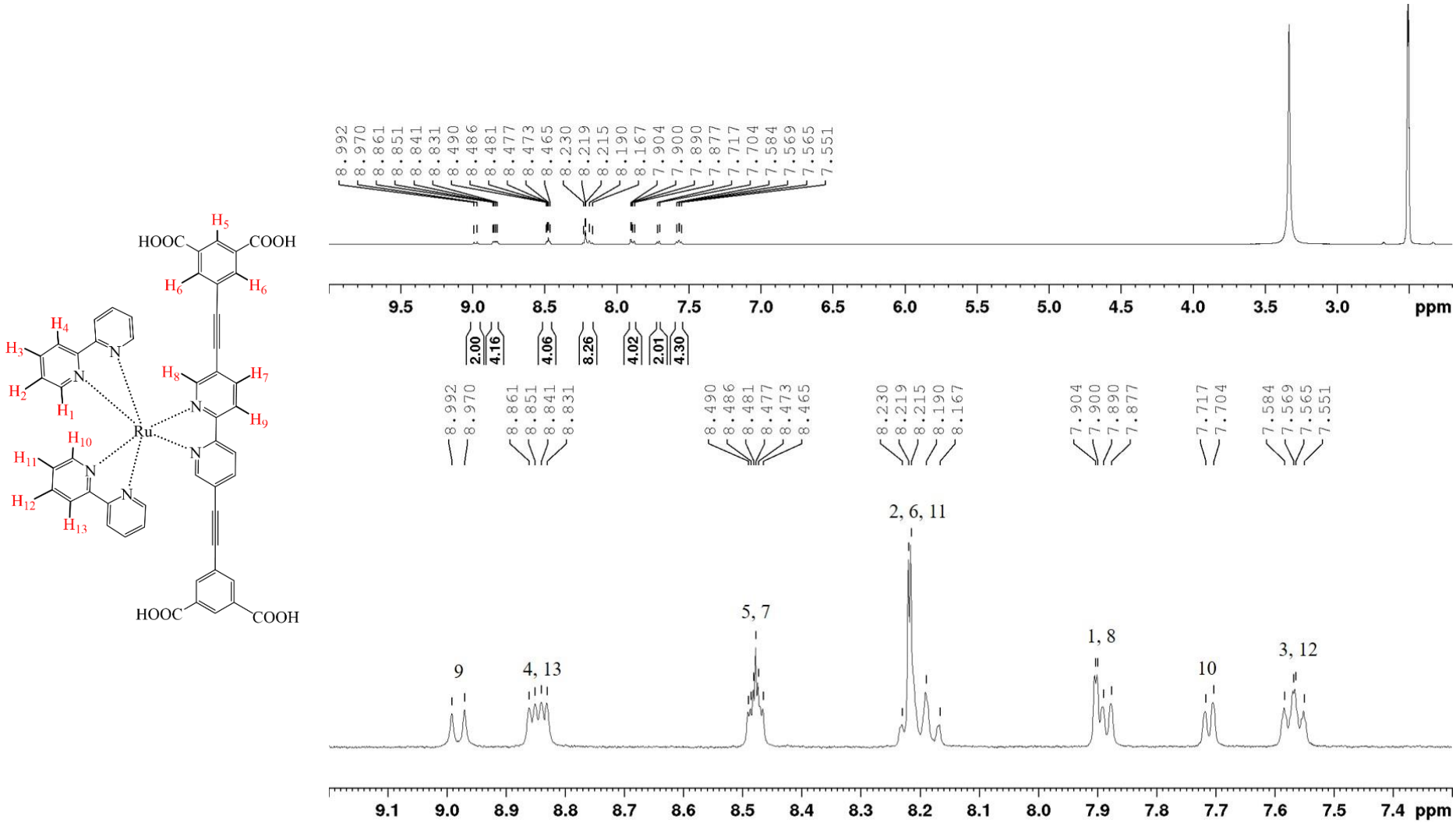

Figure 2.9: Labelled ^{1}H-NMR spectrum of $H_4[L_{bpy}\text{-}R_3]^{2+}$ in d$_6$-DMSO. Full spectrum of $H_4[L_{bpy}\text{-}R_3]^{2+}$ (top), aromatic region of $H_4[L_{bpy}\text{-}R_3]^{2+}$ (bottom).

2.4 Single Crystal X-ray Diffraction of $[8\text{-}R'_1]^{2+}$, $H_2[L_{bpy}\text{-}R_2]^{2+}$, and $H_4[L_{bpy}\text{-}R_3]^{2+}$

Single crystals of the Ru^{II} polypyridyl complexes $\mathbf{[8\text{-}R'_1]^{2+}}$, $\mathbf{H_2[L_{bpy}\text{-}R_2]^{2+}}$, and $\mathbf{H_4[L_{bpy}\text{-}R_3]^{2+}}$ were obtained by the diffusion and gradual mixing of Et_2O and a saturated solution of each of the respective complexes in MeCN, in individual H-tubes. This method of crystallisation was chosen as slow mixing of the two solvents increases the polarity of the saturated MeCN solution, thus reducing the solubility of $\mathbf{[8\text{-}R'_1]^{2+}}$, $\mathbf{H_2[L_{bpy}\text{-}R_2]^{2+}}$, and $\mathbf{H_4[L_{bpy}\text{-}R_3]^{2+}}$. Therefore, causing the respective complex to slowly crystallise as orange coloured needle-shaped single crystals. Crystal structures were determined *via* single crystal X-ray diffraction analysis.

The crystal structure of $\mathbf{[8\text{-}R'_1]^{2+}}$ (Fig. 2.10) was solved in the monoclinic space group *I2/a*. It was identified that the Ru^{II} centre adopts a distorted octahedral coordination environment, where the Ru-N bond lengths in the coordination sphere of the $\mathbf{[8\text{-}R'_1]^{2+}}$ backbone vary between 2.048(1) Å – 2.110(6) Å. Furthermore, the backbone of $\mathbf{[8\text{-}R'_1]^{2+}}$ displays a slightly bent configuration, exhibiting an angle of 171.26° measured from A to B, deviating only slightly from the ideal angle of 180°, further highlighting the distorted nature of the coordination environment. It is anticipated that this is due to the crystal packing requirements of $\mathbf{[8\text{-}R'_1]^{2+}}$. Selected bond distances and angles between the ruthenium and nitrogen atoms in $\mathbf{[8\text{-}R'_1]^{2+}}$ are summarised in Table 2.1. Complete crystallographic data and structure refinements are provided in Table 2.2.

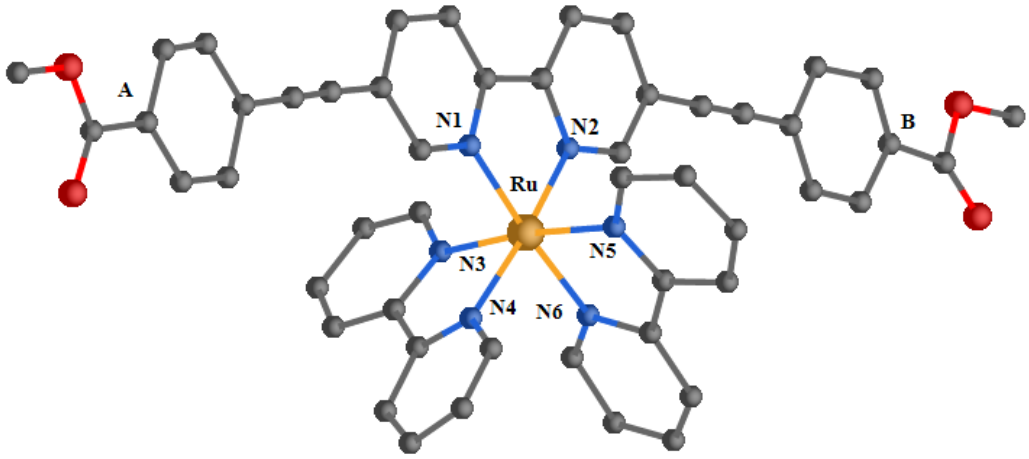

Figure 2.10: Single crystal X-ray diffraction structure, ball-and-stick representation of $[8\text{-}R'_1]^{2+}$. Colour scheme: Ru (orange), N (blue), O (red), C (grey). Solvents of crystallisation, H atoms and counter-ions were omitted for clarity.

Table 2.1: Selected bond angles and distances obtained from the single crystal X-ray diffraction for $[8\text{-}R'_1]^{2+}$.

Atom			Angle (°)	Atom		Distance (Å)
N1	Ru	N3	89.782(4)	Ru	N1	2.046(2)
N2	Ru	N4	175.47(11)	Ru	N2	2.057(1)
N2	Ru	N6	99.355(9)	Ru	N3	2.110(6)
N3	Ru	N5	173.059(8)	Ru	N4	2.048(1)
N4	Ru	N5	94.655(2)	Ru	N5	2.010(5)
N6	Ru	N5	77.370(11)	Ru	N6	2.083(1)

A better understanding of the main intermolecular forces to which complex **$[8\text{-}R'_1]^{2+}$** is subjected to can be seen when analysing the packing arrangement of the crystal structure. Figure 2.11 illustrates the packing diagram of molecules of **$[8\text{-}R'_1]^{2+}$** within a supercell, viewed along the crystallographic *a*-axis. The packing diagram displays bipyridine moieties arranging to form sheets of aromatic rings. The distances between the carbon atoms of the bipyridine aromatic rings in **$[8\text{-}R'_1]^{2+}$** range from 3.4 Å - 3.7 Å, which is consistent with π – π stacking interactions.[34] This demonstrates the importance of π – π stacking interactions for crystal formation. Therefore, this stacking effect gives directionality to the crystal, which in turn could explain the propensity of the compound to crystallise into thin needle-like structures. This is further illustrated in Figure 2.12 where the aromatic ring alignment is demonstrated when viewed along the crystallographic *c*-axis.

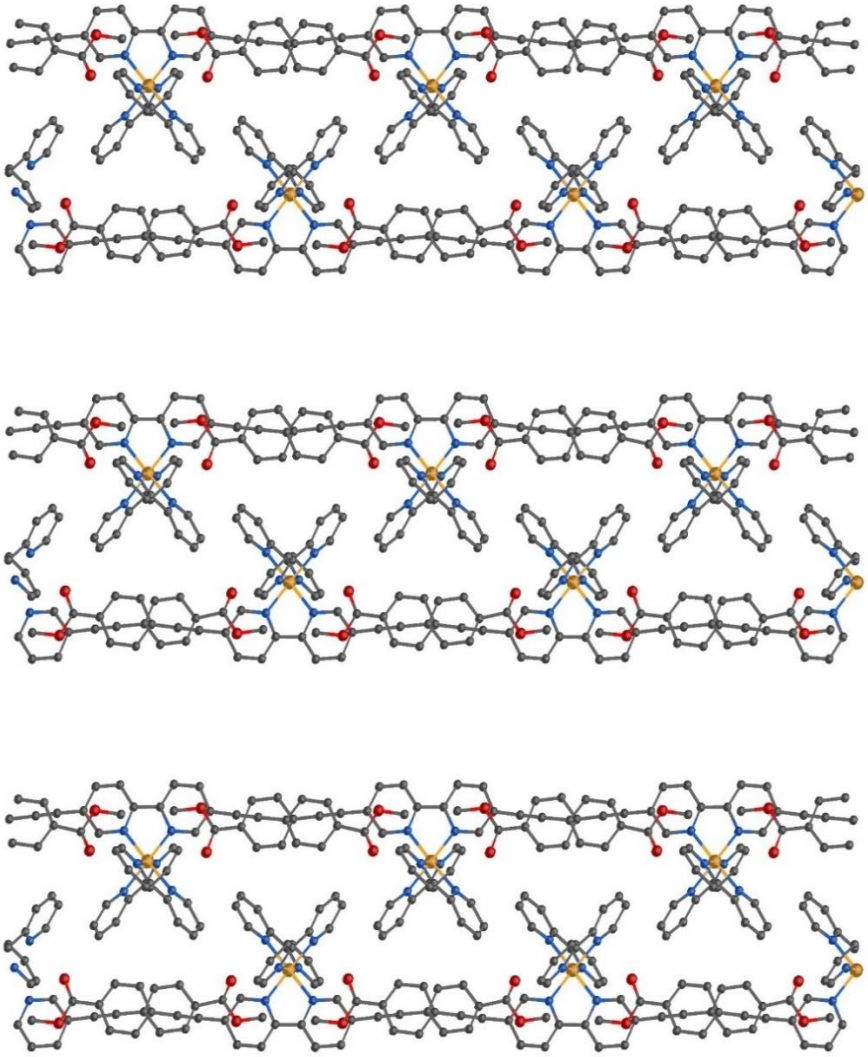

Figure 2.11: Packing diagram of $[8\text{-}R'_1]^{2+}$ viewed along the crystallographic *a*-axis. Colour scheme: Ru (orange), N (blue), O (red), C (grey). Solvents of crystallisation, H atoms and counter-ions were omitted for clarity.

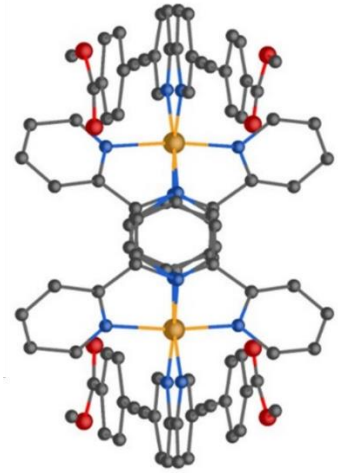

Figure 2.12: Aromatic ring alignment of $[8\text{-}R'_1]^{2+}$ viewed along the crystallographic *c*-axis. Colour scheme: Ru (orange), N (blue), O (red), C (grey). Solvents of crystallisation, H atoms and counter-ions were omitted for clarity.

Table 2.2: Single crystal X-ray diffraction data and structure refinement for $[8\text{-}R'_1]^{2+}$.

Identification code	$[8\text{-}R'_1]^{2+}$
Empirical formula	$C_{50}H_{36}F_{12}N_6O_4P_2Ru$
Formula weight	1175.86
Temperature/K	100(2)
Crystal system	monoclinic
Space group	*I*2/*a*
a/Å	16.7826(5)
b/Å	20.0977(7)
c/Å	18.1997(5)
α/°	90
β/°	114.957(2)
γ/°	90
Volume/$Å^3$	5565.4(3)
Z	4
$\rho_{calc}g/cm^3$	1.403
μ/mm^{-1}	0.426
F(000)	2368.0
Crystal size/mm^3	0.32 × 0.13 × 0.08
Radiation	MoKα (λ = 0.71073)
2Θ range for data collection/°	3.194 to 60.256
Index ranges	$-23 \leq h \leq 23$, $-28 \leq k \leq 28$, $-25 \leq l \leq 25$
Reflections collected	51262
Independent reflections	8226 [R_{int} = 0.0549, R_{sigma} = 0.0366]
Data/restraints/parameters	8226/0/340
Goodness-of-fit on F^2	1.020
Final R indexes [I>=2σ (I)]	R_1 = 0.0486, wR_2 = 0.1263
Final R indexes [all data]	R_1 = 0.0668, wR_2 = 0.1380
Largest diff. peak/hole / e $Å^{-3}$	2.04/-1.09

The crystal structure of $\mathbf{H_2[L_{bpy}\text{-}R2]^{2+}}$ (Fig. 2.13) was solved in the monoclinic space group $P2_1/c$. Like the previous complex, the Ru^{II} centre also adopts a distorted octahedral coordination environment, where Ru – N bond lengths vary from 2.040(6) Å to 2.071(6) Å. The elongated 2,2'-bipyridine of the metallo-ligand $\mathbf{H_2[L_{bpy}\text{-}R_2]^{2+}}$ is identified to be coplanar. Selected bond distances and angles between the ruthenium and nitrogen atoms in $\mathbf{H_2[L_{bpy}\text{-}R_2]^{2+}}$ are summarised in Table 2.3. Full crystallographic data and structure refinements are provided in Table 2.4.

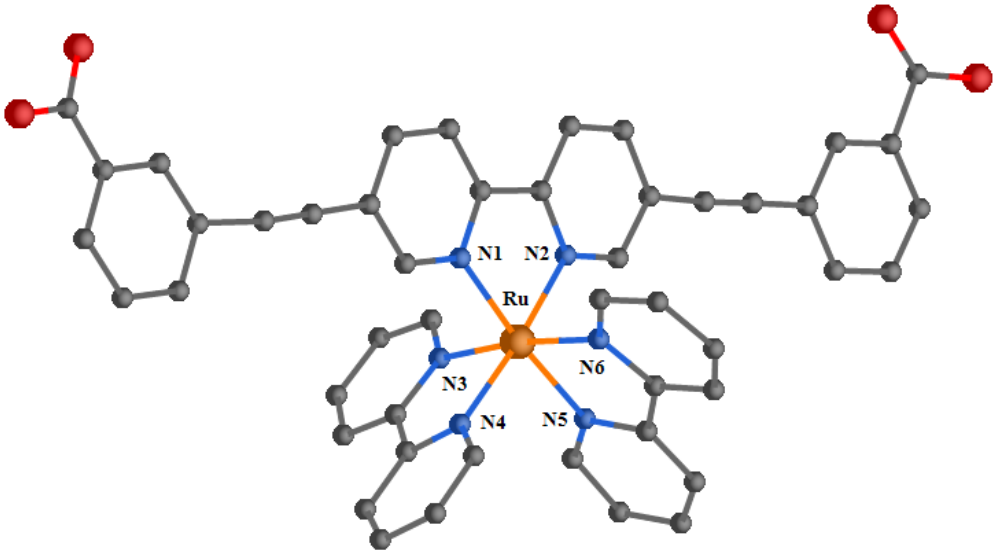

Figure 2.13: Single crystal X-ray diffraction structure, ball-and-stick representation of $\mathbf{H_2[L_{bpy}\text{-}R_2]^{2+}}$. Colour scheme: Ru (orange), N (blue), O (red), C (grey). Solvents of crystallisation, H atoms and counter-ions were omitted for clarity.

Table 2.3: Selected bond angles and distances obtained from the single crystal X-ray diffraction for $\mathbf{H_2[L_{bpy}\text{-}R_2]^{2+}}$.

Atom			Angle (°)	Atom		Distance (Å)
N1	Ru	N3	87.977(4)	Ru	N1	2.056(6)
N2	Ru	N6	90.072(4)	Ru	N2	2.062(7)
N3	Ru	N5	96.539(5)	Ru	N3	2.051(6)
N3	Ru	N4	80.048(2)	Ru	N4	2.069(7)
N4	Ru	N5	87.077(4)	Ru	N5	2.071(6)
N5	Ru	N6	78.989(10)	Ru	N6	2.040(6)

When analysing the packing arrangement of complex $\mathbf{H_2[L_{bpy}\text{-}R_2]^{2+}}$ within a supercell, viewed along the *c*-axis (Fig. 2.14) and the aromatic ring alignment viewed along the crystallographic *a* and *b* axes (Fig. 2.15) here again π – π stacking interactions are highly evident and important in the formation of the crystal. In the case of $\mathbf{H_2[L_{bpy}\text{-}R_2]^{2+}}$, the π – π stacking interactions can be seen between bipyridine moieties and the alkyne-benzoic acid groups (Fig. 2.15). Distances ranging from 3.5 Å - 3.7 Å are present between the carbon atoms of the extended bipyridine aromatic rings, and this is consistent with π – π stacking interactions.[34]

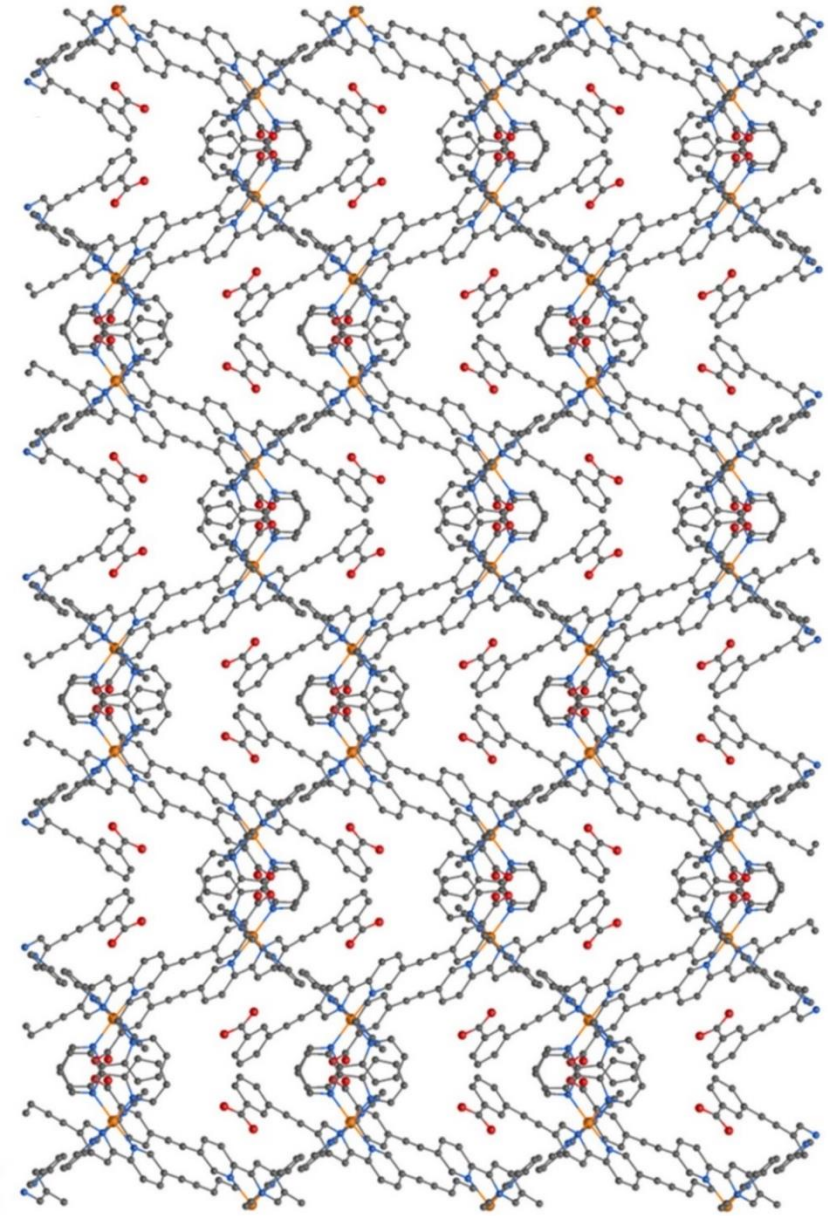

Figure 2.14: Packing diagram of $H_2[L_{bpy}\text{-}R_2]^{2+}$ viewed along the crystallographic *c*-axis. Colour scheme: Ru (orange), N (blue), O (red), C (grey). Solvents of crystallisation, H atoms and counter-ions were omitted for clarity.

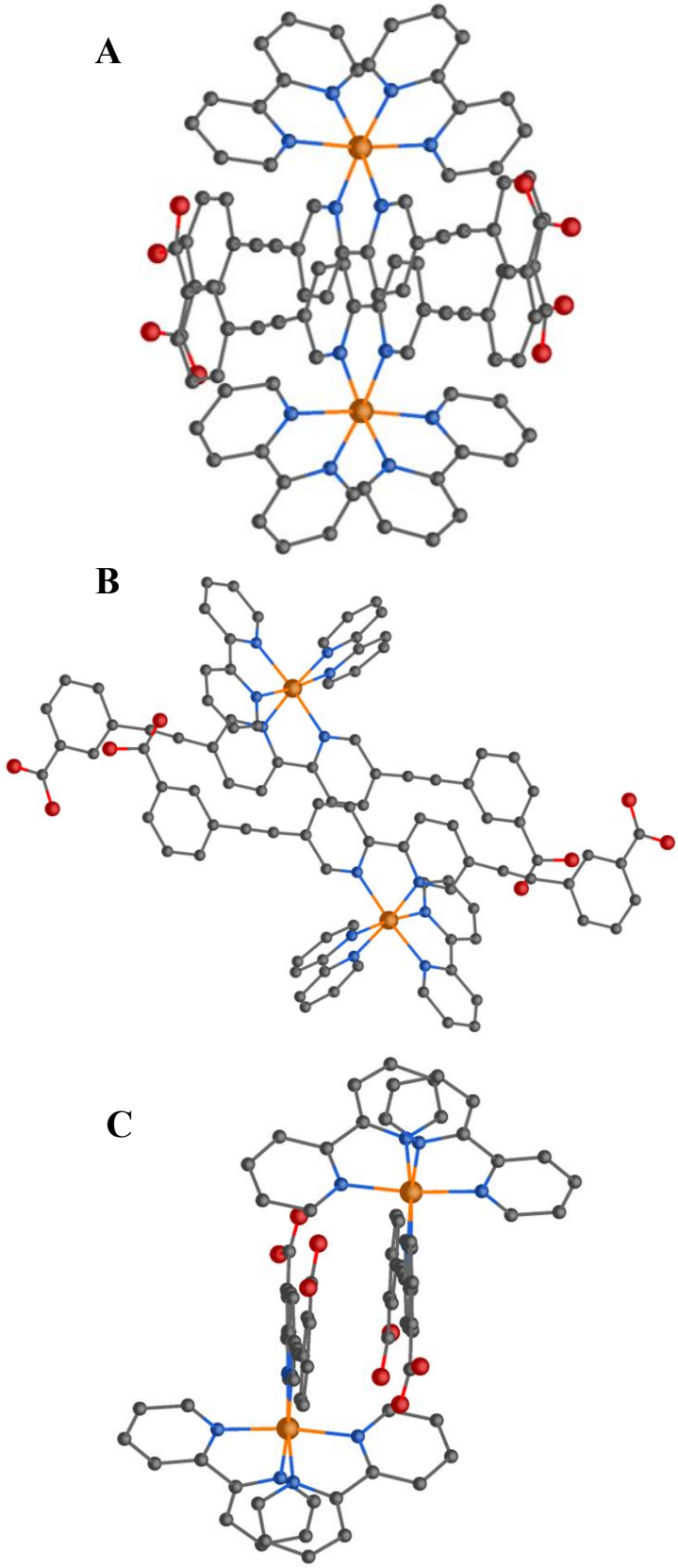

Figure 2.15: Aromatic ring alignment of $H_2[L_{bpy}\text{-}R_2]^{2+}$ viewed along the crystallographic *a*-axis (A and B) and *b*-axis (C). Colour scheme: Ru (orange), N (blue), O (red), C (grey). Solvents of crystallisation, H atoms and counter-ions were omitted for clarity.

Table 2.4: Single crystal X-ray diffraction data and structure refinement for $H_2[L_{bpy}\text{-}R_2]^{2+}$.

Identification code	$H_2[L_{bpy}\text{-}R_2]^{2+}$
Empirical formula	$[C_{48}H_{32}N_6O_4Ru](ClO_4)_2$
Formula weight	1056.78
Temperature/K	100(2)
Crystal system	monoclinic
Space group	$P2_1/c$
a/Å	15.1646(7)
b/Å	22.1187(10)
c/Å	19.1377(8
α/°	90
β/°	110.5960(10)
γ/°	90
Volume/$Å^3$	6008.9(5)
Z	2
$\rho_{calc}g/cm^3$	1.328
μ/mm^{-1}	0.416
F(000)	2460.0
Crystal size/mm^3	0.26 × 0.12 × 0.11
Radiation	MoKα (λ = 0.71073)
2Θ range for data collection/°	2.926 to 50.768
Index ranges	$-18 \leq h \leq 18$, $-26 \leq k \leq 26$, $-23 \leq l \leq 23$
Reflections collected	141529
Independent reflections	11029 [R_{int} = 0.0438, R_{sigma} = 0.0219]
Data/restraints/parameters	11029/310/870
Goodness-of-fit on F^2	1.138
Final R indexes [I>=2σ (I)]	R_1 = 0.0934, wR_2 = 0.2582
Final R indexes [all data]	R_1 = 0.1189, wR_2 = 0.2865
Largest diff. peak/hole / e $Å^{-3}$	1.73/-0.77

The crystal structure for $\mathbf{H_4[L_{bpy}\text{-}R_3]^{2+}}$ (Fig. 2.16) was solved in the monoclinic space group *C2/c*. Here again, it is observed that the Ru^{II} centre adopts a distorted octahedral coordination environment, where the bond lengths of the Ru-N bond vary between 2.054(1) Å and 2.075(1) Å. Furthermore, the bending of the elongated ligand backbone of $\mathbf{H_4[L_{bpy}\text{-}R_3]^{2+}}$ when measured from A to B in Figure 2.20 was found to be 169.68°. Thus, deviating slightly more from the ideal angle of 180° than the previously mentioned Ru^{II} polypyridyl complexes. The reason for this is most likely due to the crystal packing requirements of $\mathbf{H_4[L_{bpy}\text{-}R_3]^{2+}}$. The bent geometry of $\mathbf{H_4[L_{bpy}\text{-}R_3]^{2+}}$ is believed to facilitate further stabilisation of the structure through π – π stacking interactions. Table 2.5 below displays selected bond distances and angles between the ruthenium and nitrogen atoms in $\mathbf{H_4[L_{bpy}\text{-}R_3]^{2+}}$. Complete crystallographic data and structure refinements are provided in Table 2.6.

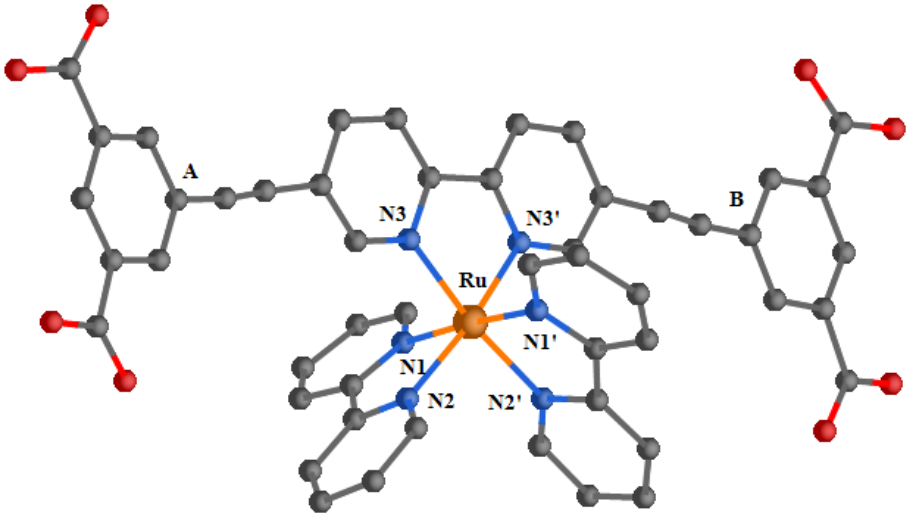

Figure 2.16: Single crystal X-ray diffraction structure, ball-and-stick representation of $\mathbf{H_4[L_{bpy}\text{-}R_3]^{2+}}$. Colour scheme: Ru (orange), N (blue), O (red), C (grey). Solvents of crystallisation, H atoms and counter-ions were omitted for clarity.

Table 2.5: Selected bond angles and distances obtained from the single crystal X-ray diffraction for $\mathbf{H_4[L_{bpy}\text{-}R_3]^{2+}}$.

Atom			Angle (°)	Atom		Distance (Å)
N1	Ru	N1'	176.318(14)	Ru	N1	2.075(1)
N1	Ru	N2'	78.692(14)	Ru	N2	2.067(2)
N1	Ru	N3	88.798(14)	Ru	N3	2.054(1)

The intermolecular forces within complex **$H_4[L_{bpy}\text{-}R_3]^{2+}$** can be seen when analysing its packing arrangement. A packing diagram of **$H_4[L_{bpy}\text{-}R_3]^{2+}$** molecules within a supercell, viewed along the crystallographic *a*-axis, can be seen in Figure 2.17. Observing the aromatic ring alignment by viewing along the crystallographic *b* and *c* axes (Fig. 2.18), the π – π stacking interactions can be seen between the bipyridine moieties. The C-C distances between the aromatic rings of the bipyridine moieties of two metallo-ligands range from 3.3 Å - 3.6 Å. The isophthalic acid moiety of the complex **$H_4[L_{bpy}\text{-}R_3]^{2+}$** allows for an extended hydrogen-bonding network within the crystal (Fig. 2.19). This dipole-dipole interaction between hydrogen and oxygen atoms of neighbouring isophthalic acid moieties and the π – π stacking interactions between the bipyridine aromatic rings greatly stabilise **$H_4[L_{bpy}\text{-}R_3]^{2+}$** and influence the packing in the crystal.

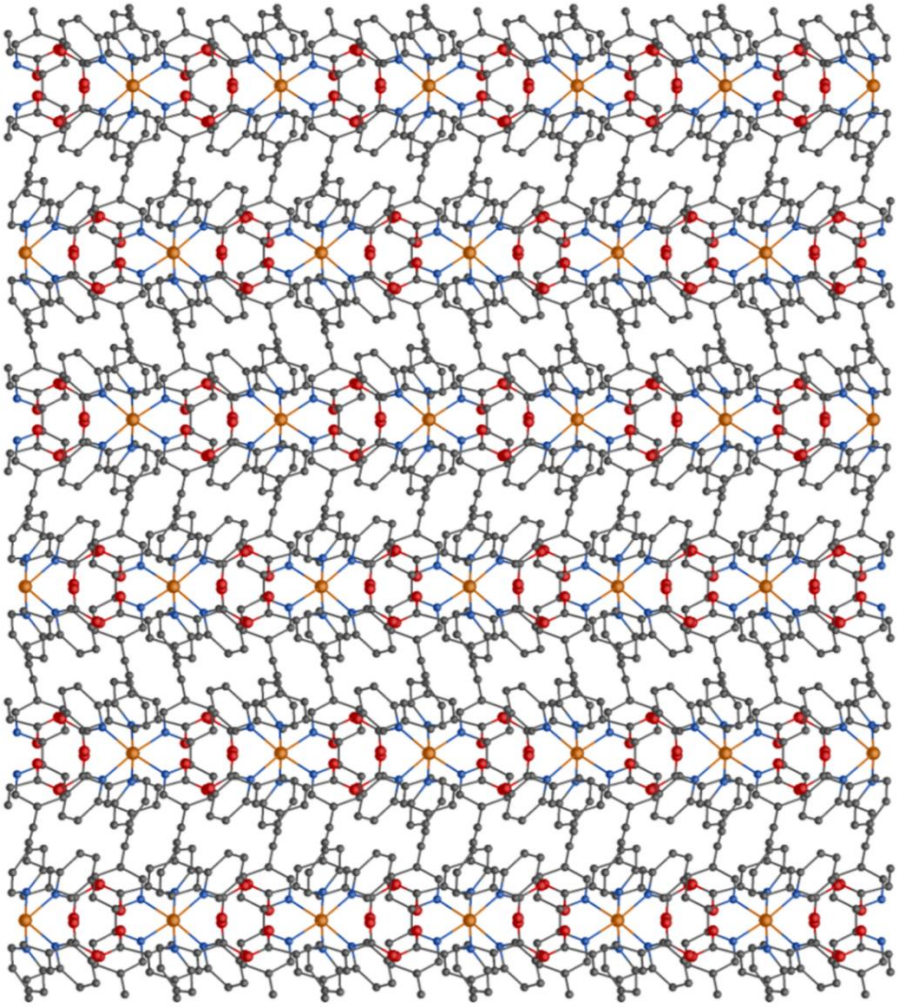

Figure 2.17: Packing diagram of $H_4[L_{bpy}\text{-}R_3]^{2+}$ viewed along the crystallographic *a*-axis. Colour scheme Ru (orange), N (blue), O (red), C (grey). Solvents of crystallisation, H atoms and counter-ions were omitted for clarity.

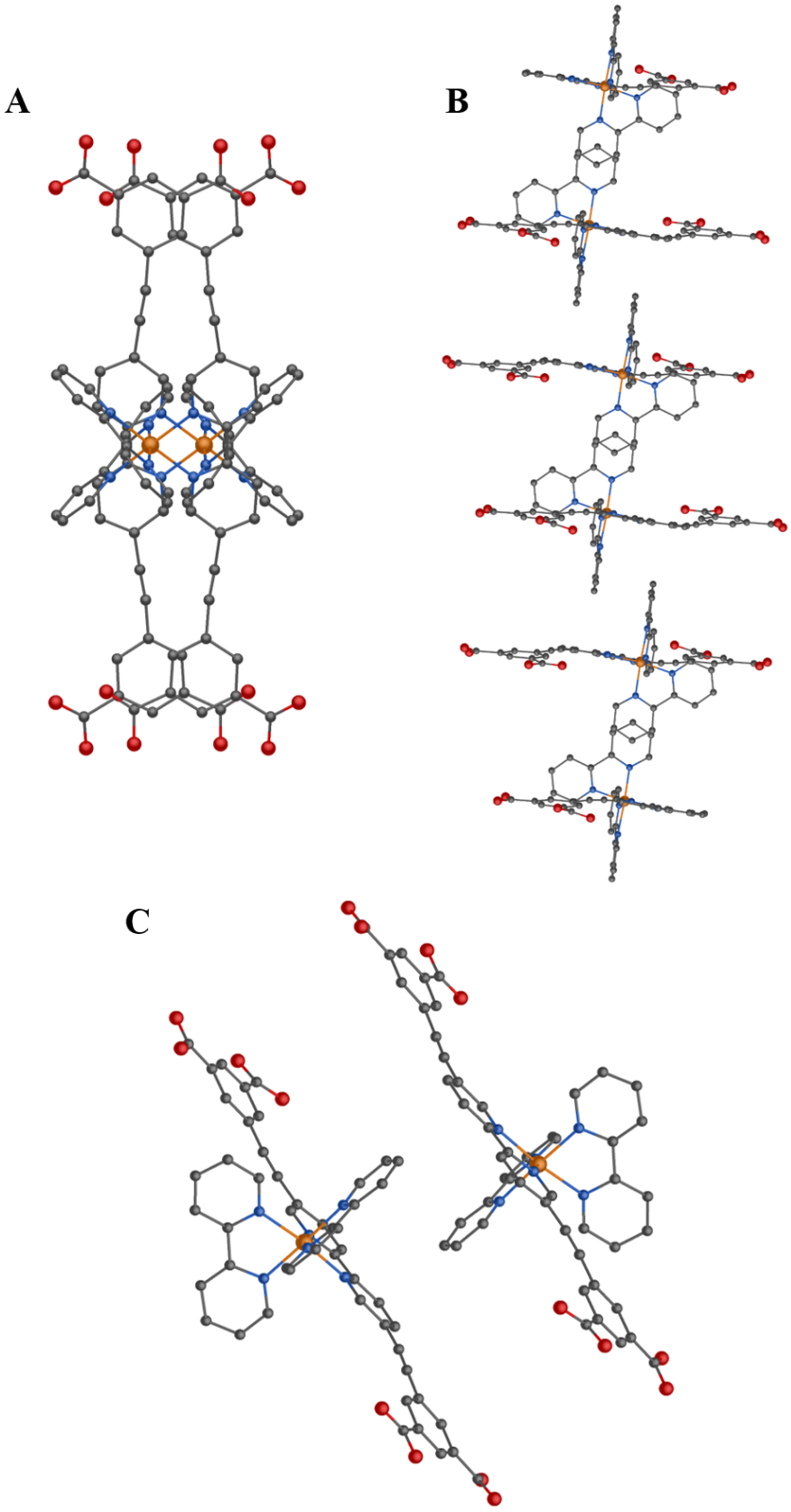

Figure 2.18: Aromatic ring alignment of $H_4[L_{bpy}\text{-}R_3]^{2+}$ viewed along the crystallographic *c*-axis (A), and *b*-axis (B and C). Colour scheme Ru (orange), N (blue), O (red), C (grey). Solvents of crystallisation, H atoms and counter-ions were omitted for clarity.

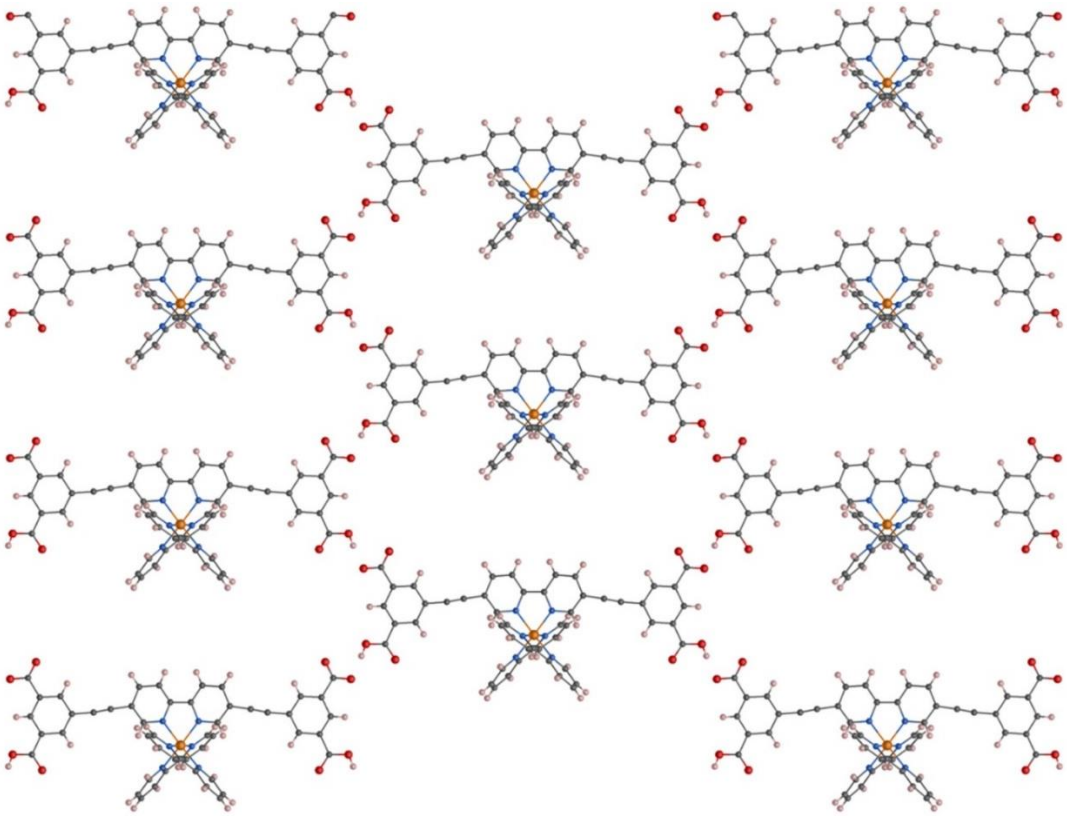

Figure 2.19: Packing diagram of $H_4[L_{bpy}\text{-}R_3]^{2+}$ viewed along the crystallographic *a*-axis, which displays the extended hydrogen-bonding network. Colour scheme: Ru (orange), N (blue), O (red), C (grey) H (pink). Solvents of crystallisation, Counter-ions were omitted for clarity.

Table 2.6: Single crystal X-ray diffraction data and structure refinement for $H_4[L_{bpy}\text{-}R_3]^{2+}$.

Identification code	$H_4[L_{bpy}\text{-}R_3]^{2+}$
Empirical formula	$[C_{50}H_{30}N_6O_8Ru](PF_6)_2$
Formula weight	1233.79
Temperature/K	100(2)
Crystal system	monoclinic
Space group	*C*2/c
a/Å	17.4005(6)
b/Å	14.5117(4)
c/Å	18.4034(7)
α/°	90
β/°	117.264(2)
γ/°	90
Volume/Å^3	4130.8(2)
Z	4
ρ_{calc}g/cm^3	1.518
μ/mm^{-1}	3.630
F(000)	1920.0
Crystal size/mm^3	0.07 × 0.04 × 0.04
Radiation	CuKα (λ = 1.54178)
2Θ range for data collection/°	8.354 to 117.922
Index ranges	$-19 \leq h \leq 19$, $-15 \leq k \leq 16$, $-20 \leq l \leq 20$
Reflections collected	17290
Independent reflections	2974 [R_{int} = 0.0652, R_{sigma} = 0.0467]
Data/restraints/parameters	2974/0/295
Goodness-of-fit on F^2	1.026
Final R indexes [I>=2σ (I)]	R_1 = 0.0549, wR_2 = 0.1401
Final R indexes [all data]	R_1 = 0.0699, wR_2 = 0.1500
Largest diff. peak/hole / e Å^{-3}	0.59/-0.52

2.5 Physicochemical Characterisation

Infrared Spectroscopy

Complexes $\mathbf{H_2[L_{bpy}\text{-}R_1]^{2+}}$, $\mathbf{H_2[L_{bpy}\text{-}R_2]^{2+}}$, and $\mathbf{H_4[L_{bpy}\text{-}R_3]^{2+}}$ were characterised *via* IR spectroscopy (Fig. 2.20 – 2.22). The FT-IR spectra for the Ru^{II} polypyridyl complexes shared significant similarities due to their related structural characteristic, thus, exhibiting highly characteristic bands of aromatic and highly conjugated compounds.

The signal which appears in the range of *ca*. 3500 cm^{-1} – 3300 cm^{-1} can be attributed to the hydrogen-bonded *v*(O–H) stretch present in all three novel complexes.[35,36] The *v*(C–H) stretching vibrations attributed to the aromatic moieties can be found between *ca.* 3080 cm^{-1} and 3070 cm^{-1}. The signals that can be seen between 1700 cm^{-1} and 1720 cm^{-1} can be assigned to the carbonyl *v*(C=O) vibrations of the free carboxylic acid groups.[37,38] The symmetric carboxylate stretching mode can be seen in the range of *ca*. 1375 cm^{-1}.[39,40] *v*(C=C) stretching vibrations attributed to the benzene and bipyridine moieties can be observed between 1500 cm^{-1} and 1300 cm^{-1}, while the *v*(C–N) stretch derived from the bipyridine moiety is seen at *ca.* 1250 cm^{-1}.[41,42] The *v*(C–O) stretch can be seen between *ca.* 1230cm^{-1} and *ca.* 1080 cm^{-1}. The weak band at *ca*. 840 cm^{-1} confirms the presence of PF_6^- in the structure.[43] Within the fingerprint region, *v*(C–H) bending vibrations corresponding to benzene and bipyridine ring moieties within the Ru^{II} polypyridyl complexes can be observed in the region of *ca.* 760 cm^{-1} and 620 cm^{-1}.[44] The {Ru-N} stretch occurs at approximately 560 cm^{-1}.[43]

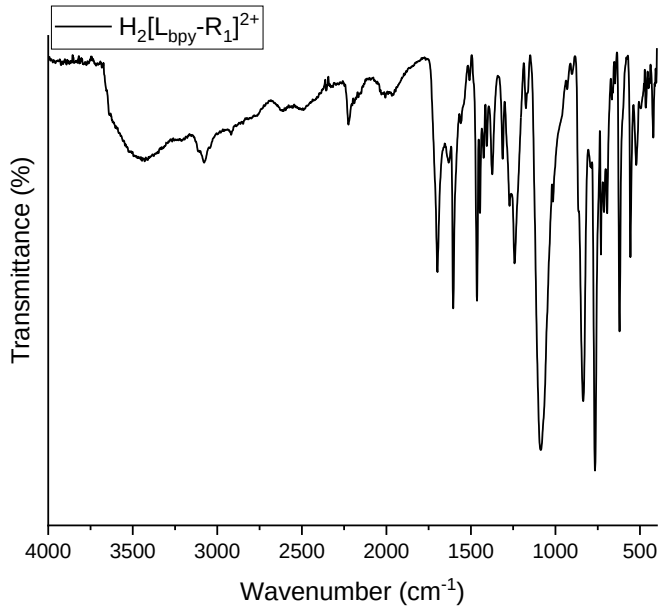

Figure 2.20: FT-IR spectrum of $\mathbf{H_2[L_{bpy}\text{-}R_1]^{2+}}$.

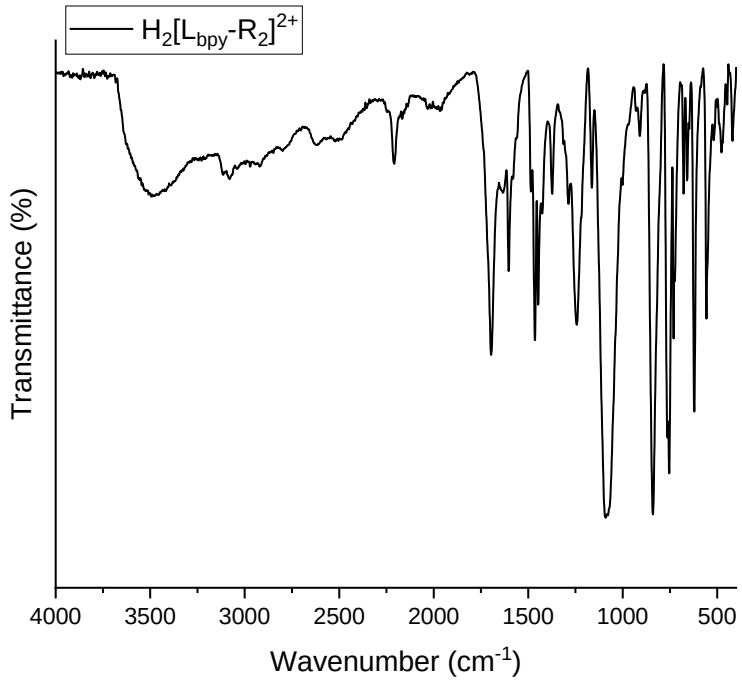

Figure 2.21: FT-IR spectrum of $H_2[L_{bpy}\text{-}R_2]^{2+}$.

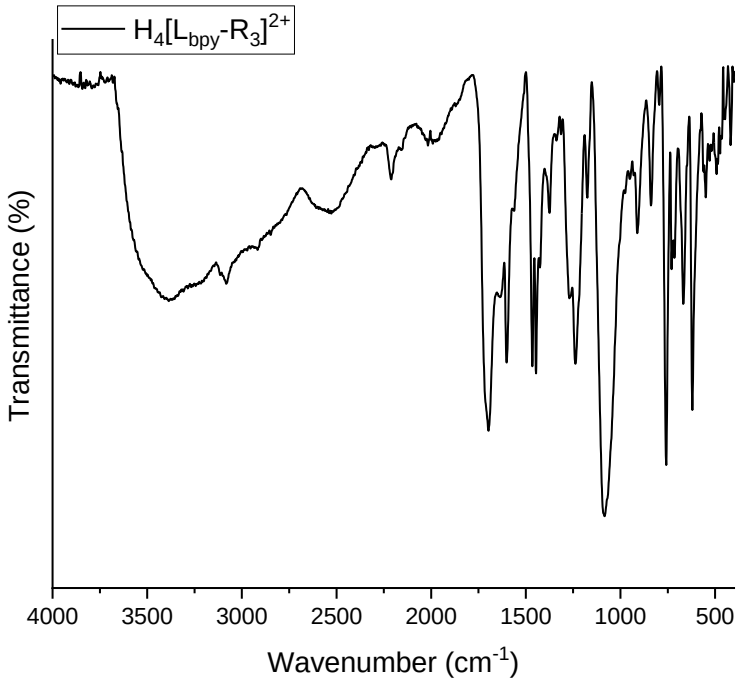

Figure 2.22: FT-IR spectrum of $H_4[L_{bpy}\text{-}R_3]^{2+}$.

Raman Spectroscopy

The complexes $\mathbf{H_2[L_{bpy}\text{-}R_1]^{2+}}$, $\mathbf{H_2[L_{bpy}\text{-}R_2]^{2+}}$, and $\mathbf{H_4[L_{bpy}\text{-}R_3]^{2+}}$ were also similarly characterised *via* Raman spectroscopy (Fig. 2.23 – 2.25). The Raman spectrum was measured from 400 cm^{-1} to 2500 cm^{-1} and the baseline was corrected using OriginLab 2020 software. Just like the FT-IR spectra, the Raman spectra were also nearly identical.

The signals between 950 cm^{-1} and 1200 cm^{-1} can be attributed to the aromatic and heteroaromatic ν(C–H) vibrations.[45] The signals in the region of *ca.* 1275 cm^{-1} and 1320 cm^{-1} derive from ν(C–C) single bond vibrations. The ν_s(C=O) vibrations that derive from the carboxylate groups of the metallo-ligands can be observed at approximately 1370 cm^{-1}. The heteroaromatic and aromatic ν(C=C) vibrations can be seen between *ca.* 1490 cm^{-1} and 1600 cm^{-1}. The final prominent signal in all obtained spectra is found at approximately 2218 cm^{-1} and derives from the C≡C vibration of the alkyne moiety. These particularly intense Raman signals assigned to the C≡C vibrations are in contrast very weak in the FT-IR spectra for the corresponding complexes.[46]

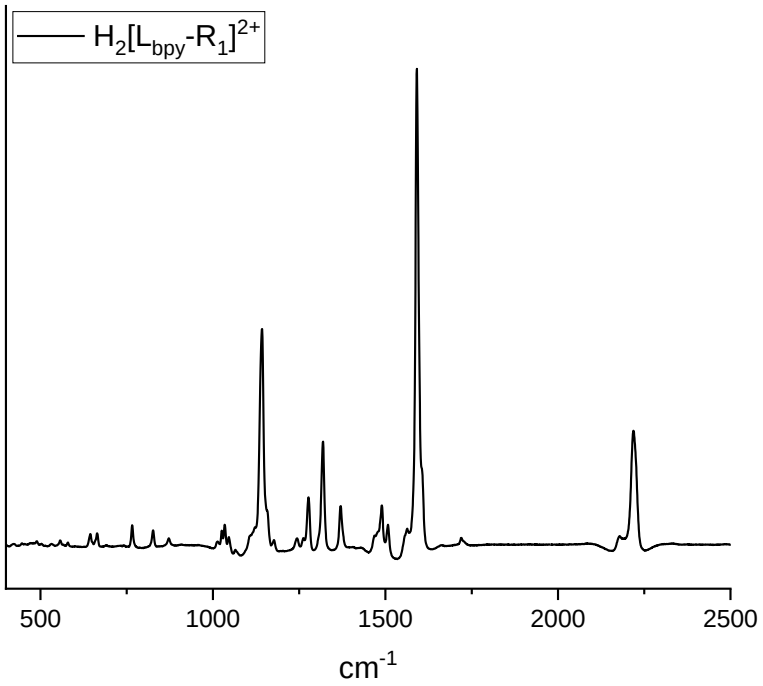

Figure 2.23: Raman spectrum of $\mathbf{H_2[L_{bpy}\text{-}R_1]^{2+}}$.

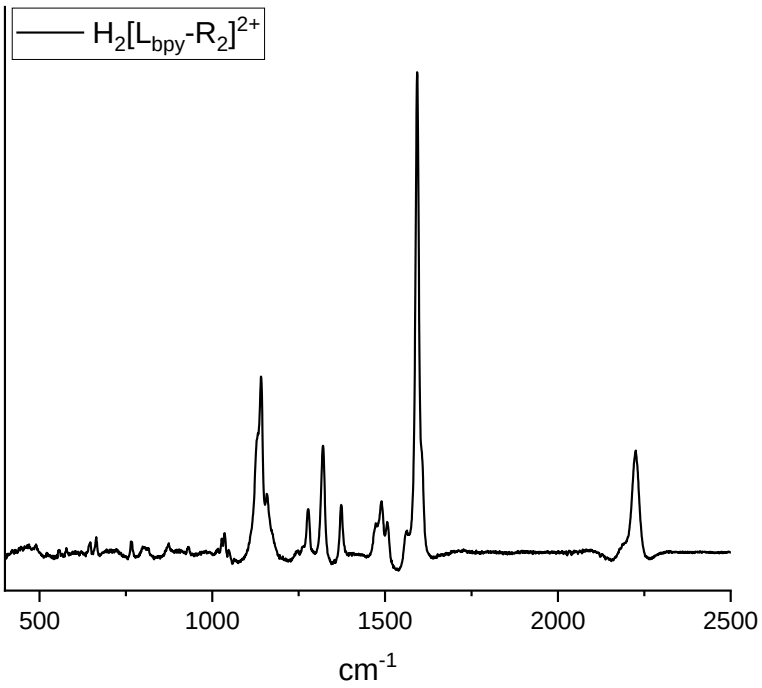

Figure 2.24: Raman spectrum of $H_2[L_{bpy}\text{-}R_2]^{2+}$.

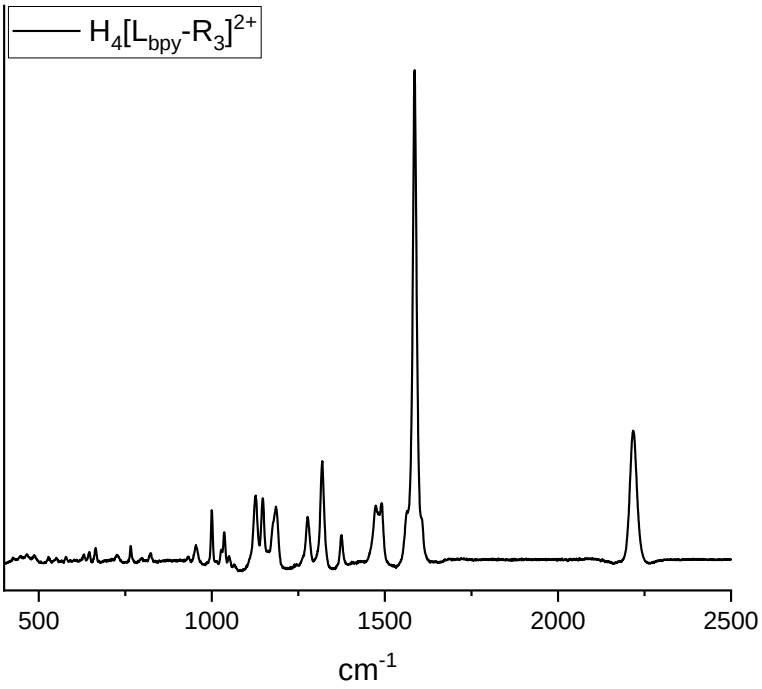

Figure 2.25: Raman spectrum of $H_4[L_{bpy}\text{-}R_3]^{2+}$.

Thermogravimetric Analysis

The thermal stabilities of **$H_2[L_{bpy}$-$R_1]$**, **$H_2[L_{bpy}$-$R_2]$**, and **$H_4[L_{bpy}$-$R_3]$** were assessed using thermogravimetric analysis (TGA). The analysis was conducted using freshly prepared samples of each Ru^{II} polypyridyl complex under a constant stream of air and in the temperature range of 30 – 600 °C. The TGA traces (Fig. 2.26 – Fig. 2.28) reveal an initial decomposition step for **$H_2[L_{bpy}$-$R_1]$**, **$H_2[L_{bpy}$-$R_2]$**, and **$H_4[L_{bpy}$-$R_3]$** when heated from *ca.* 240 °C – 280 °C. A weight loss of *ca.* 11 %, 10 % and 15 %, respectively, can be seen from the data. This weight loss is derived from the decarboxylation of **$H_2[L_{bpy}$-$R_1]$**, **$H_2[L_{bpy}$-$R_2]$**, and **$H_4[L_{bpy}$-$R_3]$**, respectively. Heating above 350 °C results in a second decomposition step. This step results in the decomposition of the Ru^{II} polypyridyl complexes and is associated with a weight loss of 54 %, 53 %, and 57 % for **$H_2[L_{bpy}$-$R_1]$**, **$H_2[L_{bpy}$-$R_2]$**, and **$H_4[L_{bpy}$-$R_3]^{2+}$**, respectively. In the case of **$H_2[L_{bpy}$-$R_1]$** and **$H_2[L_{bpy}$-$R_2]$** complete decomposition and metal oxide formation occurs at *ca.* 400 °C. In contrast, full decomposition and metal oxide formation occurs at approximately 470 °C for the **$H_4[L_{bpy}$-$R_3]$** metallo-ligand.

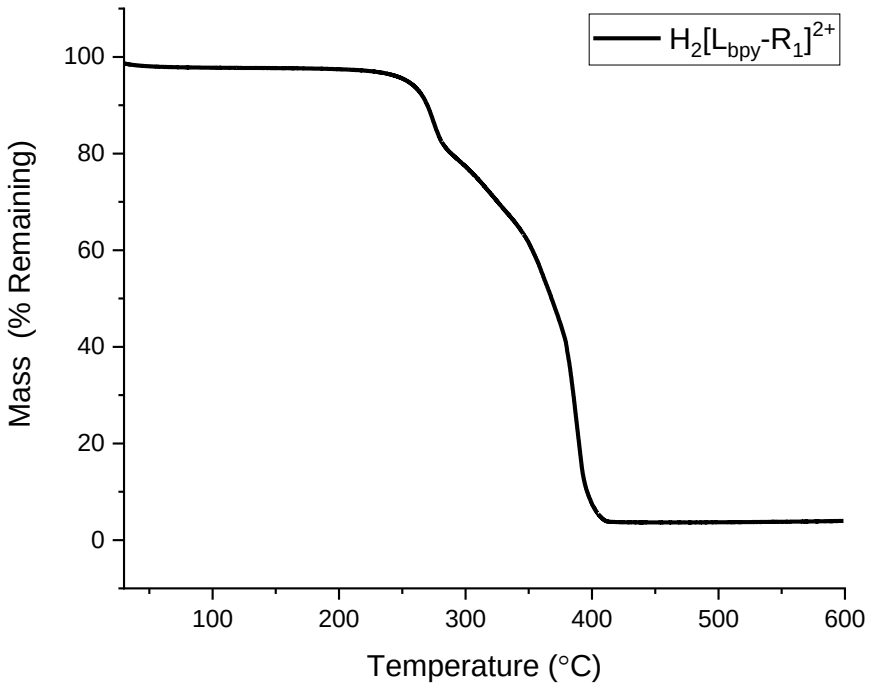

Figure 2.26: TGA trace for $H_2[L_{bpy}$-$R_1]$.

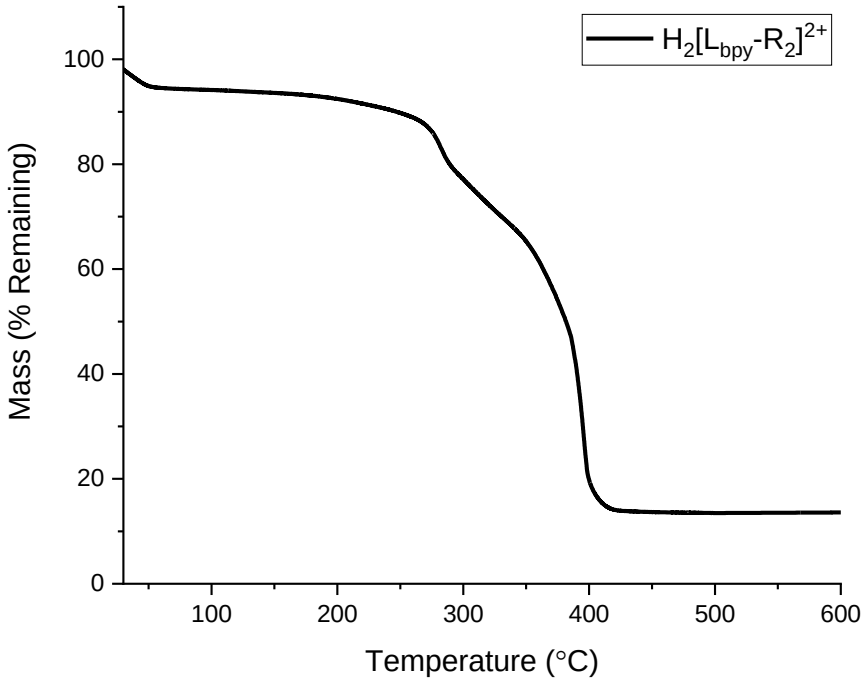

Figure 2.27: TGA trace for $H_2[L_{bpy}\text{-}R_2]$.

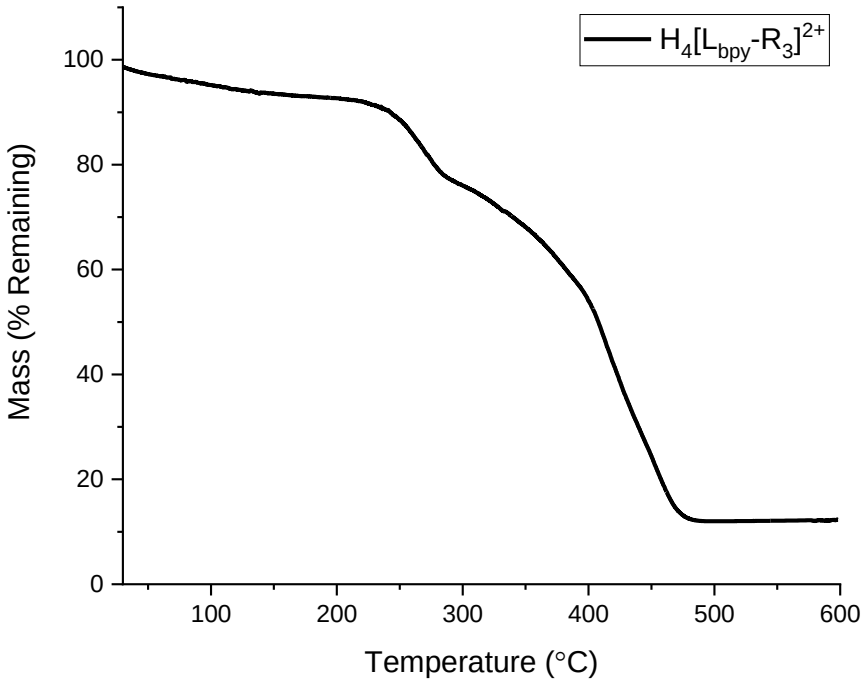

Figure 2.28: TGA trace for $H_4[L_{bpy}\text{-}R_3]$.

2.6. Synthesis of $H_4[L_{phen}\text{-}R_3]^{2+}$

$H_4[L_{phen}\text{-}R_3]^{2+}$ was prepared *via* multistep convergent reactions. The initial reaction involved a catalysed electrophilic aromatic bromination of 1,10'-phenanthroline at the 3,8' positions. 3,8'-Dibromo-1,10'-phenanthroline (**3**) was synthesised according to the literature procedure reported by Sauvage *et al.*[47] (Scheme 2.7), leading to a yield of 65%.

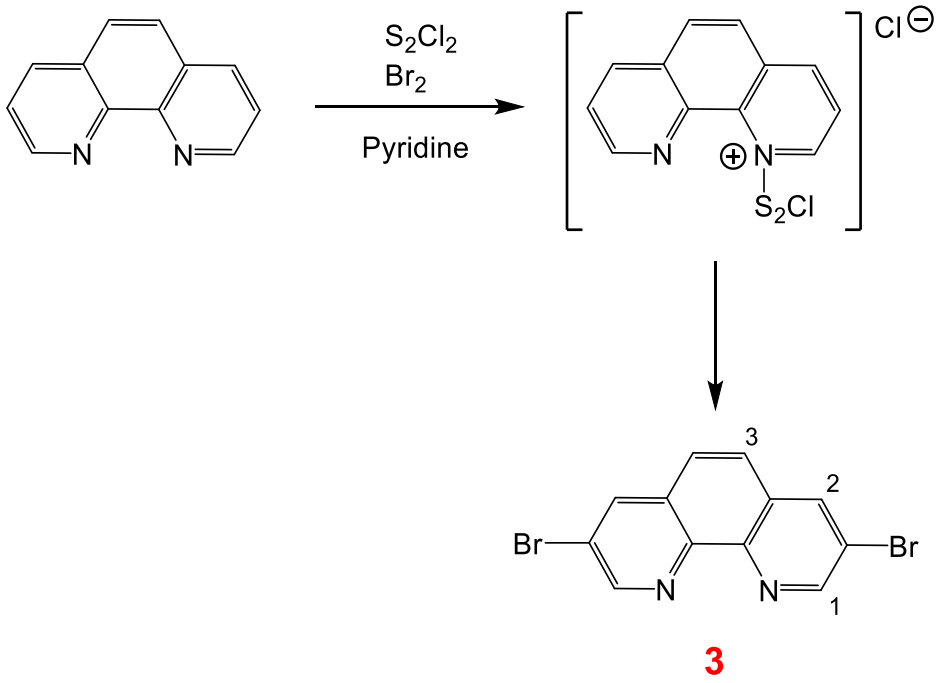

3

Scheme 2.7: Reaction pathway for the synthesis of 3,8'-dibromo-1,10'-phenanthroline (3), including proposed 1,10-phenanthrolin-1-ium salt-type intermediate.[48]

Similar to the synthesis of **2**, the electron-withdrawing imine nitrogen (C=N-) of 1,10-phenanthroline is a π deficient aromatic compound and electrophilic substitution, i.e., the direct bromination of 1,10'-phenanthroline without additives in the reaction, yield only very minute quantities of both the mono- and dibrominated products,[48] even under harsh reaction condition.[49] Therefore, the Saitoh method was employed.[48]

This method entailed the addition of an S_2Cl_2 bromination catalyst and pyridine. These additives were essential to ensure the formation of a pyridinium salt-type intermediate *in-situ*.[50] It is believed that this intermediate increases the reactivity of 1,10'-phenanthroline and provides direct bromination at the 3,8' positions. Similar to the synthesis of **2**, reaction time and quantity of bromine added to the reaction are essential as they also dictate the ratio of mono- to dibrominated products formed in the reaction.

However, in this synthesis, it was identified that a small quantity of 3-bromo-1,10'-phenanthroline was present in the crude product in contrast to that obtained during the synthesis of the dibrominated 2,2'-bipyridine (**2**). Thus, flash chromatography using chloroform as the eluent was required to ensure the separation of the mono-brominated phenanthroline from the desired dibrominated product **3**. Subsequently, recrystallisation from tetrachloroethane was necessary to obtain white crystals of 3,8'-dibromo-1,10'-phenanthroline (**3**). Analysis *via* ^{1}H-NMR spectroscopy (Fig. 2.29) and ESI Mass spectrometry demonstrated that the crystals of **3** were of high purity and did not contain detectable/significant quantities of either starting materials or by-products. The ^{1}H-NMR spectrum of **3** reveals three signals at 9.21 ppm, 8.44 ppm and 7.79 ppm, which are attributed to the H-atoms of the aromatic rings of the phenanthroline moieties of **3** and are in agreement with literature.[51]

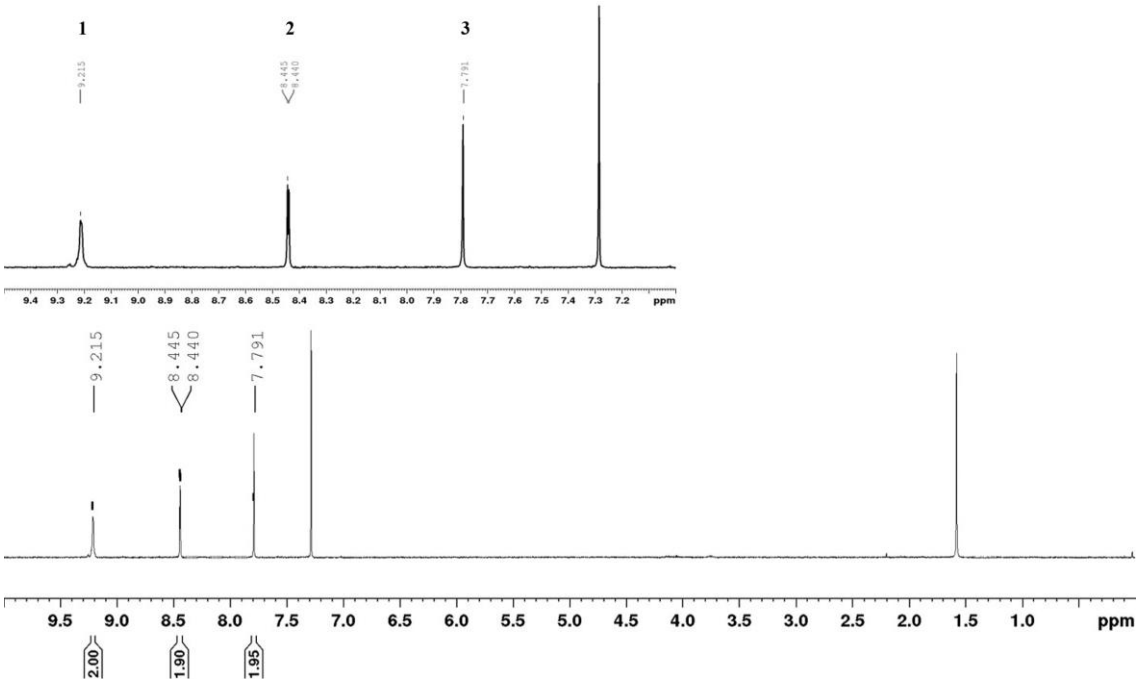

Figure 2.29: ^{1}H-NMR spectrum of 3,8'-dibromo-1,10'-phenanthroline (3) in $CDCl_3$. Full spectrum of 3 (bottom), aromatic region of 3 (top).

The new synthetic approach towards the synthesis of complex **5** previously discussed was similarly employed for the synthesis of the heteroleptic complex [bis-(2,2'-bipyridine)-ruthenium(II)(3,8'-dibromo-1,10'-phenanthroline)]$(PF_6)_2$ (**6**). To obtain compound **6**, the pure purple microcrystalline precursor **4** previously synthesised was used (Scheme 2.8).

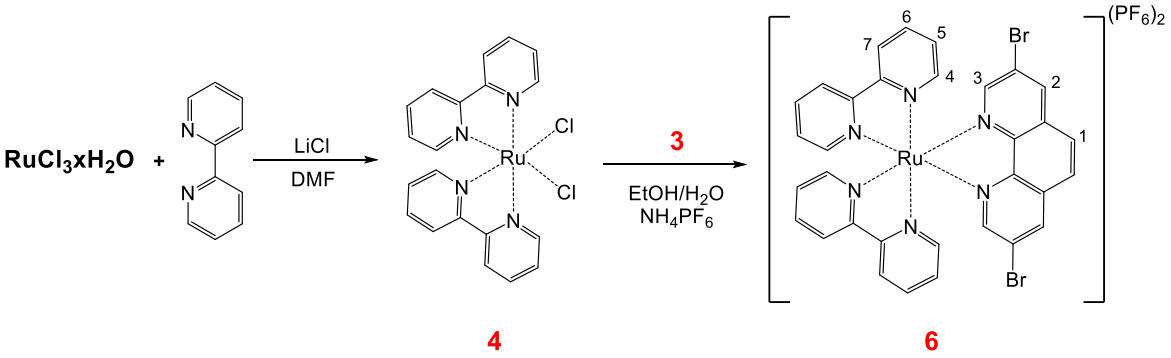

4 6

Scheme 2.8: Synthesis of bis-(2,2'-bipyridine)-ruthenium(II) dichloride (4) and [bis-(2,2'-bipyridine)-ruthenium(II)(3,8'-dibromo-1,10'-phenanthroline)]$(PF_6)_2$ (6).

One equivalent of **3** was complexed to **4** in a solvent mixture of EtOH/H_2O (Scheme 2.8). The formation of complex **6** could be seen through the distinct colour change from purple to deep red. The product was isolated by the addition of excess saturated aqueous NH_4PF_6 solution, yielding an orange precipitate. The precipitate was further recrystallised to resulting in pure red needle-like crystals of complex **6** in a high yield (85%). The identity and purity of **6** was identified through ^{1}H-NMR spectroscopy (Fig. 2.30) and ESI-mass spectrometry. Interestingly, the hydrophobic character of the dibromo-phenanthroline moiety **3** was again displayed in **6**. Similar to complex **5** previously discussed, **6** also showed good solubility in MeCN and DMSO in contrast to **3**, which enabled its further use in the synthesis of the desired metallo-ligand $\mathbf{H_4[L_{phen}\text{-}R_3]^{2+}}$. The ^{1}H-NMR spectrum of complex **6** reveals signals centred at 9.18 ppm, 8.83 ppm, 8.34 ppm, 8.17 ppm, 8.06 ppm, 7.73 and 7.49 ppm. The signals at 9.18, 8.34 ppm and 8.06 ppm are attributed to H-atoms of the 3,8'-dibromo-1,10'-phenanthroline moiety in complex **6.** The signals centred at 8.83 ppm, 8.17 ppm, 7.73 and 7.49 ppm derive from the H-atoms of the unsubstituted 2,2'-bipyridine moieties. The ^{1}H-NMR spectrum and H-atom signals are in agreement with literature.[30,52,53]

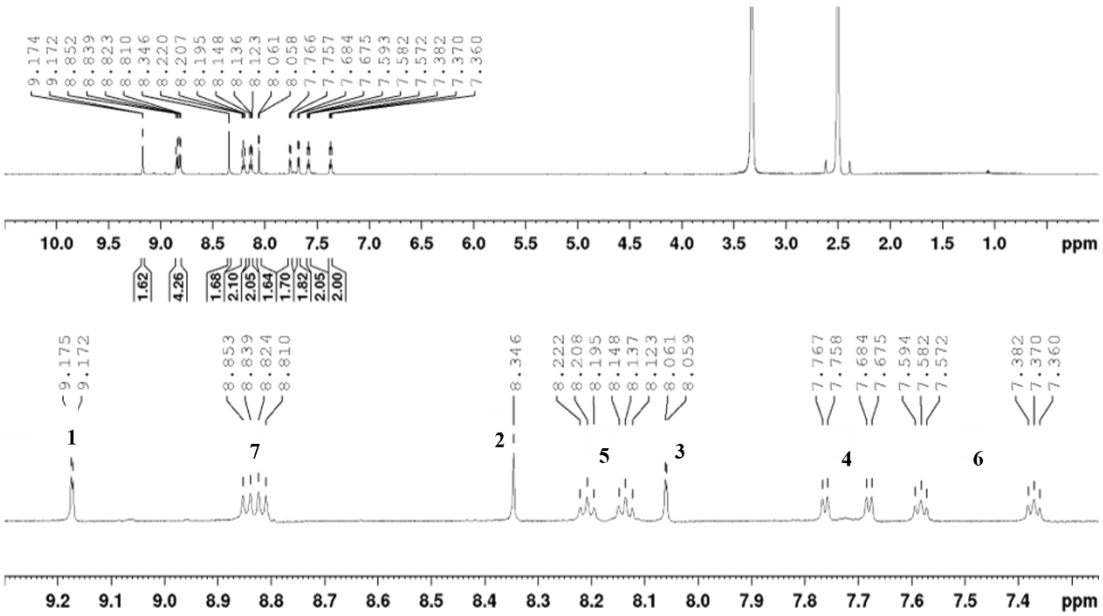

Figure 2.30: ^{1}H-NMR spectrum of [bis-(2,2'-bipyridine)-ruthenium(II)(3,8'-dibromo-1,10'-phenanthroline)]$(PF_6)_2$ (6), in d_6-DMSO. Full spectrum of 6 (top), aromatic region of 6 (bottom).

The final reaction for the synthesis of $\mathbf{H_4[L_{phen}\text{-}R_3]^{2+}}$ involved two steps. Initially a Sonogashira cross-coupling reaction between the alkyne-benzoic acid methyl ester moiety **13** and the heteroleptic ruthenium(II) complex **6** was carried out. The second step involved the base-catalysed ester hydrolysis of the methyl esters present in complex $\mathbf{[9]^{2+}}$, to yield the final Ru^{II} polypyridyl complex $\mathbf{H_4[L_{phen}\text{-}R_3]^{2+}}$ (Scheme 2.9).

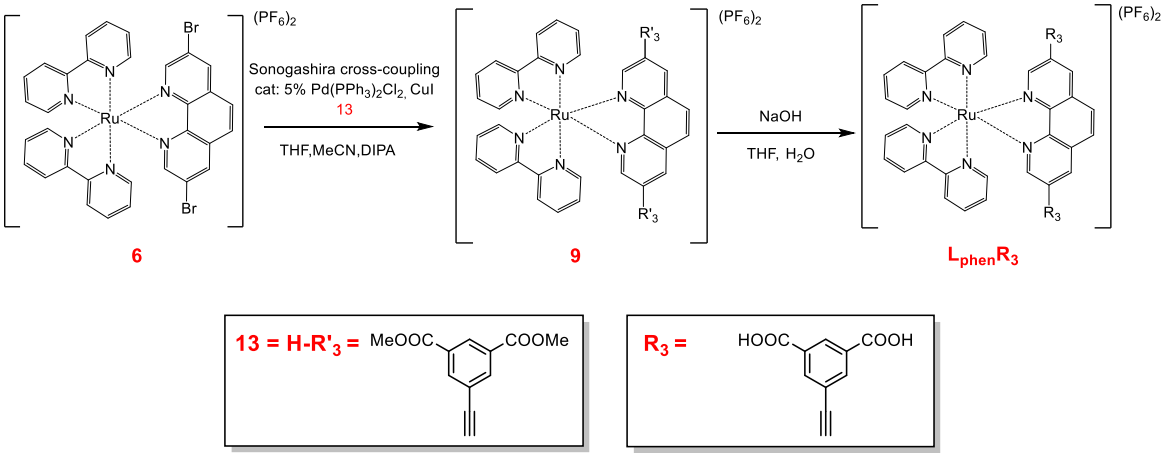

Scheme 2.9: Synthetic approach to $[9]^{2+}$ and subsequently to $H_4[L_{phen}\text{-}R_3]^{2+}$.

Following a modification of a procedure reported by Klemm *et al.*,[28] a Sonogashira cross-coupling reaction with catalyst loadings of 5 % of $Pd(PPh_3)_2Cl_2$ and CuI was carried out between two equivalents of the alkyne-benzoic acid methyl ester compound **13** and complex **6**. The synthetic approach was highly practical in the high yielding synthesis of compound $\mathbf{[9]^{2+}}$. It was identified that the starting materials dissolved readily in MeCN/THF solvent mixtures allowing the reaction to proceed. Upon completion of the reaction, it was observed that $\mathbf{[9]^{2+}}$ precipitated out of the solution due to its insolubility in THF. Therefore, allowing $\mathbf{[9]^{2+}}$ to be isolated *via* simple gravity filtration and purified by washing with THF and water. The identity and purity of complex $\mathbf{[9]^{2+}}$ were confirmed by ^{1}H-NMR spectroscopy and ESI mass spectrometry; the precipitate obtained did not include any remaining starting materials or by-products of the Sonogashira cross-coupling reaction. Similar to the previously synthesised and discussed Ru^{II} polypyridine complex, the addition of THF to the reaction mixture provided and efficient way to isolate the desired complex from the reaction mixture while avoiding any yield-reducing purification steps.

The last step in the synthesis of the Ru^{II} polypyridyl complex $\mathbf{H_4[L_{phen}\text{-}R_3]^{2+}}$ involved the base-catalysed ester hydrolysis of the alkyne-benzoic acid methyl ester moieties present in $\mathbf{[9]^{2+}}$. The reaction proceeded *via* an SN2 pathway, utilising sodium hydroxide as the base-catalyst in a solvent mixture of THF/H_2O (2:1) at room temperature under atmospheric conditions (Scheme 2.9). Upon reaction completion and removal of THF, the remaining reaction solution was added to an excess amount of perchloric acid, to yield a brick red precipitate of $\mathbf{H_4[L_{phen}\text{-}R_3]^{2+}}$ which demonstrated high solubility in a variety of solvents and retention of hydrophobic properties of the precursors used. $\mathbf{H_4[L_{phen}\text{-}R_3]^{2+}}$ was subsequently purified by washing with water prior to drying at room temperature. Analysis *via* ^{1}H-NMR (Fig. 2.31) and ^{13}C-NMR spectroscopy demonstrated a high degree of purity and loss of the methyl ester signal. In the ^{1}H-NMR spectrum of $\mathbf{H_4[L_{phen}\text{-}R_3]^{2+}}$ reveals intense signals attributed to residual solvents, water and dimethyl sulfoxide at chemical shifts of 3.32 ppm and 2.51 ppm, respectively. Two signals located at 8.49 ppm and 8.32 ppm can be attributed to the H-atoms of the alkyne-benzoic acid methyl ester moieties $\mathbf{R_3}$. Three signals with chemical shifts of 9.17 ppm, 8.42 ppm and 7.80 ppm can be attributed to the H-atoms of the extended 1,10'-phenanthroline moiety of $\mathbf{H_4[L_{phen}\text{-}R_3]^{2+}}$. The remaining signals centred at 8.62 ppm, 8.20 ppm, 7.81 ppm and 7.50 ppm are attributed to the H-atoms of the two unsubstituted 2,2'-bipyridine moieties.

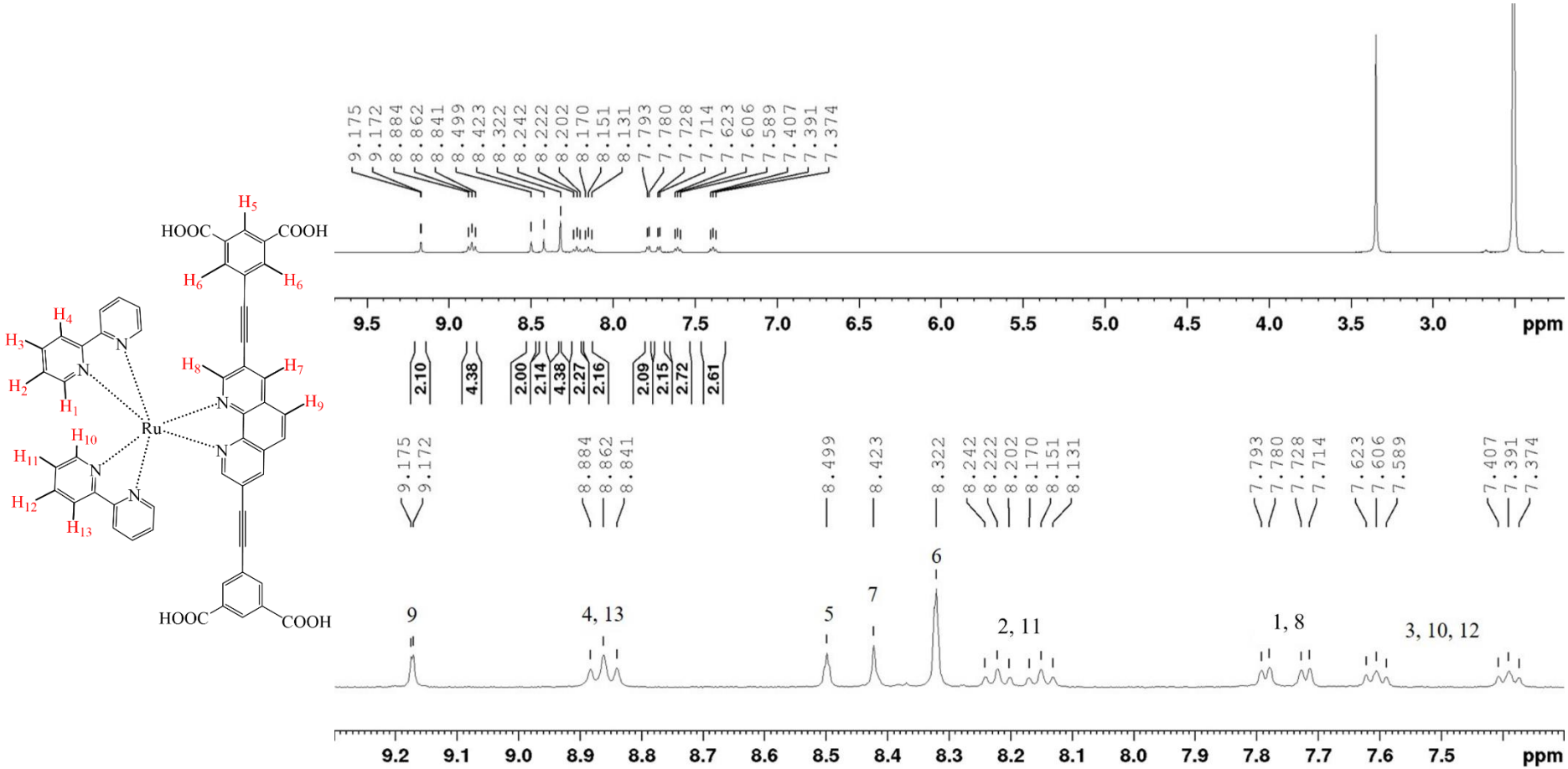

Figure 2.31: Labelled ^{1}H-NMR spectrum of $H_4[L_{phen}\text{-}R_3]^{2+}$ in d_6-DMSO. Full spectrum of $H_4[L_{phen}\text{-}R_3]^{2+}$ (top), aromatic region of $H_4[L_{phen}\text{-}R_3]^{2+}$ (bottom).

2.7 Single Crystal X-ray Diffraction of the Methyl Ester Protected $H_4[L_{phen}\text{-}R_3]^{2+}$

Single crystals of **[9]**$^{2+}$ were obtained again through the diffusion and gradual mixing of Et_2O and a saturated solution of **[9]**$^{2+}$ in MeCN. This method of crystallisation yielded orange coloured needle-shaped single crystals of **[9]**$^{2+}$. The crystal structure was determined *via* single crystal X-ray diffraction analysis.

The crystal structure for **[9]**$^{2+}$ (Fig. 2.32) was solved in the monoclinic space group $P2_1/c$. Similar to the crystal structures of the previously mentioned Ru^{II} complexes, the Ru^{II} centre in **[9]**$^{2+}$ also adopts a distorted octahedral coordination environment. While the extended 1,10'-phenanthroline was identified to be coplanar and comparable to that of $\mathbf{H_2[L_{bpy}\text{-}R_2]}^{2+}$. Furthermore, the bond lengths of the Ru-N bonds vary from 2.048(8) Å to 2.075(10) Å. Table 2.7 below displays selected bond distances and angles between the ruthenium and nitrogen atoms in **[9]**$^{2+}$. Full crystallographic data and structure refinement parameters are provided in Table 2.8.

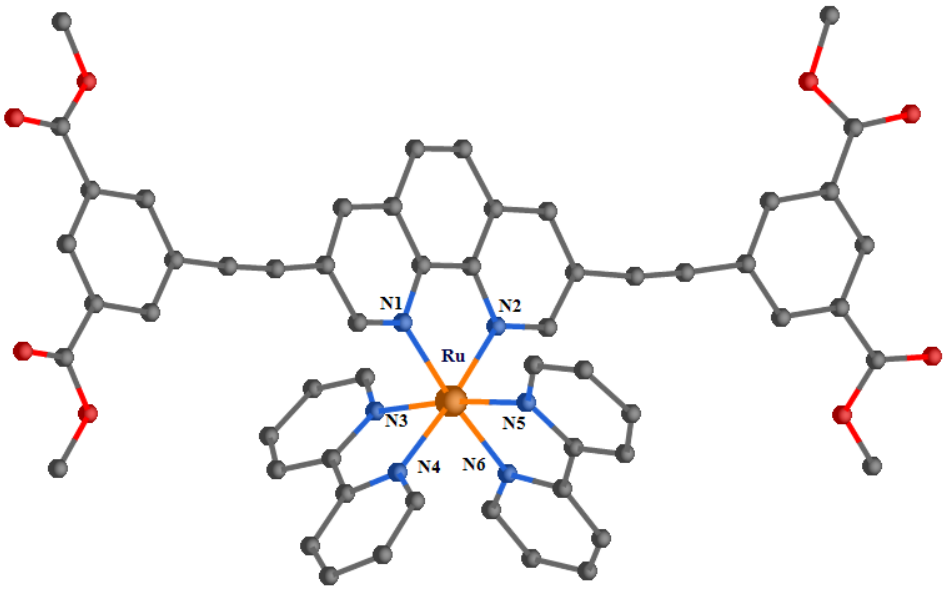

Figure 2.32: Single crystal X-ray diffraction structure, ball-and-stick representation of [9]$^{2+}$. Colour scheme: Ru (orange), N (blue), O (red), C (grey). Solvents of crystallisation, H atoms and counter-ions were omitted for clarity.

Table 2.7: Selected bond angles and distances obtained from the single crystal X-ray diffraction for $[9]^{2+}$.

Atom			Angle (°)	Atom		Distance (Å)
N1	Ru	N3	87.515(8)	Ru	N1	2.066(7)
N2	Ru	N4	175.013(9)	Ru	N2	2.070(8)
N2	Ru	N6	96.149(7)	Ru	N3	2.060(8)
N3	Ru	N5	173.041(2)	Ru	N4	2.075(10)
N4	Ru	N5	95.497(14)	Ru	N5	2.048(8)
N6	Ru	N5	78.427(8)	Ru	N6	2.054(7)

Analysing the packing arrangement within a supercell, viewed along the crystallographic *c*-axis of the crystal structure of **$[9]^{2+}$** (Fig. 2.33), the arrangement and stacking of aromatic rings can be clearly seen. The alignment of the alkyne-benzoic acid methyl ester moieties between different molecules of **$[9]^{2+}$** is thought to influence the packing of the crystal. This can be better seen in Figure 2.34 when viewed along the *a* and *b* axes. Furthermore, these π – π stacking interactions have C-C distances ranging from 3.4 Å - 3.5 Å. This stabilises the structure and is consistent with π – π interactions.[34]

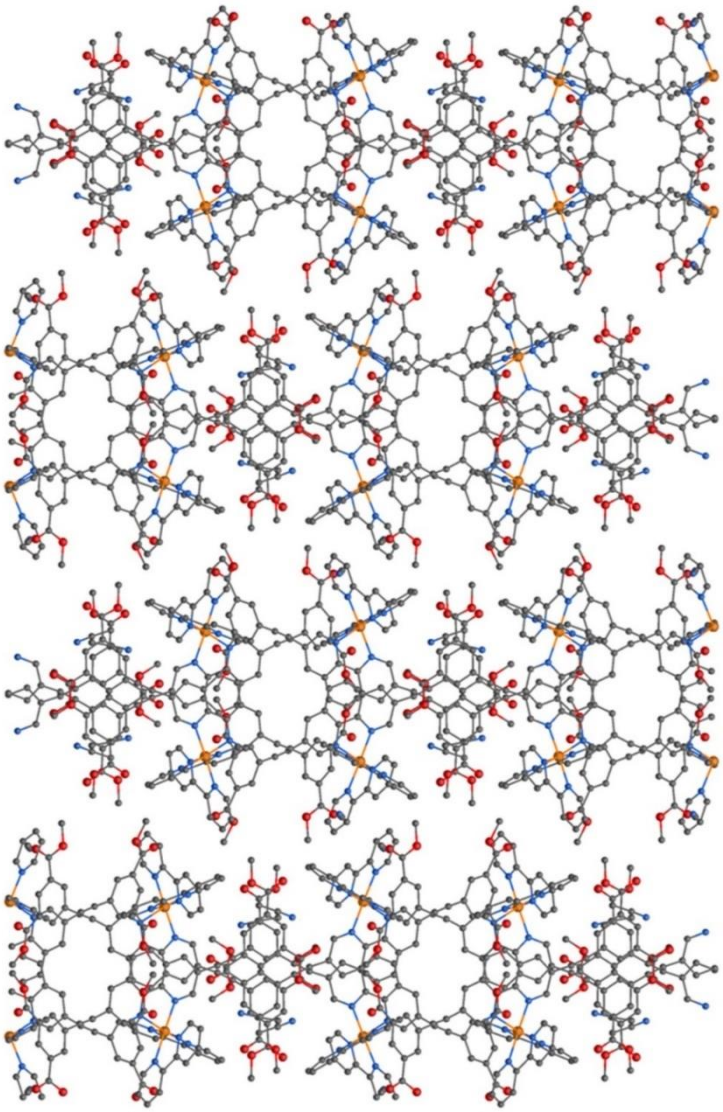

Figure 2.33: Packing diagram of $[9]^{2+}$ viewed along the crystallographic *c*-axis. Colour scheme: Ru (orange), N (blue), O (red), C (grey). Solvents of crystallisation, H atoms and counter-ions were omitted for clarity.

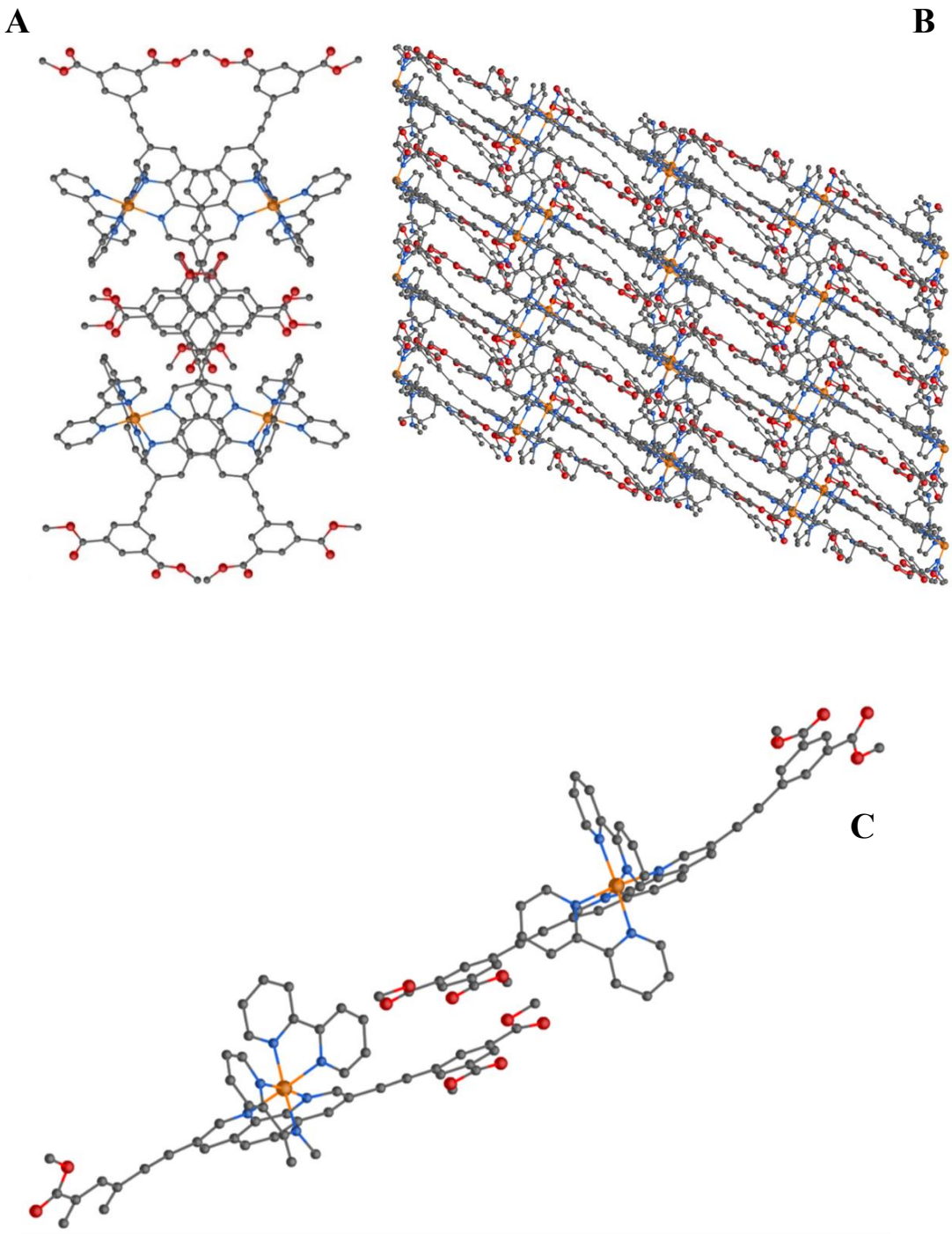

Figure 2.34: Aromatic ring alignment of $[9]^{2+}$ viewed along the crystallographic *a*-axis (A), and *b*-axis (B and C). Colour scheme: Ru (orange), N (blue), O (red), C (grey) H (grey). Solvents of crystallisation, H atoms and counter-ions were omitted for clarity.

Table 2.8: Single crystal X-ray diffraction data and structure refinement for $[9]^{2+}$.

Identification code	$[9]^{2+}$
Empirical formula	$C_{56}H_{40}F_{12}N_6O_8P_2Ru$
Formula weight	1315.95
Temperature/K	100(2)
Crystal system	monoclinic
Space group	$P2_1/c$
a/Å	23.3842(8)
b/Å	34.9291(13)
c/Å	15.7503(5)
α/°	90
β/°	106.608(2)
γ/°	90
Volume/Å^3	12328.0(7)
Z	4
ρ_{calc}g/cm^3	1.519
μ/mm^{-1}	3.507
F(000)	5698.0
Crystal size/mm^3	0.74 × 0.54 × 0.54
Radiation	CuKα (λ = 1.54178)
2Θ range for data collection/°	3.942 to 137.368
Index ranges	$-27 \leq h \leq 28$, $-42 \leq k \leq 42$, $-19 \leq l \leq 18$
Reflections collected	112856
Independent reflections	22299 [R_{int} = 0.0590, R_{sigma} = 0.0422]
Data/restraints/parameters	22299/632/1755
Goodness-of-fit on F^2	1.819
Final R indexes [I>=2σ (I)]	R_1 = 0.1318, wR_2 = 0.4068
Final R indexes [all data]	R_1 = 0.1454, wR_2 = 0.4172
Largest diff. peak/hole / e Å^{-3}	2.77/-2.34

2.8 Physicochemical Characterisation of $H_4[L_{phen}\text{-}R_3]^{2+}$

Infrared Spectroscopy

The $\mathbf{H_4[L_{phen}\text{-}R_3]^{2+}}$ complex was characterised *via* IR spectroscopy (Fig. 2.35). The FT-IR spectrum for $\mathbf{H_4[L_{phen}\text{-}R_3]^{2+}}$ shared significant similarities to the previously discussed Ru^{II} polypyridine complexes due to their similar structural characteristics.

The broad signal which appears at *ca.* 3400 cm^{-1} can be attributed to the hydrogen-bonded *ν*(O–H) stretch.[35,36] *ν*(C–H) stretching vibrations attributed to the aromatic rings can be seen at *ca.* 3080 cm^{-1}. The signal at 1715 cm^{-1} can be assigned to the carbonyl *ν*(C=O) vibrations of the free carboxylic acid groups.[37,38] The signal which appears at *ca.* 1373 cm^{-1} can be attributed to the symmetric carboxylate stretching mode.[39,40] *ν*(C=C) stretching vibrations which derive from the benzene and bipyridine moieties of $\mathbf{H_4[L_{phen}\text{-}R_3]^{2+}}$ can be observed between 1460 cm^{-1} and 1390 cm^{-1}, while the *ν*(C–N) stretch is visible at *ca.* 1240 cm^{-1}.[41,42] The *ν*(C–O) stretches can be seen between *ca.* 1230cm^{-1} and *ca.* 1090 cm^{-1}. *ν*(C–H) bending vibrations corresponding to benzene and bipyridine ring moieties can be observed at *ca.* 755 cm^{-1} and 620 cm^{-1}.[44] The weak band at 555 cm^{-1} can be attributed to the {Ru-N} stretch.[43]

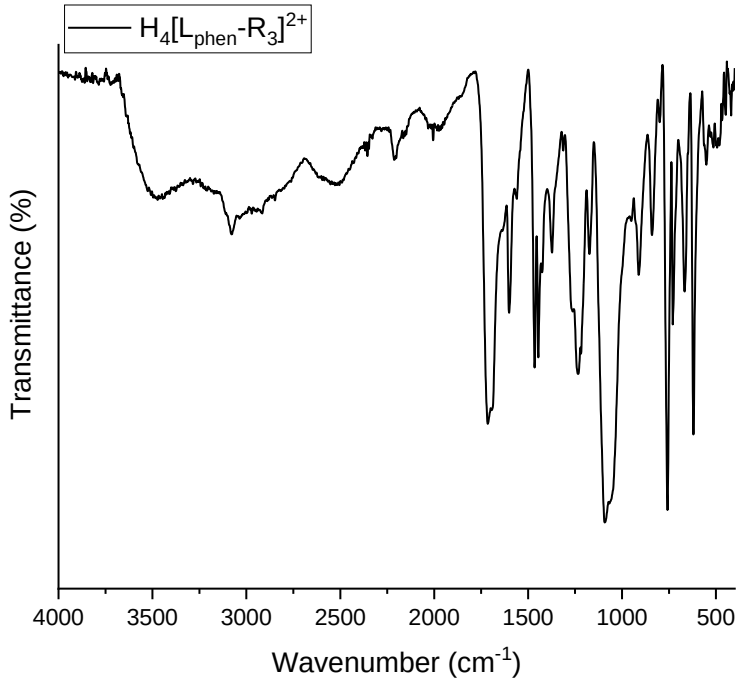

Figure 2.35: FT-IR spectrum of $H_4[L_{phen}\text{-}R_3]^{2+}$.

Raman Spectroscopy

$H_4[L_{phen}\text{-}R_3]^{2+}$ was also similarly subjected to Raman spectroscopy (Fig. 2.36). Just like the FT-IR spectrum, the Raman spectrum was also nearly identical to that previously seen for **$H_2[L_{bpy}\text{-}R_1]^{2+}$**, **$H_2[L_{bpy}\text{-}R_2]^{2+}$**, and **$H_4[L_{bpy}\text{-}R_3]^{2+}$**. The Raman spectrum was measured from 400 cm^{-1} to 2500 cm^{-1} and the baseline was corrected using OriginLab 2020 software. The aromatic and heteroaromatic ν(C–H) vibrations can be seen at approximately 1002 cm^{-1}, 1036 cm^{-1}, 1122 cm^{-1}, 1144 cm^{-1} and 1187 cm^{-1}.[45] The signals that appear at *ca.* 1277 cm^{-1} and 1316 cm^{-1} derive from the ν(C–C) single bond vibrations. The signal at 1371 cm^{-1} can be attributed to the ν_s(C=O) vibrations of the carboxylate groups. The heteroaromatic and aromatic ν(C=C) vibrations can be observed at 1492 cm^{-1}, and 1595 cm^{-1}. The C≡C vibration derived from the alkyne moiety of **$H_4[L_{phen}\text{-}R_3]^{2+}$** is responsible for the final signal at 2220 cm^{-1}.[46]

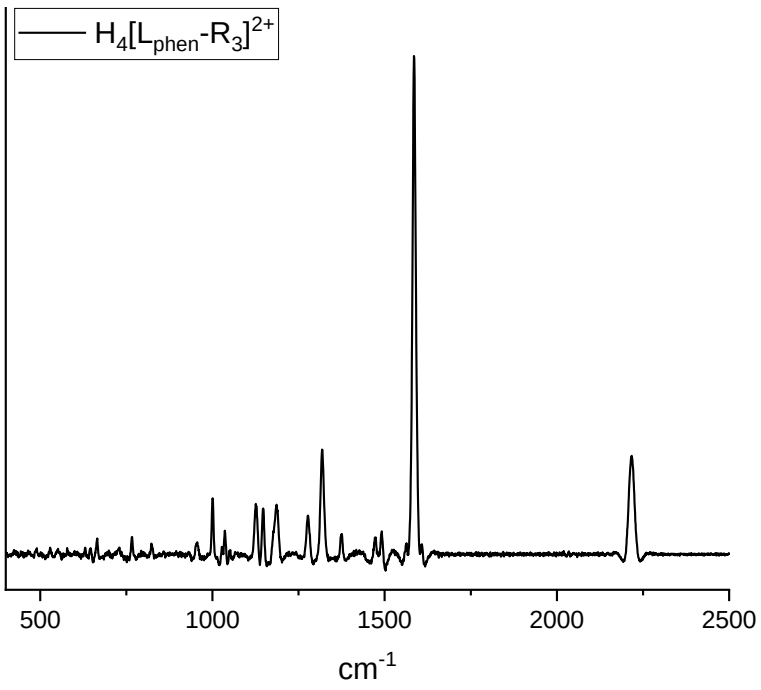

Figure 2.36: Raman spectrum of $H_4[L_{phen}\text{-}R_3]^{2+}$.

Thermogravimetric Analysis

Thermogravimetric analysis (TGA) was used to determine the thermal stability of **$H_4[L_{phen}\text{-}R_3]$**. A freshly prepared sample of **$H_4[L_{phen}\text{-}R_3]$** was analysed under a continuous stream of air and at temperatures ranging from 30 °C to 600 °C.

When heated from 260 °C to 350 °C, the TGA trace (Fig. 2.37) demonstrates an initial decomposition step for **$H_4[L_{phen}\text{-}R_3]$**. This step may derive from the decarboxylation of **$H_4[L_{phen}\text{-}R_3]$** and decomposition of perchlorate counter-ions. Thus, this decomposition step results in a weight loss of approximately 34%. When heated above 350°C, a second decomposition step occurs resulting in the complete decomposition of **$H_4[L_{phen}\text{-}R_3]$**, which is attributed to a 49% weight loss. From the TGA trace, complete decomposition and formation of a metal oxide of the **$H_4[L_{phen}\text{-}R_3]$** metallo-ligand occurs at approximately 475 °C.

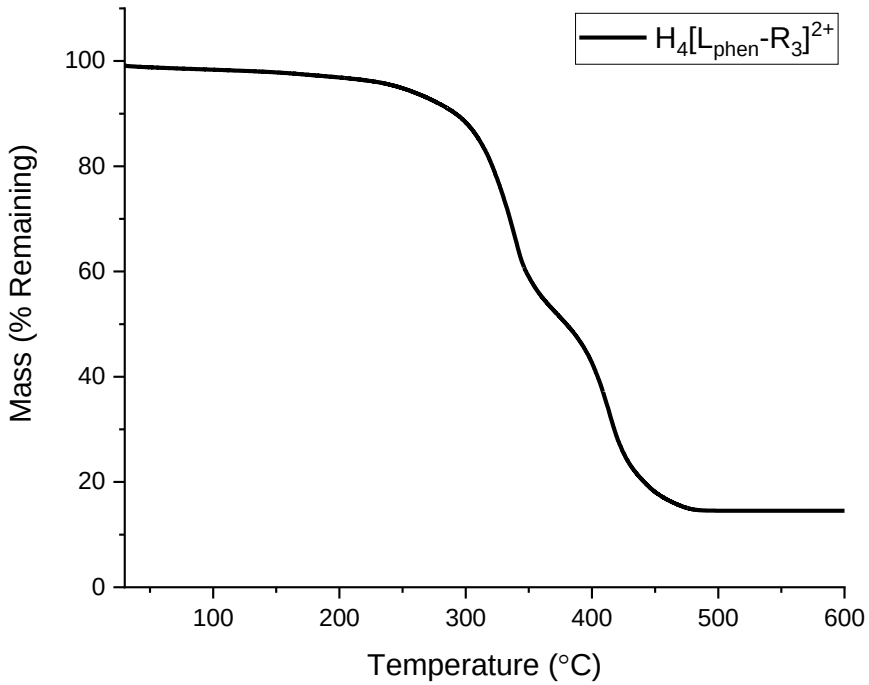

Figure 2.37: TGA trace for $H_4[L_{phen}\text{-}R_3]$.

2.9. Synthesis of $H_{12}[L_{tris}\text{-}R_3]^{2+}$

The homoleptic complex tris(5,5'-dibromo-2,2'-bipyridine)ruthenium(II)$(PF_6)_2$ (**7**) was synthesised *via* a different synthetic route in comparison to **5** and **6**. A procedure from Beves *et al*.[32] was modified to obtain **7**. The synthesis involved a reaction between a ruthenium(II) salt, *cis*-dichlorotetrakis(dimethylsulphoxide)ruthenium(II) and three mole equivalents of **2** in ethylene glycol (Scheme 2.10).

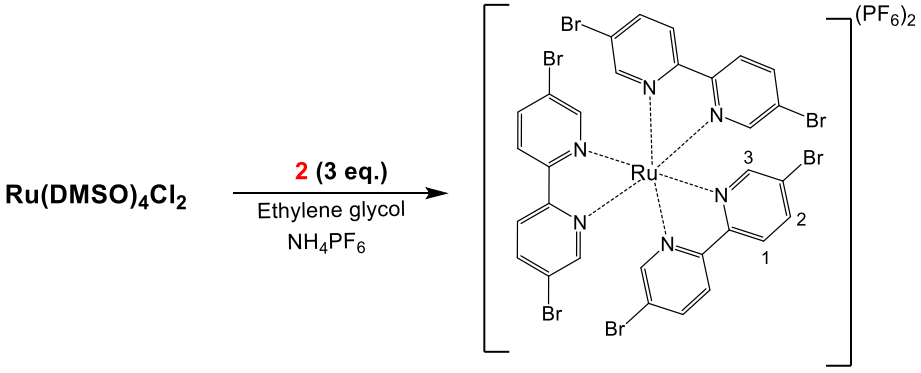

Scheme 2.10: Synthesis of tris(5,5'-dibromo-2,2'-bipyridine)ruthenium(II)$(PF_6)_2$ (7).

It was envisaged that synthesising the homoleptic ruthenium(II) complex **7** would be a versatile metallo-ligand for synthesising stable and highly connected supramolecular assemblies. The reaction required high temperatures to ensure quantitative complexation between **3** and the ruthenium(II) salt. Ethylene glycol was chosen as the reaction medium due to its high boiling point allowing higher temperatures during reflux to be reached as to ensure complete complexation of the dibrominated 2,2'-bipyridine to the ruthenium(II) salt. Upon reaction completion, the product was isolated by the addition of excess aqueous NH_4PF_6 to a clear orange solution, yielding a fine orange precipitate. Isolation and purification of complex **7** from the starting materials and by-products of the reaction *via* column chromatography proved challenging. Analysis by ^{1}H-NMR spectroscopy (Fig. 2.38) demonstrated the presence of **7** along with trace quantities of starting material and partially complexed products. It was believed that the product was unstable with respect to debromination of the 2,2'-bipyridine and thus, partial decomposition of **7** during the reaction and purification steps occurs, making it very difficult to isolate the desired product.[32] Nevertheless, the complex was used as prepared in the next reaction for the synthesis of the target $\mathbf{H_{12}[L_{tris}\text{-}R_3]^{2+}}$ complex. The ^{1}H-NMR spectrum of **7**

reveals three distinct signals at 8.74 ppm, 8.49 ppm and 7.67 ppm, each integrating to six H-atoms of the 5,5'-dibromo-2,2'-bipyridine moieties in complex **7**.[32]

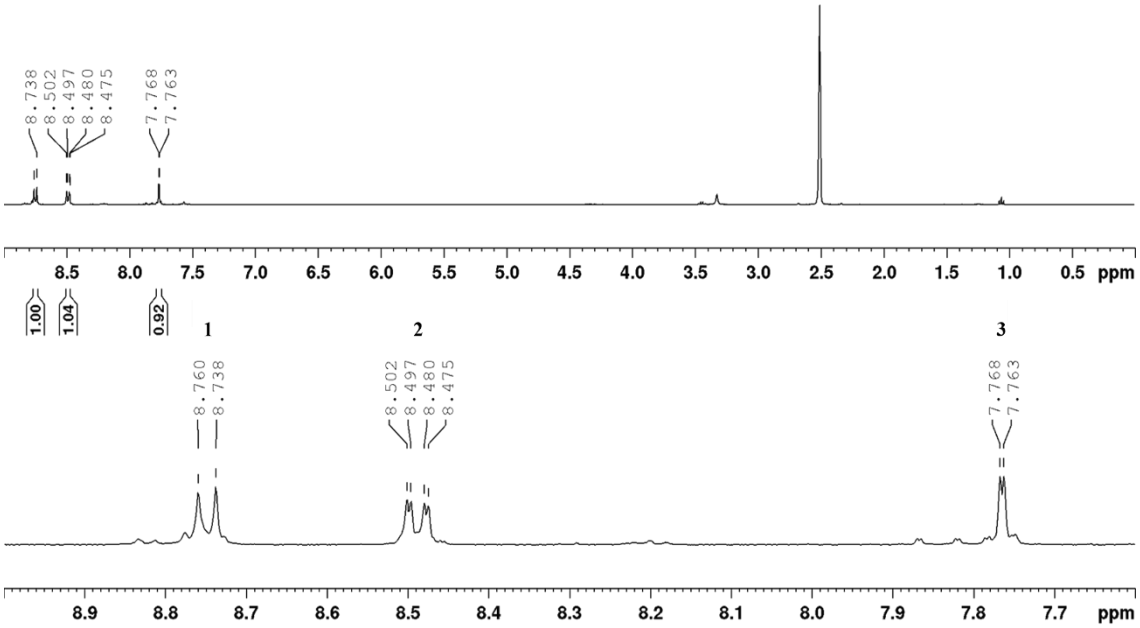

Figure 2.38: ^{1}H-NMR spectrum of tris(5,5'-dibromo-2,2'-bipyridine)ruthenium(II)$(PF_6)_2$ (7) in d_6-DMSO. Full spectrum of 7 (top), aromatic region of 7 (bottom).

The final reaction for the synthesis of $\mathbf{H_{12}[L_{tris}\text{-}R_3]^{2+}}$ involved two steps. The initial step was a Sonogashira cross-coupling reaction between the alkyne-benzoic acid methyl ester moiety **13** and the homoleptic ruthenium(II) complex **7**. The second step involved the base-catalysed ester hydrolysis of the methyl esters in $\mathbf{[10]^{2+}}$ to yield the final Ru^{II} polypyridyl complex $\mathbf{H_{12}[L_{tris}\text{-}R_3]^{2+}}$ (Scheme 2.11).

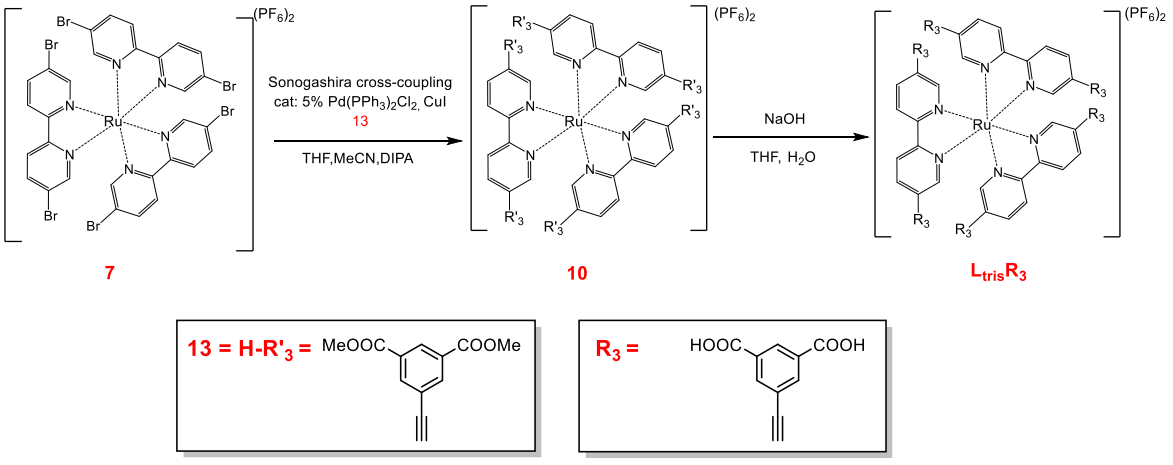

Scheme 2.11: Synthetic strategy for $[10]^{2+}$ and subsequently $\mathbf{H_{12}[L_{tris}\text{-}R_3]^{2+}}$.

The synthesis of **[10]$^{2+}$** involved the modification of a procedure described by Beves *et al*.[32] Here, it was identified that the product of the Sonogashira cross-coupling reaction could not be isolated in a similar manner to the previously discussed **[8-R$_{1-3}$]$^{2+}$** and **[9]$^{2+}$** complexes. A reason for this is most likely due to the increased quantity of alkyne-benzoic acid methyl ester moieties present in the final product which in turn increase the solubility of **[10]$^{2+}$** in THF, preventing its precipitation out of the reaction solution. It was identified that the addition of diethyl ether was required to isolate the product as an orange precipitate from the reaction mixture. Further purification *via* column chromatography was necessary. However, separation of the desired product from by-products of the reaction was challenging. One of the reasons for this is the close similarity in the chemical properties of the synthesised compounds in the reaction. Analysis by ^{1}H-NMR spectroscopy demonstrated the successful synthesis of **[10]$^{2+}$** along with additional H-atom signals in the aromatic region of the ^{1}H-NMR spectrum attributed to the starting materials.

To obtain the target complex **H$_{12}$[L$_{tris}$-R$_3$]$^{2+}$**, **[10]$^{2+}$** was subjected to a base-catalysed ester hydrolysis reaction in order to deprotect the benzoic acid moieties. The reaction proceeded *via* an SN2 pathway, utilising sodium hydroxide as the base-catalyst in a solvent mixture of THF/H_2O (2:1) at room temperature under atmospheric conditions (Scheme 2.11). Perchloric acid was subsequently added to the completed reaction mixture after the removal of the organic solvent, yielding the final brick red product. The precipitate obtained was purified by washing with water and dried at room temperature for two days. Analysis *via* ^{1}H-NMR spectroscopy (Fig. 2.39) demonstrated the presence of the desired final complex **H$_{12}$[L$_{tris}$-R$_3$]$^{2+}$** along with a small degree of starting materials and by-products. The ^{1}H-NMR indicates the prevalence of $\pi - \pi$ stacking in solution, thus, severely broadening the H-atom signals in the ^{1}H-NMR spectrum. The ^{1}H-NMR spectrum of **H$_{12}$[L$_{tris}$-R$_3$]$^{2+}$** reveals three residual solvent signals, THF, water and dimethyl sulfoxide at chemical shifts of 3.78 ppm, 3.32 ppm and 2.51 ppm, respectively. Additionally, the ^{1}H-NMR spectrum reveals five distinct signals in the aromatic region. Signals at 8.27 ppm and 8.28 ppm can be attributed to the H-atoms of the alkyne-benzoic acid moieties of **H$_{12}$[L$_{tris}$-R$_3$]$^{2+}$**. The H-atoms attributed to the 2,2'-bipyridine moieties of **H$_{12}$[L$_{tris}$-R$_3$]$^{2+}$** give rise to three signals, each integrating to six H-atoms with chemical shifts of 9.00 ppm, 8.54 ppm and 8.05 ppm. The ^{1}H-NMR spectrum and chemical shifts are closely in line with literature.[32]

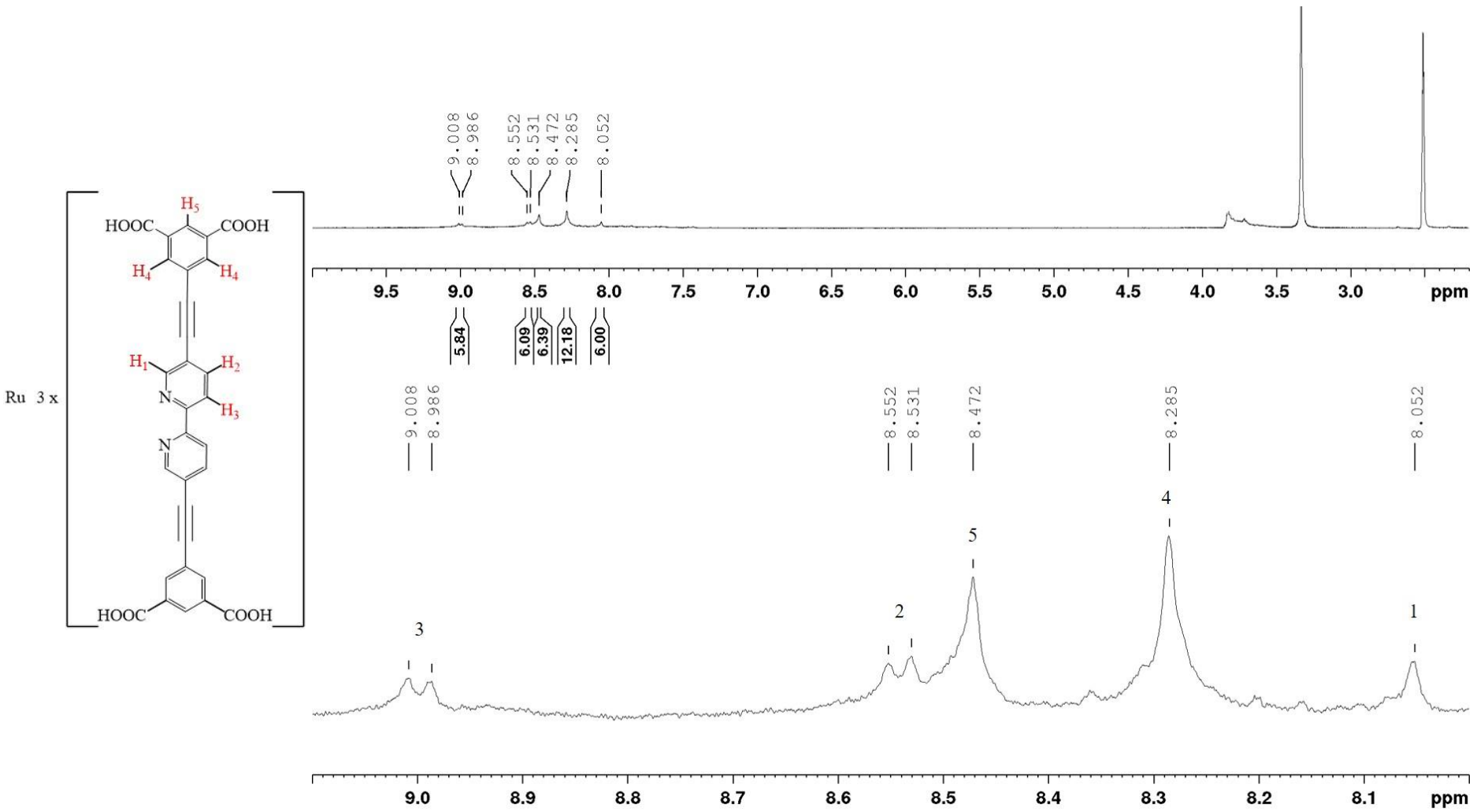

Figure 2.39: Labelled ^{1}H-NMR spectrum of $H_{12}[L_{tris}\text{-}R_3]^{2+}$ in d_6-DMSO. Full spectrum of $H_{12}[L_{tris}\text{-}R_3]^{2+}$ (top), aromatic region of $H_{12}[L_{tris}\text{-}R_3]^{2+}$ (bottom).

2.4 Physicochemical Characterisation of Ru^{II} Polypyridyl Complexes

Infrared Spectroscopy

IR spectroscopy was used to characterise $\mathbf{H_{12}[L_{tris}\text{-}R_3]^{2+}}$ (Fig. 2.40). Due to the structural similarities of $\mathbf{H_{12}[L_{tris}\text{-}R_3]^{2+}}$ with $\mathbf{H_2[L_{bpy}\text{-}R_1]^{2+}}$, $\mathbf{H_2[L_{bpy}\text{-}R_2]^{2+}}$, $\mathbf{H_4[L_{bpy}\text{-}R_3]^{2+}}$ and $\mathbf{H_4[L_{phen}\text{-}R_3]^{2+}}$, the FT-IR spectrum obtained was highly similar.

The hydrogen-bonded *ν*(O–H) stretch is responsible for the signal at *ca.* 3500 cm^{-1}.[35,36] At approximately 3090 cm^{-1}, the *ν*(C–H) stretching vibrations attributed to the aromatic moieties may be observed. The carbonyl *ν*(C=O) vibrations of the free carboxylic acid groups are responsible for the signal at *ca.* 1710 cm^{-1}.[37,38] The signal at *ca*. 1375 cm^{-1} can be attributed to the symmetric carboxylate stretching mode.[39,40] Between 1465 cm^{-1} and 1300 cm^{-1} *ν*(C=C) stretching vibrations attributed to the benzene and bipyridine moieties of $\mathbf{H_{12}[L_{tris}\text{-}R_3]^{2+}}$ can be seen, whereas the *ν*(C–N) stretch is observed at approximately 1240 cm^{-1}.[41,42] The *ν*(C–O) stretch can be seen at 1070 cm^{-1} and *ν*(C–H) bending vibrations corresponding to the benzene and bipyridine ring moieties are seen at approximately 760 cm^{-1} and 620 cm^{-1}.[44]

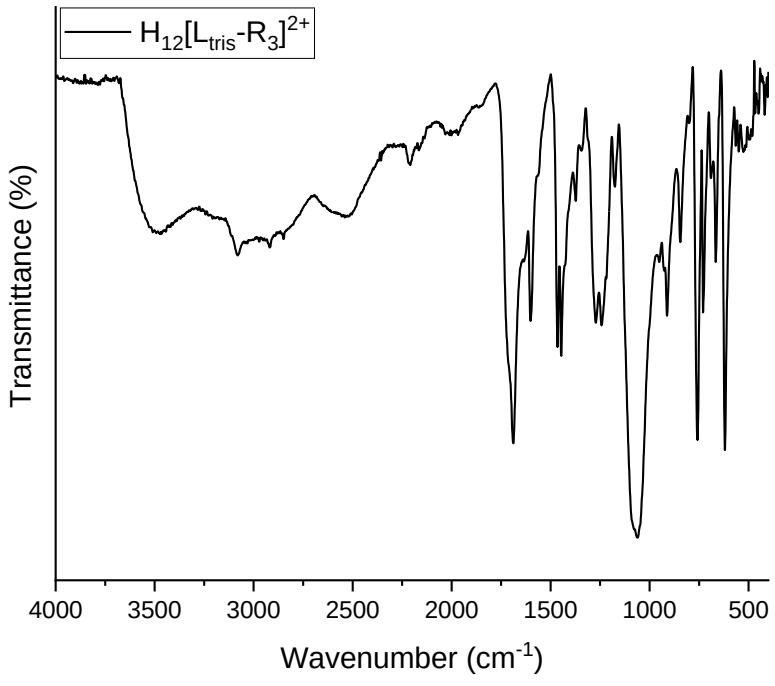

Figure 2.40: FT-IR spectrum of $\mathbf{H_{12}[L_{tris}\text{-}R_3]^{2+}}$.

Raman Spectroscopy

Raman spectroscopy was performed on $\mathbf{H_{12}[L_{tris}\text{-}R_3]^{2+}}$ (Fig. 2.41). The Raman spectrum was measured from 400 cm^{-1} to 2500 cm^{-1} and the baseline was corrected using OriginLab 2020 software. The Raman spectrum obtained was highly similar to that of the previously discussed novel Ru^{II} polypyridine complexes.

The signals at approximately 1000 cm^{-1}, 1033 cm^{-1}, 1123 cm^{-1}, 1145 cm^{-1} and 1188 cm^{-1} can be attributed to the aromatic and heteroaromatic ν(C–H) vibrations.[45] The ν(C–C) single bond vibrations appear at *ca.* 1277 cm^{-1} and 1315 cm^{-1}. At *ca*. 1370 cm^{-1}, ν_s(C=O) vibrations that derive from the carboxylate groups can be observed. The ν(C=C) vibrations attributed to the heteroaromatic, and aromatic rings can be seen at *ca.* 1490 cm^{-1}, and 1595 cm^{-1}. The final signal which can be seen at 2220 cm^{-1} can be attributed to the C≡C vibration of the alkyne moiety of $\mathbf{H_{12}[L_{tris}\text{-}R_3]^{2+}}$.[46]

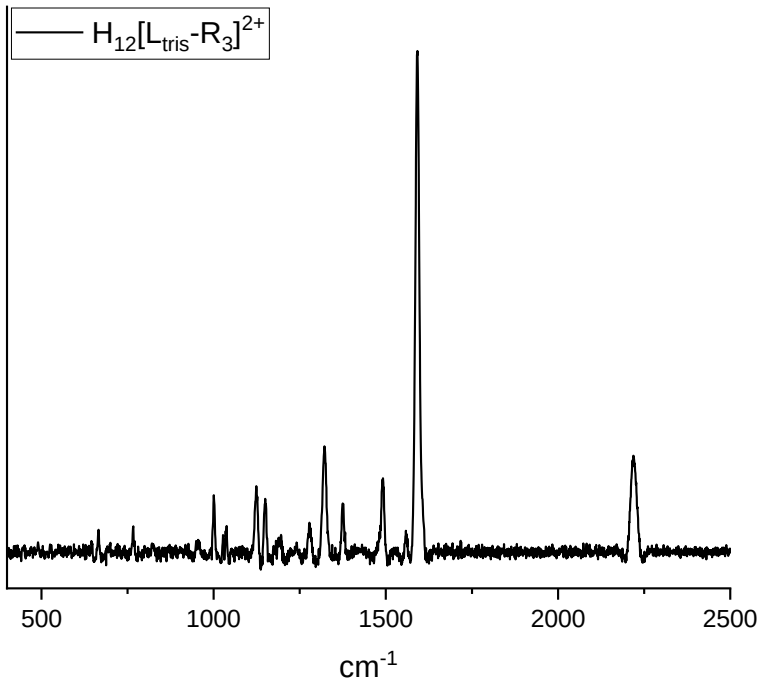

Figure 2.41: Raman spectrum of $\mathbf{H_{12}[L_{tris}\text{-}R_3]^{2+}}$.

Thermogravimetric Analysis

The thermal stability of **$H_{12}[L_{tris}$-$R_3]$** was determined by thermogravimetric analysis (TGA). A freshly prepared sample of **$H_{12}[L_{tris}$-$R_3]$** was analysed under a constant stream of air and at temperatures ranging between 30 °C to 700 °C. The TGA trace (Fig. 2.42) reveals a major decomposition event for **$H_{12}[L_{tris}$-$R_3]$** when heated above 300 °C. This step results in the decarboxylation and decomposition of **$H_{12}[L_{tris}$-$R_3]$**, attributing to a 69% weight loss. Finally, complete decomposition and the formation of a metal oxide of the **$H_{12}[L_{tris}$-$R_3]$** metallo-ligand can be observed when the sample is heated above *ca.* 515 °C.

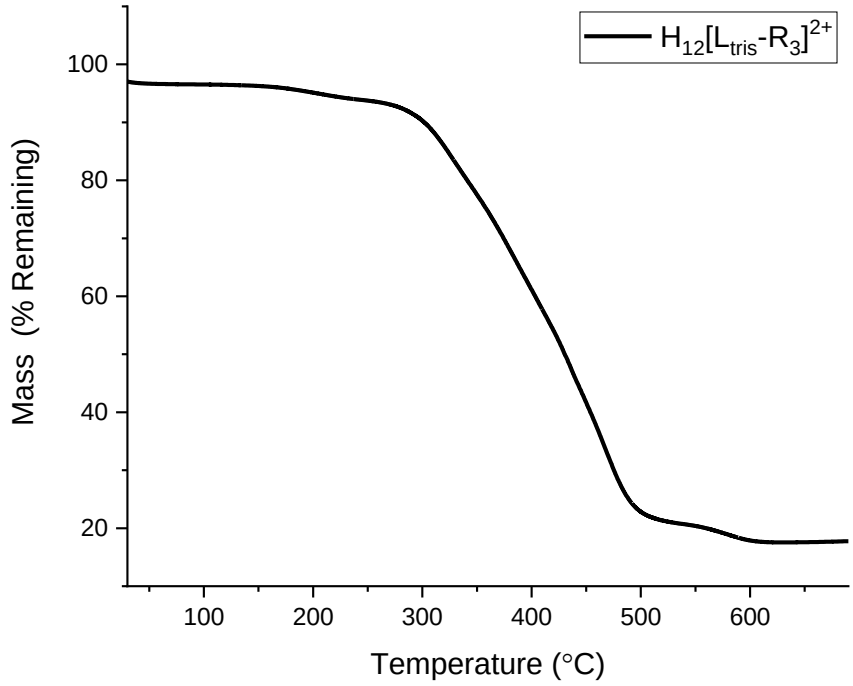

Figure 2.42: TGA trace for $H_{12}[L_{tris}$-$R_3]$.

2.5 Conclusion and Future Work

In this chapter, the preparation of five novel Ru^{II} polypyridyl complexes [bis-(2,2'-bipyridine)-ruthenium(II)(5,5'-(bis-4-ethynylbenzoic acid)-2,2'-bipyridine)]$^{2+}$, $\mathbf{H_2[L_{bpy}\text{-}R_1]^{2+}}$, [bis-(2,2'-bipyridine)-ruthenium(II)(5,5'-(bis-3-ethynylbenzoic acid)-2,2'-bipyridine)]$^{2+}$, $\mathbf{H_2[L_{bpy}\text{-}R_2]^{2+}}$, [bis-(2,2'-bipyridine)-ruthenium(II)(5,5'-(bis-5-ethynylisophthalic acid)-2,2'-bipyridine)]$^{2+}$, $\mathbf{H_4[L_{bpy}\text{-}R_3]^{2+}}$, [bis-(2,2'-bipyridine)-ruthenium(II)(3,8'-(bis-5-ethynylisophthalic acid)-1,10'-phenanthroline)]$^{2+}$, $\mathbf{H_4[L_{phen}\text{-}R_3]^{2+}}$, and [tris-(5,5'-(bis-5-ethynylisophthalic acid)-2,2'-bipyridine)-ruthenium(II)]$^{2+}$, $\mathbf{H_{12}[L_{tris}\text{-}R_3]^{2+}}$ have been described. These ligands are extended and modified forms of $Ru(bpy)_3(PF_6)_2$ with additional functionalities which provide O-donors that allow for coordination to various main group and transition metal ions *via* a variety of binding modes. In addition, the presence of aromatic systems within the synthesised complexes increases the potential for $\pi - \pi$ interactions, which in turn could further enhance the stability of supramolecular assemblies prepared using these ligands.

Furthermore, a more efficient route enabling the synthesis of the desired complexes was identified and conducted. Modification of literature procedures afforded greater purity, solubility, and scalability of the synthesised Ru^{II} polypyridyl complexes. The synthesised complexes and their structures were confirmed *via* NMR spectroscopy and ESI mass spectrometry. Single crystals of the novel Ru^{II} polypyridyl complexes were also obtained, and their structures were solved using single crystal X-ray diffraction analysis. The packing of the complexes in their 3D structures demonstrated the intermolecular forces present within the crystal structures. Finally, physicochemical characterisation using FT-IR spectroscopy, Raman spectroscopy and TGA confirmed the successful synthesis of the desired complexes. The post-synthetic characterisation also exhibits each of the Ru^{II} polypyridyl complexes' various characteristics while also showing the similarities between the synthesised complexes that derive from the $Ru(bpy)_3(PF_6)_2$ backbone.

Future work would involve the synthesis of various other extended linear metallo-ligands that include softer N-donors. Softer N-donors combined with harder carboxylate O-donors could afford the binding of the metallo-ligand to mix metals *via* various coordination modes. Such polypyridyl based ligands may provide a feasible option to establish versatile, permanently porous, and light-active MOFs stabilised by the Ru^{II} chromophore moieties.

2.6 References

1 M.-L. Han, X.-H. Chang, X. Feng, L.-F. Ma and L.-Y. Wang, *CrystEngComm*, 2014, **16**, 1687.

2 J. F. Fang, J. X. Cheng, S.-T. Huang, J. Zhang, C. Q. Ni, Y. J. Xiong, Q. Cheng, F. F. Zhu, Y. Li and S. T. Yue, *Journal of Inorganic and General Chemistry*, 2015, **641**, 2657–2663.

3 O. M. Yaghi, M. O'Keeffe, N. W. Ockwig, H. K. Chae, M. Eddaoudi and J. Kim, *Nature*, 2003, **423**, 705–714.

4 M. Eddaoudi, J. Kim, N. Rosi, D. Vodak, J. Wachter, M. O'Keeffe and O. M. Yaghi, *Science*, 2002, **295**, 469–472.

5 M. Du, Z.-H. Zhang, L.-F. Tang, X.-G. Wang, X.-J. Zhao and S. R. Batten, *Chem. - A Eur. J.*, 2007, **13**, 2578–2586.

6 I. Choi, S. Yoon, S. Huh, S. Kim and Y. Kim, *Chem. – A Eur. J.*, 2020, **26**, 14580–14584.

7 C. A. Kent, D. Liu, A. Ito, T. Zhang, M. K. Brennaman, T. J. Meyer and W. Lin, *J. Mater. Chem. A*, 2013, **1**, 14982.

8 C. A. Kent, D. Liu, T. J. Meyer and W. Lin, *J. Am. Chem. Soc.*, 2012, **134**, 3991–3994.

9 C. A. Kent, B. P. Mehl, L. Ma, J. M. Papanikolas, T. J. Meyer and W. Lin, *J. Am. Chem. Soc.*, 2010, **132**, 12767–12769.

10 A. Kudo and Y. Miseki, *Chem. Soc. Rev.*, 2009, **38**, 253–278.

11 S. Ouyang, H. Tong, N. Umezawa, J. Cao, P. Li, Y. Bi, Y. Zhang and J. Ye, *J. Am. Chem. Soc.*, 2012, **134**, 1974–1977.

12 C. Wang, Z. Xie, K. E. DeKrafft and W. Lin, *J. Am. Chem. Soc.*, 2011, **133**, 13445–13454.

13 S. Lin, Y. Pineda-Galvan, W. A. Maza, C. C. Epley, J. Zhu, M. C. Kessinger, Y. Pushkar and A. J. Morris, *ChemSusChem*, 2017, **10**, 514–522.

14 H.-Q. Xu, J. Hu, D. Wang, Z. Li, Q. Zhang, Y. Luo, S.-H. Yu and H.-L. Jiang, *J. Am. Chem. Soc.*, 2015, **137**, 13440–13443.

15 S. Guo, H. Zhang, Y. Chen, Z. Liu, B. Yu, Y. Zhao, Z. Yang, B. Han and Z. Liu, *ACS Catal.*, 2018, **8**, 4576–4581.

16 X. Lin, F. Luo, L. Zheng, G. Gao and Y. Chi, *Anal. Chem.*, 2015, **87**, 4864–4870.

17 D. Feng, Y. Wu, X. Tan, Q. Chen, J. Yan, M. Liu, C. Ai, Y. Luo, F. Du, S. Liu and H. Han, *Sensors Actuators B Chem.*, 2018, **265**, 378–386.

18 Z. Wang, J. Yang, Y. Li, Q. Zhuang and J. Gu, *Dalton Trans.*, 2018, **47**, 5570–5574.

19 A. P. Sadimenko, in *Advances in Heterocyclic Chemistry*, 2007, vol. 93, pp. 179–214.

20 P. Bora, B. Saikia and B. Sarma, *Cryst. Growth Des.*, 2018, **18**, 1448–1458.

21 D. M. D'Souza, D. A. Leigh, M. Papmeyer and S. L. Woltering, *Nat. Protoc.*, 2012, **7**, 2022–2028.

22 D. Tzalis, Y. Tor, F. Salvatorre and S. Jay Siegel, *Tetrahedron Lett.*, 1995, **36**, 3489–3490.

23 A. B. Zdravkov and N. N. Khimich, *Russ. J. Org. Chem.*, 2006, **42**, 1200–1202.

24 F. M. Romero and R. Ziessel, *Tetrahedron Lett.*, 1995, **36**, 6471–6474.

25 I. Kanwal, A. Mujahid, N. Rasool, K. Rizwan, A. Malik, G. Ahmad, S. A. A. Shah, U. Rashid and N. M. Nasir, *Catalysts*, 2020, **10**, 443.

26 C. Song, Y. Ling, Y. Feng, W. Zhou, T. Yildirim and Y. He, *Chem. Commun.*, 2015, **51**, 8508–8511.

27 Y.-S. Feng, C.-Q. Xie, W.-L. Qiao and H.-J. Xu, *Org. Lett.*, 2013, **15**, 936–939.

28 T. Pautzsch and E. Klemm, *Macromolecules*, 2002, **35**, 1569–1575.

29 D. Tzalis and Y. Tor, *Angew. Chem. Int. Ed.*, 1997, **36**, 2666–2668.

30 B. P. Sullivan, D. J. Salmon and T. J. Meyer, *Inorg. Chem.*, 1978, **17**, 3334–3341.

31 W. Frank, T. Pautzsch and E. Klemm, *Macromol. Chem. Phys.*, 2001, **202**, 2535–2537.

32 H. Iranmanesh, M. Bhadbhade, N. De Haas, E. T. Luis, H. Yan, J. Yang and J. E. Beves, *Supramol. Chem.*, 2015, **27**, 854–864.

33 D. V. Kozlov, D. S. Tyson, C. Goze, R. Ziessel and F. N. Castellano, *Inorg. Chem.*, 2004, **43**, 6083–6092.

34 C. A. Hunter and J. K. M. Sanders, *J. Am. Chem. Soc.*, 1990, **112**, 5525–5534.

35 G. Zhao, Y. Wang, X. Li, X. Dong, H. Wang, B. Du, W. Cao and Q. Wei, *ACS Appl. Mater. Interfaces*, 2018, **10**, 22932–22938.

36 X. Qin, X. Zhang, M. Wang, Y. Dong, J. Liu, Z. Zhu, M. Li, D. Yang and Y. Shao, *Anal. Chem.*, 2018, **90**, 11622–11628.

37 S. Pullen, H. Fei, A. Orthaber, S. M. Cohen and S. Ott, *J. Am. Chem. Soc.*, 2013, **135**, 16997–17003.

38 M. Sadakiyo, M. Kon-no, K. Sato, K. Nagaoka, H. Kasai, K. Kato and M. Yamauchi, *Dalton Trans.*, 2014, **43**, 11295–11298.

39 W. A. Maza and A. J. Morris, *J. Phys. Chem. C*, 2014, **118**, 8803–8817.

40 S. Alizadeh and D. Nematollahi, *J. Am. Chem. Soc.*, 2017, **139**, 4753–4761.

41 W. A. Maza, S. R. Ahrenholtz, C. C. Epley, C. S. Day and A. J. Morris, *J. Phys. Chem. C*, 2014, **118**, 14200–14210.

42 W. R. Heinz, I. Agirrezabal-Telleria, R. Junk, J. Berger, J. Wang, D. I. Sharapa, M. Gil-Calvo, I. Luz, M. Soukri, F. Studt, Y. Wang, C. Wöll, H. Bunzen, M. Drees and R. A. Fischer, *ACS Appl. Mater. Interfaces*, 2020, **12**, 40635–40647.

43 C.-Y. Chen, S.-J. Wu, J.-Y. Li, C.-G. Wu, J.-G. Chen and K.-C. Ho, *Adv. Mater.*, 2007, **19**, 3888–3891.

44 Y. P. Khanna, E. M. Pearce, B. D. Forman and D. A. Bini, *J. Polym. Sci. Polym. Chem. Ed.*, 1981, **19**, 2799–2816.

45 D. Lin-Vien, N. B. Colthup, W. G. Fateley and J. G. Grasselli, in *The Handbook of Infrared and Raman Characteristic Frequencies of Organic Molecules*, Elsevier, 1991, pp. 277–306.

46 H. G. M. Edwards, E. Smith and G. Dent., *J. Raman Spectrosc.*, 2005, **36**, 835–835.

47 C. Dietrich-Buchecker, M. C. Jime´nez and J.-P. Sauvage, *Tetrahedron Lett.*, 1999, **40**, 3395–3396.

48 D. Výprachtický, D. Kaňková, V. Pokorná, I. Kmínek, V. Dzhabarov and V. Cimrová, *Aust. J. Chem.*, 2014, **67**, 915.

49 Y. Saitoh, T. Koizumi, K. Osakada and T. Yamamoto, *Can. J. Chem.*, 1997, **75**, 1336–1339.

50 E. E. Garcia, C. V. Greco and I. M. Hunsberger, *J. Am. Chem. Soc.*, 1960, **82**, 4430–4431.

51 Y. Xiang, W. Li, Y. Fang, D. Zhang, X. Li and W. Jin, *RSC Adv.*, 2016, **6**, 27360–27369.

52 N. S. Baek, H. K. Kim, Y. Lee, J. Kang, T. J. Kim, G. T. Hwang and B. H. Kim, *Thin Solid Films*, 2002, **417**, 111–115.

53 N. Leventis, A. M. M. Rawashdeh, I. A. Elder, J. Yang, A. Dass and C. Sotiriou-Leventis, *Chem. Mater.*, 2004, **16**, 1493–1506.

Chapter 3

Photophysical Characterisation of Novel Ru^{II} Polypyridyl Complexes

3. Photophysical Characterisation of Novel Ru^{II} Polypyridyl Complexes

3.1. Introduction

Over the years, the successful development of ruthenium-based MOFs and their photoactive applications have instigated a wide array of promising research. Utilising struts that absorb light in either the visible or near-infrared region of the solar spectrum provides a feasible approach to synthesising photoactive light-harvesting MOFs. In contrast to photoactive organic molecules that primarily absorb photons in the ultraviolet (UV) region of the solar spectrum,[1–4] Ru^{II} polypyridyl based complexes generally exhibit strong, broad absorbances in the visible range.[5,6] Following the absorption process, these polypyridyl ligands can often facilitate the stabilisation of relatively long-lived excited states, in turn enabling their use as suitable building blocks for the synthesis of photoactive MOFs.[7–9] The associated excited-state characteristics involving MLCT energy states and their redox and energy transfer mechanisms are well known, along with the Ru^{II} polypyridyl moieties adaptability for integration into complex chemical and supramolecular systems.[10–14] Long excited state lifetimes, satisfactory redox potentials and high molar absorptivities in the visible region enable Ru^{II} polypyridyl moieties to function as efficient photosensitisers to promote highly endergonic, light-driven catalytic redox reactions, which include CO_2 reduction or H_2O oxidation reactions.[7,14–19] Similarly, the confinement and isolation of Ru^{II} polypyridine ligands within MOFs can prevent aggregation-induced quenching of their innate photoactivity, thus improving the heterogeneous catalytic performance and reactive oxygen species (ROS) generating ability of these photosensitisers.[20,21]

Furthermore, the photophysical, photochemical and electrochemical properties of Ru^{II} polypyridyl complexes can be modulated by the nature of the ligands coordinated to the metal centre. Ru complexes incorporating bidentate or tridentate polypyridine ligands have been extensively exploited for the design of well characterised supramolecular architectures.[22–25]

In this chapter, we evaluate the role of the Ru^{II} centre as a chromophore by investigating the photochemical, photophysical and electrochemical properties of the synthesised and previously discussed Ru^{II} polypyridyl complexes, $\mathbf{H_2[L_{bpy}\text{-}R_1]^{2+}}$, $\mathbf{H_2[L_{bpy}\text{-}R_2]^{2+}}$, $\mathbf{H_4[L_{bpy}\text{-}R_3]^{2+}}$, and $\mathbf{H_4[L_{phen}\text{-}R_3]^{2+}}$. More specifically, a comparative analysis was carried out in order to assess the photoactive performance of the named Ru^{II} polypyridyl

complexes with the well-studied core, parent complex $[Ru(bpy)_3]^{2+}$ **($[L6]^{2+}$)**. All investigations were performed at RTP *via* UV-Vis absorption spectroscopy, steady-state emission spectroscopy, time-correlated single photon counting methods, and solution phase cyclic voltammetry.

3.2 Ground State UV-Vis Absorption of Ru^{II} Polypyridyl Complexes

The electronic transitions corresponding to the ground state UV-Vis absorption spectrum of $[Ru(bpy)_3]^{2+}$ and its derivatives have been extensively studied throughout the literature. The most characteristic absorption band of $[Ru(bpy)_3]^{2+}$ at 450 nm has been reported as a metal-to-ligand charge transfer (MLCT) transition within the complex, whereby electrons are transferred from a d-orbital of primarily ruthenium character to a π* acceptor orbital of bipyridyl character (Fig. 3.1).[26] This absorption band of $[Ru(bpy)_3]^{2+}$ was noted to give rise to a luminescent complex,[27] and was further characterised at a proximal wavelength of 450 nm by Yoshimura[28] and Herrero,[29] and again at 455 nm by Kalyanasundaram.[30] Furthermore, the electronic absorption spectrum of $[Ru(bpy)_3]^{2+}$ in acetonitrile has been investigated, reinstating the existence of a (^{1}MLCT ← $^1A_1$) transition.[31] This transition was followed by low-intensity metal-centred transitions in the near UV, with ligand centred π-π* transitions occurring at shorter wavelengths.[32] Investigations by Innocenzi, a shoulder at 420 nm was assigned as an additional MLCT (t_{2g} (Ru) → π* (bpy)) transition, originating from the energy level splitting of the first excited state due to the D_3 symmetry of the complex itself.[27,33] In addition, shoulders at 325 nm and 350 nm were concluded to be metal-centred (t_{2g} (Ru) → e_g (Ru)) transitions, with an intense ligand-centred (π(bpy) → π*(bpy)) band at 285 nm. While Müller and Brettel observed an additional MLCT (t_{2g} (Ru) → π* (bpy)) transition at 243 nm ($\varepsilon = 2.72 \times 10^4$ $M^{-1}cm^{-1}$).[34] This was confirmed by Ji *et al*. who provided further credible evidence for the aforementioned transitions at proximal wavelengths of 246 nm, 286 nm and 422 nm.[35] Finally, a distinct ligand-centred π-π* transition was reported to occur at 208 nm. This transition was characterised through comparison of the UV-Vis absorption spectra of $[Ru(bpy)_3]^{2+}$ with protonated bipyridyl complexes.[27,36]

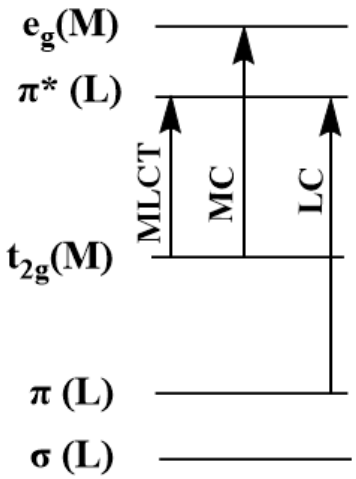

Figure 3.1: Molecular Orbital (MO) diagram for octahedral Ru^{II} polypyridine complexes, indicating the electronic transitions that take place within the UV-Vis region. Metal-to-Ligand Charge-Transfer (MLCT), Metal-Centered (MC) and Ligand-Centered (LC). Adapted from reference 26.

Initially, the UV-Vis absorption spectrum of $[Ru(bpy)_3]^{2+}$ **$[L6]^{2+}$)** (Fig. 3.2) measured at room temperature in an aerated acetonitrile solution (5 μM) was examined as a benchmark for comparison with the synthesised Ru^{II} polypyridyl complexes **$H_2[L_{bpy}\text{-}R_1]^{2+}$**, **$H_2[L_{bpy}\text{-}R_2]^{2+}$**, **$H_4[L_{bpy}\text{-}R_3]^{2+}$** and **$H_4[L_{phen}\text{-}R_3]^{2+}$**. Spectra of 5 μM solutions were recorded in a cuvette with 1 cm pathlength within a wavelength range of 600 – 200 nm using a Perkin Elmer Lambda 35 UV-Vis spectrometer. From the recorded spectrum of **$[L6]^{2+}$** (Fig. 3.2), a ligand-centred (π(bpy) → π*(bpy)) transition at 287 nm (ε = 19.4 x 10^4 $M^{-1}cm^{-1}$) can be observed, this wavelength corresponds well with results reported previously.[33,34,36] The presence of metal-to-ligand charge transfer bands at 244 nm (ε = 6.19 x 10^4 $M^{-1}cm^{-1}$), 252 nm (ε = 5.36 x 10^4 $M^{-1}cm^{-1}$), 420 nm (ε = 2.55 x 10^4 $M^{-1}cm^{-1}$) and 451 nm (ε = 3.3 x 10^4 $M^{-1}cm^{-1}$) can be seen.[28,29,33,35] Furthermore, the broadness of the absorption bands can be correlated to multiple unresolved spectroscopic transitions in the visible region, such as charge transfer transitions facilitated by solvent interactions.[32]

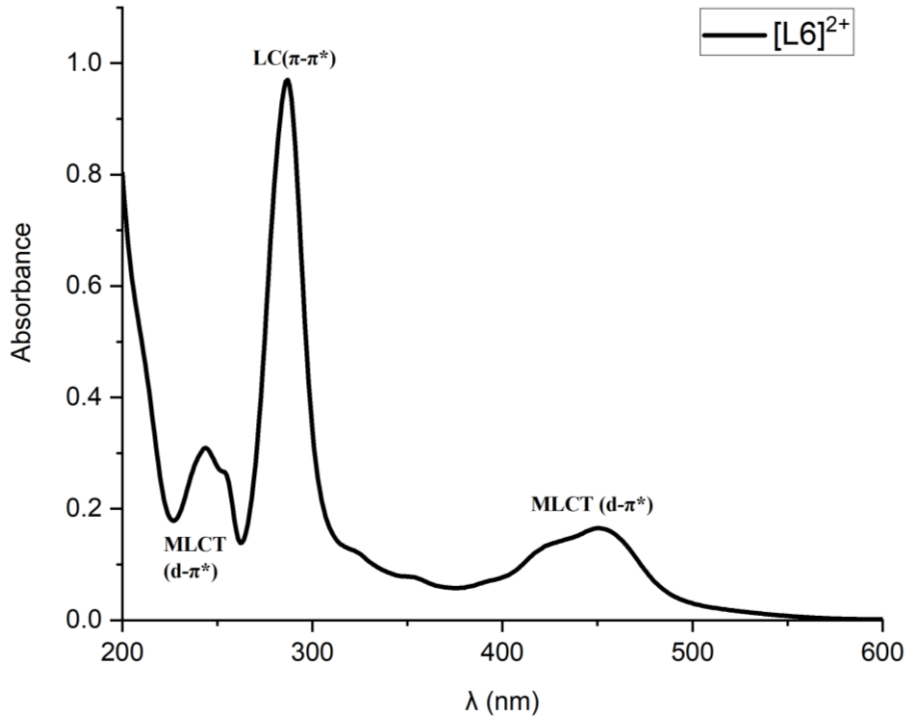

Figure 3.2: UV-Vis absorption spectrum of a 5 µM acetonitrile solution of $[L6]^{2+}$.

When comparing the ground state UV-Vis absorption spectra of $\mathbf{H_2[L_{bpy}\text{-}R_1]^{2+}}$, $\mathbf{H_2[L_{bpy}\text{-}R_2]^{2+}}$, $\mathbf{H_4[L_{bpy}\text{-}R_3]^{2+}}$, and $\mathbf{H_4[L_{phen}\text{-}R_3]^{2+}}$ in MeCN with $\mathbf{[L6]^{2+}}$, all recorded spectra presented the typical properties of Ru^{II} polypyridyl complexes with high similarity (Fig. 3.3 a-d, Table 3.1). Therefore, the photophysical characterisation of the synthesised Ru^{II} polypyridyl complexes was achieved by considering the extent of red and blue-shifted absorption bands (Fig. 3.4). This was most notably seen for the MLCT absorption band located at 450 nm in $\mathbf{[L6]^{2+}}$, which is red-shifted to the approximate region of 490 nm in $\mathbf{H_2[L_{bpy}\text{-}R_1]^{2+}}$, $\mathbf{H_2[L_{bpy}\text{-}R_2]^{2+}}$, $\mathbf{H_4[L_{bpy}\text{-}R_3]^{2+}}$, and $\mathbf{H_4[L_{phen}\text{-}R_3]^{2+}}$.[37] It can be said that this bathochromic shift is due to the increased conjugation in the ligand system as a result of the bis-alkynyl functionalisation. In particular, the MLCT absorption of $\mathbf{H_4[L_{phen}\text{-}R_3]^{2+}}$ showed strong similarities to $\mathbf{H_2[L_{bpy}\text{-}R_1]^{2+}}$, $\mathbf{H_4[L_{bpy}\text{-}R_2]^{2+}}$ and $\mathbf{H_4[L_{bpy}\text{-}R_3]^{2+}}$, highlighting the involvement of the π* acceptor orbitals located on the pyridyl moieties of the phenanthroline unit.[38] From this, it can be concluded that bipyridine is a strong π-acceptor ligand in the coordination sphere of the ruthenium centre.[39]

Moreover, heteroleptic Ru^{II} complexes generally present ligands with varying electron accepting or donating abilities. They can promote an increase or decrease in the donation of electron density to the metal centre and a destabilisation or stabilisation of the filled metal d-orbitals, respectively. Thus, an increase in electron density at the metal centre and destabilisation of the filled metal d-orbitals provides an explanation for the shift to higher wavelengths of the MLCT transitions for $\mathbf{H_2[L_{bpy}\text{-}R_1]^{2+}}$, $\mathbf{H_2[L_{bpy}\text{-}R_2]^{2+}}$, $\mathbf{H_4[L_{bpy}\text{-}R_3]^{2+}}$, and $\mathbf{H_4[L_{phen}\text{-}R_3]^{2+}}$ respectively, when compared to the homoleptic $\mathbf{[L6]^{2+}}$ complex.[40] The splitting of the MLCT band in the $[Ru(bpy)_3]^{2+}$-derived complexes account for the identity of the two ligands with differing π-systems. Therefore, the absorption band at *ca.* 440 nm is assigned as a $((t_{2g}(Ru) \rightarrow \pi^*(bpy))$ MLCT, while the lower energy transition at approximately 490 nm is denoted as a $((t_{2g}(Ru) \rightarrow \pi^*(L))$ transition.[41] The data obtained demonstrates that the extended π system of the $[Ru(bpy)_3]^{2+}$-based ligands results in enhanced absorption of light in the visible region.[42]

In addition, the UV-Vis spectra of $\mathbf{H_2[L_{bpy}\text{-}R_1]^{2+}}$, $\mathbf{H_2[L_{bpy}\text{-}R_2]^{2+}}$, $\mathbf{H_4[L_{bpy}\text{-}R_3]^{2+}}$, and $\mathbf{H_4[L_{phen}\text{-}R_3]^{2+}}$ displayed a similar degree of hypochromic effect for the observed MLCT and LC transitions when compared to $\mathbf{[L6]^{2+}}$. Also, in contrast to the parent complex $\mathbf{[L6]^{2+}}$, an additional ligand-centred transition can be distinctly observed in the spectra of $\mathbf{H_2[L_{bpy}\text{-}R_1]^{2+}}$, $\mathbf{H_2[L_{bpy}\text{-}R_2]^{2+}}$, $\mathbf{H_4[L_{bpy}\text{-}R_3]^{2+}}$, and $\mathbf{H_4[L_{phen}\text{-}R_3]^{2+}}$. This transition appears at *ca.* 350 nm and has been previously confirmed in literature for 5-ethynyl-substituted $[Ru(bpy)_3]^{2+}$-derived complexes.[44] It has been suggested that the enhanced intensities can be likely due to greater electron delocalisation in either the ground or excited state of the ligand system by the two 5-ethynyl substitutions on the extended bipyridine and phenanthroline moieities.[39,44] All complexes displayed almost identical absorption bands with varying intensities at roughly 287 nm, attributed to the ligand-centred transitions of the 2,2'-bipyridine units.[37,43] These intense relatively sharp bands, allowed the facile discerning of ligand substitution effects at this wavelength.

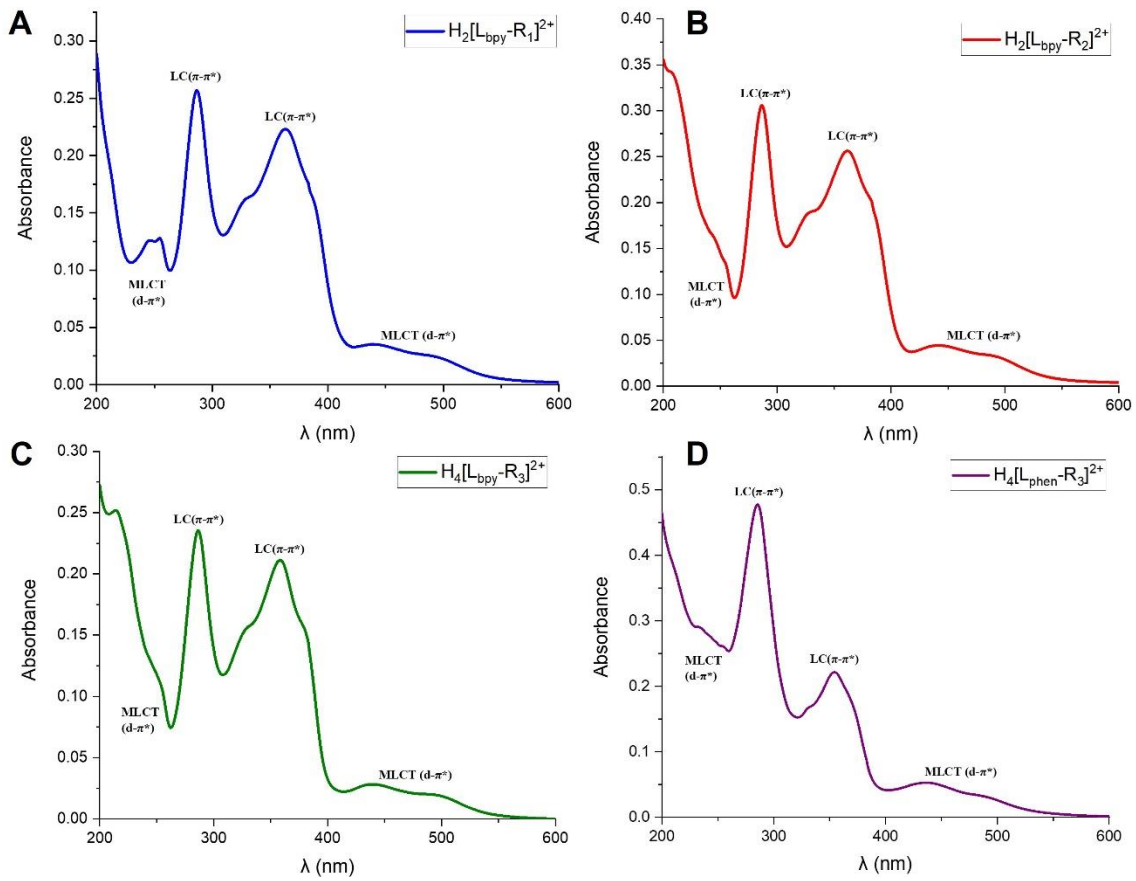

Figure 3.3: UV-Vis absorption spectra of a 5 µM acetonitrile solutions of $H_2[L_{bpy}\text{-}R_1]^{2+}$ (A), $H_2[L_{bpy}\text{-}R_2]^{2+}$ (B), $H_4[L_{bpy}\text{-}R_3]^{2+}$ (C), and $H_4[L_{phen}\text{-}R_3]^{2+}$ (D).

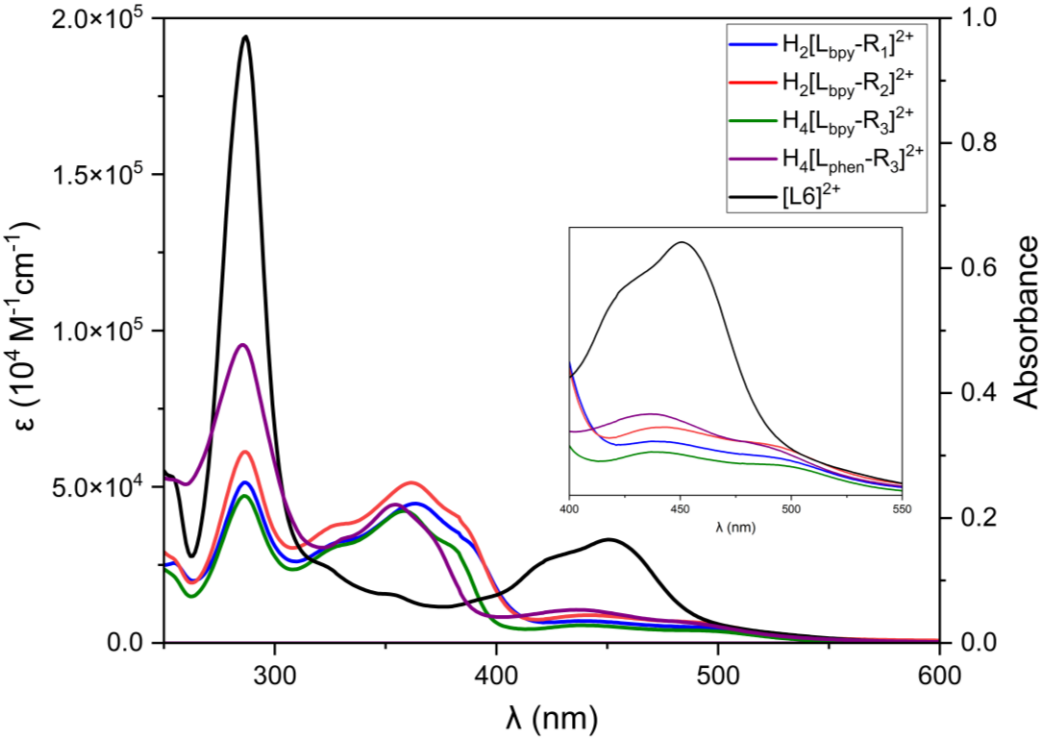

Figure 3.4: UV-Vis absorption spectrum of a 5 µM acetonitrile solution of $H_2[L_{bpy}\text{-}R_1]^{2+}$ (blue), $H_2[L_{bpy}\text{-}R_2]^{2+}$ (red), $H_4[L_{bpy}\text{-}R_3]^{2+}$ (green), $H_4[L_{phen}\text{-}R_3]^{2+}$ (purple), and $[L6]^{2+}$ (black), with corresponding extinction coefficient (ε) values.

Table 3.1: UV-Vis absorption spectral data of 5 µM acetonitrile solutions of $H_2[L_{bpy}\text{-}R_1]^{2+}$, $H_2[L_{bpy}\text{-}R_2]^{2+}$, $H_4[L_{bpy}\text{-}R_3]^{2+}$, $H_4[L_{phen}\text{-}R_3]^{2+}$, and $[L6]^{2+}$.

Complex	*Mass (mg)*	*UV-Vis λ_{max} / nm (ε_{max} / $M^{-1}cm^{-1}$)*	*Assigned Transition*
$[L6]^{2+}$	3.74	451 (33 000), 420sh (25 500), 252sh (53 600), 244 (61 900) 287 (194 000)	MLCT ($(t_{2g}$ (Ru) → π* (bpy)) LC (π(bpy) → π*(bpy))
$H_2[L_{bpy}\text{-}R_1]^{2+}$	5.78	490 (5 000), 439 (7 000), 254 (25 600), 246 (25 200) 363 (44 600), 287 (51 300)	MLCT ($(t_{2g}$ (Ru) → π* (L/bpy)) LC (π(bpy) → π*(bpy))
$H_2[L_{bpy}\text{-}R_2]^{2+}$	5.76	497 (61 100), 443 (8 900), ~245 (32 300) 362 (51 300), 287 (61 200)	MLCT ($(t_{2g}$ (Ru) → π* (L/bpy)) LC (π(bpy) → π*(bpy))
$H_4[L_{bpy}\text{-}R_3]^{2+}$	5.92	493 (4 000), 437sh (5 700), 254sh (21 700) 358 (42 200), 286 (47 000)	MLCT ($(t_{2g}$ (Ru) → π* (L/bpy)) LC (π(bpy) → π*(bpy))
$H_4[L_{phen}\text{-}R_3]^{2+}$	6.25	490sh (6 300), 436 (10 600), 256 (51 900) 354 (44 300), 286 (95 400)	MLCT ($(t_{2g}$ (Ru) → π* (L/bpy)) LC (π(bpy) → π*(bpy))

3.3 Steady-State Emission of Ru^{II} Polypyridyl Complexes

$[Ru(bpy)_3]^{2+}$-derived complexes are known for their wide range of emission wavelengths, quantum yields, and decay lifetimes.[45–47] Such emissions originate from charge-transfer states occurring within the excited complex in solution, resulting in lifetimes between 100 – 4000 ns with substantial quantum yields.[48] For these reasons, many photophysical applications are investigated that incorporate ruthenium polypyridyl species.[5,49–54]

The excitation of $[Ru(bpy)_3]^{2+}$ at its corresponding UV-Vis absorption wavelengths produces a broad orange emission band centred at approximately 620 nm. However, the energy, quantum yield, lifetime, and emission intensity depend highly on the chosen solvent and temperature.[36] For example, it was reported by Quang that a broad emission band of $[Ru(bpy)_3]^{2+}$ in deaerated acetonitrile solvent at room temperature was centred near 600 nm. This transition has an excited state lifetime of approximately 1 μs (Φ = 0.06).[55] Additional phosphorescence bands of $[Ru(bpy)_3]^{2+}$ are known to occur at 610 nm,[56] 620 nm,[33] 623 nm,[43] 635 nm[57] and 640 nm.[58]

Furthermore, because the absorption bands of $[Ru(bpy)_3]^{2+}$ are adequately distanced from its emission band, the possibility of self-absorption is generally prohibited.[59] Upon $^1A_1$ photon excitation,[31] there is an initial population of the excited singlet metal-to-ligand charge transfer state (^{1}MLCT), which subsequently can undergo rapid intersystem crossing (~15 fs) favoured by a heavy atom effect with near-unity quantum yields to an excited triplet charge-transfer state (^{3}MLCT).[31,34,60,61] Alternatively, fluorescence and/or non-radiative decays can occur from the fleeting ^{1}MLCT state. Emission of the ^{3}MLCT excited state can be characterised by phosphorescence processes as schematically represented *in* a Jablonski diagram shown in Figure 3.5. The ^{3}MLCT state can also be deactivated through non-radiative decay (heat loss) and/or the population of a triplet metal-centred (^{3}MC) state. Deactivation of the ^{3}MC state can thus lead to non-radiative decay as well as the dissociation of a chelated bipyridine ligand.[55]

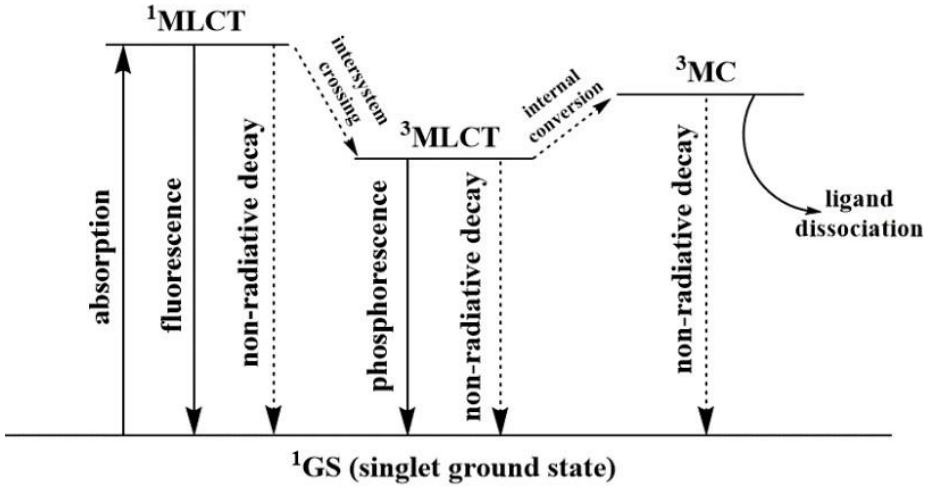

Figure 3.5: Jablonski diagram indicating the various electronic transitions that take place between the ground and excited states. Reproduced from reference 55.

The earliest assignment for the emission of $[Ru(bpy)_3]^{2+}$ was postulated by Paris and Brandt,[62] who proposed the idea of π*-d charge transfer fluorescence. This was later rejected and the emission was attributed to d*-d ligand field fluorescence, d-d* ligand field phosphorescence,[63] π*-d charge transfer fluorescence[64] and finally π*-d charge transfer luminescence.[65] The majority of this work was achieved by Crosby *et al*. in the attempt to rationalise the photophysical properties of $[Ru(bpy)_3]^{2+}$ and substituted derivatives based on theoretical models.[66–69] Although it is satisfactory to deduce a metal-ligand interaction as a precursor to luminescence, significant contribution from the ruthenium d-orbital will allow the spin-orbit coupling to perturb singlet and triplet states so that the emission is redefined as a product of delocalised spin-orbit states rather than the agreed spin triplet electronic state.[70] Ultimately, the emission can be described in terms of a $4d^5$ Ru^{III} centre with one electron transferred from a metal t_{2g} orbital to the lowest energy π* antibonding orbital of a single bipyridine ligand, in accordance with Kasha's rule.[71,72] Furthermore, it has been widely discussed throughout literature whether the fate of this excited electron remains localised on a single chelate or becomes delocalised equally throughout the three bipyridyl units present.[73,74] It is confirmed that upon excitation, the localisation of a single electron results in the formation of a significant dipole moment in the excited state, orientated along the ruthenium metal core and extending to the centre of one bipyridine unit in space. The solvation dynamics of the nascent excited dipole has been analysed *via* femtosecond time-resolved anisotropy, and related to the creation of a photoinduced charge-transfer event.[75] Consequently, it is found that an initial delocalisation of electron density exists across all three bipyridine

units before inducing an ultrafast localisation of charge onto a single chelate, depending on the specific extent of non-diffusive solvation.[56]

The luminescent properties of $\mathbf{H_2[L_{bpy}\text{-}R_1]^{2+}}$, $\mathbf{H_2[L_{bpy}\text{-}R_2]^{2+}}$, $\mathbf{H_4[L_{bpy}\text{-}R_3]^{2+}}$, $\mathbf{H_4[L_{phen}\text{-}R_3]^{2+}}$, and $\mathbf{[L6]^{2+}}$ were studied *via* steady-state emission techniques (λ_{ex} = 450 nm) in acetonitrile solvent (Fig 3.6 and 3.7 (a-d), Table 3.2) using a Fluoromax-4P spectrofluorometer. Phosphorescent emission was recorded for all 5 µM solutions in ambient temperature and exciting at 450 nm within a wavelength range of 460 – 825 nm. The absorbances obtained were subsequently normalised to allow for a comparative analysis of spectral properties based on ligand modification (Fig. 3.8). The luminescence of $\mathbf{[L6]^{2+}}$ at 620 nm was in good agreement with the literature previously discussed, signifying a relaxation of the ^{3}MLCT state consistent with Kasha's rule.

The data obtained demonstrated that the metallo-ligands are all highly emissive, with broad emission bands centred at 698 nm for $\mathbf{H_2[L_{bpy}\text{-}R_1]^{2+}}$, 689 nm for $\mathbf{H_2[L_{bpy}\text{-}R_2]^{2+}}$, 702 nm for $\mathbf{H_4[L_{bpy}\text{-}R_3]^{2+}}$ and 674 nm for $\mathbf{H_4[L_{phen}\text{-}R_3]^{2+}}$. However, a change in intensity was apparent in the decreasing order of $\mathbf{H_4[L_{phen}\text{-}R_3]^{2+}}$, $\mathbf{H_2[L_{bpy}\text{-}R_2]^{2+}}$, $\mathbf{H_2[L_{bpy}\text{-}R_1]^{2+}}$ and $\mathbf{H_4[L_{bpy}\text{-}R_3]^{2+}}$, with a simultaneous increase in the broadness of the bands.[76] As the phosphorescence intensities of the Sonogashira cross-coupled products decreased steadily, a red-shift was also observed, indicating that the emission was significantly dependent on the bis-alkynyl functionality.[44,72,77–79] The electron-withdrawing nature of this individual bis-alkynyl moieties and the greater extent of π-conjugation when compared to the parent complex $\mathbf{[L6]^{2+}}$ can effectively lower the LUMO energy of the ligands π* acceptor orbital and decrease the energy of the emissive ^{3}MLCT state.[38,56] Thus, one can assume that this excited state is associated with the movement of electrons between the Ru^{II} metal centre and the extended bipyridine ligand instead of being delocalised across all bipyridine ligands equally. The bathochromic shift evident from the comparison of emission spectra is in agreement with the red shift seen in the corresponding UV-Vis absorption data.[37,80] With this observation, the dependence of photophysical properties was reinstated with each ruthenium core substitution pattern.

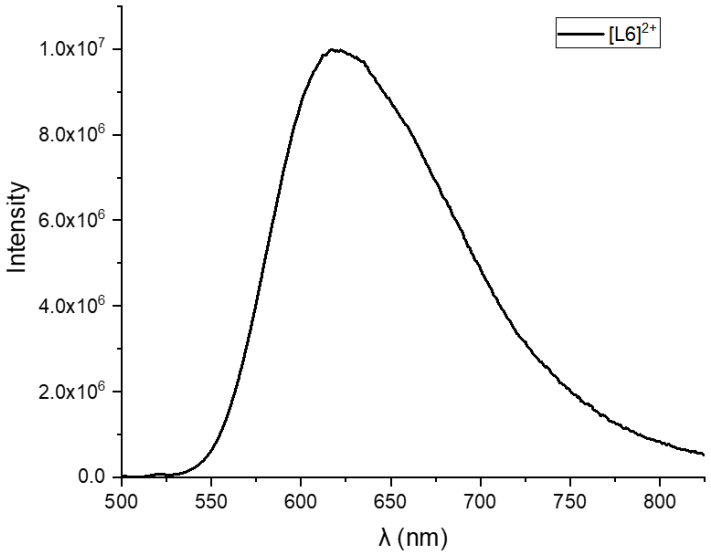

Figure 3.6: Steady-state emission spectrum within a range of 500 – 825 nm of a 5 µM acetonitrile solution of $[L6]^{2+}$ using an excitation wavelength of 450 nm and 5 nm emission and 5 nm excitation slit.

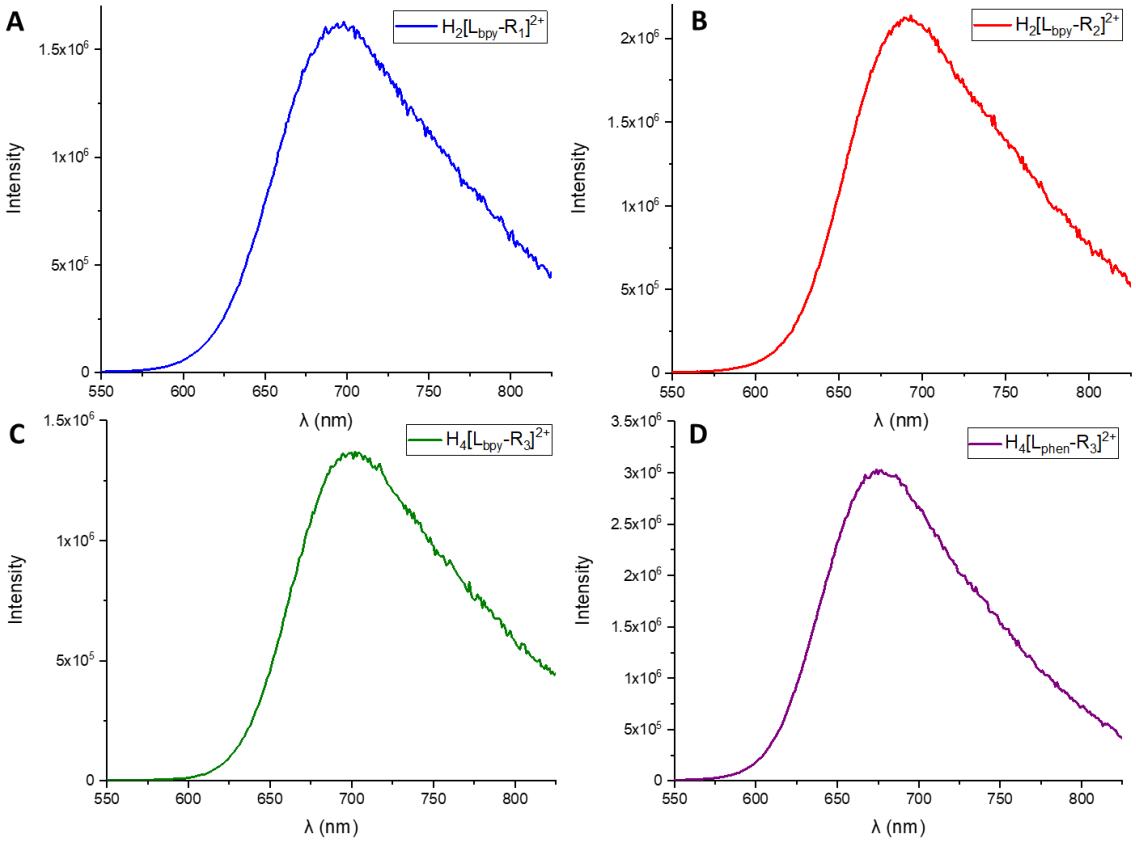

Figure 3.7: Steady-state emission spectra within a range of 550 – 825 nm of 5 µM acetonitrile solutions of $H_2[L_{bpy}\text{-}R_1]^{2+}$ (A), $H_2[L_{bpy}\text{-}R_2]^{2+}$ (B), $H_4[L_{bpy}\text{-}R_3]^{2+}$ (C) and $H_4[L_{phen}\text{-}R_3]^{2+}$ (D). Excitation wavelength of 450 nm and 5 nm emission and 5 nm excitation slit.

Table 3.2: Emission peak wavelengths (nm) corresponding to 5 µM acetonitrile solutions of $H_2[L_{bpy}\text{-}R_1]^{2+}$, $H_2[L_{bpy}\text{-}R_2]^{2+}$, $H_4[L_{bpy}\text{-}R_3]^{2+}$, $H_4[L_{phen}\text{-}R_3]^{2+}$, and $[L6]^{2+}$ (λ_{ex} = 450 nm).

Ligand	*Wavelength of Emission Peak*
$H_2[L_{bpy}\text{-}R_1]^{2+}$	698 nm
$H_2[L_{bpy}\text{-}R_2]^{2+}$	689 nm
$H_4[L_{bpy}\text{-}R_3]^{2+}$	702 nm
$H_4[L_{phen}\text{-}R_3]^{2+}$	674 nm
$[L6]^{2+}$	620 nm

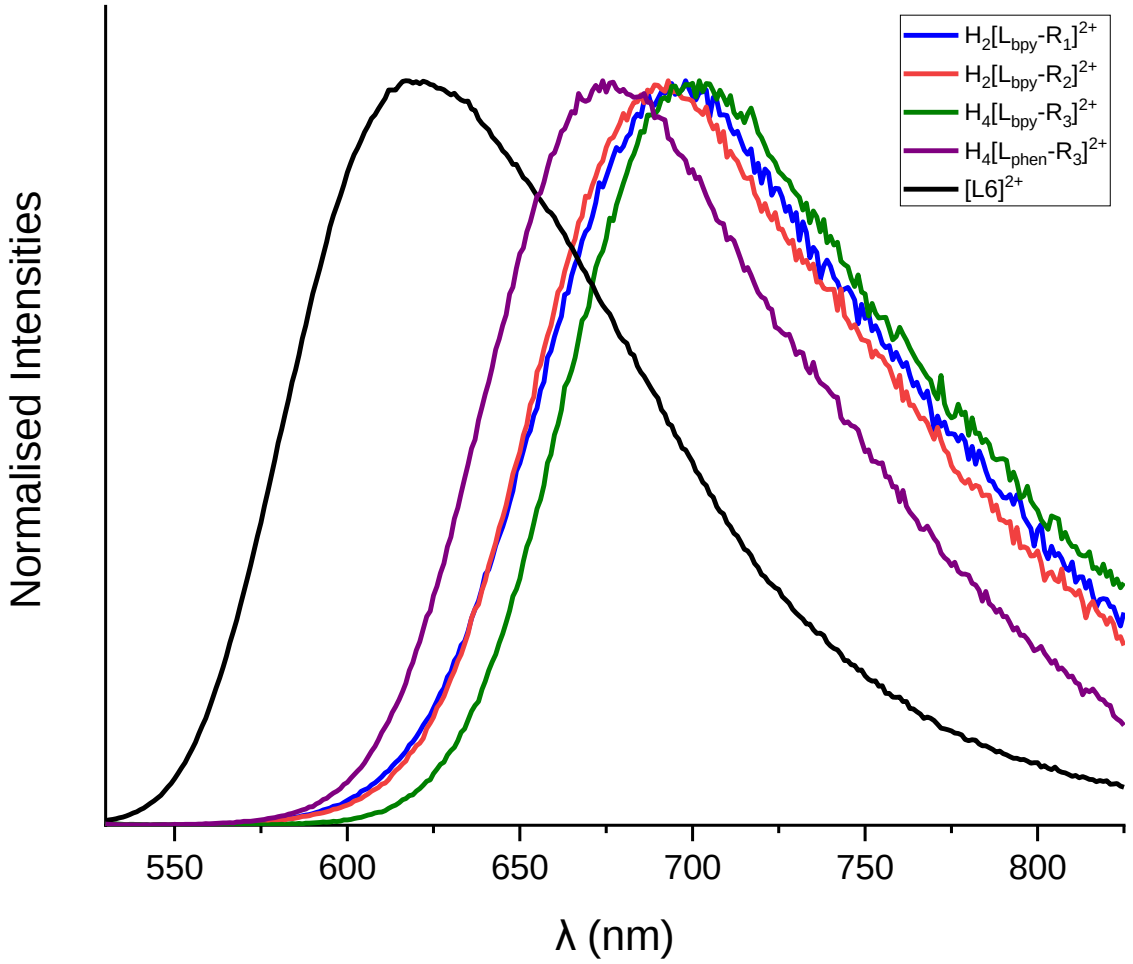

Figure 3.8: Steady-state emission spectrum of a 5 µM acetonitrile solutions of $H_2[L_{bpy}\text{-}R_1]^{2+}$ (blue), $H_2[L_{bpy}\text{-}R_2]^{2+}$ (red), $H_4[L_{bpy}\text{-}R_3]^{2+}$ (green), $H_4[L_{phen}\text{-}R_3]^{2+}$ (purple), and $[L6]^{2+}$ (black) (λ_{ex} = 450 nm).

3.4 Fluorescent Lifetime Analysis of Ru^{II} Polypyridyl Complexes

Continuing from the previous section, fluorescent lifetime (τ) can be defined as the time a molecule exists in the excited singlet state before undergoing a radiative decay pathway. The variation in lifetimes for ruthenium polypyridyl complexes was noted as an important characteristic of these materials, demonstrating lifetimes within the broad range of 100 ns to 10 μs.[81] Additionally, various external factors such as temperature, solvent polarity and the presence of fluorescence quenchers affect the fluorescence lifetimes.[82] It is also important to note the difference in lifetimes between phosphorescent and fluorescent events within $[Ru(bpy)_3]^{2+}$-derived complexes. Due to the spin-forbidden change in multiplicity as a result of intersystem crossing, phosphorescent decays have an increased lifetime (10^{-3} to 10^{-2} s) over fluorescent decays (10^{-9} to 10^{-7} s).

The fluorescent lifetimes and χ^2 values of $\mathbf{H_2[L_{bpy}\text{-}R_1]^{2+}}$, $\mathbf{H_2[L_{bpy}\text{-}R_2]^{2+}}$, $\mathbf{H_4[L_{bpy}\text{-}R_3]^{2+}}$, $\mathbf{H_4[L_{phen}\text{-}R_3]^{2+}}$, and $\mathbf{[L6]^{2+}}$ were recorded in acetonitrile solvent, using a Fluorolog-3 Time-Correlated Single Photon Counting (TCSPC) instrument. A repetition rate of 500 kHz and 10,000 counts were collected for each lifetime experiment. A 372 nm pulsed laser diode was employed in all experiments, and a 458 nm laser diode was additionally used to confirm the validity of all lifetime measurements'. $\mathbf{H_2[L_{bpy}\text{-}R_1]^{2+}}$, $\mathbf{H_2[L_{bpy}\text{-}R_2]^{2+}}$, $\mathbf{H_4[L_{bpy}\text{-}R_3]^{2+}}$, $\mathbf{H_4[L_{phen}\text{-}R_3]^{2+}}$ and $\mathbf{[L6]^{2+}}$ were excited at a wavelength of 450 nm. All measurements were carried out using Data6 v6.3 software by fitting mono-exponential decay functions to each decay curve. The goodness of fit was evaluated from the obtained χ^2 values using TCSPC experiments and summarised below (Fig. 3.11, Table 3.3). With specific relation to $[Ru(bpy)_3]^{2+}$, $\mathbf{[L6]^{2+}}$, a lifetime of 162.94 ns was measured and obtained (Fig 3.9) and can be compared to similar results found in the literature.[33,43]

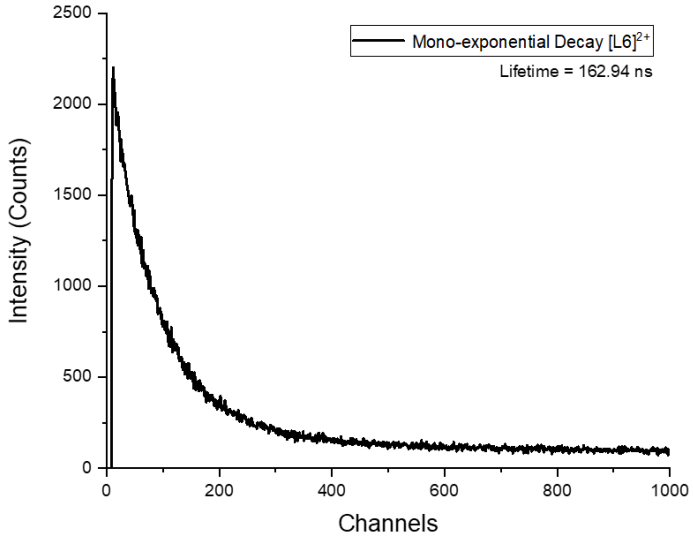

Figure 3.9: Mono-exponential decay curve of a 10 µM acetonitrile solution of $[L6]^{2+}$, with corresponding fluorescent lifetime.

From the data obtained a fluorescent lifetime of 206 ns for $\mathbf{H_2[L_{bpy}\text{-}R_1]^{2+}}$, 218 ns for $\mathbf{H_2[L_{bpy}\text{-}R_2]^{2+}}$, 201 ns for $\mathbf{H_4[L_{bpy}\text{-}R_3]^{2+}}$ and 277 for $\mathbf{H_4[L_{phen}\text{-}R_3]^{2+}}$ was calculated. When analysing emission lifetimes obtained for the synthesised Ru^{II} polypyridyl complexes, an increase in the lifetime is observed in the order of $\mathbf{[L6]^{2+} < H_4[L_{bpy}\text{-}R_3]^{2+} < H_2[L_{bpy}\text{-}R_1]^{2+} < H_2[L_{bpy}\text{-}R_2]^{2+} < H_4[L_{phen}\text{-}R_3]^{2+}}$. This increase can be correlated to the degree of conjugation within the framework of the ligands (Fig. 3.10). It was reported by Biswas that the fluorescent properties of a molecule, such as the emission lifetime, are sensitive to structural factors present within the complex. In addition, the quenching of the excited singlet state during various decay pathways can be related to the dissipation of the maximum amount of excited state electrons towards the conjugated π-system of the complex. This phenomenon accounts for the stabilisation of the excited state and the longer lifetimes observed.[83]

It was also noted that the presence of electron-donating groups, such as weakly activating phenyl rings, can enhance the conjugation and stabilisation of the excited electronic structures. Moreover, because the fluorescent lifetimes of $\mathbf{H_2[L_{bpy}\text{-}R_1]^{2+}}$, $\mathbf{H_2[L_{bpy}\text{-}R_2]^{2+}}$, $\mathbf{H_4[L_{bpy}\text{-}R_3]^{2+}}$, and $\mathbf{H_4[L_{phen}\text{-}R_3]^{2+}}$ were in close proximity to the parent complex, one can assume there was a significant contribution from the bis-alkynyl moiety present in each ligand structure.[38] In relation to $\mathbf{H_4[L_{phen}\text{-}R_3]^{2+}}$, the recorded fluorescent lifetime of 277 ns can be compared to values obtained for similar structures in the literature.[84] Finally, the high similarity between lifetimes recorded using laser diodes of different wavelengths (372 nm and 458 nm) as well as the acceptable values for χ^2 reinstated the

validity of the collected measurements. Thus, the extended fluorescent lifetimes obtained for the novel metallo-ligands in comparison to **$[L6]^{2+}$** makes them good candidates for their use as ligands in the synthesis of novel photoactive MOFs.

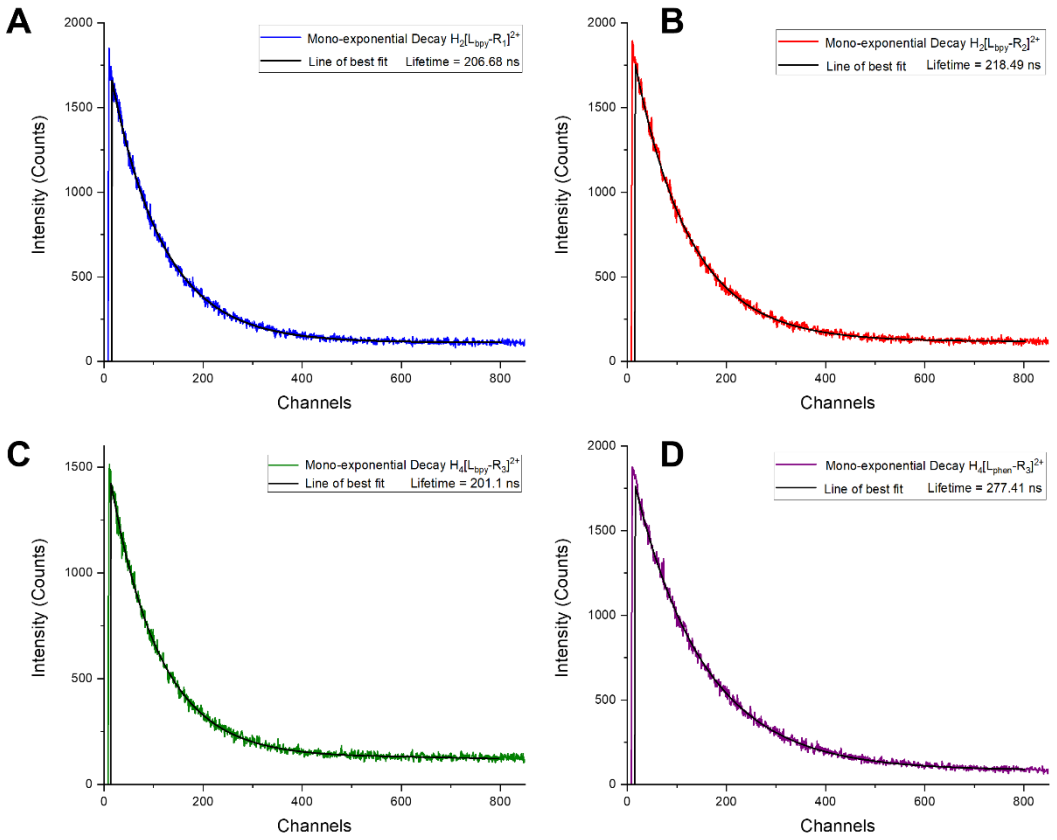

Figure 3.10: Mono-exponential decay curve including line of best fit (black) of a 10 µM acetonitrile solution of $H_2[L_{bpy}\text{-}R_1]^{2+}$ (A), $H_2[L_{bpy}\text{-}R_2]^{2+}$ (B), $H_4[L_{bpy}\text{-}R_3]^{2+}$ (C) and $H_4[L_{phen}\text{-}R_3]^{2+}$ (D), with corresponding fluorescent lifetimes.

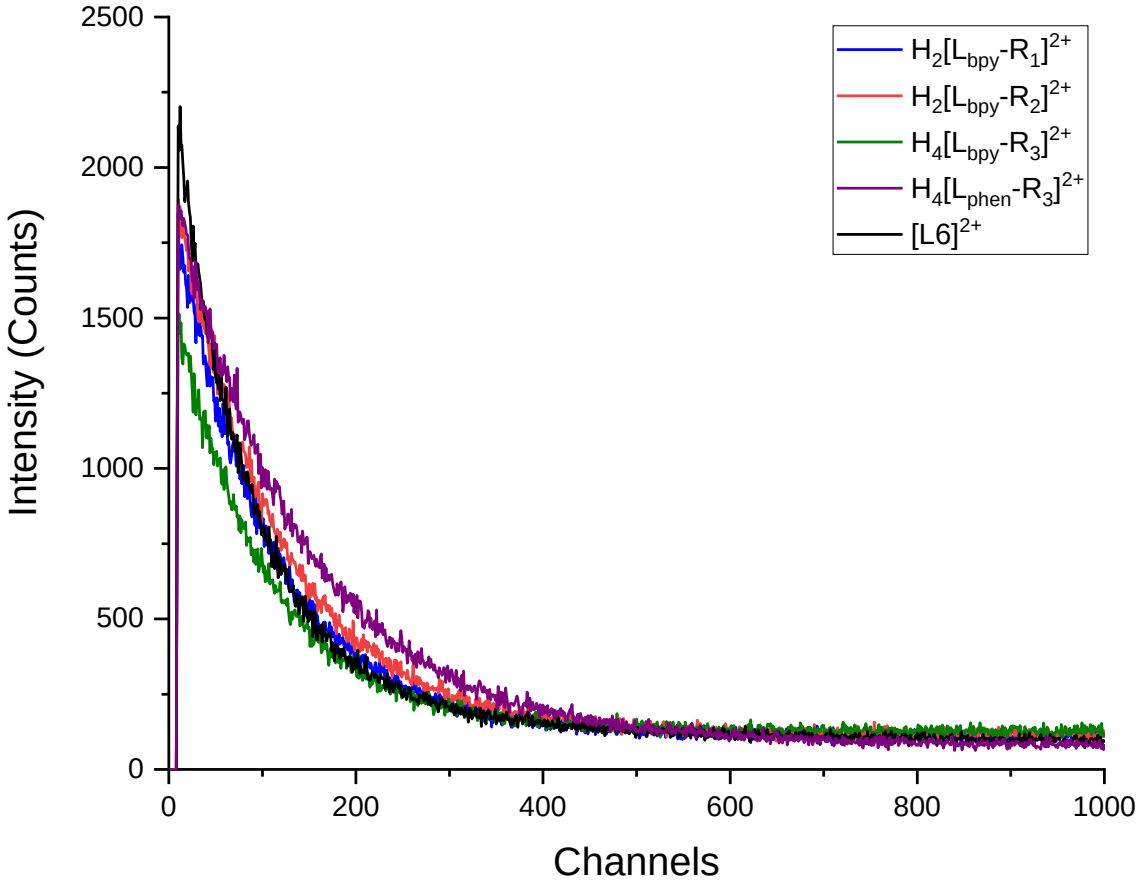

Figure 3.11: Comparative analysis of the mono-exponential decay curves of 10 µM acetonitrile solutions of $H_2[L_{bpy}\text{-}R_1]^{2+}$ (blue), $H_2[L_{bpy}\text{-}R_2]^{2+}$ (red), $H_4[L_{bpy}\text{-}R_3]^{2+}$ (green), $H_4[L_{phen}\text{-}R_3]^{2+}$ (purple), and $[L6]^{2+}$ (black) with corresponding fluorescent lifetimes.

Table 3.3: Fluorescent lifetimes (ns) and χ^2 values of $H_2[L_{bpy}\text{-}R_1]^{2+}$, $H_2[L_{bpy}\text{-}R_2]^{2+}$, $H_4[L_{bpy}\text{-}R_3]^{2+}$, $H_4[L_{phen}\text{-}R_3]^{2+}$, and $[L6]^{2+}$.

Ligand	*Lifetime (ns)*	X^2
$H_2[L_{bpy}\text{-}R_1]^{2+}$	206.6771	1.056222
$H_2[L_{bpy}\text{-}R_2]^{2+}$	218.4886	1.043693
$H_4[L_{bpy}\text{-}R_3]^{2+}$	201.0965	0.9673514
$H_4[L_{phen}\text{-}R_3]^{2+}$	277.4142	1.073174
$[L6]^{2+}$	162.9419	1.004567

3.5 Phosphorescence Quantum Yield of Ru^{II} Polypyridyl Complexes

Phosphorescence quantum yield, also referred to as the emission or luminescence quantum yield, can be defined as the ratio of photons emitted through phosphorescence to those initially absorbed by a complex. This particular photophysical parameter can also be related to the probability of the complex's excited state being deactivated *via* various radiative and non-radiative mechanisms. The calculation of absolute emission quantum yields can be variable and complex, as numerous external factors determine the end result. These variables include the experimental conditions, solution concentrations, solvent polarity and viscosity, concentration of dissolved oxygen in solution, external temperature, excitation wavelength, internal charge transfer rates, as well as radiative and non-radiative decay rates.[82]

Accurate phosphorescence quantum yields can be determined using absolute methods involving complex equations and corrections, due to the extension of emission signals into the near-IR region. Hence, most calculations make use of secondary methods that allow the determination of emission quantum yields by comparing the values of test samples to standard samples recorded in the literature. With that being said, the aforementioned variables should remain consistent throughout all tests and standard sample measurements in order to ensure reliability and accuracy in the final results. The phosphorescence quantum yields (Φ) of $\mathbf{H_2[L_{bpy}\text{-}R_1]^{2+}}$, $\mathbf{H_2[L_{bpy}\text{-}R_2]^{2+}}$, $\mathbf{H_4[L_{bpy}\text{-}R_3]^{2+}}$ and $\mathbf{H_4[L_{phen}\text{-}R_3]^{2+}}$ were calculated with respect to $\mathbf{[L6]^{2+}}$ using Equation 3.5.1, whereby ST and X denote standard and test samples, respectively. The term 'Grad' is derived from the linear slope of the integrated phosphorescence intensity versus absorbance curve, with η being the refractive index of the chosen solvent.

$$\Phi_X = \Phi_{ST} \left(\frac{Grad_X}{Grad_{ST}}\right)\left(\frac{\eta_X^2}{\eta_{ST}^2}\right) \qquad (3.5.1)$$

In this experiment, $[Ru(bpy)_3]^{2+}$ **($\mathbf{[L6]^{2+}}$)** was chosen as the standard sample, as numerous phosphorescence quantum yields for this photoluminescent complex have been previously calculated and reported. As mentioned previously, the intersystem crossing rate of $[Ru(bpy)_3]^{2+}$ is enhanced by the heavy atom effect, leading to highly efficient excited triplet states and detection of room temperature phosphorescence.[85] For this reason, $\mathbf{[L6]^{2+}}$ can be employed as an attractive representative for its derivatives. The range of phosphorescence quantum yields for $[Ru(bpy)_3]^{2+}$ varies greatly, with recorded

values of Φ existing between 0.018 - 0.090. For example, in deaerated solutions of H_2O, the emission quantum yield for $[Ru(bpy)_3]^{2+}$ was reported to be 0.042, using fluorescein in a 0.1 M NaOH solution as the chosen standard (Φ = 0.90).[86,87] This value has often been used as a reference standard for luminescent biological studies [88] In contrast to this, higher quantum yields for $[Ru(bpy)_3]^{2+}$ in deaerated H_2O have been reported, Φ = 0.055[89] and Φ = 0.053[90]. In deaerated acetonitrile solution, the emission quantum yield of $[Ru(bpy)_3]^{2+}$ was initially determined by Tazuke to be 0.086, with lower results obtained by Nakamaru (Φ = 0.059)[88] and Caspar and Meyer (Φ = 0.062)[91], as well as higher values achieved by Nozaki (Φ = 0.090)[92] and Suzuki (Φ = 0.094 and 0.095).[85]

Moreover, because the phosphorescent triplet state of $[Ru(bpy)_3]^{2+}$ is significantly quenched by molecular oxygen, the observed quantum yield values will be considerably lower in aerated solutions. Such measurements carried out in aerated H_2O gave values of Φ = 0.028,[93] while in aerated acetonitrile a quantum yield of Φ = 0.018[85] was obtained. In order to assess the influence of different counter anions on the phosphorescence quantum yield of $[Ru(bpy)_3]^{2+}$, emission of both $[Ru(bpy)_3](PF_6)_2$ and $[Ru(bpy)_3](Cl)_2$ in deaerated H_2O and again in deaerated acetonitrile were previously recorded. The attained emission wavelengths and quantum yields were of high similarity between both complexes, concluding that there was negligible difference in the photophysical properties of $[Ru(bpy)_3]^{2+}$ when complexed with hexafluorophosphate or chloride salts.[85]

The emission quantum yields (Φ) for $\mathbf{H_2[L_{bpy}\text{-}R_1]^{2+}}$, $\mathbf{H_2[L_{bpy}\text{-}R_2]^{2+}}$, $\mathbf{H_4[L_{bpy}\text{-}R_3]^{2+}}$ and $\mathbf{H_4[L_{phen}\text{-}R_3]^{2+}}$ were calculated using a secondary method previously developed by Williams *et al*..[94] $\mathbf{[L6]^{2+}}$ was substituted as the standard sample with a quantum yield of 0.018, as stated in the literature.[85] Taking the same MLCT excitation wavelength of 450 nm for all Ru^{II} polypyridyl complex solutions, the extinction coefficients (ε) were calculated based on the UV-Vis absorption spectra previously obtained in aerated acetonitrile solutions (5 μM). Linearly increasing absorbance values of 0.02, 0.04, 0.06, 0.08 and 0.1 were then chosen and using the previously obtained unique extinction coefficient values, the desired concentrations were subsequently calculated using the Beer-Lambert law. From this, five freshly prepared acetonitrile solutions of increasing concentration were produced for each Ru^{II} polypyridyl complex. UV-Vis absorption spectra, as well as phosphorescence emission spectra, were recorded for all solutions. The integrated phosphorescence intensities were calculated for all emission spectra, and various graphs displaying integrated phosphorescence intensity versus absorbance were

produced. A line of best fit was applied to each curve, and the corresponding slopes were applied to Equation 3.5.1 in order to calculate the quantum yield of each individual ligand with respect to **[L6]$^{2+}$** ($\Phi = 0.018$).

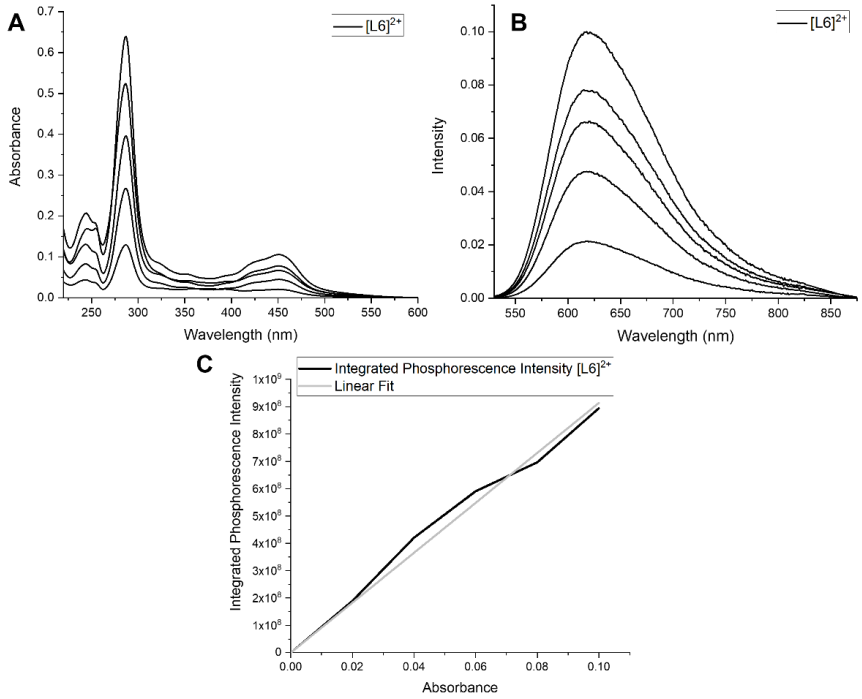

Figure 3.12: Comparative analysis of the UV-Vis absorption spectra (A) and steady state emission spectra (λ_{ex} = 450 nm) (B) of various [L6]$^{2+}$ solutions of increasing concentration, recorded in acetonitrile. Linear correlation between absorbance and integrated phosphorescence intensity, with calculated gradient (Grad$_{ST}$) of [L6]$^{2+}$ (C).

The phosphorescence quantum yields (ΦX) of **H$_2$[L$_{bpy}$-R$_1$]$^{2+}$**, **H$_2$[L$_{bpy}$-R$_2$]$^{2+}$**, **H$_4$[L$_{bpy}$-R$_3$]$^{2+}$** and **H$_4$[L$_{phen}$-R$_3$]$^{2+}$** were recorded with respect to the reference standard **[L6]$^{2+}$** (ΦST = 0.018 in aerated acetonitrile[28]) (Fig. 3.13 – 3.16 (a-c) Table 3.4). All ligands displayed unique quantum yield values based on their specific emission intensities, Stoke shifts, and bis-alkynyl moieties.[95] Quantum yield values of $\Phi = 0.0132$ for **H$_2$[L$_{bpy}$-R$_1$]$^{2+}$**, $\Phi = 0.0142$ for **H$_2$[L$_{bpy}$-R$_2$]$^{2+}$**, $\Phi = 0.013$ for **H$_4$[L$_{bpy}$-R$_3$]$^{2+}$** and $\Phi = 0.0163$ for **H$_4$[L$_{phen}$-R$_3$]$^{2+}$** was calculated. According to the data obtained, the calculated quantum yields were lower than the literature value of $\Phi = 0.018$ for **[L6]$^{2+}$**. A reason for such a decrease can be attributed to the presence of a reactive state of the modified bipyridine moieties within the deactivation pathway of the phosphorescent triplet state of each metallo-ligand.[96]

Table 3.4: Linear gradients and corresponding phosphorescence quantum yields (Φ_X) of $H_2[L_{bpy}\text{-}R_1]^{2+}$, $H_2[L_{bpy}\text{-}R_2]^{2+}$, $H_4[L_{bpy}\text{-}R_3]^{2+}$, and $H_4[L_{phen}\text{-}R_3]^{2+}$ relative to the phosphorescence quantum yield (Φ_{ST}) of $[L6]^{2+}$ obtained from the literature. All phosphorescence quantum yields were obtained using Equation 3.5.1.

Ligand	
$[Ru(bpy)_3]^{2+}$ ($[L6]^{2+}$)	
Linear Gradient	9.4×10^9
Φ_{ST} (Literature)	0.018
$H_2[L_{bpy}\text{-}R_1]^{2+}$	
Linear Gradient	6.68×10^9
Φ_X	0.0132
$H_2[L_{bpy}\text{-}R_2]^{2+}$	
Linear Gradient	7.18×10^9
Φ_X	0.0142
$H_4[L_{bpy}\text{-}R_3]^{2+}$	
Linear Gradient	6.6×10^9
Φ_X	0.013
$H_4[L_{phen}\text{-}R_3]^{2+}$	
Linear Gradient	8.26×10^9
Φ_X	0.0163

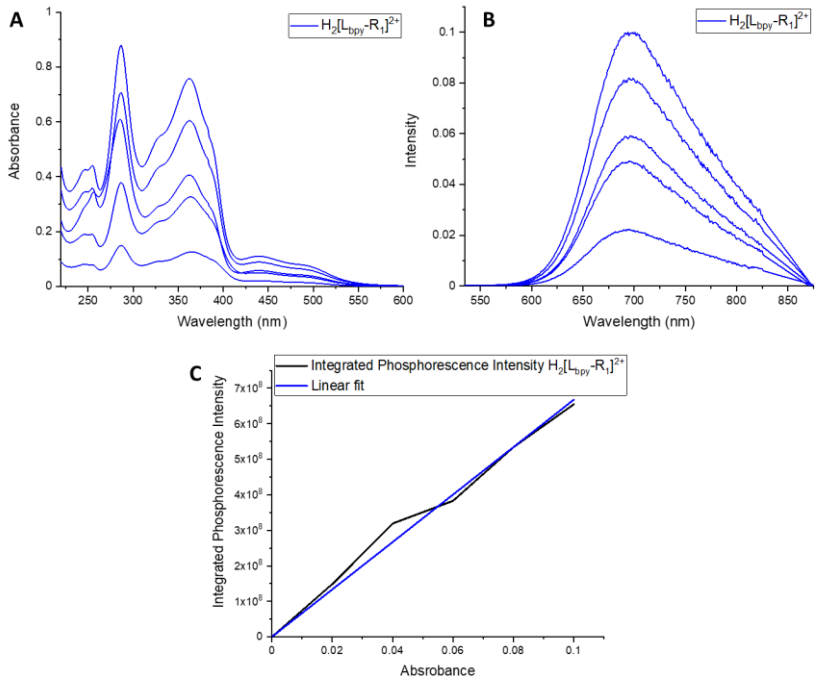

Figure 3.13: Comparative analysis of the UV-Vis absorption spectra (A) and steady state emission spectra (λ_{ex} = 450 nm) (B) of various $H_2[L_{bpy}\text{-}R_1]^{2+}$ solutions of increasing concentration, recorded in acetonitrile. Linear correlation between absorbance and integrated phosphorescence intensity, with calculated Gradient ($Grad_{ST}$) of $H_2[L_{bpy}\text{-}R_1]^{2+}$ (C).

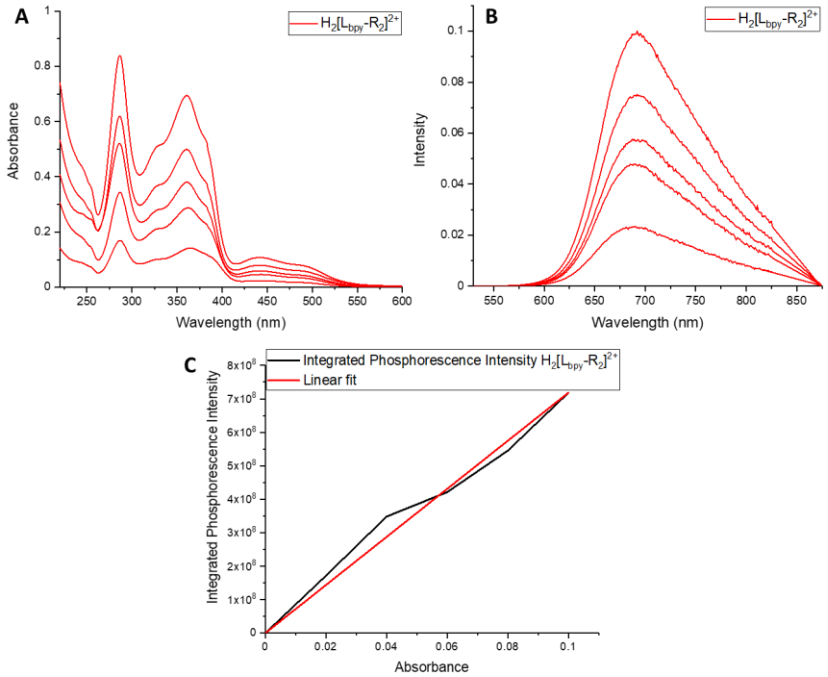

Figure 3.14: Comparative analysis of the UV-Vis absorption spectra (A) and steady state emission spectra (λ_{ex} = 450 nm) (B) of various $H_2[L_{bpy}\text{-}R_2]^{2+}$ solutions of increasing concentration, recorded in acetonitrile. Linear correlation between absorbance and integrated phosphorescence intensity, with calculated Gradient ($Grad_{ST}$) of $H_2[L_{bpy}\text{-}R_2]^{2+}$ (C).

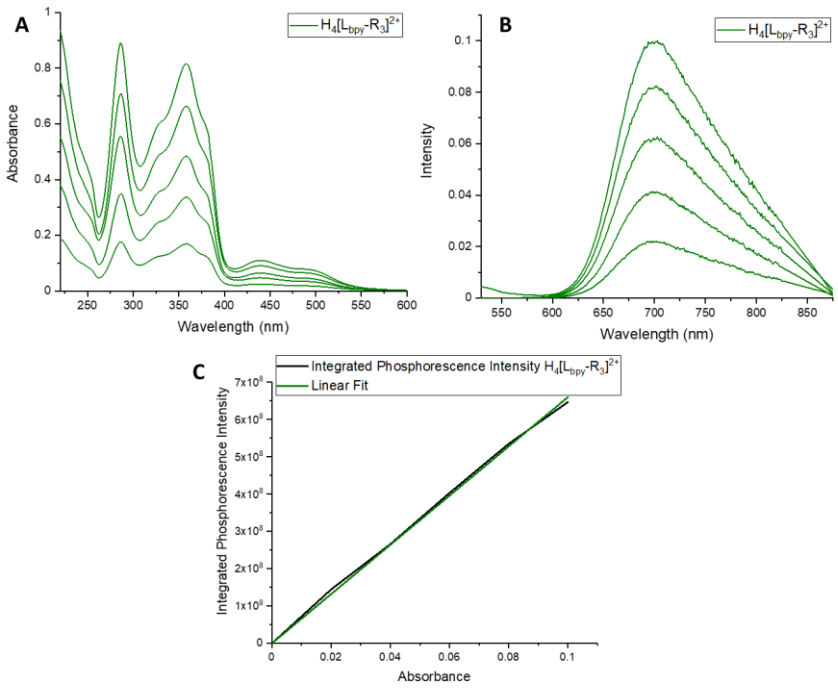

Figure 3.15: Comparative analysis of the UV-Vis absorption spectra (A) and steady state emission spectra (λ_{ex} = 450 nm) (B) of various $H_4[L_{bpy}\text{-}R_3]^{2+}$ solutions of increasing concentration, recorded in acetonitrile. Linear correlation between absorbance and integrated phosphorescence intensity, with calculated Gradient ($Grad_{ST}$) of $H_4[L_{bpy}\text{-}R_3]^{2+}$ (C).

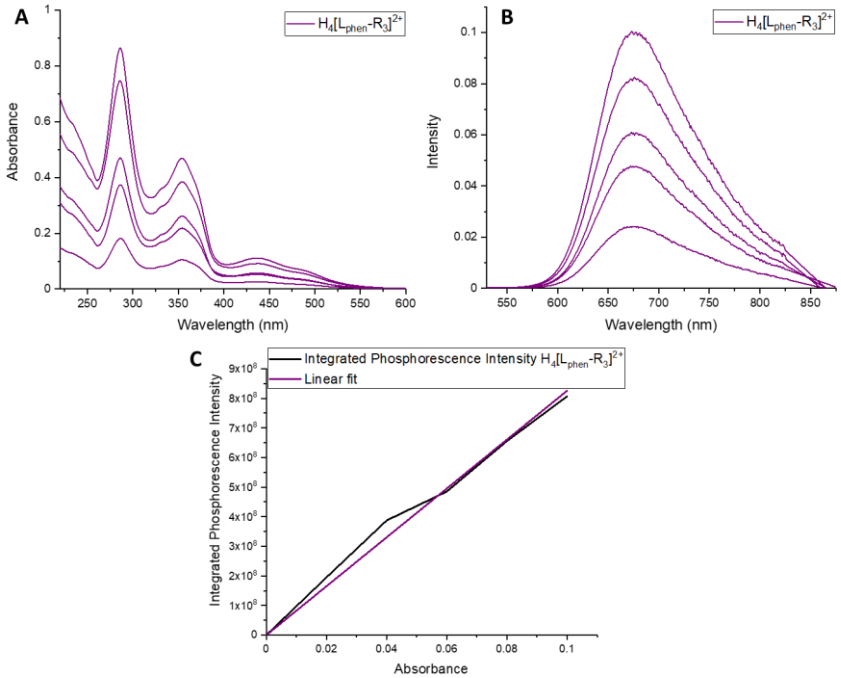

Figure 3.16: Comparative analysis of the UV-Vis absorption spectra (A) and steady state emission spectra (λ_{ex} = 450 nm) (B) of various $H_4[L_{phen}\text{-}R_3]^{2+}$ solutions of increasing concentration, recorded in acetonitrile. Linear correlation between absorbance and integrated phosphorescence intensity, with calculated Gradient ($Grad_{ST}$) of $H_4[L_{phen}\text{-}R_3]^{2+}$ (C).

3.6 Optical Energy Band Gap Estimations of Ru^{II} Polypyridyl Complexes

The optical energy band gap (E_g), the energy difference between the lowest conduction band and the highest valence band, was estimated experimentally from the obtained UV-Vis absorption spectra of all novel metallo-ligands. More accurately, Tauc plots derived from the Tauc and Davis-Mott relation[97–100] (Eq. 3.6.1) were used to probe the optical energy band gaps from the UV-Vis absorption data:

$$(\alpha h\nu)^{\frac{1}{n}} = K(h\nu - E_g) \tag{3.6.1}$$

where α is the absorption coefficient, hν is incident photo energy, K is an energy independent constant and where the value of n denotes the specific probability of an observed transition i.e. the nature of the transition. Values of 0.5, 2, 1.5 and 3 describe allowed direct, allowed indirect, forbidden direct and forbidden indirect optical transitions, respectively.

The Max Plank equation (Eq. 3.6.2) was used to calculate energy from our obtained wavelengths.

$$E_g = h\nu \tag{3.6.2}$$

Where *h* is *planks* constant, and ν is the frequency of the incident photon.

$$\nu = \frac{c}{\lambda} \tag{3.6.3}$$

Where *c* is the speed of light and λ is the wavelength of the incident photon. We further combine the two equations to obtain equation 3.6.4.

$$E_g = \frac{hc}{\lambda} \tag{3.6.4}$$

Using the values of the constants we can solve equation 3.6.4 to obtain the final equation (Eq. 3.6.5).

$$E_g = \frac{1239.3\ eV\ nm}{\lambda} \tag{3.6.5}$$

The absorption coefficient α can be calculated using Beer lambert's law.

Where *I* is the intensity of transmitted light, I_0 is the intensity of incident light, and *L* is the path length of light.

$$I = I_0 e^{-\alpha L} \tag{3.6.6}$$

Modifying equation 3.6.6, we can obtain equation 3.6.7.

$$log\frac{I_0}{I} = \alpha L log(e) \quad (3.6.7)$$

Using the constant value for *e* and having our path length as 1, we can solve equation 3.6.7 to obtain the equation for the absorption coefficient, where A is our absorbance value attained from the spectra (Eq. 3.6.8).

$$\alpha = 2.303\ x\ A\ (cm^{-1}) \quad (3.6.8)$$

Finally, to obtain the Tauc relation, the absorbance coefficient and energy must be combined (Eq. 3.6.9).

$$(\alpha hv)^{\frac{1}{2}} = (2.303\ x\ A\ x\ hv)^{\frac{1}{2}}\ (eV\ cm^{-1}) \quad (3.6.9)$$

Tauc plots displaying $(\alpha h\nu)^{(1/n)}$ versus photon energy ($h\nu$) were tabulated. Indirect optical energy band gaps were obtained from linear extrapolations of various segments of the respective Tauc plots and compared with those from literature.[101] The estimated indirect optical band gap energies are summarised in Table 3.5 below.

The optical band gaps for $\mathbf{H_2[L_{bpy}\text{-}R_1]^{2+}}$, $\mathbf{H_2[L_{bpy}\text{-}R_2]^{2+}}$, $\mathbf{H_4[L_{bpy}\text{-}R_3]^{2+}}$, $\mathbf{H_4[L_{phen}\text{-}R_3]^{2+}}$ and $\mathbf{[L6]^{2+}}$ were calculated in order to assess and confirm their respective photoactivities (Fig. 3.16 and Fig. 3.17). When estimating the indirect optical band gaps for the parent complex, $[Ru(bpy)_3]^{2+}$, $\mathbf{[L6]^{2+}}$, the obtained values were recorded as 2.45 eV and 3.99 eV. These values were in good agreement with those previously recorded by Kumar and co-workers, who calculated energy band gap values of 2.55 eV and 4.05 eV, respectively.[101] Despite this slight deviation in energy, the obtained Tauc Plot for $\mathbf{[L6]^{2+}}$ was highly similar to those obtained by Kumar *et al*.. It has been previously stated that variation can occur from one author to another when estimating optical band gaps for the same semiconductor. The main reasons being the variations in UV-Vis spectra, the type of transition band considered, the corresponding 'n' value, and the linear extrapolation method used.[102] According to Kumar, the MLCT band gap can be assigned at 2.05 eV, confirming the absorption of visible light by $\mathbf{[L6]^{2+}}$ at 450 nm. Additionally, the LC band gap can be correlated to the band gap energy value of 4.05 eV, representing the absorption peak at 287 nm.

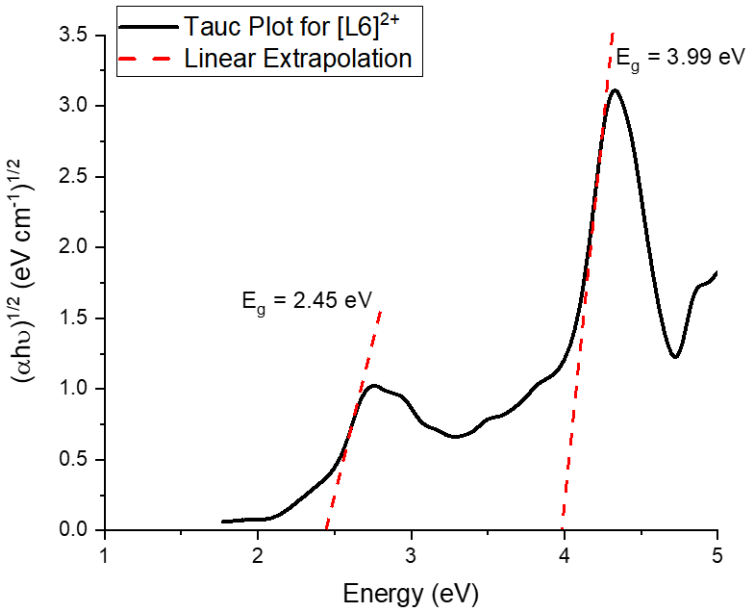

Figure 3.16: Tauc Plot based on the UV-Vis absorption spectrum of $[L6]^{2+}$, indicating the linearly extrapolated MLCT, and LC indirect optical band gap energies.

Table 3.5: Estimated indirect optical band gap energies, E_g (eV), $H_2[L_{bpy}\text{-}R_1]^{2+}$, $H_2[L_{bpy}\text{-}R_2]^{2+}$, $H_4[L_{bpy}\text{-}R_3]^{2+}$, $H_4[L_{phen}\text{-}R_3]^{2+}$ and $[L6]^{2+}$ based on their corresponding UV-Vis absorption spectral data (Table 3.1).

Ligand	*Estimated Indirect Optical Band Gap Energies, Eg (eV)*
$H_2[L_{bpy}\text{-}R_1]^{2+}$	2.12; 2.89; 3.72
$H_2[L_{bpy}\text{-}R_2]^{2+}$	2.10; 2.93; 3.68
$H_4[L_{bpy}\text{-}R_3]^{2+}$	2.15; 2.99; 3.76
$H_4[L_{phen}\text{-}R_3]^{2+}$	2.14; 3.03; 3.59
$[L6]^{2+}$	2.45; 3.99

The band gap energies of the Ru^{II}-derived metallo-ligands $H_2[L_{bpy}\text{-}R_1]^{2+}$, $H_2[L_{bpy}\text{-}R_2]^{2+}$, $H_4[L_{bpy}\text{-}R_3]^{2+}$, and $H_4[L_{phen}\text{-}R_3]^{2+}$ were compared to those of $[L6]^{2+}$, and in all cases, lower indirect optical band gaps were achieved. As mentioned previously, the electron-withdrawing nature of the synthesised novel cross-coupled Ru^{II} polypyridyl complexes can lower the energy of the LUMO (π*) and thus decrease the observed band gap for indirect LC and MLCT transitions.[83,103] Moreover, it can be said that the band gap energies recorded at 2.12, 2.10, 2.15, 2.14 and 2.45 eV for $H_2[L_{bpy}\text{-}R_1]^{2+}$, $H_2[L_{bpy}\text{-}R_2]^{2+}$, $H_4[L_{bpy}\text{-}R_3]^{2+}$, $H_4[L_{phen}\text{-}R_3]^{2+}$ and $[L6]^{2+}$ respectively, were representative of the onset energy gaps. In contrast, the fundamental energy gaps (Soret bands) relating to the inter-ligand π → π* transitions can be observed at 3.72, 3.68, 3.76, 3.59 and 3.99 eV,

respectively.[104,105] Interestingly, the modified ligands presented an additional band gap energy that was absent in the Tauc Plot of the parent complex. This band gap was visible at 2.89, 2.93, 2.99 and 3.03 eV for $\mathbf{H_2[L_{bpy}\text{-}R_1]^{2+}}$, $\mathbf{H_2[L_{bpy}\text{-}R_2]^{2+}}$, $\mathbf{H_4[L_{bpy}\text{-}R_3]^{2+}}$, and $\mathbf{H_4[L_{phen}\text{-}R_3]^{2+}}$ respectively, (Fig 3.17). When considering the obtained UV-Vis absorption spectra, a distinctive increase in intensity was observed for the Ru^{II} polypyridyl complexes $\mathbf{H_2[L_{bpy}\text{-}R_1]^{2+}}$, $\mathbf{H_2[L_{bpy}\text{-}R_2]^{2+}}$, $\mathbf{H_4[L_{bpy}\text{-}R_3]^{2+}}$, and $\mathbf{H_4[L_{phen}\text{-}R_3]^{2+}}$ in comparison to $\mathbf{[L6]^{2+}}$. This increase can be attributed to the additional ligand-centred ($\pi \rightarrow \pi^*$) transitions present which are due to the increased conjugation in the metallo-ligand systems as a result of the bis-alkynyl functionalisation. This transition is attributed to the additional band gap that was not apparent in the Tauc Plot for $[Ru(bpy)_3]^{2+}$.[101] For this reason, a linear extrapolation distinguishing an MC band gap for $\mathbf{[L6]^{2+}}$ could not be achieved.

The fact that the metallo-ligands have lower band gap energies than $\mathbf{[L6]^{2+}}$ implies that the metallo-ligands could be good chromophores in photoactive MOFs as they possess a significant potential to readily absorb photons and undergo conduction. As a result, this could potentially be highly beneficial in MOF solar cells and photo/electro-catalytic applications.

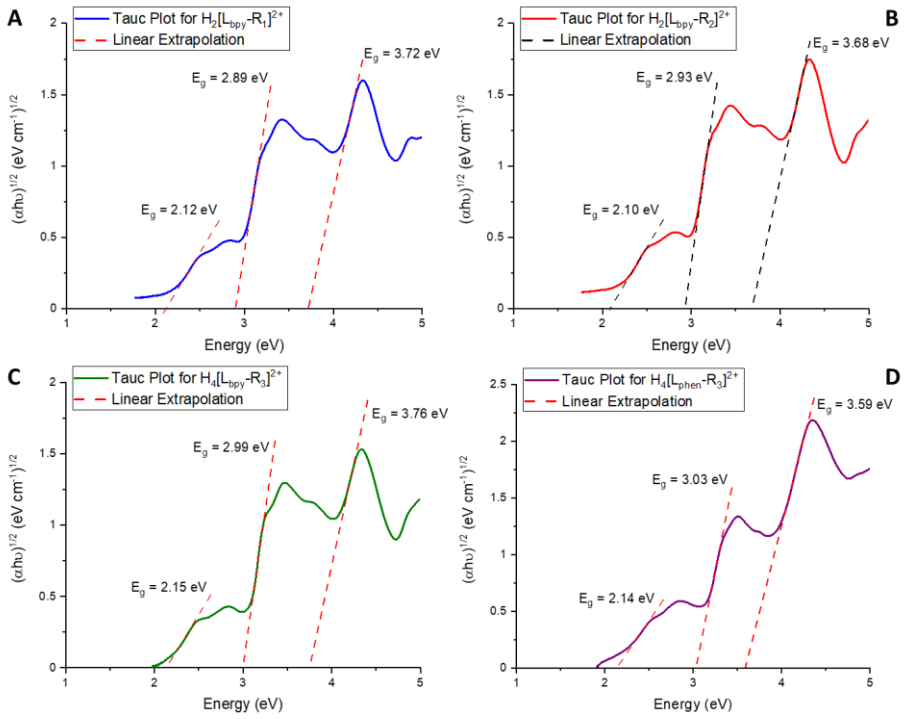

Figure 3.17: Tauc Plot based on the UV-Vis absorption spectrum of $\mathbf{H_2[L_{bpy}\text{-}R_1]^{2+}}$ (A), $\mathbf{H_2[L_{bpy}\text{-}R_2]^{2+}}$ (B), $\mathbf{H_4[L_{bpy}\text{-}R_3]^{2+}}$ (C) and $\mathbf{H_4[L_{phen}\text{-}R_3]^{2+}}$ (D), indicating the linearly extrapolated MLCT, MC and LC indirect optical band gap energies.

3.7 Solution Phase Cyclic Voltammetry of Ru^{II} Polypyridyl Complexes

The electrochemical properties of Ru^{II} polypyridyl complexes have received considerable attention over the years due to their desirable use as electrochromic materials and photo-redox catalysts. Significant of the research carried out has centred around Ru^{III} species and their ability to induce the oxidation of H_2O to O_2 (E_0 (O_2/H_2O) = + 1.23 V vs NHE). Equivalently, Ru^{II} complexes have the ability to reduce H_2O to H_2 (E_0 ($H+/H_2$) = 0.0 V vs NHE).[36] In this investigation, the electrochemical behaviours and reversible redox properties of $[Ru(bpy)_3]^{2+}$ (**[L6]$^{2+}$**), **H$_2$[L$_{bpy}$-R$_1$]$^{2+}$**, **H$_2$[L$_{bpy}$-R$_2$]$^{2+}$**, **H$_4$[L$_{bpy}$-R$_3$]$^{2+}$**, and **H$_4$[L$_{phen}$-R$_3$]$^{2+}$** were probed using solution-phase cyclic voltametric methods. The experiments were carried out under an N_2 flow using a 3-electrode set-up consisting of a glassy carbon working electrode, a platinum wire auxiliary electrode, a saturated calomel electrode (SCE) as the reference electrode and tetrabutylammonium hexafluorophosphate ($(NBu_4)PF_6$) (0.1 M) as the electrolyte. Cyclic voltammetry (CV) at room temperature within a potential range of -1.5 V to 1.9 V (vs SCE) in dry MeCN was initially used as reference data. Redox potentials were calibrated to the ferrocene/ferrocenium redox couple according to the conversion -0.400 V vs Fc/Fc^+.

In relation to the parent complex, **[L6]$^{2+}$** (Fig. 3.19), a quasi-reversible metal-based oxidation process was observed at the anodic potential of 1.00 V, representing the redox couple Ru^{II}/Ru^{III}.[35,106–109] The corresponding Ru^{III}/Ru^{II} reduction process was later observed at 0.91 V.[77] In addition, three sequential ligand-based oxidation waves were observed that correlated to the bipyridine units, at -0.23 V, -0.69 V and -1.15 V respectively.[44] These oxidations were subsequently reduced at -1.30 V, -1.66 V and -1.88 V.[44]

The corresponding cyclic voltammograms for **H$_2$[L$_{bpy}$-R$_1$]$^{2+}$**, **H$_2$[L$_{bpy}$-R$_2$]$^{2+}$**, **H$_4$[L$_{bpy}$-R$_3$]$^{2+}$**, and **H$_4$[L$_{phen}$-R$_3$]$^{2+}$** (Fig. 3.18 and 3.19) appeared to be slightly shifted to more positive potentials with respect to **[L6]$^{2+}$**, in accordance with their corresponding UV-Vis absorption and emission spectra (Fig. 3.3 and 3.7). This observation can be attributed to these ligands' increased electron-withdrawing ability *via* a negative inductive (-I) effect. The addition of a bis-alkynyl aromatic moiety to a bipyridine unit increases the π-acceptor ability of the ligand. With that being said, the modification of one bipyridine unit in each complex does not significantly affect the oxidation potentials in each of the respective voltammograms.

When considering the signals recorded at cathodic potentials, all complexes displayed voltammograms of high similarity. As mentioned above, **[L6]$^{2+}$** displayed three ligand-based one-electron reduction potentials in acetonitrile solvent.[72,110,111] From the obtained electrochemical data, **H$_2$[L$_{bpy}$-R$_1$]$^{2+}$**, **H$_2$[L$_{bpy}$-R$_2$]$^{2+}$**, **H$_4$[L$_{bpy}$-R$_3$]$^{2+}$**, and **H$_4$[L$_{phen}$-R$_3$]$^{2+}$** can be compared to the parent complex **[L6]$^{2+}$**, along with an additional reduction potential accounting for the unique Ru^{II} polypyridyl complex of interest.[112] This signal was present at -1.10 V, -1.09 V, -1.05 V and -1.89 V for **H$_2$[L$_{bpy}$-R$_1$]$^{2+}$**, **H$_2$[L$_{bpy}$-R$_2$]$^{2+}$**, **H$_4$[L$_{bpy}$-R$_3$]$^{2+}$**, and **H$_4$[L$_{phen}$-R$_3$]$^{2+}$** respectively, and varied depending on the nature of the cross-coupled substituent.[107] These signals were subsequently followed by unique oxidation potentials of -1.10 V, -1.12 V, -1.21 V and -1.72 V, respectively.[107] For all solutions, signals observed between -2.00 V and -1.30 V were attributed to the ligand-based one-electron reductions and oxidations of the bipyridine moieties. However, the reduction potentials of the Ru^{II} polypyridyl complexes were shifted to more positive potentials, supporting the assumption that the effective nuclear charge of the Ru^{II} metal centre enhanced the electron-accepting ability of the modified chelates *via* charge interaction.[72,113], **H$_2$[L$_{bpy}$-R$_1$]$^{2+}$**, **H$_2$[L$_{bpy}$-R$_2$]$^{2+}$**, **H$_4$[L$_{bpy}$-R$_3$]$^{2+}$**, and **H$_4$[L$_{phen}$-R$_3$]$^{2+}$** presented significantly weak first or only second and third bipyridine redox signals when compared to the parent complex **[L6]$^{2+}$**, reinstating the electrochemical effects of ligand variation.[114] One can conclude that the improved π-acceptor ability of **H$_2$[L$_{bpy}$-R$_1$]$^{2+}$**, **H$_2$[L$_{bpy}$-R$_2$]$^{2+}$**, **H$_4$[L$_{bpy}$-R$_3$]$^{2+}$**, and **H$_4$[L$_{phen}$-R$_3$]$^{2+}$** allowed for a more facile reduction process when compared to unsubstituted bipyridine.[115,116] Additionally, the stabilised, lower-lying π* orbitals of the cross-coupled ligands allowed for increased mixing with the Ru-based orbitals, thus altering the observed metal-based oxidation potentials.[77,114,117] In essence, the idea behind this observation can be said that complexes with lower energy MLCT states are oxidised more easily, as the MLCT excited state is related to the extent of ligand reduction and metal oxidation.[37] Interestingly, it has been reported by Chaignon that the attachment of a conjugated spacer to the 5'-position of bipyridine decreases the LUMO energy of the ligand more noticeably than couplings at the 4'-position. This can be explained by an increased π-conjugation length upon reacting at the 5'-position of bipyridine, due to a higher spin density of the π* orbital at this position on the ring.[77,118,119] The **H$_4$[L$_{phen}$-R$_3$]$^{2+}$** metallo-ligand displayed a unique signals at -1.89 V and at -1.72 V accounting for the phenanthroline unit of the complex, supporting the argument that bipyridine is more readily reduced compared to phenanthroline.[35]

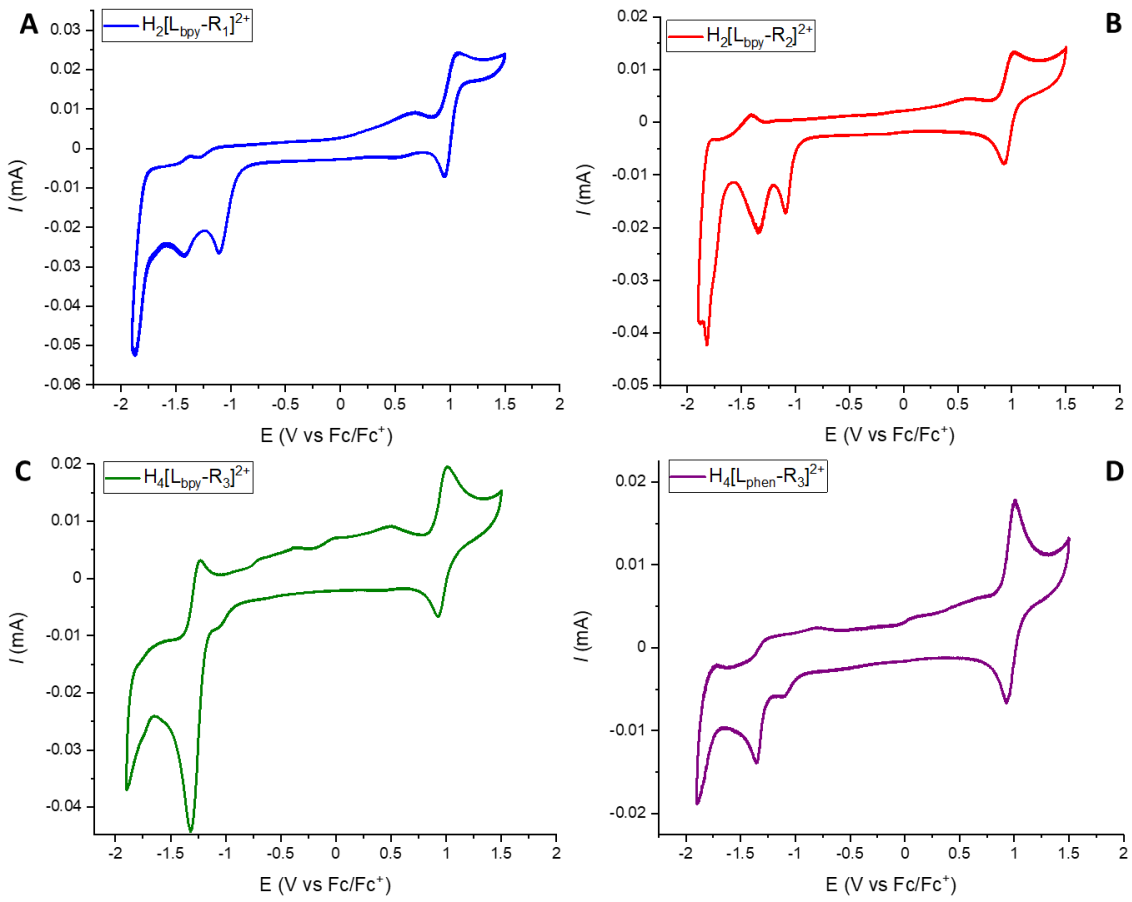

Figure 3.18: CV of a 1 mM solution of $H_2[L_{bpy}\text{-}R_1]^{2+}$ (A), $H_2[L_{bpy}\text{-}R_2]^{2+}$ (B), $H_4[L_{bpy}\text{-}R_3]^{2+}$ (C) and $H_4[L_{phen}\text{-}R_3]^{2+}$ (D), recorded in dry acetonitrile with 0.1 M $(NBu_4)PF_6$ electrolyte, relative to the Fc/Fc^+ redox couple.

Table 3.6: CV Data of 1 mM solutions of $H_2[L_{bpy}\text{-}R_1]^{2+}$, $H_2[L_{bpy}\text{-}R_2]^{2+}$, $H_4[L_{bpy}\text{-}R_3]^{2+}$, $H_4[L_{phen}\text{-}R_3]^{2+}$ and $[L6]^{2+}$, recorded in dry acetonitrile with 0.1 M $(NBu_4)PF_6$ electrolyte. All reported oxidation and reduction potentials were relative to the Fc/Fc^+ redox couple.

Ligand	E_P *(Ru^{III}/Ru^{II}) (V) Red*	E_P *(Ru^{II}/Ru^{III}) (V) Ox*	E_P *(Ru Complexes) (V) Red*	E_P *(Ru Complexes) (V) Ox*	E_P *(bpy/bpy^-) (V) Red*	E_P *(bpy^-/bpy) (V) Ox*
$H_2[L_{bpy}\text{-}R_1]^{2+}$	+0.94	+1.07	-1.10	-1.10	-1.42 -1.69 -1.88	-0.40 -1.34 -1.72
$H_2[L_{bpy}\text{-}R_2]^{2+}$	+0.93	+1.02	-1.09	-1.12	-1.34 -1.82	-1.42 -1.78
$H_4[L_{bpy}\text{-}R_3]^{2+}$	+0.93	+1.00	-1.05	-1.21	-1.32 -1.74 -1.89	-0.67 -0.91 -1.66
$H_4[L_{phen}\text{-}R_3]^{2+}$	+0.93	+1.01	-1.89	-1.72	-1.09 -1.35	-0.81 -1.26
$[L6]^{2+}$	+0.91	+1.00	-	-	-1.30 -1.66 -1.88	-0.23 -0.69 -1.15

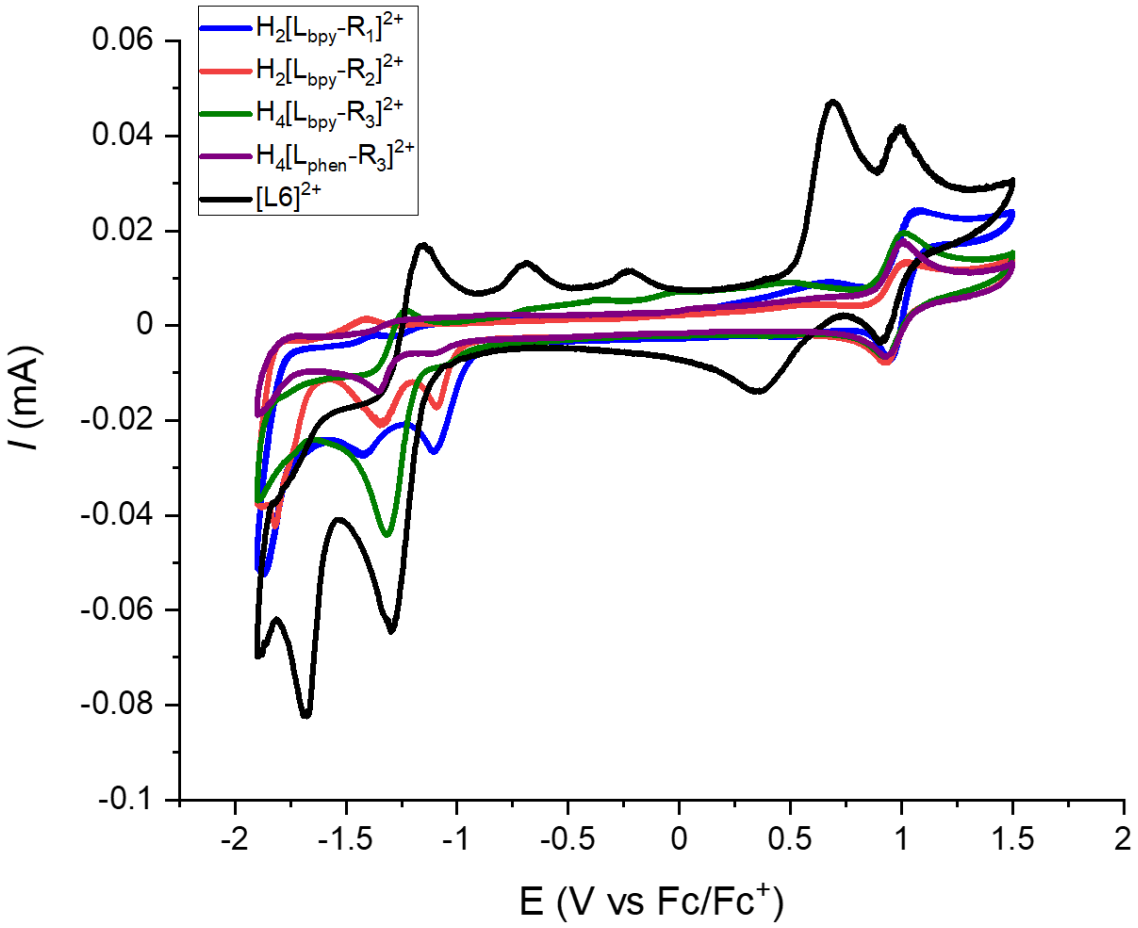

Figure 3.19: Comparative analysis of the CV's of a 1 mM solution of $H_2[L_{bpy}\text{-}R_1]^{2+}$ (blue), $H_2[L_{bpy}\text{-}R_2]^{2+}$ (red), $H_4[L_{bpy}\text{-}R_3]^{2+}$ (green), $H_4[L_{phen}\text{-}R_3]^{2+}$ (purple) and $[L6]^{2+}$ (black), recorded in dry acetonitrile with 0.1 M $(NBu_4)PF_6$ electrolyte, relative to the Fc/Fc^+ redox couple.

3.8 Conclusion and Future Work

In this chapter, the photophysical, photochemical and electrochemical properties of four novel Ru^{II} polypyridyl complexes are described and compared to $[Ru(bpy)_3]^{2+}$. Pure samples of $\mathbf{H_2[L_{bpy}\text{-}R_1]^{2+}}$, $\mathbf{H_2[L_{bpy}\text{-}R_2]^{2+}}$, $\mathbf{H_4[L_{bpy}\text{-}R_3]^{2+}}$, and $\mathbf{H_4[L_{phen}\text{-}R_3]^{2+}}$ were examined using various spectroscopic and characterisation methods; UV-Vis absorption, steady-state emission, solution-phase cyclic voltammetry, and TCSPC methods.

The obtained UV-Vis absorption and steady-state emission spectra demonstrated that the novel Ru^{II} complexes maintained the characteristic properties of $[Ru(bpy)_3]^{2+}$. There was substantial evidence of characteristic Ru^{II} polypyridyl transitions, LC and MLCT. These transitions were slightly red-shifted compared to the core complex $\mathbf{[L6]^{2+}}$, due to the increased conjugation in the ligand system as a result of the bis-alkynyl functionalisation.

Furthermore, the estimation of the optical band gap energies for $\mathbf{H_2[L_{bpy}\text{-}R_1]^{2+}}$, $\mathbf{H_2[L_{bpy}\text{-}R_2]^{2+}}$, $\mathbf{H_4[L_{bpy}\text{-}R_3]^{2+}}$, and $\mathbf{H_4[L_{phen}\text{-}R_3]^{2+}}$ was carried out based on the obtained UV-Vis absorption spectra. Optical band gap energies were calculated for various transitions (MLCT and LC) and demonstrated a reduction in band gap energies in comparison to that of $\mathbf{[L6]^{2+}}$. This reduction highlights the novel metallo-ligands improved ability to absorb photons and undergo conduction in comparison to $\mathbf{[L6]^{2+}}$. As a result, these metallo-ligands could be incorporated into a MOF framework and used as chromophores in various photo/electro-catalytic applications.

The obtained fluorescent lifetimes measured through TCSPC methods of the aforementioned Ru^{II} polypyridyl complexes were comparable to similar complexes analysed in the literature, demonstrating fluorescent lifetime retention post-bis-alkynyl functionalisation. Additionally, the extended lifetimes in comparison to $\mathbf{[L6]^{2+}}$ demonstrate that the metallo-ligands potentially are suitable photoactive ligands in MOF frameworks and would be highly applicable in photocatalytic applications. The determination and calculation of phosphorescence quantum yields suggested that there were significant effects on the photoactive properties of the $[Ru(bpy)_3]^{2+}$ derivatives upon modification of a chelated bipyridine unit. Finally, solution-phase cyclic voltammetry highlighted the retention of the reversible redox nature of $\mathbf{[L6]^{2+}}$ within the cross-coupled ligands $\mathbf{H_2[L_{bpy}\text{-}R_1]^{2+}}$, $\mathbf{H_2[L_{bpy}\text{-}R_2]^{2+}}$, $\mathbf{H_4[L_{bpy}\text{-}R_3]^{2+}}$, and $\mathbf{H_4[L_{phen}\text{-}R_3]^{2+}}$.

Future work would involve photophysical and photochemical characterisation of other bis-alkynyl functionalised Ru^{II} polypyridyl complexes and comparison with the core

complex **[L6]$^{2+}$**. Similarly, improvement of the fluorescent lifetimes and investigation into the influence of various factors such as solvent and temperature. Additionally, a future investigation on improving the quantum yields of the metallo-ligands and an examination into the factors which influence the quantum yields could be carried out.

3.9 References

1 M. C. So, G. P. Wiederrecht, J. E. Mondloch, J. T. Hupp and O. K. Farha, *Chem. Commun.*, 2015, **51**, 3501–3510.

2 T. Bach and J. P. Hehn, *Angew. Chem. Int. Ed.*, 2011, **50**, 1000–1045.

3 D. Gust, T. A. Moore and A. L. Moore, *Acc. Chem. Res.*, 2001, **34**, 40–48.

4 N. Hoffmann, *Chem. Rev.*, 2008, **108**, 1052–1103.

5 A. Juris, V. Balzani, F. Barigelletti, S. Campagna, P. Belser and A. von Zelewsky, *Coord. Chem. Rev.*, 1988, **84**, 85–277.

6 D. M. Schultz and T. P. Yoon, *Science*, 2014, **343**, 6174.

7 T. Zhang and W. Lin, *Chem. Soc. Rev.*, 2014, **43**, 5982–5993.

8 I. Choi, S. Yoon, S. Huh, S. Kim and Y. Kim, *Chem. – A Eur. J.*, 2020, **26**, 14580–14584.

9 T. P. Yoon, M. A. Ischay and J. Du, *Nat. Chem.*, 2010, **2**, 527–532.

10 K. Teegardin, J. I. Day, J. Chan and J. Weaver, *Org. Process Res. Dev.*, 2016, **20**, 1156–1163.

11 T. J. Meyer, *Acc. Chem. Res.*, 1989, **22**, 163–170.

12 L. Wang, L. Duan, Y. Wang, M. S. G. Ahlquist and L. Sun, *Chem. Commun.*, 2014, **50**, 12947–12950.

13 C. K. Prier, D. A. Rankic and D. W. C. MacMillan, *Chem. Rev.*, 2013, **113**, 5322–5363.

14 L. Duan, F. Bozoglian, S. Mandal, B. Stewart, T. Privalov, A. Llobet and L. Sun, *Nat. Chem.*, 2012, **4**, 418–423.

15 C. S. Diercks, Y. Liu, K. E. Cordova and O. M. Yaghi, *Nat. Mater.*, 2018, **17**, 301–307.

16 A. Dhakshinamoorthy, A. M. Asiri and H. García, *Angew. Chem. Int. Ed.*, 2016, **55**, 5414–5445.

17 J. Hao, X. Xu, H. Fei, L. Li and B. Yan, *Adv. Mater.*, 2018, **30**, 1705634.

18 E. Bae, W. Choi, J. Park, H. S. Shin, S. Bin Kim and J. S. Lee, *J. Phys. Chem. B*, 2004, **108**, 14093–14101.

19 K. Manna, T. Zhang, F. X. Greene and W. Lin, *J. Am. Chem. Soc.*, 2015, **137**, 2665–2673.

20 J. Park, D. Feng, S. Yuan and H. Zhou, *Angew. Chemie*, 2015, **127**, 440–445.

21 V. Lykourinou, Y. Chen, X. Wang, L. Meng, T. Hoang, L. Ming, R. L. Musselman and S. Ma, *J. Am. Chem. Soc.*, 2011, **133**, 10382–10385.

22 S. Lin, Y. Pineda-Galvan, W. A. Maza, C. C. Epley, J. Zhu, M. C. Kessinger, Y. Pushkar and A. J. Morris, *ChemSusChem.*, 2017, **10**, 514–522.

23 T.-Z. Xie, S.-Y. Liao, K. Guo, X. Lu, X. Dong, M. Huang, C. N. Moorefield, S. Z. D. Cheng, X. Liu, C. Wesdemiotis and G. R. Newkome, *J. Am. Chem. Soc.*, 2014, **136**, 8165–8168.

24 T. Toyao, M. Saito, S. Dohshi, K. Mochizuki, M. Iwata, H. Higashimura, Y. Horiuchi and M. Matsuoka, *Chem. Commun.*, 2014, **50**, 6779.

25 S. Campagna, F. Puntoriero, F. Nastasi, G. Bergamini and V. Balzani, in *Photochemistry and Photophysics of Coordination Compounds I*, Springer Berlin Heidelberg, Berlin, Heidelberg, 2007, vol. 280, pp. 117–214.

26 A. Duchovnay, *J. Am. Chem. Soc.*, 2011, **2**, 253–257.

27 F. E. Lytle and D. M. Hercules, *J. Am. Chem. Soc.*, 1969, **91**, 253–257.

28 A. Yoshimura, M. Z. Hoffman and H. Sun, *J. Photochem. Photobiol. A Chem.*, 1993, **70**, 29–33.

29 K. Kalyanasundaram, M. K. Nazeeruddin, M. Grätzel, G. Viscardi, P. Savarino and E. Barni, *Inorganica Chim. Acta*, 1992, **198**–**200**, 831–839.

30 K. Kalyanasundaram, G. Viscardi, K. Nazeeruddin and M. Gr, *Inorganica Chim. Acta*, 1992, **200**, 831–839.

31 N. H. Damrauer, G. Cerullo, A. Yeh, T. R. Boussie, C. V. Shank and J. K. McCusker, *Science*, 1997, **275**, 54–57.

32 S. Xu, J. E. T. Smith and J. M. Weber, *J. Chem. Phys.*, 2016, **145**, 024304.

33 P. Innocenzi, H. Kozuka and T. Yoko, *J. Phys. Chem. B*, 1997, **101**, 2285–2291.

34 P. Müller and K. Brettel, *Photochem. Photobiol. Sci.*, 2012, **11**, 632.

35 Z. Ji, S. D. Huang and A. R. Guadalupe, *Inorg. Chim. Acta*, 2000, **305**, 127–134.

36 K. Kalyanasundaram, *Coord. Chem. Rev.*, 1982, **46**, 159–244.

37 P. A. Mabrouk and M. S. Wrighton, *Inorg. Chem.*, 1986, **25**, 526–531.

38 P. Wintergerst, K. Witas, D. Nauroozi, M. Schmid, E. Dikmen, S. Tschierlei and S. Rau, *Journal of Inorganic and General Chemistry*, 2020, **646**, 842–848.

39 S. Fraysse, C. Coudret and J.-P. Launay, *J. Am. Chem. Soc.*, 2003, **125**, 5880–5888.

40 S. Klein, W. G. Dougherty, W. S. Kassel, T. J. Dudley and J. J. Paul, *Inorg. Chem.*, 2011, **50**, 2754–2763.

41 A. Garoufis, A. Koutsodimou, N. Katsaros, C.-A. Mitsopoulou and N. Hadjiliadis, *Polyhedron*, 1998, **18**, 361–369.

42 C.-A. Wang, Y.-F. Han, K. Nie and Y.-W. Li, *Mater. Chem. Front.*, 2019, **3**, 1909–1917.

43 N. Yoshikawa, H. Kimura, S. Yamabe, N. Kanehisa, T. Inoue and H. Takashima, *J. Mol. Struct.*, 2016, **1117**, 49–56.

44 M. Shiotsuka, Y. Tsuji, K. Keyaki and K. Nozaki, *Inorg. Chem.*, 2010, **49**, 4186-4193.

45 E. M. Kober, J. L. Marshall, W. J. Dressick, B. P. Sullivan, J. V. Caspar and T. J. Meyer, *Inorg. Chem.*, 1985, **24**, 2755–2763.

46 R. H. Fabian, D. M. Klassen and R. W. Sonntag, *Inorg. Chem.*, 1980, **19**, 1977–1982.

47 L. Sacksteder, M. Lee, J. N. Demas and B. A. DeGraff, *J. Am. Chem. Soc.*, 1993, **115**, 8230–8238.

48 J. N. Demas, E. W. Harris and R. P. McBride, *J. Am. Chem. Soc.*, 1977, **99**, 3547–3551.

49 M. Seiler, H. Dürr, I. Willner, E. Joselevich, A. Doron and J. F. Stoddart, *J. Am. Chem. Soc.*, 1994, **116**, 3399–3404.

50 E. Terpetschnig, H. Szmacinski, H. Malak and J. R. Lakowicz, *Biophys. J.*, 1995, **68**, 342–350.

51 J. N. Demas and B. A. DeGraff, *J. Chem. Educ.*, 1997, **74**, 690–695.

52 Y. Li, H. Qi, Q. Gao and C. Zhang, *Biosens. Bioelectron.*, 2011, **26**, 2733–2736.

53 A. E. Friedman, J. C. Chambron, J. P. Sauvage, N. J. Turro and J. K. Barton, *J. Am. Chem. Soc.*, 1990, **112**, 4960–4962.

54 H. Song, J. T. Kaiser and J. K. Barton, *Nat. Chem.*, 2012, **4**, 615–620.

55 L. Le Quang, *TiO2/[Ru(bpy)3]2+ based hybrid nanomaterials associated with [Cr(ttpy)2]3+ or [Mn(ttpy)(CO)3Br] or pyrrole moiety: Synthesis, spectroscopic studies and applications in solar energy conversion*., Inorganic chemistry, Université Grenoble Alpes, 2017.

56 A. C. Bhasikuttan, M. Suzuki, S. Nakashima and T. Okada, *J. Am. Chem. Soc.*, 2002, **124**, 8398–8405.

57 A. Schramm, C. Stroh, K. Dössel, M. Lukas, O. Fuhr, H. V. Löhneysen and M. Mayor, *Chem. Commun.*, 2013, **49**, 1076–1078.

58 S. I. Khan, A. E. Beilstein, G. D. Smith, M. Sykora and M. W. Grinstaff, *Inorg. Chem.*, 1999, **38**, 2411–2415.

59 E. L. Sciuto, M. F. Santangelo, G. Villaggio, F. Sinatra, C. Bongiorno, G. Nicotra and S. Libertino, *Sens. Bio-Sensing Res.*, 2015, **6**, 67–71.

60 M. Vonlanthen, A. Cevallos-Vallejo, E. Aguilar-Ortíz, A. Ruiu, P. Porcu and E. Rivera, *Polymer (Guildf).*, 2016, **99**, 13–20.

61 V. Balzani, *Tetrahedron*, 1992, **48**, 10443–10514.

62 J. P. Paris and W. W. Brandt, *J. Am. Chem. Soc.*, 1959, **81**, 5001–5002.

63 H. . Schläfer, H. Gausmann and H. Witzke, *J. Mol. Spectrosc.*, 1966, **21**, 125–129.

64 G. A. Crosby, W. G. Perkins and D. M. Klassen, *J. Chem. Phys.*, 1965, **43**, 1498–1503.

65 D. M. Klassen and G. A. Crosby, *J. Chem. Phys.*, 1968, **48**, 1853–1858.

66 D. M. Klassen and G. A. Crosby, *Chem. Phys. Lett.*, 1967, **1**, 127–128.

67 G. A. Crosby and J. N. Demas, *J. Am. Chem. Soc.*, 1970, **92**, 7262–7270.

68 R. W. Harrigan and G. A. Crosby, *J. Chem. Phys.*, 1973, **59**, 3468–3476.

69 G. D. Hager and G. A. Crosby, *J. Am. Chem. Soc.*, 1975, **97**, 7031–7037.

70 N. Yoshikawa, S. Yamabe, S. Sakaki, N. Kanehisa, T. Inoue and H. Takashima, *J. Mol. Struct.*, 2015, **1094**, 98–108.

71 F. Felix, J. Ferguson, H. U. Guedel and A. Ludi, *J. Am. Chem. Soc.*, 1980, **102**, 4096–4102.

72 Y. Sun, Z. M. Hudson, Y. Rao and S. Wang, *Inorg. Chem.*, 2011, **50**, 3373–3378.

73 A. T. Yeh, C. V. Shank and J. K. McCusker, *Science.*, 2000, **289**, 935–938.

74 N. H. Damrauer, T. R. Boussie, M. Devenney and J. K. McCusker, *J. Am. Chem. Soc.*, 1997, **119**, 8253–8268.

75 E. M. Kober, B. P. Sullivan and T. J. Meyer, *Inorg. Chem.*, 1984, **23**, 2098–2104.

76 R. Horvath, J. Lombard, J.-C. Leprêtre, M.-N. Collomb, A. Deronzier, J. Chauvin and K. C. Gordon, *Dalt. Trans.*, 2013, **42**, 16527.

77 F. Chaignon, F. Buchet, E. Blart, M. Falkenström, L. Hammarström and F. Odobel, *New J. Chem.*, 2009, **33**, 408–416.

78 F. Chaignon, J. Torroba, E. Blart, M. Borgström, L. Hammarström and F. Odobel, *New J. Chem.*, 2005, **29**, 1272.

79 J. R. Deye, A. N. Shiveley, S. M. Goins, L. Rizzo, S. A. Oehrle and K. A. Walters, *Inorg. Chem.*, 2008, **47**, 23–25.

80 D. P. Rillema, G. Allen, T. J. Meyer and D. Conrad, *Inorg. Chem.*, 1983, **22**, 1617–1622.

81 R. Victoria, *Development of luminescent ruthenium complexes for in-vitro fluorescence imaging of angiogenesis with the RGD peptide*, University of Central Florida, 2012.

82 J. R. Lakowicz, in *Principles of Fluorescence Spectroscopy*, Springer US, Boston, MA, 2006, pp. 205–235.

83 S. Biswas, S. S. Panja and S. Bose, *Nanoscale Adv.*, 2020, **2**, 4464–4472.

84 P. L. Higgs, A. W. McKinley and E. M. Tuite, *Chem. Commun.*, 2016, **52**, 1883–1886.

85 K. Suzuki, A. Kobayashi, S. Kaneko, K. Takehira, T. Yoshihara, H. Ishida, Y. Shiina, S. Oishi and S. Tobita, *Phys. Chem. Chem. Phys.*, 2009, **11**, 9850–9860.

86 J. Van Houten and R. J. Watts, *J. Am. Chem. Soc.*, 1976, **98**, 4853–4858.

87 J. Van Houten and R. J. Watts, *J. Am. Chem. Soc.*, 1975, **97**, 3843–3844.

88 K. Nakamaru, *Bull. Chem. Soc. Jpn.*, 1982, **55**, 1639–1640.

89 A. Harriman, *J. Chem. Soc., Chem. Commun.*, 1977, 777–778.

90 S. Tazuke, H.-B. Kim and N. Kitamura, in *Photochemistry and Photophysics of Coordination Compounds*, Springer Berlin Heidelberg, Berlin, Heidelberg, 1987, vol. 27, pp. 113–118.

91 J. V. Caspar and T. J. Meyer, *J. Am. Chem. Soc.*, 1983, **105**, 5583–5590.

92 Z. Abedin-Siddique, T. Ohno, K. Nozaki and T. Tsubomura, *Inorg. Chem.*, 2004, **43**, 663–673.

93 K. Nakamaru, *Bull. Chem. Soc. Jpn.*, 1982, 55, 2697–2705.

94 A. T. Rhys Williams, S. A. Winfield and J. N. Miller, *Analyst*, 1983, **108**, 1067–1071.

95 A. Byrne, *The application of Ru (II) polypyridyl complexes to cellular imaging and sensing*, Dublin City University, 2016.

96 R. T. F. Jukes, V. Adamo, F. Hartl, P. Belser and L. De Cola, *Inorg. Chem.*, 2004, **43**, 2779–2792.

97 P. Makuła, M. Pacia and W. Macyk, *J. Phys. Chem. Lett.*, 2018, **9**, 6814–6817.

98 J. Tauc, R. Grigorovici and A. Vancu, *Phys. status solidi*, 1966, **15**, 627–637.

99 E. A. Davis and N. F. Mott, *Philos. Mag.*, 1970, **22**, 0903–0922.

100 N. F. Mott and E. A. Davis, *Electronic processes in non-crystalline materials*, Oxford University, 2012.

101 P. Kumar, C. Joshi, N. Labhsetwar, R. Boukherroub and S. L. Jain, *Nanoscale*, 2015, **7**, 15258–15267.

102 R. López and R. Gómez, *J. Sol-Gel Sci. Technol.*, 2012, **61**, 1–7.

103 K. Ocakoglu, S. Okur, H. Aydin and F. M. Emen, *Thin Solid Films*, 2016, **612**, 225–230.

104 F. S. Bahabri and A. A. A. L. Ghamdi, *Egypt. J. Sol.*, 2002, **25**, 307–321.

105 M. Wojdyła, B. Derkowska, W. Bała, A. Bratkowski and A. Korcala, *Opt. Mater. (Amst).*, 2006, **28**, 1000–1005.

106 D. Lawrence, V. G. Vaidyanathan and B. U. Nair, *J. Inorg. Biochem.*, 2006, **100**, 1244–1251.

107 V. Goudy, J. Maynadié, X. Le Goff, D. Meyer and M. Fontecave, *New J. Chem.*, 2016, **40**, 1704–1714.

108 D. P. Rillema and K. B. Mack, *Inorg. Chem.*, 1982, **21**, 3849–3854.

109 T. McCormac, B. Fabre and G. Bidan, *J. Electroanal. Chem.*, 1997, **427**, 155–159.

110 N. Fay, E. Dempsey, A. Kennedy and T. McCormac, *J. Electroanal. Chem.*, 2003, **556**, 63–74.

111 J. Hankache and O. S. Wenger, *Chem. Commun.*, 2011, **47**, 10145.

112 H. Xia, Y. Zhu, D. Lu, M. Li, C. Zhang, B. Yang and Y. Ma, *J. Phys. Chem. B*, 2006, **110**, 18718–18723.

113 R. W. Callahan, G. M. Brown and T. J. Meyer, *Inorg. Chem.*, 1975, **14**, 1443–1453.

114 S. Hohloch, D. Schweinfurth, M. G. Sommer, F. Weisser, N. Deibel, F. Ehret and B. Sarkar, *Dalt. Trans.*, 2014, **43**, 4437–4450.

115 S. Munery, J. Jaud and J. Bonvoisin, *Inorg. Chem. Commun.*, 2008, **11**, 975–977.

116 S. Yoon, P. Kukura, C. M. Stuart and R. A. Mathies, *Mol. Phys.*, 2006, **104**, 1275–

1282.

117 H. Rensmo, S. Lunell and H. Siegbahn, *J. Photochem. Photobiol. A Chem.*, 1998, **114**, 117–124.

118 K. C. Zheng, J. P. Wang, W. L. Peng, X. W. Liu and F. C. Yun, *J. Mol. Struct.*, 2002, **582**, 1–9.

119 H. Zabri, I. Gillaizeau, C. A. Bignozzi, S. Caramori, M. Charlot, J. Cano-Boquera and F. Odobel, *Inorg. Chem.*, 2003, **42**, 6655–6666.

Chapter 4

Synthesis of Hetero-Metallic Ru^{II}-Based Photoactive MOFs

4. Synthesis of Hetero-Metallic Ru^{II}-Based Photoactive MOFs

4.1 Introduction

MOFs can be described as crystalline polymerous arrangements in which individual metal ions or coordination clusters are linked through organic ligands in multiple dimensions.[1–5] Owing to their modular, reticular design principles and their amenability to chemical functionalisation,[6] MOFs provide promising platforms for the development of advanced functional materials.[7–11] Focus areas of research include energy storage and energy conversion systems exploiting their porosity, surface areas, high diffusion coefficients and high density of active sites which may not be attainable by molecular species in condensed phases.[12–15] Such unique chemical and physical properties can also be tuned *via* multiple experimental methods, such as modifying the secondary building units (SBUs). This allows the use of MOFs and more particularly photoactive 3rd generation MOFs for synthetic platforms to advanced materials or devices for sensing or light-emitting technologies, artificial photosynthesis, photocatalysis.[16–20] drug delivery,[21] gas adsorption/storage[22] and food preservation.[23]

The modular design principles of MOFs allow for molecular construction of photoanodes for *direct* 'solar-to-fuel' H_2 technologies and H_2O oxidation, operating under benign conditions at high electron transfer rates, whereby organic ligand residues and organic solvent/water mixtures can replicate the natural dielectric, indeed, hydrophobic lipid environment of photosystem-II.[24] This *direct* and molecular approach is distinctive from currently applied *indirect* industrial electrolysis processes that proceed in strongly acidic or basic solutions and require external photovoltaic cells that are not stable in such highly corrosive media.[25] Furthermore, the photoactivity of MOFs can be tailored by integrating photosensitisers as organic ligands, metal node active sites, framework decorations or encapsulated guests. The infinite scope of potential photosensitising materials allows researchers to design MOFs that operate within a specific spectrum of light. As mentioned previously, the well-defined crystallinity of MOFs allows for an accessible insight into complex energy transfer pathways that accompany many photocatalytic processes. The quantum efficiencies of the systems, *e.g.* in photo-electrochemical cells or in photocatalysis (H_2 or O_2 evolution; CO_2 reduction) depend on suitable excited state lifetimes and electron- and energy-transfer processes.[26] In addition, the structured

porosity of photoactive MOFs can accelerate the diffusion of substrates and products, and their reproducibility as catalysts allows for reduced waste and extended lifetimes.[27]

The successful development of ruthenium-based MOFs and their photoactive applications have instigated a wide array of promising research. Many Ru^{II}-based ligands, such as $[Ru(bpy)_3]^{2+}$, have been synthesised and incorporated into MOFs as photosensitisers in order to enhance their innate photocatalytic activity due to their previously discussed advantageous optical properties and reversible redox potentials.[28] Furthermore, the Ru^{II} polypyridyl coordination environment, when incorporated into a framework is preserved by using pyridyl-carboxylate ligands. At the same time, the bimetallic MOF is constructed using another metal centre as the structure-directing unit when bound by carboxylate groups.[29,30]

In this chapter, three highly augmented MOFs (**Ni-MOF**, **Co-MOF** and **Zn-MOF**) that are composed of acetylene-extended, light-harvesting Ru^{II}-bipyridyl metallo-ligands (**$H_4[L_{bpy}\text{-}R_3]^{2+}$**) and 12-connected cubohemioctahedral cages forming face-centred cubic networks, are reported. Furthermore, their syntheses, crystal structures, physicochemical and photophysical properties are investigated. Electrochemical *in-situ* deposition on conductive substrates of the novel synthesised photoactive MOFs are also demonstrated and further examined. Finally, to determine the applicability of the novel systems, **Ni-MOF/FTO** and **Co-MOF/FTO** electrodes were applied as photoanodes in preliminary photoelectrochemical H_2O oxidation studies in organic media.

4.2 Synthesis of Ni-MOF ($Ni_6(L_{bpy}\text{-}R_3)_{12}(H_2O)_{12}$)

The photoactive **Ni-MOF** forms reproducibly under solvothermal conditions in anhydrous DMF during the reaction between $\mathbf{H_4[L_{bpy}\text{-}R_3]^{2+}}$ and $Ni(NO_3)_2{\cdot}6H_2O$ at a mole ratio of 1:8. The reactant mixture was sonicated at room temperature for 10 minutes, during which both reactants dissolved resulting in a homogenous deep, red solution. On heating at 85 °C for 48 hours, red octahedral-shaped crystals of **Ni-MOF**, $[Ni(\mathbf{L_{bpy}\text{-}R_3})(H_2O)_2]$, suitable for single-crystal X-ray diffraction studies were obtained in high yields (Fig 4.1).

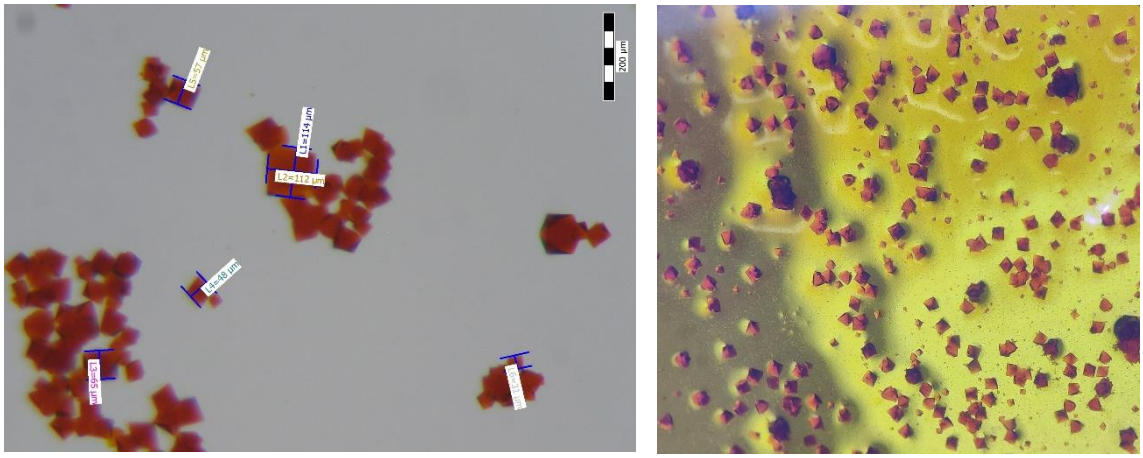

Figure 4.1: Optical microscope images of synthesised crystals of Ni-MOF after 48 hours.

4.3 Structural Characterisation of Ni-MOF

Single-crystal X-ray diffraction studies demonstrate that **Ni-MOF** crystallises in the cubic space group $Fm\bar{3}m$ (Fig 4.2). The framework structure consists of cubohemioctahedral $\{Ni_6(\mathbf{L_{bpy}\text{-}R_3})_{12}(H_2O)_{12}\}$ coordination cages in which six individual metal centres adopt the vertices of an octahedron; isophthalate moieties that derive from 12 $\mathbf{L_{bpy}\text{-}R_3^{2-}}$ metallo-ligands cap the edges of the polyhedron, each connecting two metal ions in a *syn*-η^1 binding mode. The individual Ni^{II} centres in **Ni-MOF** adopt tetragonally distorted octahedral coordination environments whereby four symmetry equivalent O-donors of four $\mathbf{L_{bpy}\text{-}R_3^{2-}}$ ligands are complemented by two coordinated water molecules that occupy the *trans*-located apical positions pointing radial to the inside or the outside of the cage. This coordination environment is further stabilised by H-bonds between these coordinating H_2O ligands and the carboxylate O-donors of the $\mathbf{L_{bpy}\text{-}R_3^{2-}}$ ligands (Fig. 4.3). Furthermore, it is believed that these water molecules are labile and therefore can

disassociate from the metal centre, providing cavities rich in coordinatively-unsaturated metal sites where photocatalysis can be achieved. The supramolecular cage has been found to consist of an internal diameter (Ni^{II} – Ni^{II}) of 11.22 Å. Table 4.1 lists the detailed bond angles and lengths for the metal centres for the **Ni-MOF.** Complete crystallographic data and structure refinements are provided in Table 4.2.

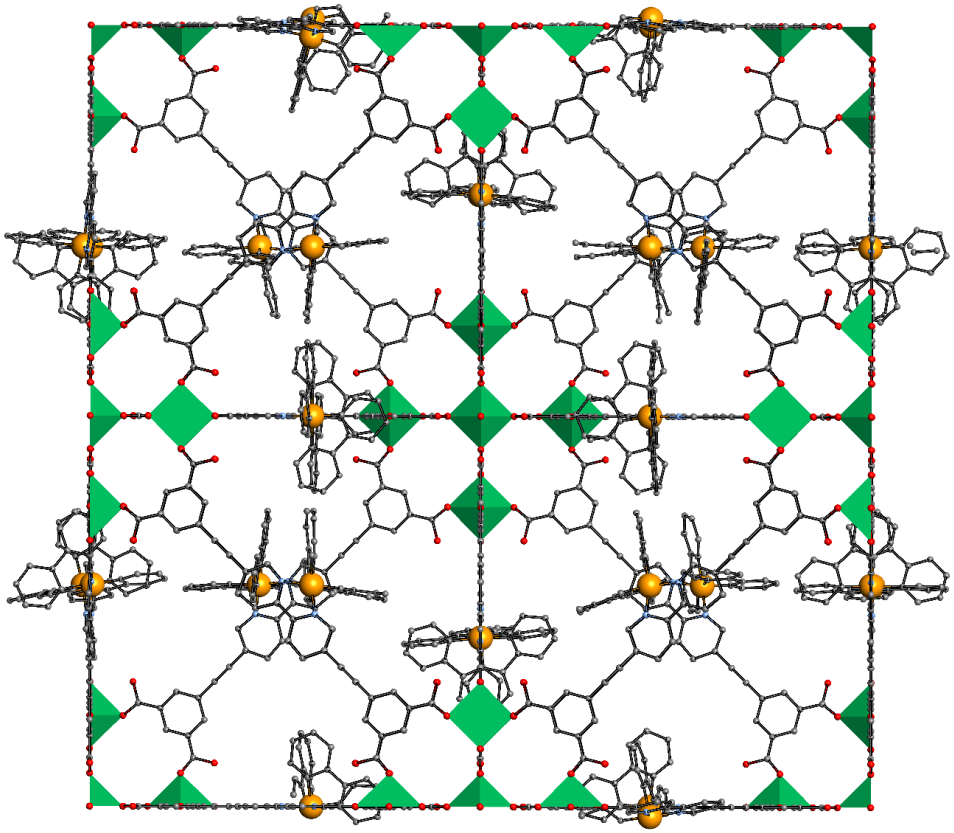

Figure 4.2: Structure of Ni-MOF with a view in the direction of the crystallographic *c*-axis. Colour scheme: Ru (orange), Ni (green), O (red), and C (grey). H atoms were omitted for clarity.

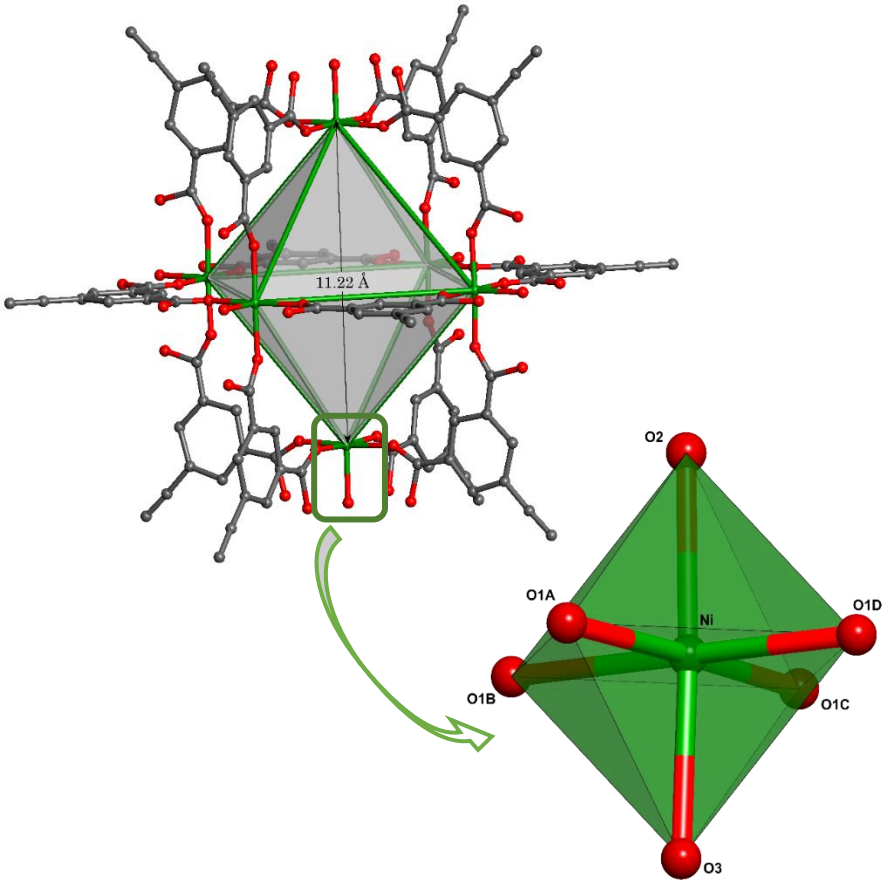

Figure 4.3: Octahedral coordination environment for Ni^{II} in Ni-MOF (top). Subscripts indicate symmetry-generated atoms. Ni cubohemioctahedral coordination cage $\{Ni_6(L_{bpy}\text{-}R_3)_{12}(H_2O)_{12}\}$ unit (bottom). Colour scheme: Ni (green), O (red), and C (grey). H atoms are omitted for clarity.

Table 4.1: Selected bond lengths and angles from single-crystal XRD for the Ni-MOF.

Atom			Angle (°)	Atom		Distance (Å)
$O1_A$	Ni	O2	91.758(1)	Ni	$O1_A$	1.986(4)
$O1_B$	Ni	O3	85.952(2)	Ni	$O1_B$	1.991(3)
$O1_C$	Ni	$O1_B$	88.256(1)	Ni	$O1_C$	1.986(4)
$O1_D$	Ni	$O1_B$	176.48(4)	Ni	$O1_D$	1.986(2)
$O1_D$	Ni	$O1_C$	88.237(2)	Ni	O2	2.024(2)
O2	Ni	O3	180.00(5)	Ni	O3	2.022(3)

Within the network, these $\{Ni_6(\mathbf{L_{bpy}\text{-}R_3})_{12}(H_2O)_{12}\}$ cages represent nanoscopic, 12-connected nodes. Each node is linked through linear $\mathbf{L_{bpy}\text{-}R_3}^{2-}$ metallo-ligands, stabilising a highly augmented, quasiregular face-centred cubic **fcu-a** net that is characterised by $m\bar{3}m$ (O_h) symmetry (Fig. 4.4).[31–33] This observed connection mode gives rise to exceptionally large cage-type cavities with truncated tetrahedral and octahedral geometries. The Ru^{II} centres in **Ni-MOF** surround the central $\{Ni_6\}$ cage in an icosahedral $\{Ru_{12}\}$ fashion, adopting the symmetry of a regular Platonic body with the Schläfli symbol {3, 5} (Fig. 4.5 1c).

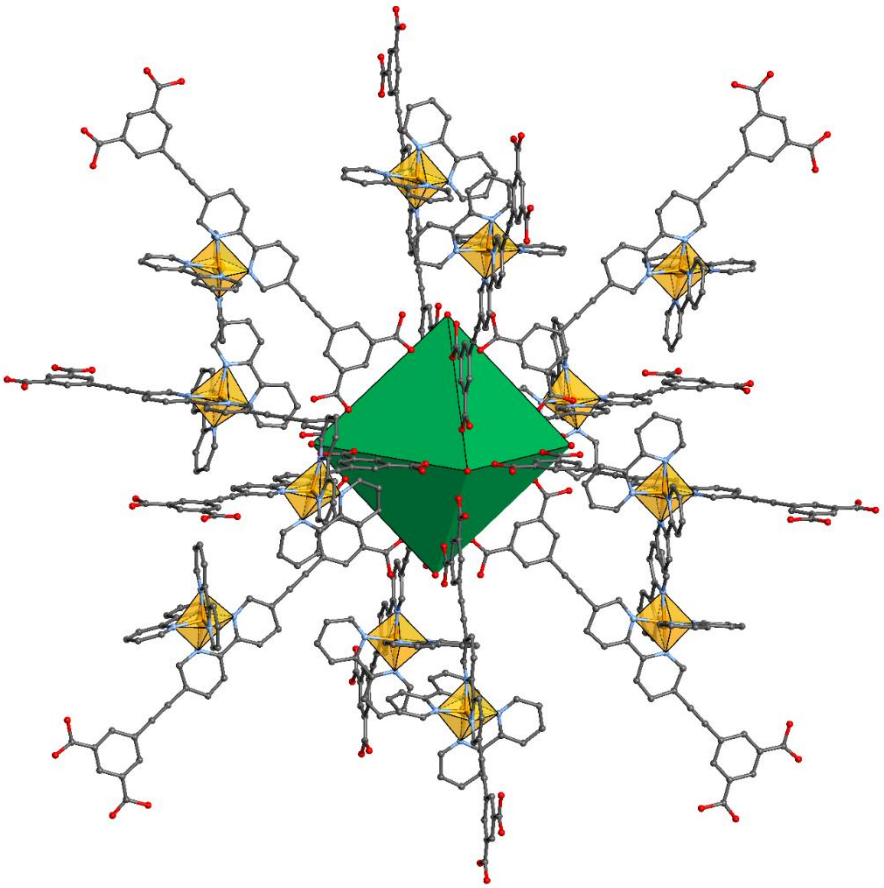

Figure 4.4: 12-Connected octahedra forming the *fcu-a* network characterised by $m\bar{3}m$ (O_h) symmetry. Colour scheme: Ru (orange), Ni (green), O (red), and C (grey). H atoms were omitted for clarity.

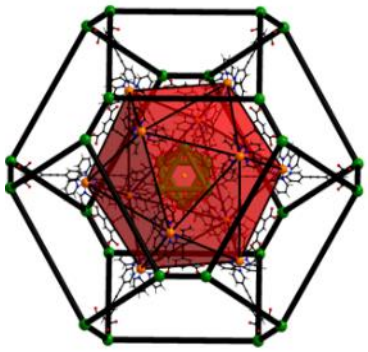

Figure 4.5: Endohedral arrangements of Platonic and Archimedean polygons in the MOF structure: {Ni_6-octahedron}⊂{Ru_{12}-icosahedron}⊂{Ni_{24}-polygon}. Colour scheme: Ru (orange), Ni (green), O (red), and C (grey). H atoms omitted for clarity.

The connectivity within the framework can be seen by analysing the packing arrangement of the MOF (**Ni-MOF**) (Fig. 4.6). Interestingly, what can be observed are a series of channels which are formed by the arrangement of Ru^{II} polypyridine metallo-ligands. As expected, these channels are lined with ruthenium centres, which in turn are expected to provide photoactive capabilities to the MOF and may play a role in photocatalysis.[34,35]

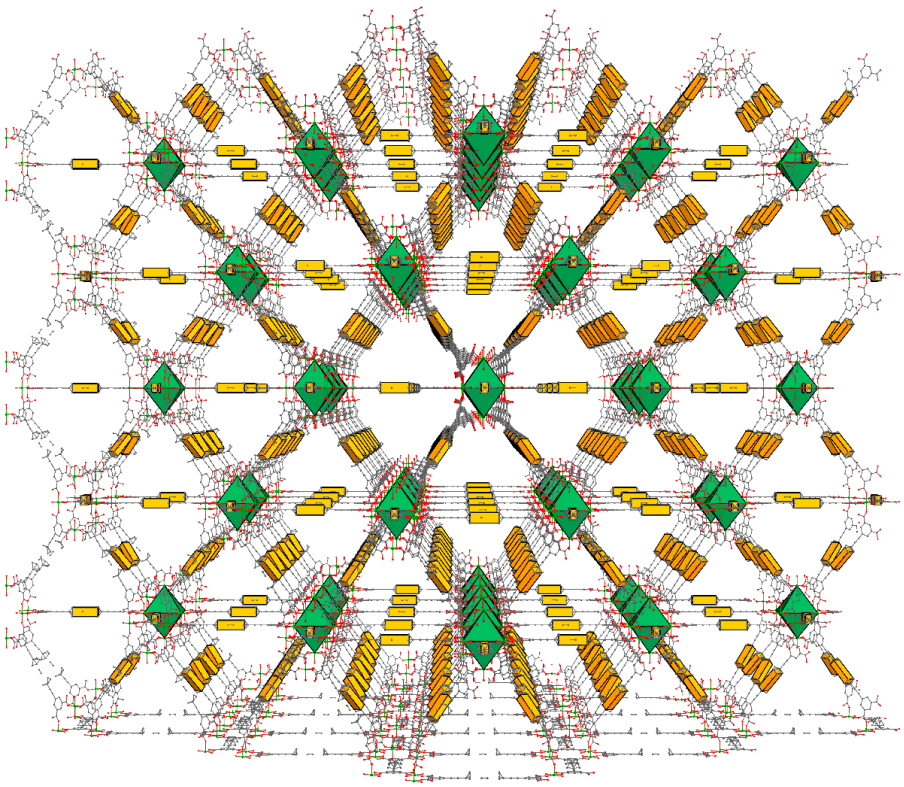

Figure 4.6: Packing diagram Ni-MOF viewed along the crystallographic *a*-axis demonstrating the channels present within the framework. Colour scheme: Ru (orange), Ni (green), O (red), and C (grey). H atoms were omitted for clarity.

Table 4.2: Single-crystal X-ray diffraction data and structure refinement for Ni-MOF.

Identification code	Ni-MOF
Empirical formula	$C_{300}H_{240}N_{36}Ni_6O_{60}Ru_6$
Formula weight	6267.95
Temperature/K	215(2)
Wavelength/Å	1.54184
Crystal system	Cubic
Space group	$Fm\bar{3}m$
a/Å	47.713(8)
b/Å	47.713(8)
c/Å	47.713(8)
α/°	90
β/°	90
γ/°	90
Volume/$Å^3$	108623(55)
Z	4
$\rho_{calc}Mg/m^3$	0.383
μ/mm^{-1}	0.947
F(000)	12816
Crystal size/mm^3	0.23 x 0.23 x 0.23
Radiation	CuKα (λ = 1.54184)
2Θ range for data collection/°	3.208 to 86.4
Index ranges	-25<=h<=33,-41<=k<=35,-42<=l<=24
Reflections collected	29312
Independent reflections	2004 [R_{int} = 0.0554, R_{sigma} = 0.0227]
Completeness to theta = 43.200°	99.8%
Absorption correction	Semi-empirical from equivalents

Max. and min. transmission	0.7485 and 0.2892
Refinement method	Full-matrix least-squares on F^2
Data/restraints/parameters	2004/41/54
Goodness-of-fit on F^2	2.518
Final R indexes [I>=2σ (I)]	R_1 = 0.2032, wR_2 = 0.5789
Final R indexes [all data]	R_1 = 0.2299, wR_2 = 0.5987
Largest diff. peak/hole / e $Å^{-3}$	0.621/-0.435

It should also be noted that the Ru^{II}-2,2'-bipyridyl moieties of the $\mathbf{L_{bpy}\text{-}R_3^{2-}}$ ligands are highly disordered due to the low rotational energy barrier along two acetylene moieties. For determining the energy barrier for rotation of the Ru^{II} polypyridine unit in **Ni-MOF**, Density Functional Theory (DFT) calculations were performed. For this purpose, the structure was truncated, as shown in Figure 4.7 and modelled in a non-periodic environment in vacuum. The calculations were carried out with the cluster code gaussian09[36] using the PBE0[37] functional in conjunction with the SDDALL[38] basis set with an effective core potential for Ru, the 6-31G(d)[36] basis set for C and N, and the 6-31G(p)[39] basis set for H. To determine the energy barrier, constrained geometry calculations were performed. The positions of the centres C19, C24, C39 and C40 (Fig. 4.7) were frozen and the N2-C30-C43-N5 dihedral angle was fixed to 0° to simulate the rigidity observed in the MOF. The dihedral C32-C38-C39-C40 angle was varied between 0° and 180° to determine the rotation barrier at 5° increments between 0° and 90° and 15° increments between 90° and 180° (Fig. 4.8). The energy barrier was determined on the basis of the energy of the system and not the free energy because the model allows for additional entropic freedom that is not available in the MOF. The inclusion of energy associated with entropy would introduce an additional source of error. The DFT calculations (Fig. 4.8) estimate that the rotation in **Ni-MOF** is characterised by an energy barrier for free rotation of *ca.* 12 kJ mol^{-1}, which is in agreement with literature values.[40,41] Hence at room temperature, it is expected that the {Ru^{II}-2,2'-bipyridyl} moieties rotate rapidly even in a solvated state at frequencies which are consistent with reported molecular rotors and motors that contain acetylene-connected structural motifs.[42,43] The high R_1 value of 0.2032 for **Ni-MOF** can be attributed to the low energy barrier for rotation. The rotational flexibility of acetylene-extended linkers is also

observable in augmented MOF topologies or in structurally related metal-organic polyhedra that are stabilised by trifunctional carboxylate ligands.[44–46]

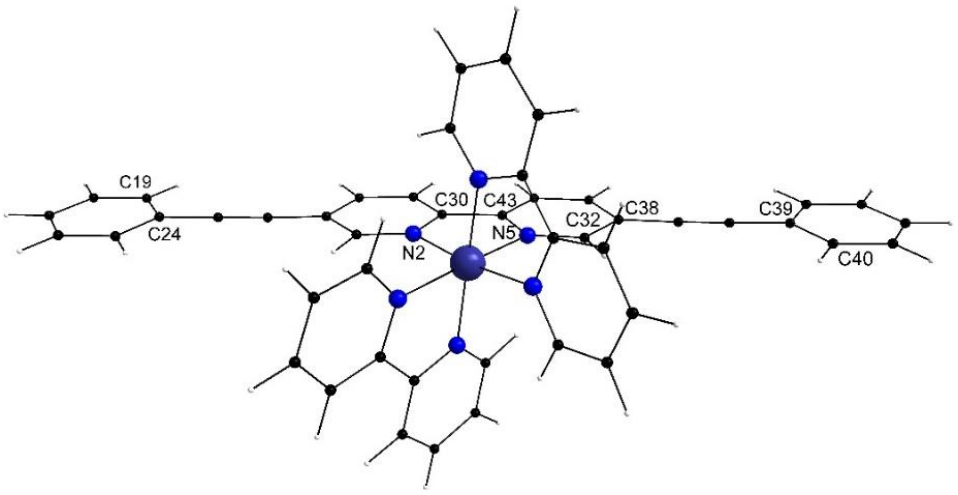

Figure 4.7: Ru^{II} polypyridyl complex model used in the DFT energy barrier for free rotation calculation. Colour scheme: Ru (purple), N (blue), C (black) and H (white).

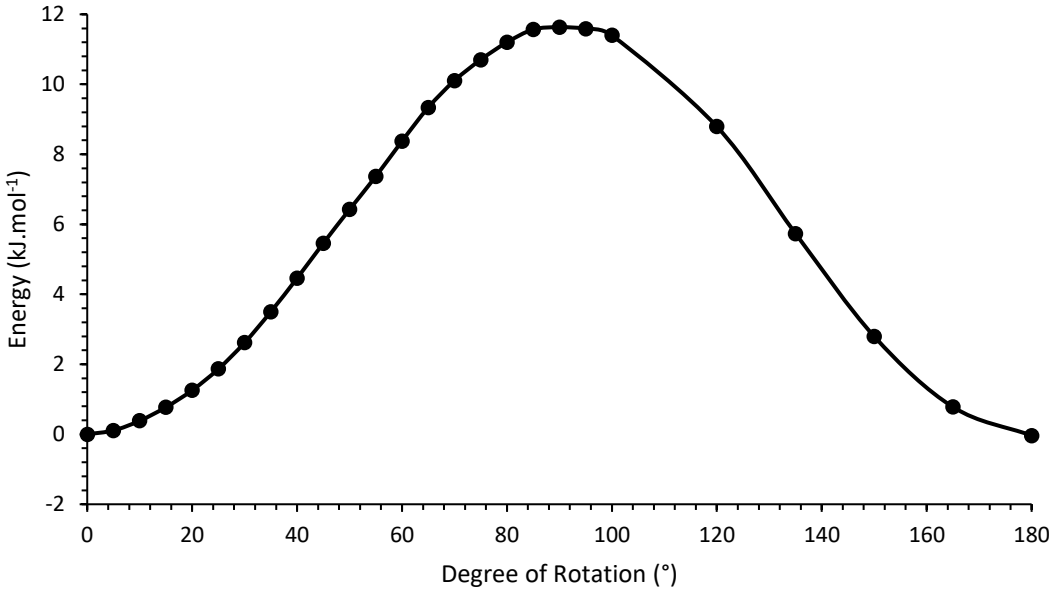

Figure 4.8: DFT energy barrier for rotation calculation for the Ru^{II} polypyridyl complex model.

Furthermore, RASPA[47] has been used to estimate the geometrical properties of the **Ni-MOF**. This simulation package can be used to simulate the adsorption and diffusion of molecules in porous materials and allows for the determination of the helium void fraction, the pore volume, the surface area and the pore size distribution. As a simulation box, a 2 x 2 x 2 simulation cell of a volume of 868,960 $Å^3$ containing 19,512 atoms was

used. Five thousand simulation cycles were found to be sufficient to obtain stable output simulation values. The values are presented in Table 4.3 and the pore size distribution is presented in Figure 4.9. It was found that a rigid, idealised model of the **Ni-MOF** structure that considers non-disordered, simplified {Ru^{II}-2,2'-bipyridyl} moieties (Fig. 4.10 and 4.11) give rise to exceptionally large cavities with cross-sectional diameters of 18 Å and 25 Å, respectively. However, the presence of the rotating bipyridyl moieties significantly reduces the effective pore diameters of the smaller voids that can be attributed to tetrahedral cavities, to *ca.* 9.4 Å, as calculated using RASPA.[47] The latter geometrical simulation software estimates a surface area of the desolvated MOF of 5082(5) m^2/g with a void fraction of 0.827(2) cm^3/cm^3.

Table 4.3: Geometrical properties and values obtained from RASPA.

Geometrical Properties	Value	Unit
Helium Void Fraction	0.827(2)	cm^3/cm^3
Pore Volume	2.172(5)	cm^3/g
Surface Area	5082(5)	m^2/g

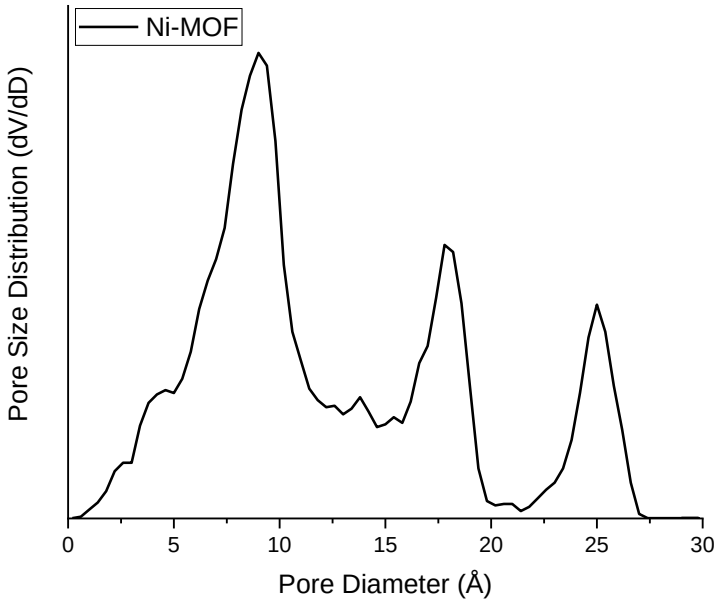

Figure 4.9: Pore size distribution of Ni-MOF obtained using RASPA.

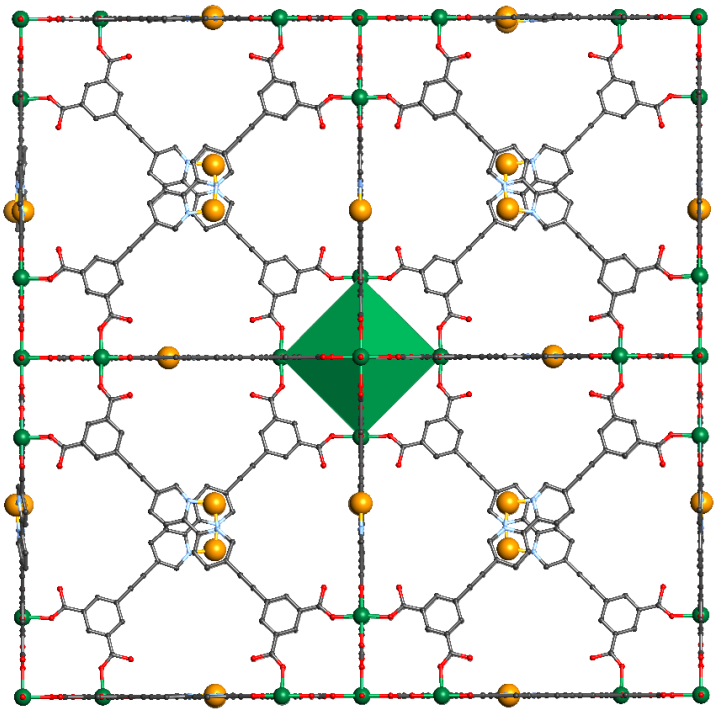

Figure 4.10: Unit cell of Ni-MOF. Colour scheme: Ru (orange), Ni (green), O (red), and C (grey). H atoms were omitted for clarity.

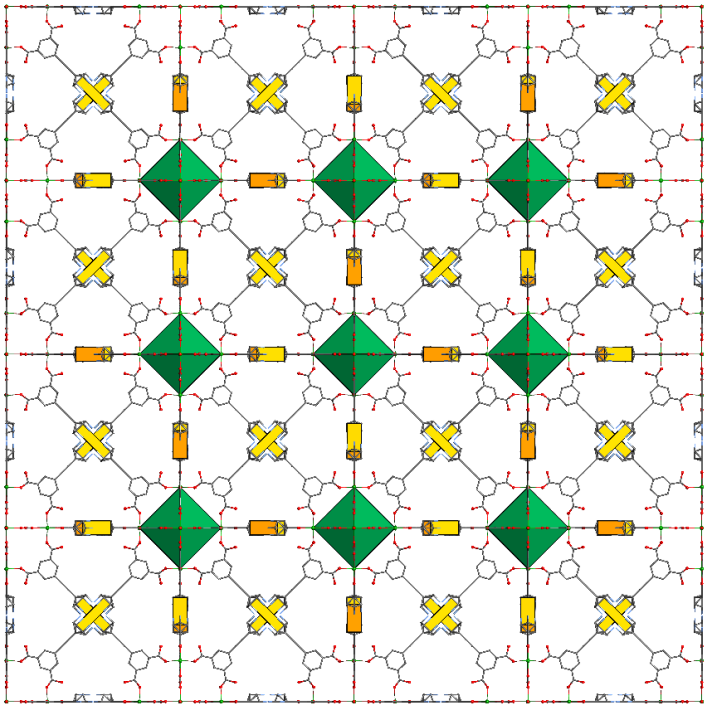

Figure 4.11: Simplified structural representation of Ni-MOF in which the Ru-pyridyl moieties are represented as orange stereocylinders with a view in the crystallographic [111] direction. Colour scheme: Ru (orange), Ni (green), O (red), and C (grey). H atoms were omitted for clarity.

The phase purity of a bulk sample of **Ni-MOF** was confirmed *via* X-ray powder diffraction (PXRD) experiments which were conducted in capillaries containing DMF to avoid rapid desolvation and amorphisation even at room temperature. Figure 4.12 demonstrates closely matching signals for the X-ray powder diffraction pattern of the as-synthesised **Ni-MOF** compared to that of a powder pattern calculated from the single-crystal X-ray diffraction data of **Ni-MOF**. The calculated data were obtained using the Olex2 software.[48] The experimental pattern is characterised by signals that appear at 2θ = 5.24°, 6.43°, 7.41°, 8.07°, 9.05°, 9,61° and 11.03°. The matching powder patterns indicate the phase purity of the bulk sample and support the accuracy of the refined crystallographic model.

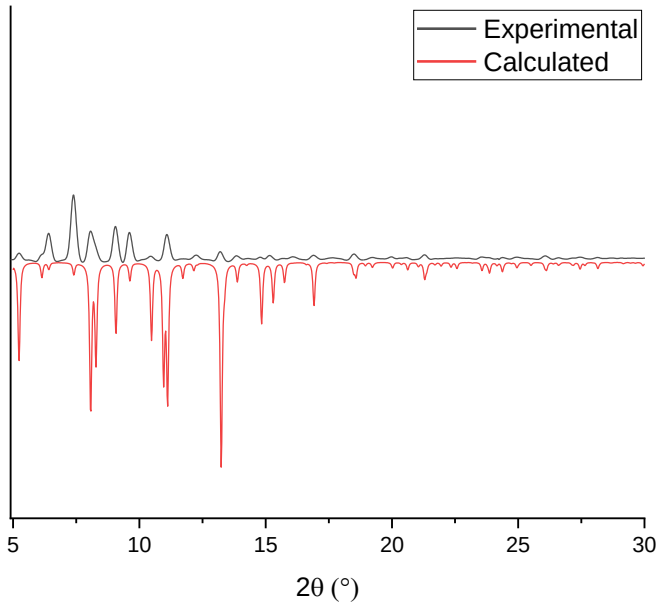

Figure 4.12: Powder X-ray Diffraction (PXRD) patterns for Ni-MOF experimental and Ni-MOF calculated.

4.4 Physicochemical Characterisation of Ni-MOF

Upon obtaining a crystal structure of **Ni-MOF**, further characterisation of the MOF was conducted. FT-IR spectroscopy was initially carried out (Fig. 4.13). The broad band which appears at *ca.* 3390 cm^{-1} can be attributed to the ν(O–H) stretch owning to the H_2O in the axial positions on the Ni sites in the MOF and to potential solvent molecules within the pores of the framework structure.[49,50] Weak bands at 2931 cm^{-1} and 2871 cm^{-1} can be attributed to ν(C-H) vibrations derived from the aldehyde functionalities and methyl moieties of DMF solvent molecules located within the pore structure of the MOF.[51,52] Particularly characteristic signals which can be seen are the vibrational bands that derive for the asymmetric ν_{as}(COO) and symmetric ν_s(COO) carboxylate stretches at 1563 cm^{-1} and 1419 cm^{-1}, respectively.[53,54] Their positions and a Deacon-Phillips value of $\Delta = (\nu_{as}-\nu_s) = 144$ cm^{-1} are characteristic of the observed *syn-*η^1 carboxylate coordination mode of the carboxylate functions in **Ni-MOF**.[55–57] A strong band due to the ν(C=O) stretching vibrations in the DMF solvent molecules is found at 1651 cm^{-1}.[51,52,58] The ν(C=C) stretching vibrations derived from the benzene and bipyridine moieties can be observed at *ca.* 1499 cm^{-1}.[30,59] Finally, the weak broad signal at *ca.* 560 cm^{-1} can be attributed to the ν(Ni–O) stretching vibration mode present within the framework.[60]

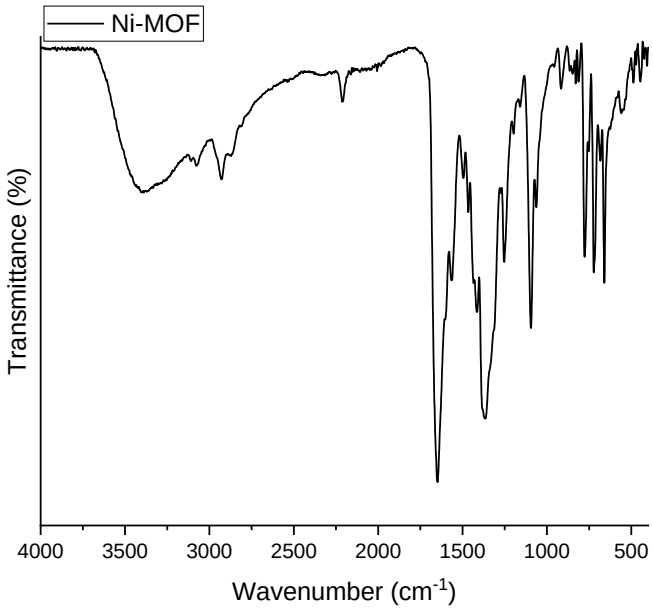

Figure 4.13: FT-IR spectrum of Ni-MOF.

Ni-MOF was similarly subjected to Raman spectroscopy (Fig. 4.14). The Raman spectrum was measured from 200 cm^{-1} to 2500 cm^{-1} and the baseline was corrected using the OriginLab 2020 software. The *ν*(C–H) vibrations derived from the aromatic and heteroaromatic moieties can be seen at *ca*. 1005 cm^{-1}, 1033 cm^{-1}, 1119 cm^{-1} and 1147 cm^{-1}.[61] The band at *ca*. 1202 cm^{-1} can be attributed to the δ(C–H) bending vibrations.[62] The bands at *ca.* 1276 cm^{-1} and 1320 cm^{-1} derive from *ν*(C–C) single bond vibrations. At *ca*. 1375 cm^{-1} ν_s(C=O), vibrations derived from the carboxylate groups can be observed. The *ν*(C=C) vibrations attributed to the aromatic and heteroaromatic moieties in the **Ni-MOF** appear at *ca.* 1489 cm^{-1} and 1590 cm^{-1}. The significant characteristic Raman signal is found at 2218 cm^{-1} and can be attributed to the *ν*(C≡C) vibration of the alkyne-moieties, which can also be seen at the same Raman shift for $\mathbf{H_4[L_{bpy}\text{-}R_3]^{2+}}$ (Fig. 2.25). This particularly intense Raman signal that can be assigned to the alkyne-moiety derived vibration, in contrast is very weak in the FT-IR spectrum for the corresponding **Ni-MOF** and Ru^{II} polypyridine complex $\mathbf{H_4[L_{bpy}\text{-}R_3]}$.[63,64]

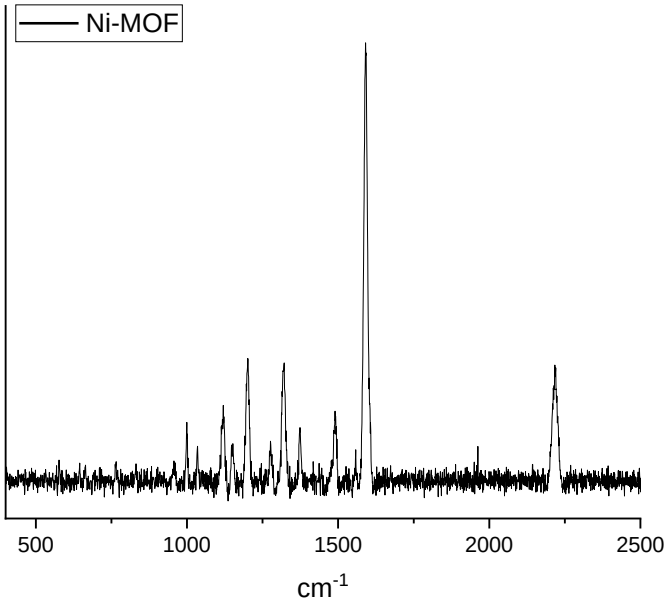

Figure 4.14: Raman spectrum of Ni-MOF.

The thermal stability of **Ni-MOF** was assessed using thermogravimetric analysis (TGA). The analysis was conducted using a freshly prepared crystalline sample of **Ni-MOF** under a constant stream of air and in the temperature range of 30 °C – 500 °C. The experiment revealed that **Ni-MOF** undergoes a decomposition pathway that follows two main steps. The TGA trace (Fig. 4.15) reveals an initial step between *ca.* 30 °C – 145 °C which is associated with a weight loss of *ca.* 58 %. This weight loss can be attributed to the removal of the constitutional solvent and coodination water molecules. A second thermogravimetric step above 350 °C leads to a weight loss of *ca.* 30 % due to the oxidative degradation of the organic ligand moieties. [65–67]

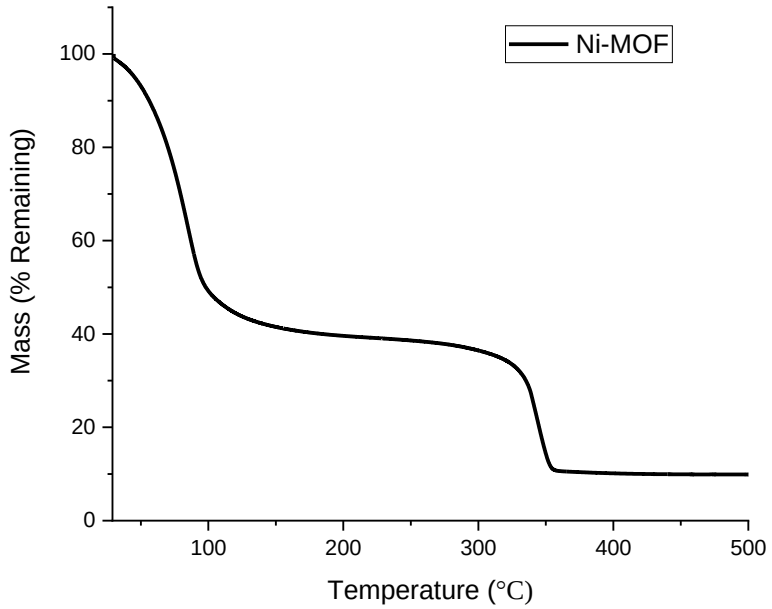

Figure 4.15: Thermogravimetic analysis of Ni-MOF measured in an air atmosphere, at heating rate of 5 °C per minute.

Scanning Electron Microscopy (SEM) and Energy Dispersive X-ray spectroscopy (EDX) measurements were carried out on a freshly prepared crystalline sample of **Ni-MOF** (Fig 4.16 and Fig 4.17). The crystals were dispersed on adhesive carbon tape and an acceleration of 10 keV was used for the EDX analysis of the material. The data obtained revealed the expected atomic weight percentage ratio of approximately 1:1 of Ru^{II} to Ni^{II}. The EDX data was therefore confirmative of the composition of the **Ni-MOF**.

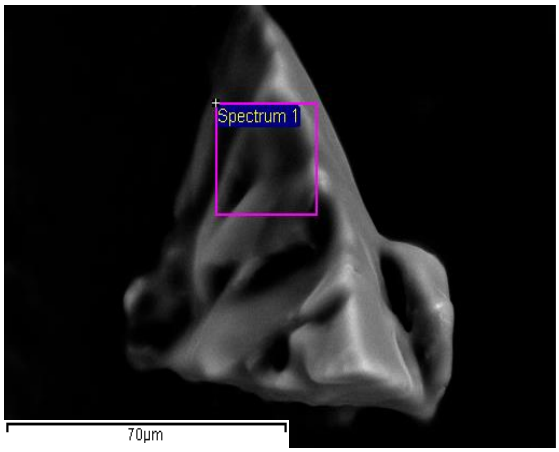

Figure 4.16: SEM image of a crystal of Ni-MOF .

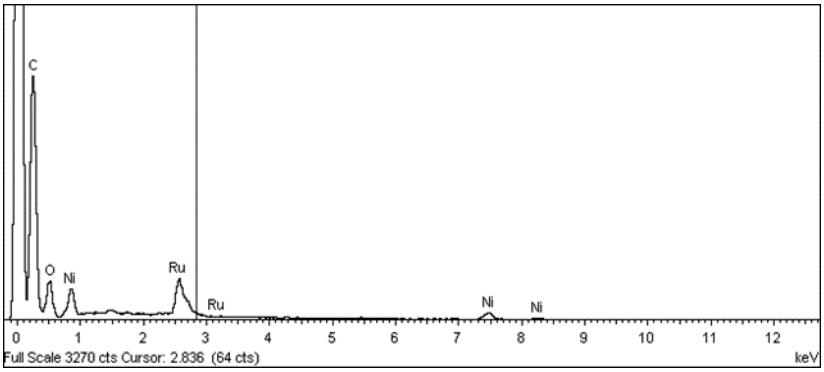

Figure 4.17: EDX analysis for Ni-MOF.

Table 4.4: EDX data obtained for Ni-MOF.

Element	App Conc.	Intensity	Atomic (%)
C	8.05	1.4307	76.15
O	1.12	0.5773	19.79
Ni	0.61	0.798	2.13
Ru	0.93	0.7781	1.93

4.5 Photophysical Characterisation of Ni-MOF

To investigate the photophysical properties of **Ni-MOF**, UV-vis absorption, spectral and time-resolved photoluminescence (PL and TRPL) experiments were conducted. The absorption spectra (Fig. 4.19) were measured using a Cary 50 UV-vis spectrophotometer. A small sample of the **Ni-MOF** was dispersed in DMF in a quartz cuvette and shaken well to ensure that the crystalline MOF was suspended in solution during the measurement. Time-resolved photoluminescence (TRPL) measurements were performed using a PicoQuant Micro-time 200 time-resolved confocal microscope system using an excitation of 90 ps pulses at a wavelength of 405 nm (λ_{ex}) with a repetition rate of 10 MHz and an integration time of 4 ms per pixel. The laser spot size was approximately 430 nm. The **Ni-MOF** was drop-casted and dried on quartz slides. The sample was excited through a 40x objective (NA = 0.65) with an excitation power of 0.2 µW. All scans were performed over 10 µm x 10 µm square areas.

The steady-state PL measurements (Fig. 4.20) were collected through the same objective and areas as the TRPL measurements, however, with a higher excitation power of 4 µW. The studies confirm that the optical and light-harvesting attributes of the {Ru^{II}-bipyridyl} moieties are maintained within the MOF and suggest efficient electronic communication between the Ru^{II} polypyridine complex and Ni^{II} nodes (Fig. 4.18). Absorption bands of ligand-centred transitions in the UV-vis spectrum (Fig. 4.19) of the crystalline **Ni-MOF** appear at *ca.* 200–300 nm, whereas ^{1}MLCT transitions give rise to broad absorbance bands at *ca.* 480 nm, confirming only slightly varied excitation energies in comparison to the uncomplexed $\mathbf{H_4[L_{bpy}\text{-}R_3]^{2+}}$. The PL emission spectrum of **Ni-MOF** (Fig. 4.20) gives rise to a broad emission band, centred at 690 nm, which is slightly blue-shifted in relation to the emission spectrum of $\mathbf{H_4[L_{bpy}\text{-}R_3]^{2+}}$.

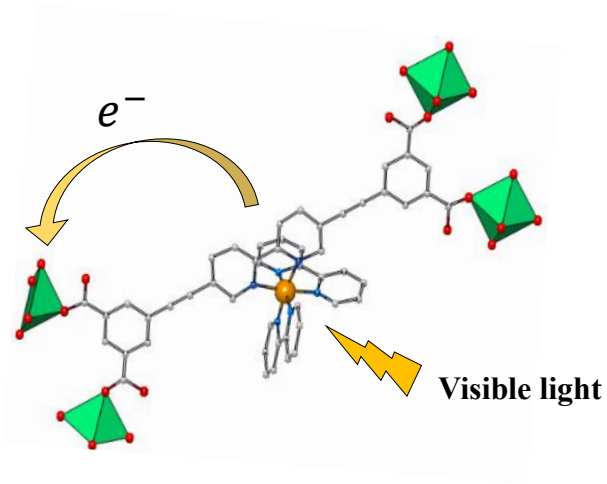

Figure 4.18: Schematic showing visible-light excitation of the photosensitiser and electron transfer to the metal node. Colour scheme: Ru (orange), Ni (green), O (red), and C (grey). H atoms were omitted for clarity.

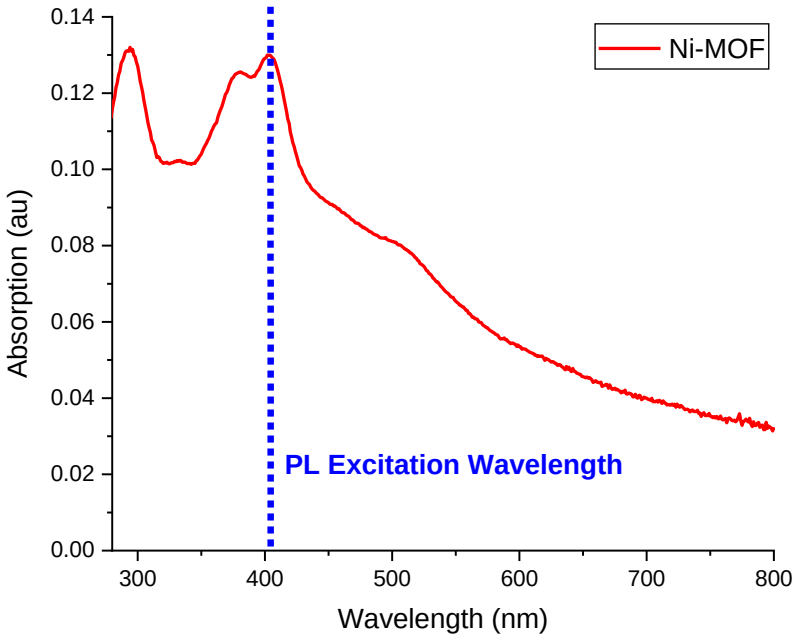

Figure 4.19: Visible light absorption spectrum of Ni-MOF. The dotted line indicates the photoluminescence (PL) excitation wavelength of 405 nm.

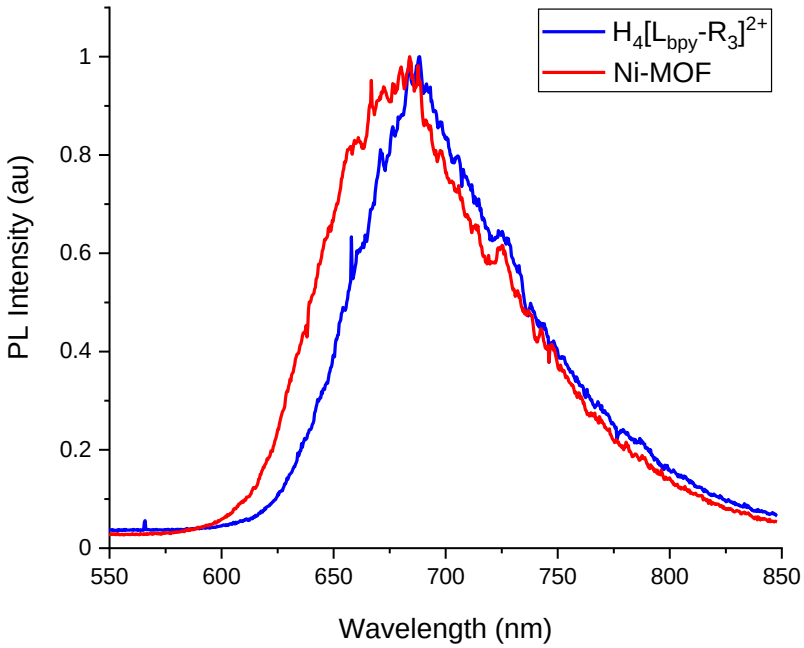

Figure 4.20: Normalised steady-state photoluminescence (PL) spectra of Ni-MOF (red) and $H_4[L_{bpy}\text{-}R_3]^{2+}$ (blue). (λ_{ex} = 405 nm).

TRPL decays were measured using a 700 nm bandpass filter with a full width at half maximum (FWHM) of 10 nm and excitation power of 0.2 µW (Fig. 4.21). The results demonstrate strong quenching effects of the excited state lifetime for the **Ni-MOF** compared to the uncomplexed $\mathbf{H_4[L_{bpy}\text{-}R_3]^{2+}}$, signifying an evident decrease in lifetime when the metallo-ligand is incorporated within **Ni-MOF**. Furthermore, it was identified that the decay of the Ru^{II} polypyridine complex $\mathbf{H_4[L_{bpy}\text{-}R_3]^{2+}}$ displays a mono-exponential decay whilst the PL decay of **Ni-MOF** displays a bi-exponential decay character. The data demonstrates that the incorporation of $\mathbf{H_4[L_{bpy}\text{-}R_3]^{2+}}$ into the MOF network allows for rapid shuttling or redistribution of excited electrons from the photosensitiser *via* the conjugated ligand backbone towards the metal nodes.[68–71] Thus, providing an alternative decay pathway involving the Ni^{II} centres and affecting the electronic structure of the Ru^{II} polypyridine complex ($\mathbf{H_4[L_{bpy}\text{-}R_3]^{2+}}$) within the MOF.

In order to extract the lifetimes from the PL decays, the PL decay of the $\mathbf{H_4[L_{bpy}\text{-}R_3]^{2+}}$ was fitted with a single exponential decay curve, given by;

$$I(t) = I_0 e^{-\frac{t}{\tau}} \tag{4.5.1}$$

where I_0 is the intensity amplitude of the single decay having a lifetime of τ. Fitting of the $\mathbf{H_4[L_{bpy}\text{-}R_3]^{2+}}$ decay using the above fitting parameters gives a lifetime of 74.3 ± 0.7 ns. The fits to the experimentally measured decays are shown in solid black lines in Figure 4.21.

Given that the PL decays of the **Ni-MOF** display a bi-exponential character, these decays were fitted with a bi-exponential fitting curve, given by;

$$I(t) = I_1 e^{-\frac{t}{\tau_1}} + I_2 e^{-\frac{t}{\tau_2}} \tag{4.5.2}$$

where I_1 and I_2 are the intensity amplitudes for both decays having lifetimes of τ_1 and τ_2, respectively. In order to define a single lifetime value for these decays, a single representative lifetime was extracted from the bi-exponential decay through the use of an intensity weighted average lifetime, τ_{Avg}, given by;

$$\tau_{Avg} = \frac{I_1\tau_1^2 + I_2\tau_2^2}{I_1\tau_1 + I_2\tau_2} \tag{4.5.3}$$

The intensity-weighted average lifetimes of the Ru^{II} polypyridine complex $\mathbf{H_4[L_{bpy}\text{-}R_3]^{2+}}$ within **Ni-MOF** is 16.8 ± 0.2 ns.

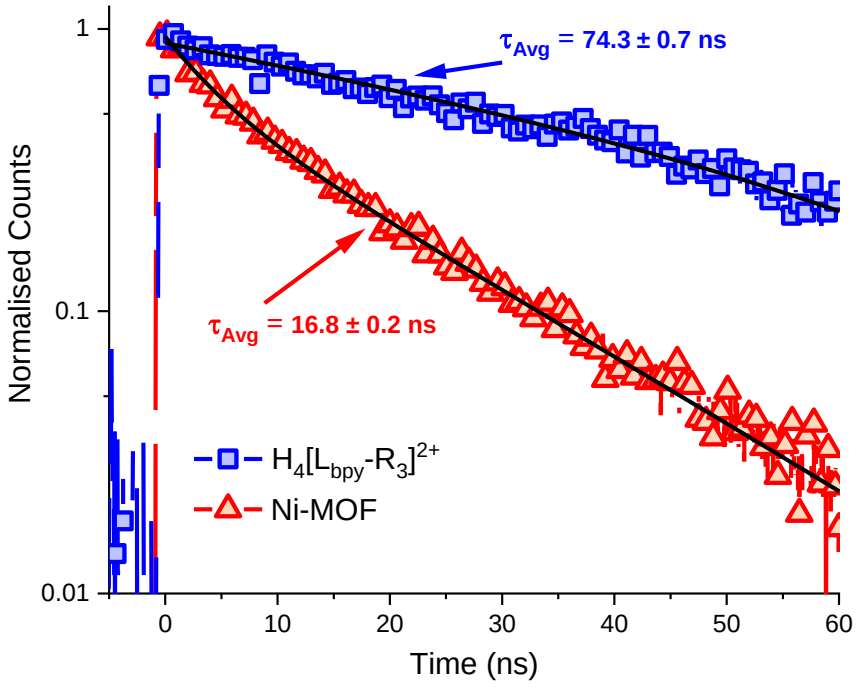

Figure 4.21: Normalised photoluminescence decays of Ni-MOF and $\mathbf{H_4[L_{bpy}\text{-}R_3]^{2+}}$ measured in DMF upon excitation at 405 nm using a 10 nm bandpass filter centred at 700 nm.

Furthermore, spectrally time-resolved photoluminescence decays were measured using bandpass filters (FWHM = 10 nm) with five centre wavelengths across the photoluminescence spectra (635 nm, 650 nm, 750 nm, and 800 nm) (Fig. 4.22). The data obtained reveal that the lifetime of the ^{3}MLCT state of the Ru^{II} polypyridine complex **$H_4[L_{bpy}\text{-}R_3]^{2+}$** is consistently reduced upon coordination with Ni^{II} ions in **Ni-MOF**.

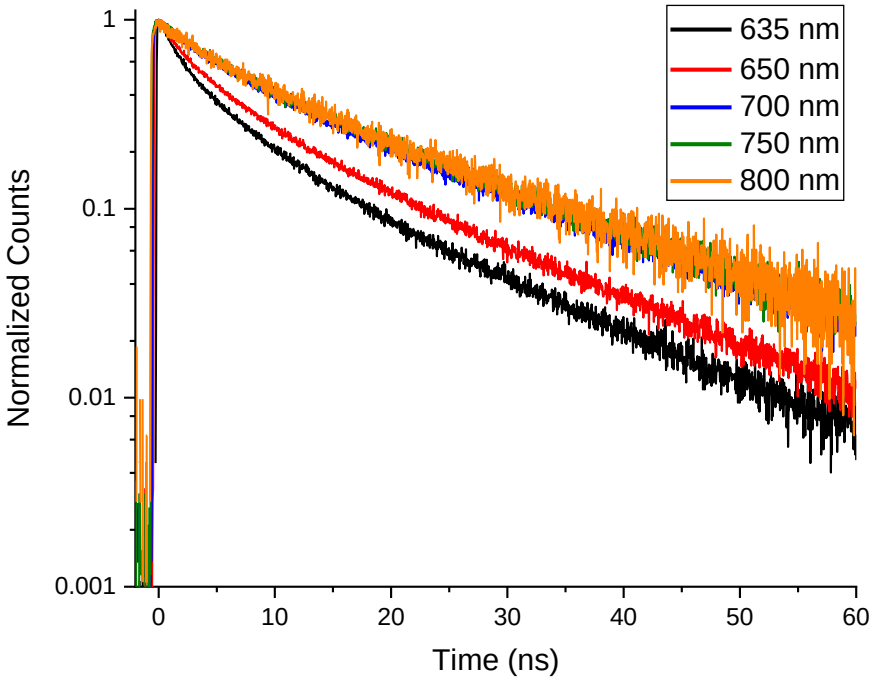

Figure 4.22: Normalised time-resolved photoluminescence decays of Ni-MOF measured at five different central emission wavelengths using 10 nm bandpass filters (λ_{ex} = 405 nm).

Additionally, Figure 4.23 illustrates the average lifetimes at an excitation power of 0.2 µW, obtained for both the Ru^{II} polypyridine complex **$H_4[L_{bpy}\text{-}R_3]^{2+}$** and the **Ni-MOF** at centre wavelengths of 635 nm, 650 nm, 700 nm, 750 nm, and 800 nm using bandpass filters (FWHM = 10 nm). The results demonstrate an increase in the average lifetime for longer emission wavelengths.

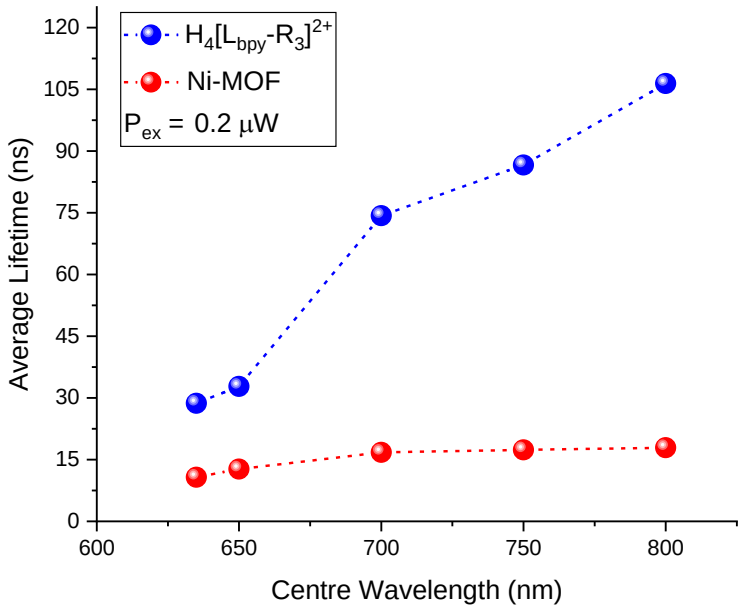

Figure 4.23: Average lifetime measurements in ns at different centre wavelengths of $H_4[L_{bpy}\text{-}R_3]$ in the Ni-MOF (red) and $H_4[L_{bpy}\text{-}R_3]$ (blue).

The dependence of the average lifetimes (Fig 4.24), integrated lifetimes (Fig 4.25), and peak intensities (Fig 4.26) of **Ni-MOF** on various excitation powers (0.2 µW, 0.5 µW, 1.0 µW, 2.0 µW, 10.0 µW), at an excitation wavelength of λ_{ex} = 405 nm and various centre wavelengths using bandpass filters (635 nm, 650 nm, 750 nm, and 800 nm) (FWHM = 10 nm), were investigated. The measurements confirm the spectral and power dependence of the average lifetimes, integrated lifetimes and peak intensities, through which the integrated lifetimes and peak intensities increase linearly with the excitation powers of the incident laser light. From the data obtained, slightly overlapping higher values for the spectrally resolved lifetimes were recorded at λ_{emis} = 635 nm, 650 nm and 700 nm and the lowest values were observed at λ_{emis} = 800 nm. A similar trend, however, with slightly less overlapping can be seen for the spectrally resolved peak intensities. The data illustrates higher intensities and partial overlapping at λ_{emis} = 635 nm and 650 nm, while lower intensity was again obtained at λ_{emis} = 800 nm.

Furthermore, the lifetimes and peak intensities at various central emission wavelengths demonstrate an equivalent power dependence trend in the analysis. Thus, it can be seen that varying the excitation power of the laser between 0.02 µW and 10.00 µW results in a decrease in average lifetimes and subsequently an increase in the integrated lifetimes by a factor of *ca.* 15. Similarly, the peak intensities increase by a factor of *ca.* 22 upon variation of the excitation power of the laser.

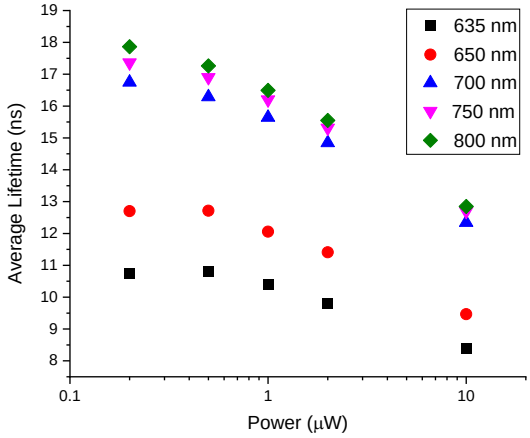

Figure 4.24: Dependence of the average lifetimes measured at different centre wavelengths on the excitation power (P_{ex}) at the excitation wavelength of λ_{ex} = 405 nm

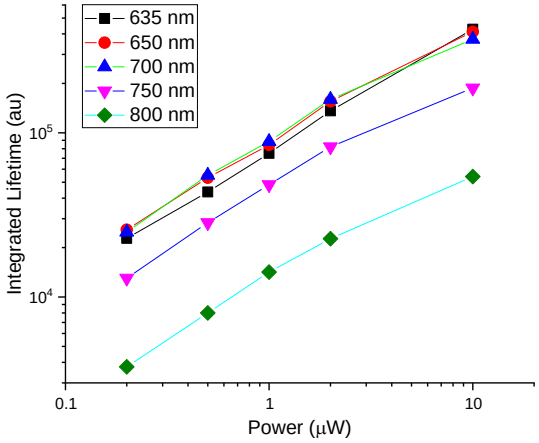

Figure 4.25: Dependence of the integrated lifetimes measured at different centre wavelengths on the excitation power (P_{ex}) at the excitation wavelength of λ_{ex} = 405 nm.

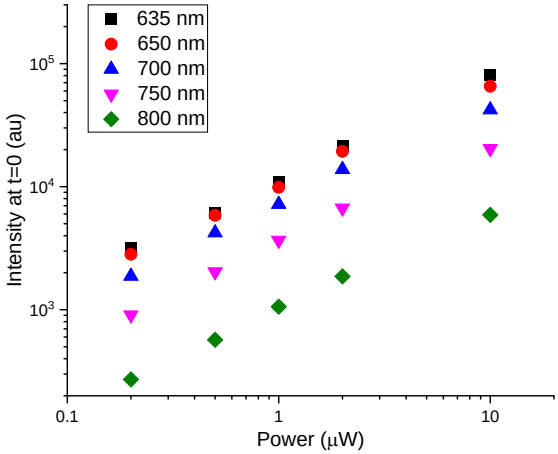

Figure 4.26: Dependence of the photoluminescence intensity (I_{PL}) measured at different centre wavelengths on the excitation power (P_{ex}) at the excitation wavelength of λ_{ex} = 405 nm.

The interaction between the **$H_4[L_{bpy}\text{-}R_3]^{2+}$** and the **Ni-MOF** can be quantified from the reduction in a lifetime in terms of an increase in the decay rate, given that the decay rate, $k = 1/\tau$. Here, we define the Quenching Efficiency as;

$$Quenching\ Efficiency = 1 - \frac{\tau_{Avg}}{\tau} \tag{4.5.4}$$

where τ_{Avg} represents the intensity weighted average lifetime of the **Ni-MOF** and τ is the lifetime of the **$H_4[L_{bpy}\text{-}R_3]^{2+}$**. The Quenching Efficiency (%) calculated from the decays presented in Figure 4.21 gives a value of 77 ± 4% for the crystalline **Ni-MOF**.

To further probe the interaction between **$H_4[L_{bpy}\text{-}R_3]^{2+}$** and the **Ni-MOF** the Quenching Efficiency (%) was also calculated from the PL decays measured at centre wavelengths of 635 nm, 650 nm, 700 nm, 750 nm, and 800 nm using bandpass filters (FWHM = 10 nm) (Fig 4.22). The resultant spectral dependence of the Quenching Efficiency (%) is shown in Figure 4.27. From the data obtained, it can be seen that the Quenching Efficiency (%) is smallest on the blue side (650 nm) of the emission spectrum, where the emission spectrum of the **$H_4[L_{bpy}\text{-}R_3]^{2+}$** has been broadened in the **Ni-MOF**. In comparison, the most significant change in the Quenching Efficiency (%) was measured between 700 – 800 nm where the emission spectrum of the **$H_4[L_{bpy}\text{-}R_3]^{2+}$** has remained unchanged in the MOF.

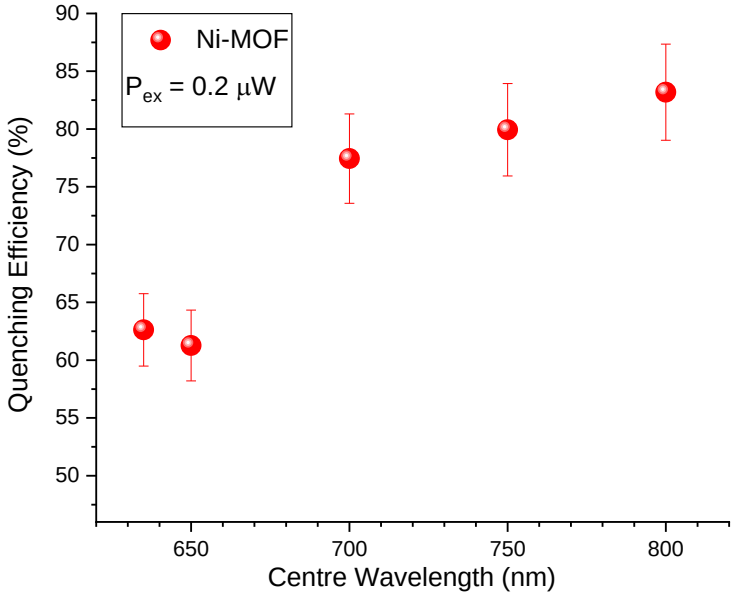

Figure 4.27: Percentage quenching efficiency measured at different centre wavelengths of Ni-MOF.

Finally, a Tauc plot derived from the Tauc and Davis-Mott relation[72–75] (Eq. 3.6.9) was used to probe the optical energy band gaps (E_g) from the UV-Vis absorption data (Fig 4.19). The metallo-ligands **$H_4[L_{bpy}\text{-}R_3]^{2+}$** estimated band gap energies (Fig 3.17) were compared to that of the **Ni-MOF** calculated energy band gaps (Fig 4.28). From the data obtained, it can be seen that **Ni-MOF** exhibits enhanced semiconductor properties in comparison to the metallo-ligand, facilitating energy transfer between the Ru^{II} polypyridine complex and the Ni^{II} nodes.[76] The charge redistribution between **$H_4[L_{bpy}\text{-}R_3]^{2+}$** and the Ni^{II} nodes decreases the interfacial energy in the **Ni-MOF**, and thus all relevant band gaps appear significantly reduced in energy.[77] LC, MC and MLCT absorption bands (Fig 4.19) are red-shifted to lower energies compared to **$H_4[L_{bpy}\text{-}R_3]^{2+}$** and appear at 295 nm, 400 nm and 510 nm, respectively. Similarly, in comparison to **$H_4[L_{bpy}\text{-}R_3]^{2+}$**, the photonic energy (E_{ph}) required to excite an electron from the valance band to the conduction band in **Ni-MOF** is reduced.

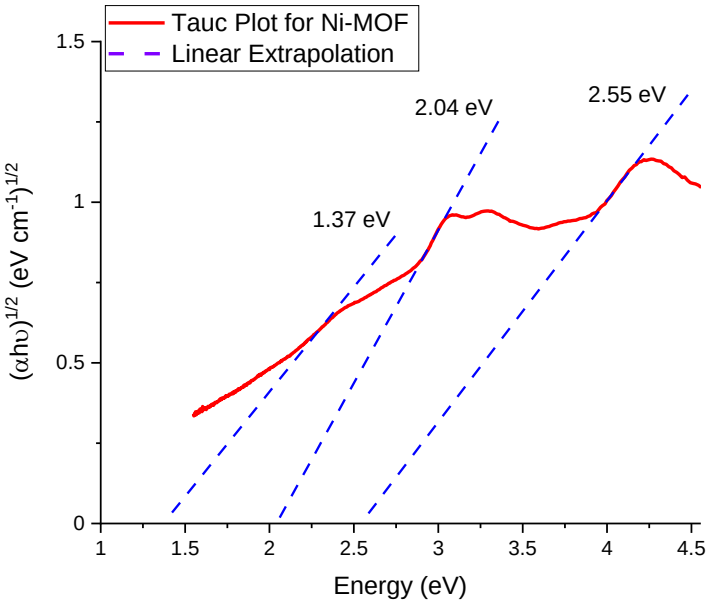

Figure 4.28: Tauc Plot calculated from the UV-Vis absorption spectrum of Ni-MOF, indicating the linearly extrapolated MLCT, MC & LC estimated optical band gap energies.

4.6 Cathodic Electrochemical Synthesis and *in-situ* Film Deposition of Ni-MOF

In order to demonstrate processability for photoelectrochemical energy conversion systems, cathodic electrochemical synthesis and *in-situ* film deposition of the **Ni-MOF** were carried out. It was anticipated that this method would yield a porous, thin film of the MOF framework on transparent fluorine-doped tin oxide (FTO) coated glass electrodes. It was expected that fabricating these electrodes would take full advantage of the MOFs photoactive capabilities for the design of a photoelectrochemical system for photo-electrocatalytic applications. Furthermore, the production of photoactive MOF thin films increases the available area of the MOF while further permitting its use in applications such as optoelectronics and smart devices.[19,78] Similarly, the ability to deposit photoactive porous MOFs as thin films at lateral boundaries of electrodes is of importance to achieve high MOF-derived functionality whilst maintaining satisfactory charge mobilities and photo-response characteristics.[79] The latter is proportional to the spectral absorption efficiency of a material and the light penetration depth, which is influenced by the film thickness and size of particles of the photosensitising material.

Ni-MOF was electrochemically synthesised on fluorine-doped tin oxide (FTO) electrodes using a conventional 3-electrode setup involving a platinum wire counter electrode and an Ag/Ag(cryptand)$^+$/DMF reference electrode in a DMF/H_2O (100/1 v/v) solvent mixture using tetrabutylammonium hexafluorophosphate ($(NBu_4)PF_6$) (0.1 M) as electrolyte (Fig 4.29). The synthesis and deposition of **Ni-MOF** were achieved from diluted reaction mixtures containing millimole quantities of $\mathbf{H_4[L_{bpy}\text{-}R_3]^{2+}}$ and $Ni(NO_3)_2{\cdot}6H_2O$ within less than 5 minutes at a potential of –1.5 V in ambient temperature, resulting in a homogeneous film on the conductive surface of the FTO electrode (Fig. 4.30). Subsequently, the deposited **Ni-MOF/FTO** electrode was removed from the reaction mixture and washed with DMF in order to remove any excess reaction mixture. The **Ni-MOF/FTO** was stored in fresh DMF to prevent the loss of crystallinity due to desolvation. The potential of -1.5 V (vs Ag/Ag(cryptand)$^+$ in DMF) used for the cathodic electrochemical synthesis and *in-situ* film deposition of the **Ni-MOF** was deliberately applied as under these conditions hydroxide ions are formed electrochemically through the reduction of the NO_3^- anions, which in turn increases the pH of the reaction solution, resulting in the *in-situ* deprotonation of the metallo-ligand and the formation of the MOF on the conductive surface of the electrode.[80,81]

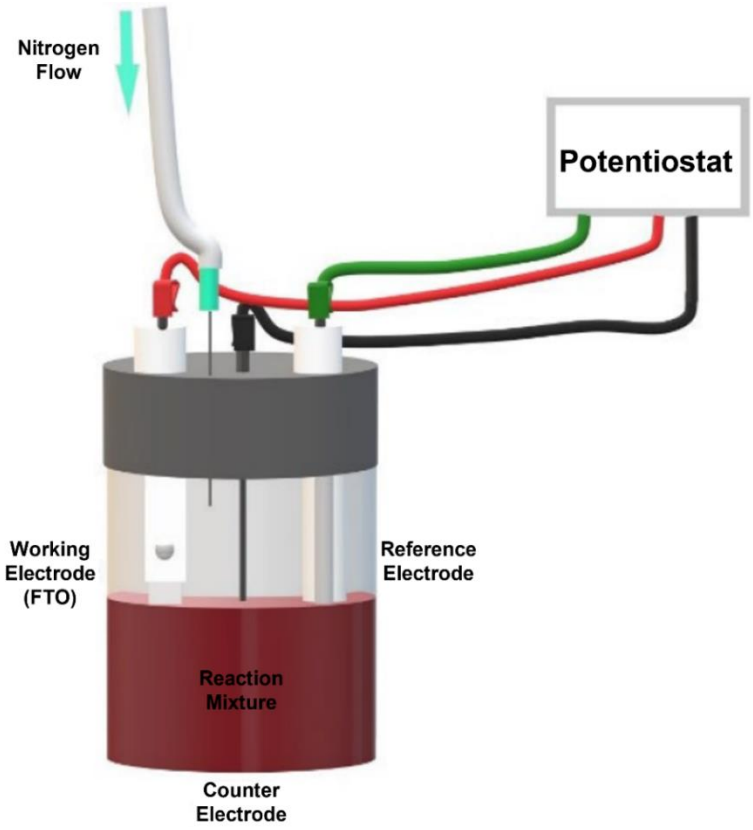

Figure 4.29: Illustration of the three-electrode experimental set-up used for the cathodic electrochemical synthesis and *in-situ* film deposition of Ni-MOF.

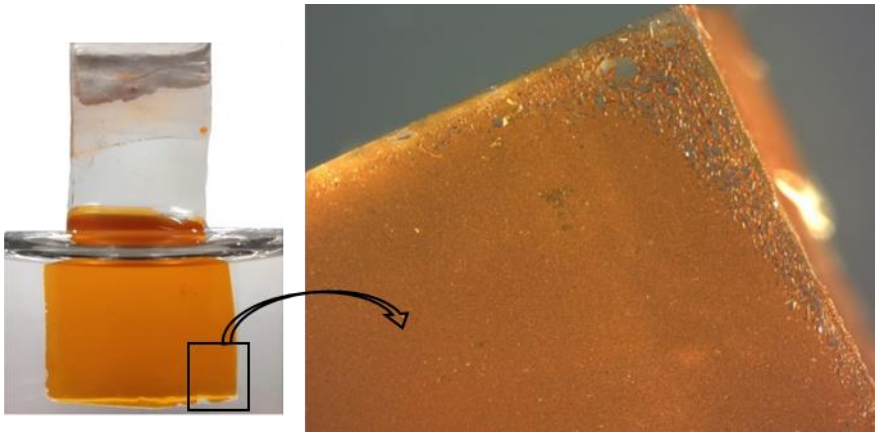

Figure 4.30: Optical images of electrodeposited Ni-MOF/FTO.

After obtaining the **Ni-MOF/FTO** from millimole quantities of $\mathbf{H_4[L_{bpy}\text{-}R_3]^{2+}}$ and $Ni(NO_3)_2{\cdot}6H_2O$, infrared spectroscopy was conducted as to confirm the successful cathodic electrochemical synthesis and *in-situ* film deposition of the **Ni-MOF** on FTO electrodes.

The IR-spectrum (Fig. 4.31) below of **Ni-MOF/FTO** illustrates an essentially identical spectrum to that of the bulk-synthesised **Ni-MOF** (Fig. 4.13). Bands characteristic to the **Ni-MOF** and particularly the matching vibrational bands that derive from the asymmetric ν_{as}(COO) and symmetric ν_s(COO) carboxylate stretches, which are typical of the monodentate carboxylate moieties present in the structure, can be seen at *ca.* 1552 cm^{-1} and 1424 cm^{-1}, respectively.

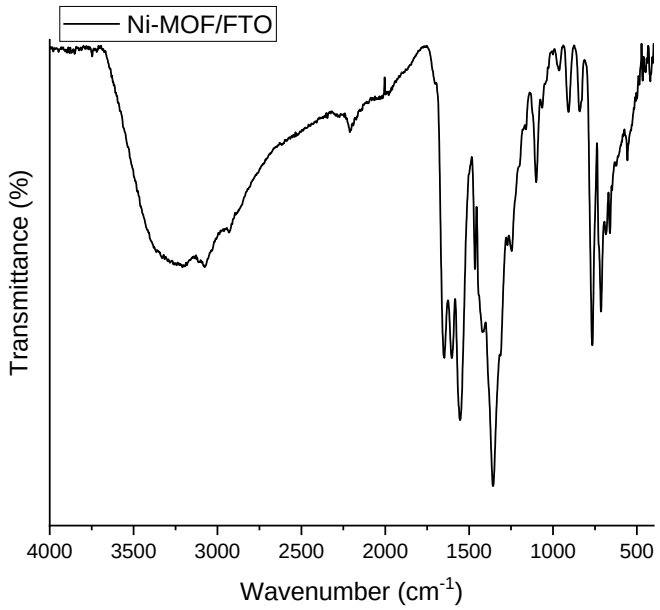

Figure 4.31: FT-IR spectrum of Ni-MOF/FTO.

Raman spectroscopy was carried out on the electrodeposited **Ni-MOF/FTO** thin films. The Raman spectrum of **Ni-MOF/FTO** was measured from 200 cm^{-1} to 2500 cm^{-1} and the baseline was corrected using OriginLab 2020 software. The Raman spectra of **Ni-MOF** and **Ni-MOF/FTO** (Fig. 4.32) correlate well, revealing signals that can be assigned to the *ν*(C≡C) vibrations at *ca.* 2200 cm^{-1}, which in contrast is very weak or not visible in the FT-IR spectra for the corresponding **Ni-MOF** (Fig. 4.13) and **Ni-MOF/FTO** (Fig. 4.31).[63,64] The *ν*(C=C) vibrations derived from the heteroaromatic moieties can be seen at *ca.* 1590 cm^{-1} and *ν*(C–C) vibrations are observed at *ca.* 1321 cm^{-1} and *ca.* 1278 cm^{-1}. The *ν*(C–H) vibrations attributed to the aromatic rings can be seen at *ca*. 1034 cm^{-1}, 1120 cm^{-1} and 1149 cm^{-1}.[61] Finally, very weak bands below 650 cm^{-1} can be attributed to inorganic and metal-organic groups.[64]

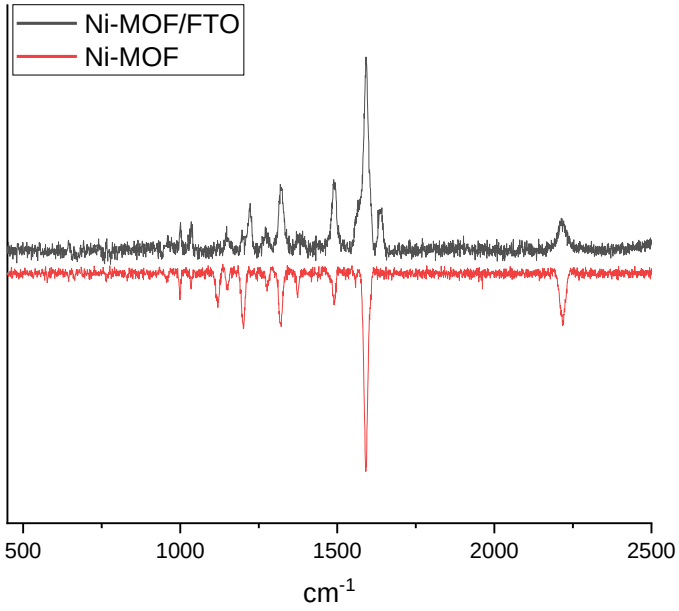

Figure 4.32: Raman spectra of Ni-MOF (red) vs Ni-MOF/FTO (black).

SEM and EDX measurements were carried out on freshly electrochemically deposited **Ni-MOF/FTO** electrodes. The FTO electrode was mounted on adhesive carbon tape and an acceleration of 10 keV was used for the EDX analysis of the material. The data demonstrated an expected atomic weight percentage ratio of approximately 1:1 of Ru^{II} to Ni^{II}. Figure 4.33a shows the SEM image for the **Ni-MOF/FTO**. The image illustrates the homogenous electrochemically synthesised **Ni-MOF/FTO**. Figure 4.33b below shows the effect of desolvation on the **Ni-MOF/FTO**, causing aggregation and amorphisation and formation of cracks in the MOF thin film on the FTO electrode.

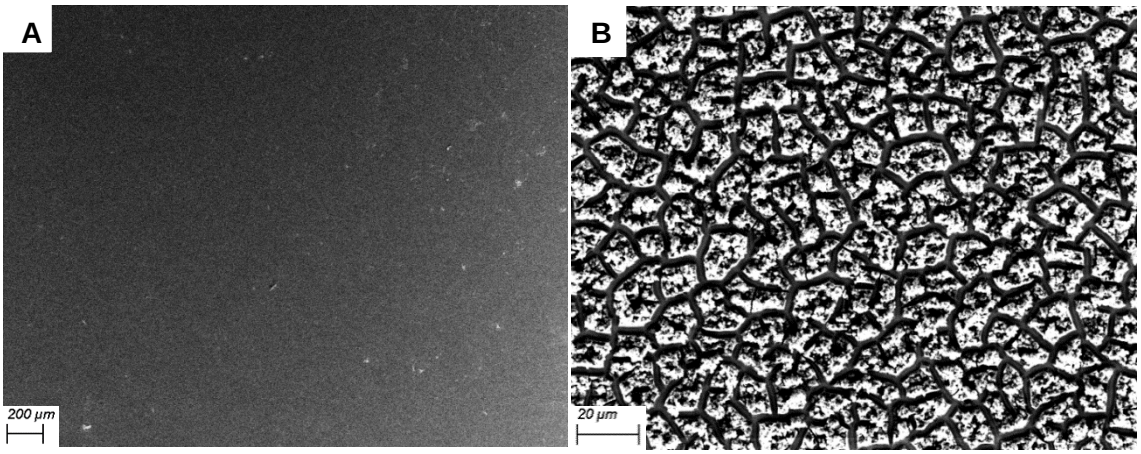

Figure 4.33: SEM images of a Ni-MOF/FTO at different magnifications.

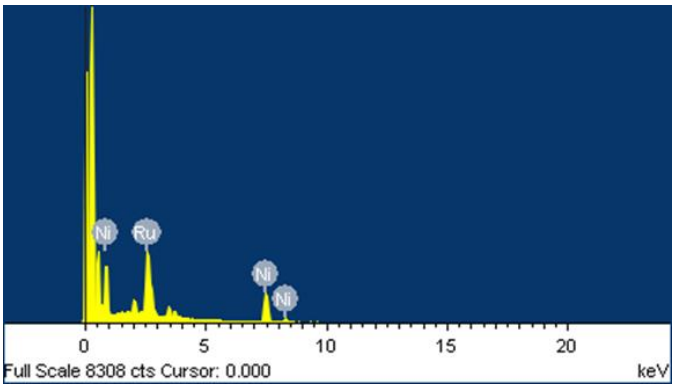

Figure 4.34: EDX analysis for Ni-MOF/FTO.

Table 4.5: EDX data obtained for Ni-MOF/FTO.

Element	Atomic (%)
Ni	53.42
Ru	46.58

4.7 Photo-Electrocatalytic Water Oxidation Studies of Ni-MOF/FTO

As mentioned previously, the flexible design principles of MOFs enable the molecular construction of photoanodes for *direct* 'solar-to-fuel' H_2 technologies and H_2O oxidation, operating under mild conditions at high electron transfer rates. Photoexcited Ru^{II} polypyridyl complexes and their analogues can be used to drive processes such as chemical transformations through electron transfer reactions initiated by light absorption.[82–85] Thus, the natural dielectric, hydrophobic lipid environment of photosystem-II can be replicated through the use of organic ligand residues and organic solvent/water mixtures.[24] However, *indirect* industrial electrolysis processes that are currently used operate in harsh conditions of strongly acidic or basic solutions and require external photovoltaic cells that are not stable in such highly corrosive media.[25] Therefore, *direct* and molecular approaches are highly favourable and analytical protocols have previously been developed to access the H_2O activity of biomimetic cluster species or polygons that contain earth-abundant metal ions.[86–88]

Electrochemical techniques are imperative in coupling photo-induced electron-transfer processes of photoactive materials to electrochemical transformations, such as photoelectrochemical (PEC) H_2O oxidation, as it relates the flow of electrons to chemical changes.[89] Cyclic voltammetry (CV) is a valuable electrochemical technique employed to study reaction mechanisms that involve the transferring of electrons, *i.e.* the reduction and oxidation processes of molecular species. This technique comprises of linearly varying an applied electrode potential (E) between two limits at a specific scan rate while monitoring the current density (j) response that develops in the electrochemical cell.[89] Linear sweep voltammetry (LSV) is a basic potentiostatic sweep method that is equivalent to a one-segment CV experiment. The current density (j) response at a working electrode is measured while the applied electrode potential (E) between the working electrode and a reference electrode is swept linearly in time between the initial and final limit values.

To characterise the functionality and applicability of the **Ni-MOF/FTO** electrodes, preliminary photo-electrocatalytic H_2O oxidation studies were conducted. To ensure the stability of **Ni-MOF/FTO** films and avoid hydrolytic decompositions often observed for MOFs, the experiments were conducted in MeCN solutions to which specific quantities of H_2O were added. The use of organic solvents is in line with biomimetic experiments that replicate the dielectric, hydrophobic environment of the membrane protein of photosystem-II, which operates using stoichiometrically controlled amounts of H_2O.[24]

CV and LSV experiments were conducted using a Bio-logic VSP potentiostat (a Bio-logic VSP instrument, 600D) in a photoelectrochemical cell (LED 0.149 W, $\lambda = 470$ nm) under N_2 flow using a 3-electrode set-up consisting of a **Ni-MOF/FTO** working electrode, a Pt-mesh counter electrode, a saturated calomel electrode (SCE) as the reference electrode and using tetrabutylammonium hexafluorophosphate ($(NBu_4)PF_6$) (0.1 M) as electrolyte.

A solvent mixture of 5% (v/v) H_2O in MeCN was chosen for the experiments as higher water concentration lead to hydrolysis of the **Ni-MOF/FTO**. Research by Hidalgo-Acosta *et al*. has also shown that the rate of H_2O oxidation in MeCN solutions containing high water concentrations to be significantly slower then MeCN solutions containing lower water concentrations.[90] They identified that highly stable and less reactive hydrogen bonding arrangements of H_2O exist in MeCN solutions containing high water concentrations. Whereas, in solutions containing lower water concentrations, clustering of H_2O molecules brings about the formation of water-rich micro-domains where the overall concentration of H-bonded H_2O molecules is reduced. Therefore, this non-H-bonded H_2O present in the micro-domains of MeCN/H_2O solvent mixtures containing low water concentrations has been found to be highly more reactive towards oxygen production.[90]

Cyclic voltammetry (CV) within a potential range of -1.0 V to 1.3 V (vs SCE) (all potentials herein are referenced vs SCE unless otherwise stated) in dry MeCN was initially used as reference data. A detected suppressed catalytic signal is attributable to the oxidation of residual constitutional and coordination H_2O present in the structure of **Ni-MOF** (Fig. 4.35). Following, the addition of 5-vol-% H_2O clearly highlights a substantial deviation from the reference experiment due to the appearance of an oxidative multielectron process attributed to electrocatalytic water oxidation. The onset potential

appears at *ca.* 1.12 V. Upon blue light irradiation, a strong photo-response is observed in the CV, whereby the onset potential of the electrocatalytic H_2O oxidation is reduced by >90 mV to 1.03 V. At an applied potential of 1.3 V, the catalytic current density was found to increase dramatically from 0.12 mA for the reference experiment to 0.57 mA upon light irradiation.

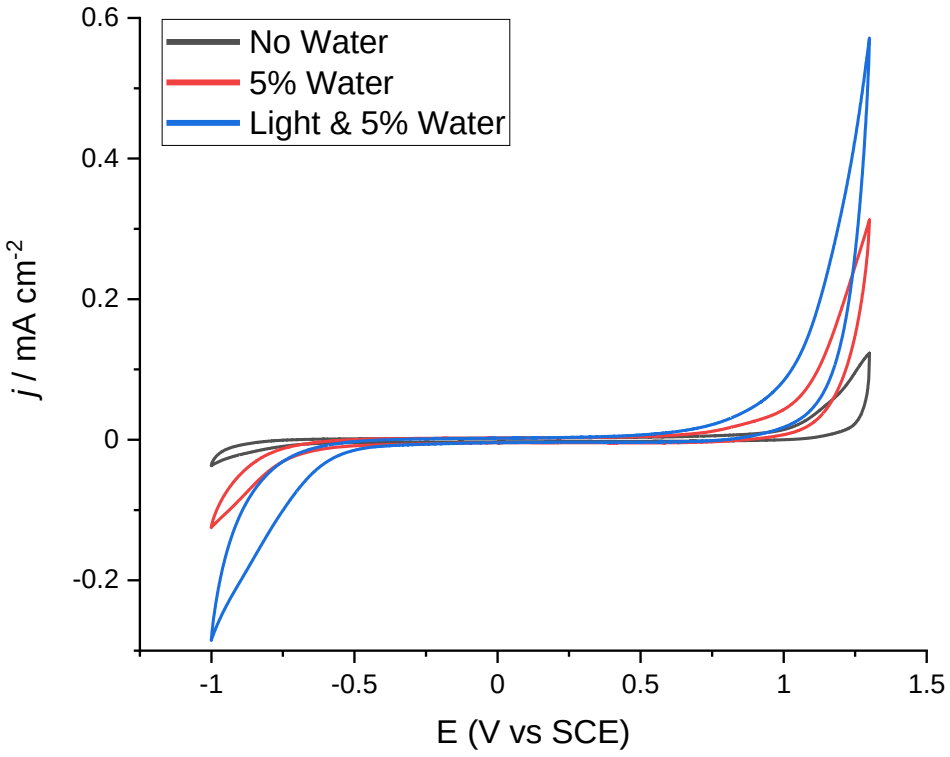

Figure 4.35: CV highlighting the light-influenced water oxidation process in the presence of variable quantities of H_2O; 0% H_2O reference experiment (black), 5% H_2O experiment (red) and 5% H_2O and LED light irradiation (blue).

Similarly, linear sweep voltammetry (LSV) experiments were further used to characterise the catalytic behaviour in the dark and under light irradiation (Fig. 4.36). An electrocatalytic onset potential of 1.18 V (vs SCE) was recorded under dark conditions for systems that contain 5-vol-% H_2O. In comparison, the onset potential shifts significantly under light irradiation by 140 mV to 1.04 V (vs SCE) due to the photo-generated oxidative current.

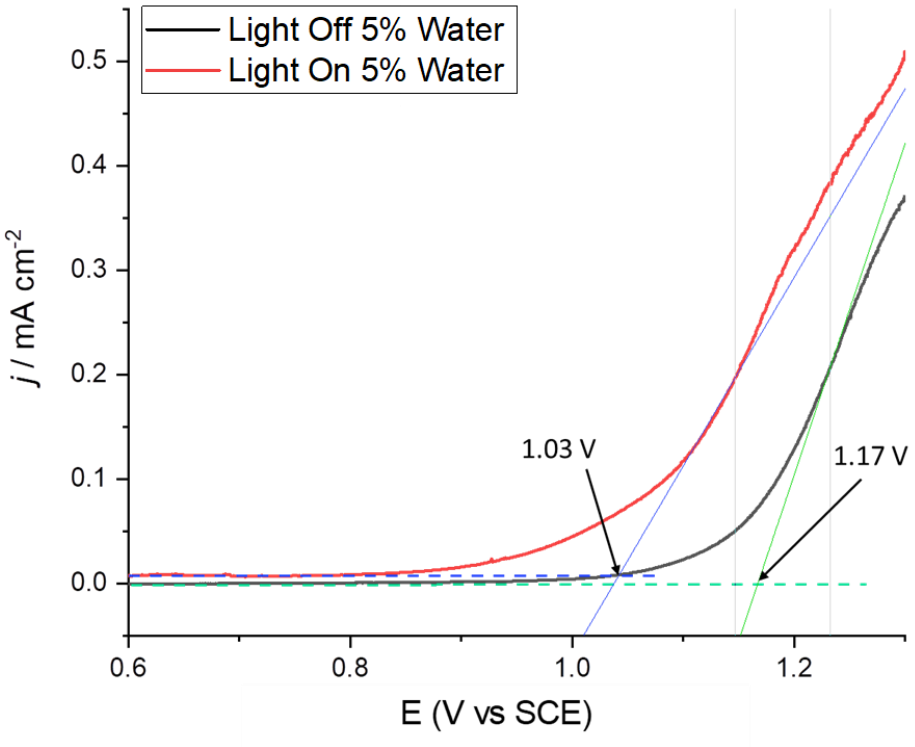

Figure 4.36: LSV in the dark (black) and upon LED light irradiation (red).

After completion of the CV and LSV experiments, visual inspection of the **Ni-MOF/FTO** films indicated neither loss of material nor a colour variation of the deposited MOF (Fig. 4.37).

Pre-Catalysis Post-Catalysis

Figure 4.37: Optical images of Ni-MOF/FTO pre-catalysis (left) and post-catalysis (right).

To further evaluate **Ni-MOF/FTO** as a photoanode, its photo-voltage at an open circuit (V_{photo}), defined as the difference between the potential in the dark (V_{dark}) and under light irradiation (V_{light}), was measured (Fig. 4.38). These measurements characterise the electrode's photo-induced charge separation and light-induced charge accumulation processes.[91] Upon light irradiation at $\lambda = 470$ nm, an initial cathodic shift with a V_{photo} of

300 mV was obtained, indicating an accumulation of electrons at the electrode upon light irradiation. **Ni-MOF/FTO** was subsequently irradiated at intervals of *ca.* 9 min., followed by short relaxation periods, giving a reoccurring V_{photo} of 150 mV. The photoanodic behaviour of **Ni-MOF/FTO** was substantiated, demonstrating good stability with no detectable photobleaching.

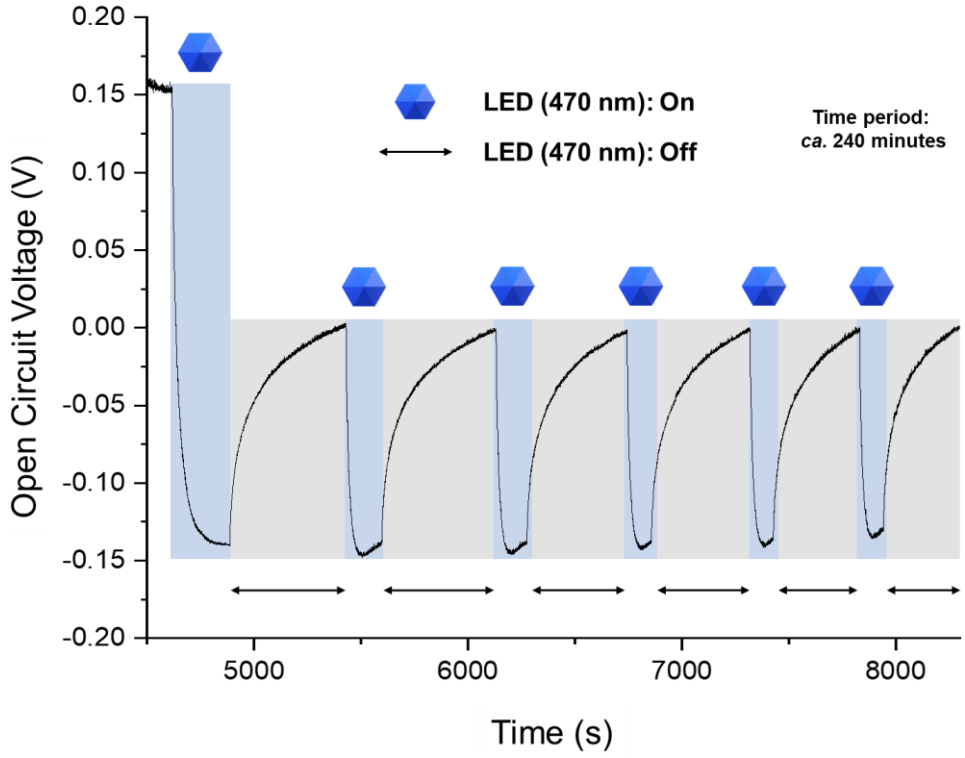

Figure 4.38: Photo-voltage characteristics of Ni-MOF upon light irradiation (LED, λ = 470 nm)

The data obtained from the catalytic experiments underline the ability of **Ni-MOF/FTO** to promote the light-induced hole-formation involving the HOMO levels of the $\mathbf{L_{bpy}\text{-}R_3^{2-}}$ chromophores facilitating the oxidation of the Ni^{II} centres and the H_2O substrates, which act as electron donors. The process results in the accumulation of negative charges at the **Ni-MOF/FTO** electrode. The pronounced light influence on the onset-overpotentials of the H_2O oxidation reaction is remarkable within the literature.[92] It highlights the scope of photoactive MOFs as photo-electrocatalysts in highly endergonic energy conversion processes. The prepared electrodes appear stable and are applicable in consecutive catalytic test runs.

Upon successful completion of the photo-electrocatalytic water oxidation experiments, post-catalytic characterisation of the **Ni-MOF/FTO** was conducted. FT-IR, Raman and EDX spectroscopy analyses were used in order to investigate the stability of the MOF thin films and to identify whether any decomposition products, such as metal oxides had formed on the electrodes during the photo-electrocatalytic studies.

Figure 4.39 illustrates the FT-IR spectrum of **Ni-MOF/FTO** post-photo-electrocatalytic water oxidation experiments. Identical characteristic vibrational bands to that of freshly prepared **Ni-MOF/FTO** thin films can be observed. Additionally, no detectable impurities can be seen. Similar to the FT-IR, Raman spectroscopy indicated neither a change in the **Ni-MOF/FTO** thin film electrodes nor the formation of metal oxides or other impurities. These experiments indicate that the post-photoelectro-catalytic **Ni-MOF/FTO** films are identical to that of pristine, freshly prepared **Ni-MOF/FTO** thin films previously discussed in this chapter.

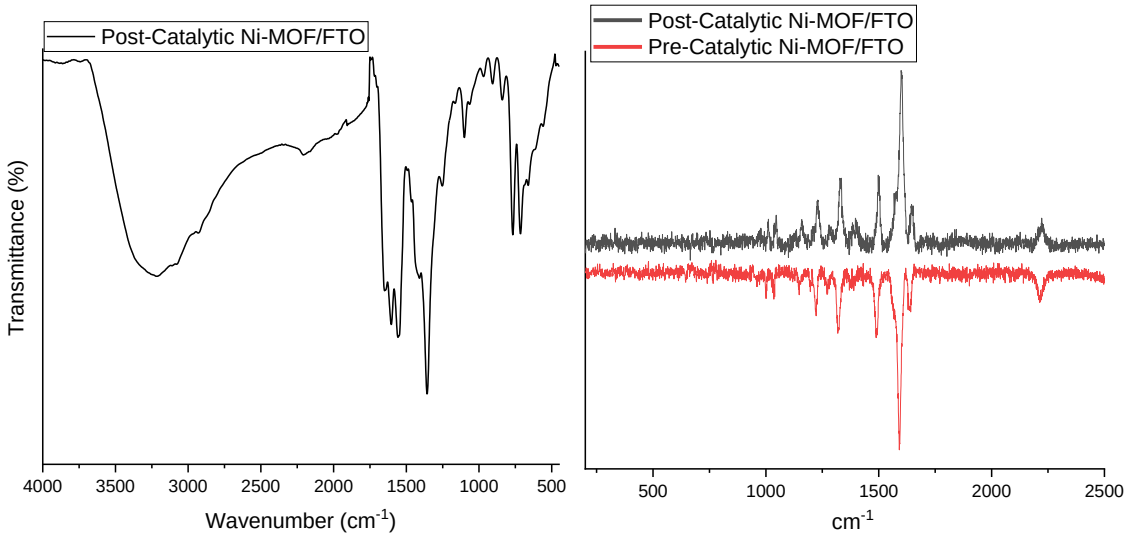

Figure 4.39: FT-IR spectrum of Ni-MOF/FTO post-catalysis and Raman spectra of Ni-MOF/FTO pre-catalysis (red) and post-catalysis (black).

Finally, SEM and EDX measurements were performed on the post-catalytic **Ni-MOF/FTO** thin films. The data demonstrated the expected atomic weight percentage ratio of approximately 1:1 of Ru^{II} to Ni^{II} which was previously obtained for both **Ni-MOF** and pre-catalysis **Ni-MOF/FTO**. Figure 4.40a shows an SEM image for the post-catalytic **Ni-MOF/FTO**, demonstrating retention of the homogenous MOF thin film post-catalysis. As described before, the removal of the **Ni-MOF/FTO** from the electrolyte mixture leads to the aggregation and amorphisation of the crystals (Fig 4.40b).

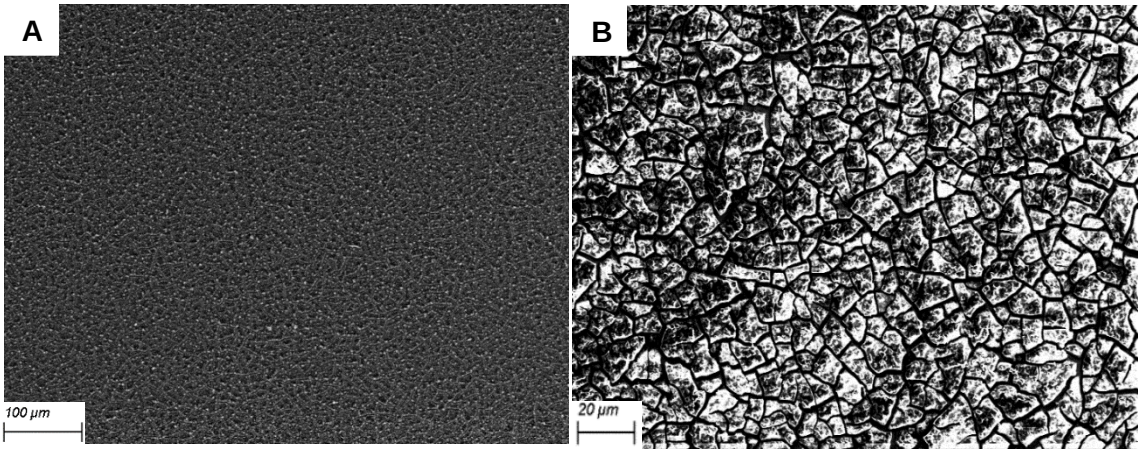

Figure 4.40: SEM images of Ni-MOF/FTO post-catalysis at different magnifications.

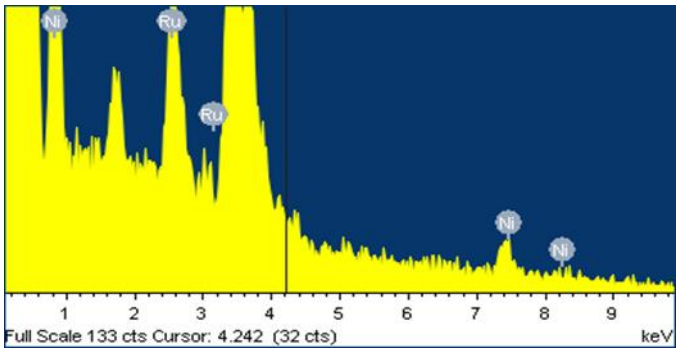

Figure 4.41: EDX analysis for Ni-MOF/FTO post-catalysis.

Table 4.6: EDX data obtained for Ni-MOF/FTO post-catalysis.

Element	Atomic (%)
Ni	52.37
Ru	47.63

4.8 Preliminary Absorption Studies of Guest Molecules Within Ni-MOF and Ni-MOF/FTO

Upon obtaining the crystal structure of the **Ni-MOF** and estimating its available pore sizes using RASPA,[47] it was anticipated that the large cavities discussed previously could be utilised for the absorption of guest molecules. The pores of the **Ni-MOF** were utilised to absorb buckminsterfullerene molecules (C_{60}). Cramer *et al*. revealed that incorporating C_{60} into the pores of porphyrin-containing MOFs increases electrical conductivity *via* π-mediated donor-acceptor interactions, as evidenced by the calculation of electronic transfer integrals for materials with and without C_{60}.[93] Therefore, it was anticipated that the absorption of such highly conductive compounds would in turn improve the conductivity of the photoanodes for *direct* 'solar-to-fuel' H_2 technologies and H_2O oxidation applications.[94,95]

In order to achieve successful absorption of the guest molecule a concentrated solution of C_{60} in DMF was added to a quantity of **Ni-MOF** single crystals. The solution was allowed to sit in the dark for a period of two weeks prior to observing a change in colour of the crystals and a reduction in the colour intensity of the mother liquor (Fig. 4.43). The DMF solvent mixture containing excess C_{60} was removed, and the crystals were washed prior to analysis *via* Raman spectroscopy. Figure 4.42 below illustrates the Raman spectra measured between 200 cm^{-1} and 2500 cm^{-1} of **Ni-MOF** with C_{60} and freshly prepared **Ni-MOF**. The data obtained demonstrate three new signals for the **Ni-MOF** at *ca.* 267 cm^{-1}, *ca.* 494 cm^{-1} and *ca.* 1459 cm^{-1} corresponding to C_{60} which are not visible when compared to the freshly prepared **Ni-MOF** Raman spectrum.[96]

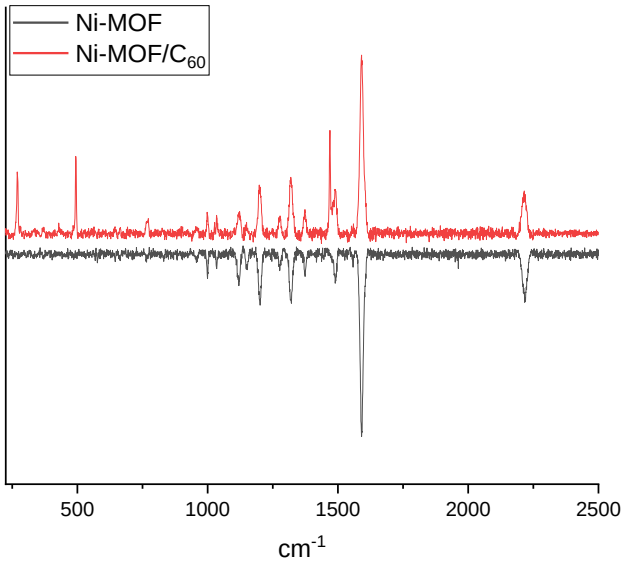

Figure 4.42: Raman spectra of Ni-MOF (red) and Ni-MOF with C_{60} (black).

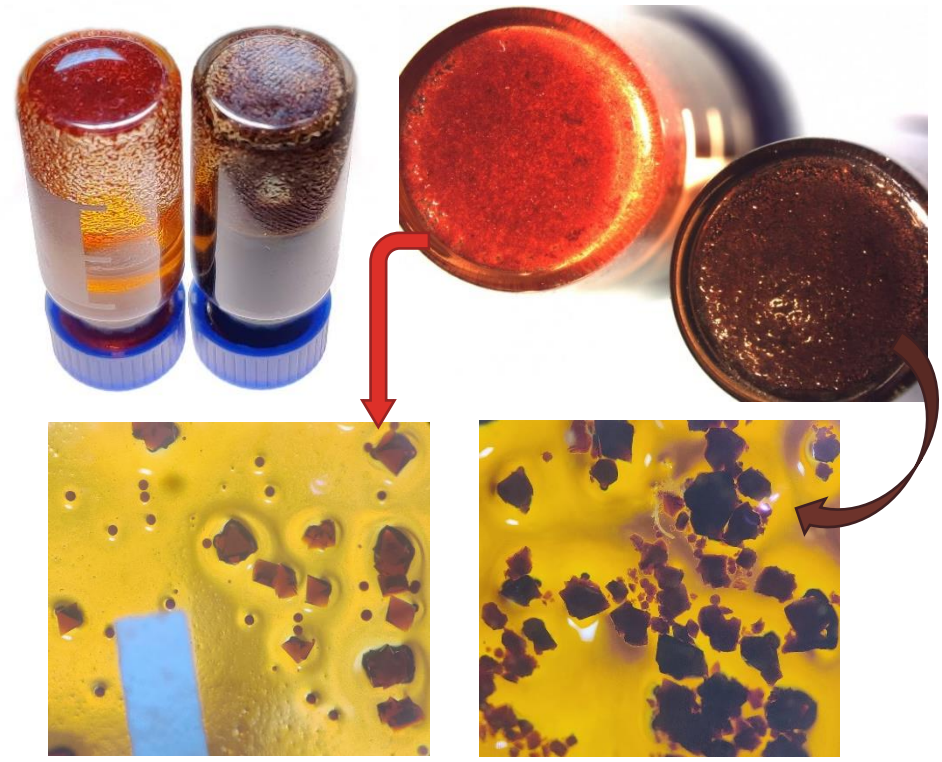

Figure 4.43: Optical images of Ni-MOF without C_{60} (orange) and Ni-MOF with C_{60} (brown) after two weeks.

Following the successful uptake of C_{60} within the cavities of the single crystals of **Ni-MOF**, an identical procedure was carried out with freshly prepared **Ni-MOF/FTO** electrodes. The thin films were placed in a vial containing a saturated solution of C_{60} for again two weeks. A colour change from orange to deep brick red was observed (Fig. 4.44). Raman spectroscopy of the **Ni-MOF/FTO** was conducted after washing the film with fresh DMF. The Raman spectrum was measured from 200 cm^{-1} to 2500 cm^{-1} and the baseline was corrected using OriginLab 2020 software. The Raman spectrum (Fig. 4.45) again demonstrated additional signals at *ca.* 265 cm^{-1}, *ca.* 492 cm^{-1} and *ca.* 1457 cm^{-1} that can be attributed to C_{60}.[96]

Preliminary water oxidation studies using the **Ni-MOF/FTO** electrodes containing C_{60} demonstrated a reduction in the onset potential and an increase in the current density. However, it was found that light irradiation had no impact on the onset potential or current density in the case of these electrodes as C_{60} inhibits the photoactive capabilities of **Ni-MOF/FTO**.

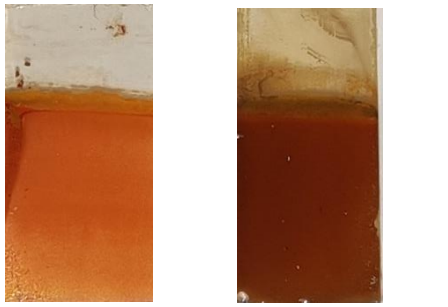

Figure 4.44: Optical images of Ni-MOF/FTO without C_{60} (orange) and Ni-MOF/FTO with C_{60} (brown) after two weeks.

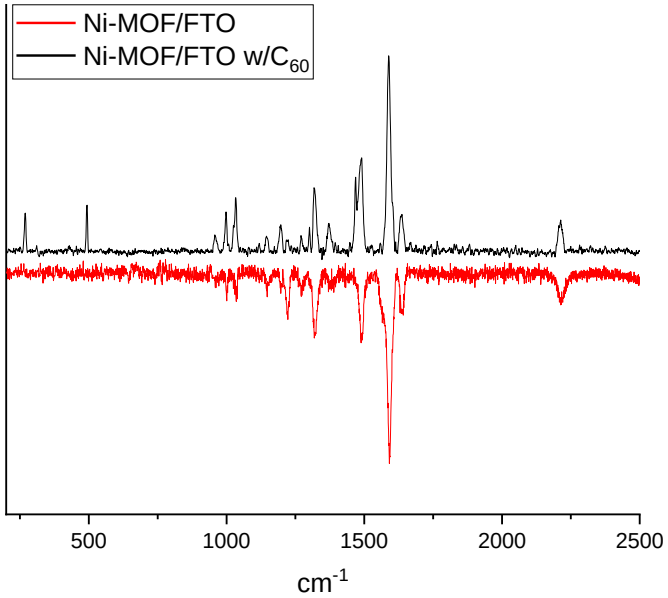

Figure 4.45: Raman spectra of Ni-MOF/FTO (red) and Ni-MOF/FTO with C_{60} (black).

4.9 Synthesis of Co-MOF ($Co_6(L_{bpy}\text{-}R_3)_{12}(H_2O)_{12}$)

Red octahedral-shaped single crystals suitable for single-crystal X-ray diffraction studies of the photoactive MOF, **Co-MOF**, $[Co(\mathbf{L_{bpy}\text{-}R_3})(H_2O)_2]$, were obtained in high yields under solvothermal conditions in anhydrous DMF. Crystallisation occurs between $\mathbf{H_4[L_{bpy}\text{-}R_3]^{2+}}$ and $Co(NO_3)_2{\cdot}6H_2O$ at a mole ratio of 1:8. To ensure a homogenous solution, the reactant mixture was sonicated at room temperature for 10 minutes, during which both reactants dissolved resulting in a deep, red solution. On heating at 65 °C for 72 hours, the red octahedral-shaped crystals of **Co-MOF** were obtained (Fig 4.46).

Figure 4.46: Optical microscope images of synthesised crystals of Co-MOF.

4.10 Structural Characterisation of Co-MOF

Single-crystal X-ray diffraction studies demonstrate that **Co-MOF** is isostructural to the previously discussed **Ni-MOF**. **Co-MOF** was identified to crystallise in the cubic space group $Fm\bar{3}m$ (Fig 4.47). The framework structure, identical to **Ni-MOF**, consists of cubohemioctahedral $\{Co_6(\mathbf{L_{bpy}\text{-}R_3})_{12}(H_2O)_{12}\}$ coordination cages which have been described in detail in **Section 4.3**. The individual Co^{II} centres in **Co-MOF** again adopt tetragonally distorted octahedral coordination environments. This environment consists of four symmetry equivalent O-donors of four $\mathbf{L_{bpy}\text{-}R_3^{2-}}$ ligands accompanied by two coordinated H_2O molecules occupying the trans-located apical positions positioning radial to the inside or outside of the cage (Fig 4.47). The supramolecular cage for **Co-MOF** has been measured to comprise of an internal diameter (Co^{II} – Co^{II}) of

11.12 Å. From the crystal structure data, the bond distances in the **Co-MOF** octahedral coordination environment vary slightly in comparison to that of **Ni-MOF**. The **Co-MOF** shows slightly longer Co-O bond distances compared to the Ni-O bonds in **Ni-MOF**. Table 4.7 lists the detailed coordination data for the metal centres of **Co-MOF**. Complete crystallographic data and structure refinements are provided in Table 4.8.

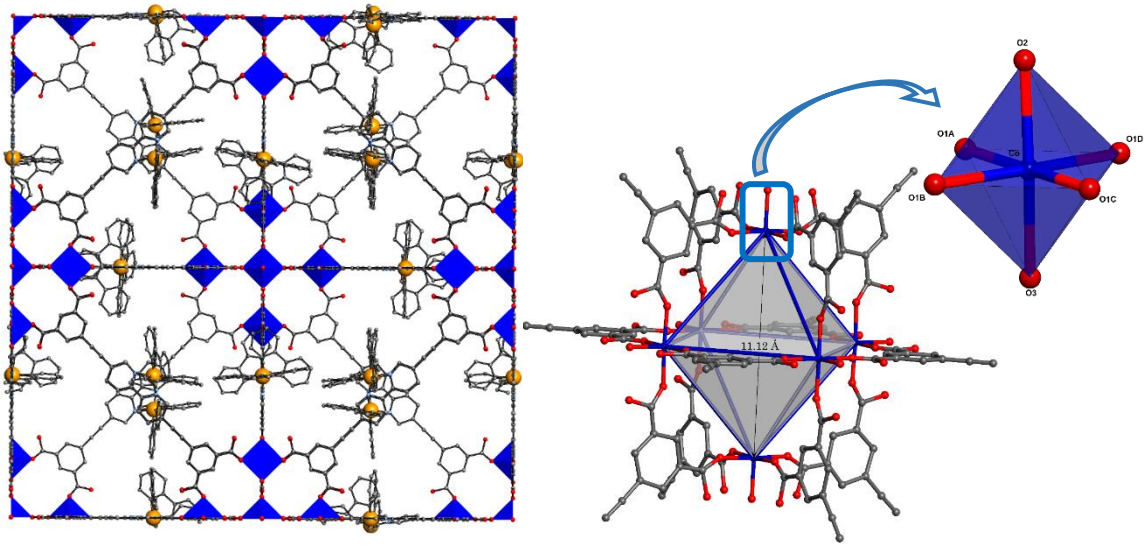

Figure 4.47: Structure of Co-MOF with a view in the direction of the crystallographic *c*-axis (left). Co cubohemioctahedral coordination cage {$Co_6(L_{bpy}\text{-}R_3)_{12}(H_2O)_{12}$} unit and octahedral coordination environment for Co^{II} in Co-MOF (right). Subscripts indicate symmetry-generated atoms. Colour scheme: Co (blue), O (red), C (grey). H atoms were omitted for clarity.

Table 4.7: Selected bond lengths and angles from single-crystal XRD for the Co-MOF.

Atom			Angle (°)	Atom		Distance (Å)
$O1_A$	Co	$O1_C$	177.149(4)	Co	$O1_A$	2.054(1)
$O1_A$	Co	$O1_B$	89.965(3)	Co	$O1_B$	2.054(4)
$O1_B$	Co	O3	88.572(4)	Co	$O1_C$	2.054(1)
$O1_C$	Co	O2	91.425(2)	Co	$O1_D$	2.054(4)
$O1_D$	Co	O3	88.572(4)	Co	O2	2.164(2)
O2	Co	O3	180.002(1)	Co	O3	2.114(1)

The **Co-MOF** $\{Co_6(\mathbf{L_{bpy}\text{-}R_3})_{12}(H_2O)_{12}\}$ cages which are seen in the network, represent nanoscopic, 12-connected nodes. Each node, akin to the **Ni-MOF** previously discussed in this chapter, is linked through linear $\mathbf{L_{bpy}\text{-}R_3^{2-}}$ metallo-ligands which stabilise the highly augmented, quasiregular face-centred cubic **fcu-a** net that is characterised by $m\bar{3}m$ (O_h) symmetry (Fig. 4.48).[31–33] Within the framework of the **Co-MOF**, substantial cage-type cavities with truncated tetrahedral and octahedral geometries can be found and were previously seen in the isostructural **Ni-MOF**. As discussed previously for the **Ni-MOF**, the **Co-MOF** (Fig. 4.48) also contains a sequence of channels which are lined with photoactive ruthenium centres that have the potential to be utilised in photocatalytic applications.[34,35] Since the same metallo-ligand was used for the synthesis of the **Co-MOF**, it was expected that the **Co-MOF** would retain the same rotational flexibility as the **Ni-MOF**. The high R_1 value of 0.1946 obtained for the **Co-MOF** can partly be attributed to this structural disorder caused by the low energy barrier for rotation.

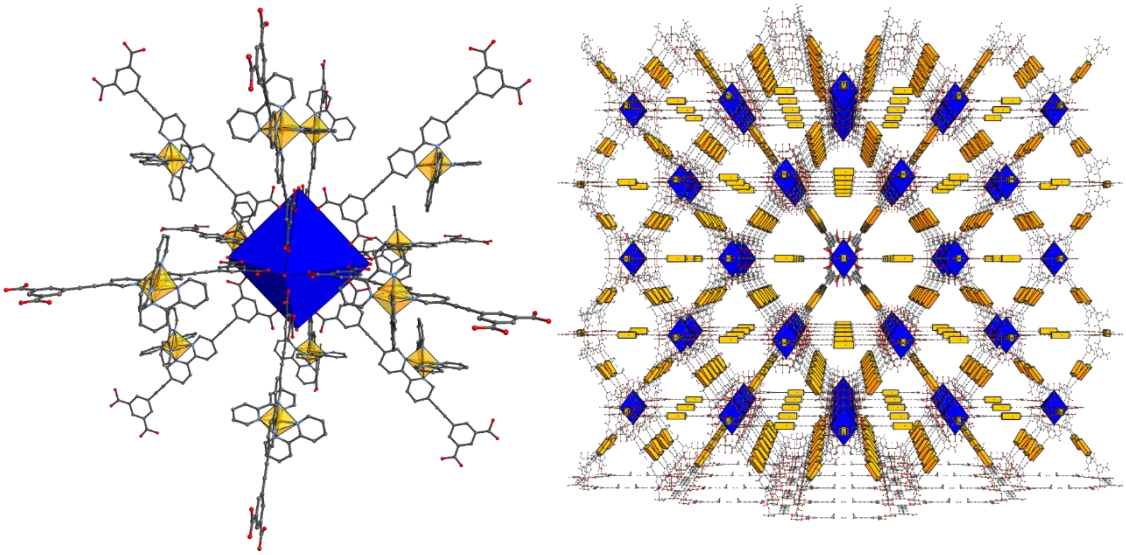

Figure 4.48: 12-connected octahedra forming *fcu-a* network characterised by $m\bar{3}m$ (O_h) symmetry (left). Packing diagram of Co-MOF viewed along the crystallographic *a*-axis demonstrating the channels present within the framework (right. Colour scheme: Ru (orange), Co (blue), O (red), and C (grey). H atoms were omitted for clarity.

Table 4.8: Single-crystal X-ray diffraction data and structure refinement for Co-MOF.

Identification code	Co-MOF
Empirical formula	$C_{300}H_{240}N_{36}Co_6O_{60}Ru_6$
Formula weight	6456.30
Temperature/K	215(2)
Wavelength/Å	1.54184
Crystal system	Cubic
Space group	$Fm\bar{3}m$
a/Å	47.733(8)
b/Å	47.733(8)
c/Å	47.733(8)
α/°	90
β/°	90
γ/°	90
Volume/$Å^3$	108754(55)
Z	4
$\rho_{calc}Mg/m^3$	0.394
μ/mm^{-1}	1.658
F(000)	13156
Crystal size/mm^3	0.33 x 0.33 x 0.33
Radiation	CuKα (λ = 1.54184)
2Θ range for data collection/°	3.206 to 69.834
Index ranges	-32<=h<=28,-35<=k<=17,-35<=l<=19
Reflections collected	17172
Independent reflections	1225 [R_{int} = 0.0626, R_{sigma} = 0.0290]
Completeness to theta = 34.917°	100%
Absorption correction	Semi-empirical from equivalents

Max. and min. transmission	0.7504 and 0.0439
Refinement method	Full-matrix least-squares on F^2
Data/restraints/parameters	1225/49/57
Goodness-of-fit on F^2	2.600
Final R indexes [I>=2σ (I)]	R_1 = 0.1946, wR_2 = 0.5322
Final R indexes [all data]	R_1 = 0.2144, wR_2 = 0.5519
Largest diff. peak/hole / e $Å^{-3}$	0.764/-0.814

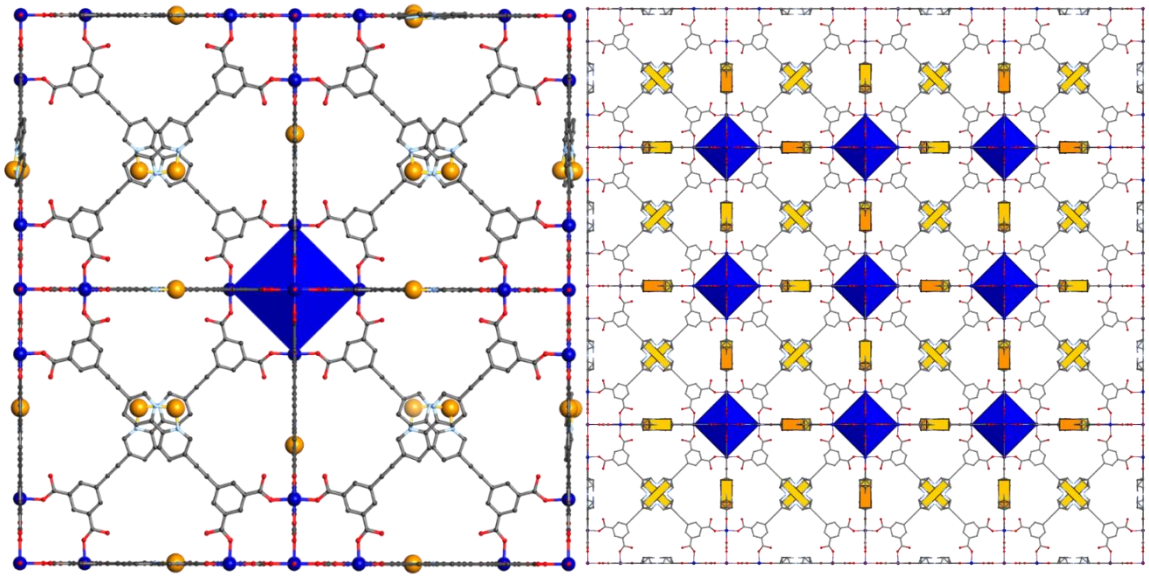

Figure 4.49: Unit cell of Co-MOF (left). Simplified structural representation of Co-MOF in which the Ru-pyridyl moieties are represented as orange stereocylinders with a view in the crystallographic [111] direction (right). Colour scheme: Ru (orange), Co (blue), O (red), and C (grey). H atoms were omitted for clarity.

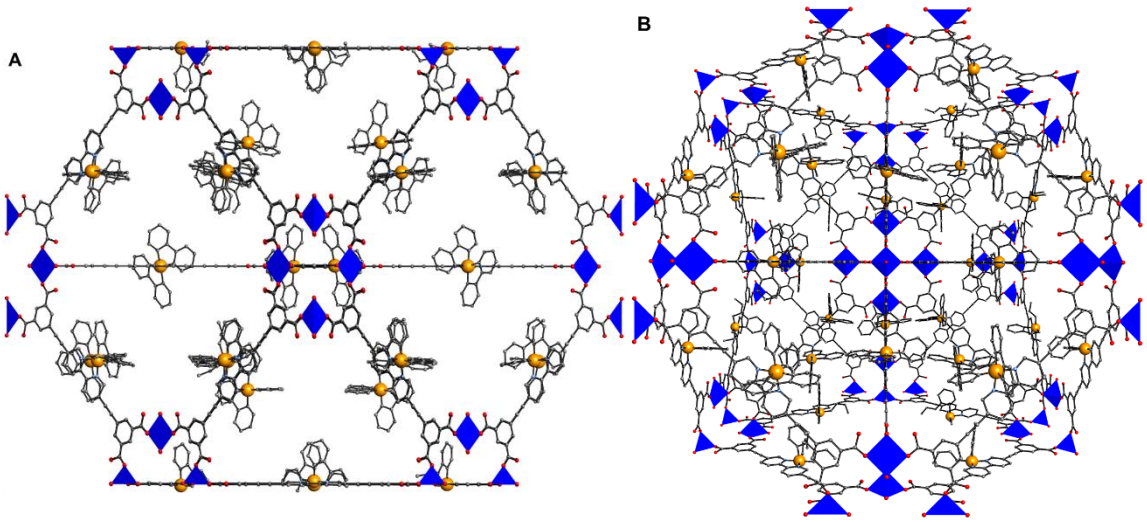

Figure 4.50: Co-MOF structure viewed in the direction of the crystallographic [111] (A) and *c*-axis (B). Colour scheme: Ru (orange), Co (blue), O (red), and C (grey). H atoms were omitted for clarity.

The phase purity of a bulk sample of **Co-MOF** was confirmed *via* PXRD experiments which were carried out in capillaries containing DMF. A PXRD pattern of an as-synthesised **Co-MOF** compared to a powder pattern calculated from the respective single-crystal X-ray diffraction data can be seen in Figure 4.51. The data obtained demonstrates closely matching signals between the two spectra, confirming the phase purity of the sample. The experimental pattern is characterised by signals that appear at 2θ = 5.23°, 7.78°, 9.19°, 11.11°, and 13.20°. Additionally, highly similar signals can be seen when comparing the PXRD patterns of **Co-MOF** and **Ni-MOF**.

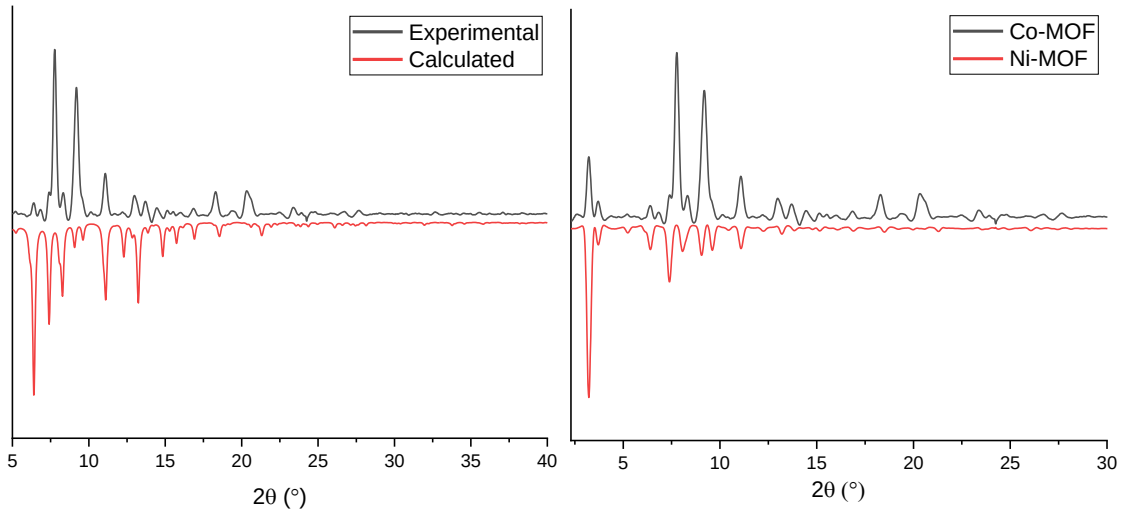

Figure 4.51: Powder X-ray Diffraction patterns for Co-MOF experimental and Co-MOF calculated (left), Co-MOF and Ni-MOF (right).

4.11 Physicochemical Characterisation of Co-MOF

Co-MOF was further characterised to obtain an insight into its physicochemical properties. The FT-IR spectrum (Fig. 4.52) demonstrated signals closely matching to that previously seen for **Ni-MOF**. The *ν*(O–H) stretches associated with solvent molecules in the pores of the MOF along with the H_2O molecules in the axial positions on the Co sites in the MOF are responsible for the broad signal seen at around *ca.* 3396 cm^{-1}.[49,50] The vibrational stretching bands derived from asymmetric ν_{as}(COO) and symmetric ν_s(COO) carboxylate stretches associated with the Ru^{II} polypyridine moieties within **Co-MOF** and can be seen at *ca.* 1568 cm^{-1} and *ca.* 1420 cm^{-1}, respectively.[53,54] The positions of these bands and their Deacon-Phillips value of $\Delta = (\nu_{as}-\nu_s) = 148$ cm^{-1} is characteristic of the observed *syn-η¹* carboxylate coordination mode of the carboxylate functions in **Co-MOF**.[55–57] The *ν*(Co–O) stretching vibration mode is characterised by a weak broad signal at *ca.* 559 cm^{-1}.[97]

Raman spectroscopy was performed on freshly prepared crystals of **Co-MOF**. The data obtained (Fig. 4.52) demonstrates that the signals are also closely matching to those seen previously for both **Ni-MOF** and $\mathbf{H_4[L_{bpy}\text{-}R_3]^{2+}}$. The signals between 1007 $cm^{-1}$and 1159 cm^{-1} can be attributed to the *ν*(C-H) vibrations.[61] The band at *ca*. 1207 cm^{-1} can be attributed to the δ(C–H) bending mode.[62] Signals at 1282 cm^{-1} and 1327 cm^{-1} arise from *ν*(C–C) single bond vibrations. The ν_s(C=O) vibrations that derive from the carboxylate groups can be observed at *ca*. 1380 cm^{-1}. The *ν*(C=C) vibrations are visible at *ca.* 1498 cm^{-1} and 1600 cm^{-1}. The particularly characteristic signal found at 2220 cm^{-1} can be attributed to the alkyne-moiety derived *ν*(C≡C) vibration.[63,64]

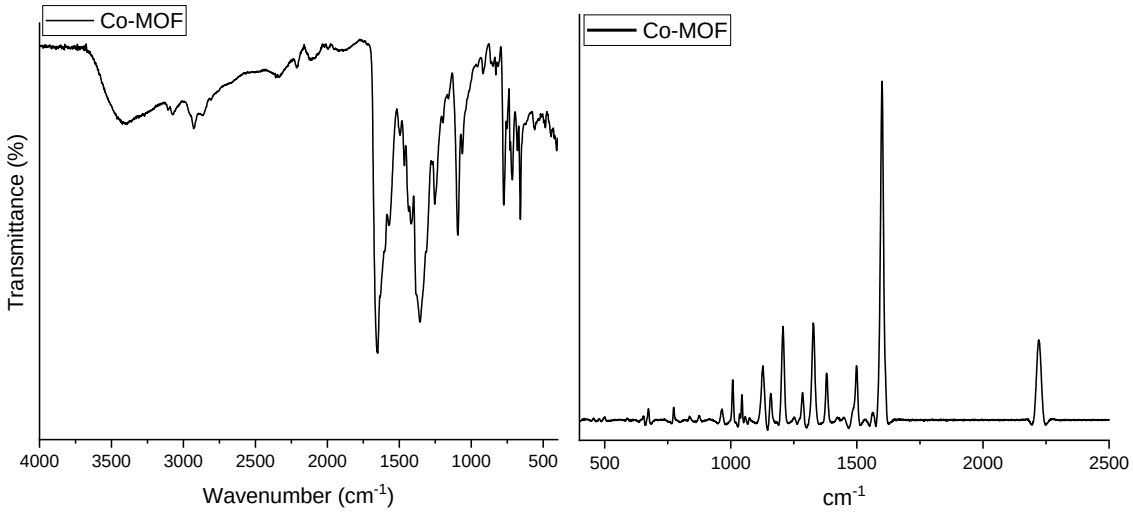

Figure 4.52: FT-IR spectrum (left) and Raman spectrum (right) of Co-MOF.

Thermogravimetric analysis was used to determine the thermal stability of a freshly prepared crystalline sample of **Co-MOF** (Fig. 4.53). Under a steady stream of air and in a temperature range of 30 °C to 600 °C, the data obtained confirms the expected decomposition pathway that proceeds two main steps. The first is associated with the removal of constitutional solvent molecules when heated between *ca.* 30 °C – 115 °C, resulting in a weight loss of *ca.* 16 %. When heated above 350 °C, a second thermogravimetric process occurs, which is attributed to the oxidative degradation of the organic ligand moieties present in **Co-MOF** and results in a weight loss of approximately 45 %.[65–67]

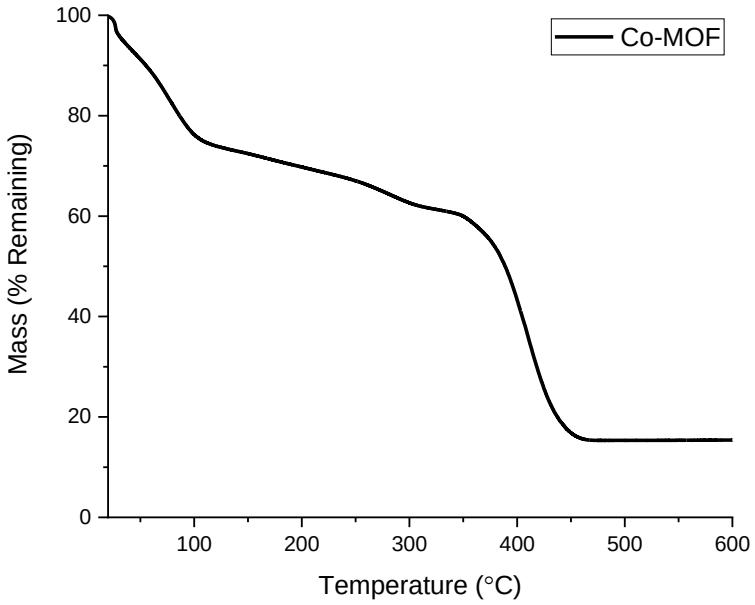

Figure 4.53: Thermogravimetic analysis of Co-MOF measured in an air atmosphere, at heating rate of 5 °C per minute.

On a freshly prepared sample of **Co-MOF**, SEM and EDX studies were performed (Fig 4.54. The data obtained verified the anticipated Ru^{II} to Co^{II} atomic weight percentage ratio of approximately 1:1. The EDX data supports the expected constitutional composition, indicating that both the Ru^{II}-based metallo-ligand and the Co^{II} SBU are present in the framework of **Co-MOF**.

Figure 4.54: SEM image of Co-MOF crystals.

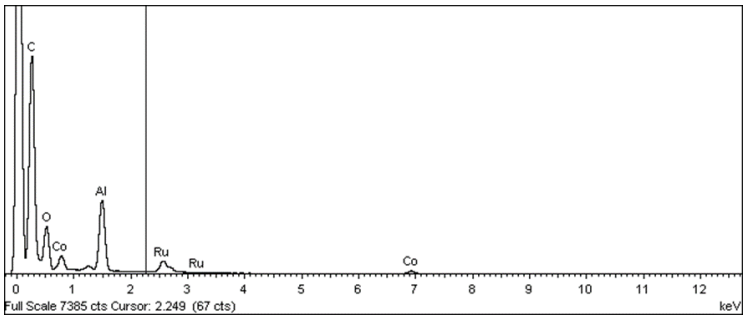

Figure 4.55: EDX analysis for Co-MOF.

Table 4.9: EDX data obtained for Co-MOF.

Element	App Conc.	Intensity	Atomic (%)
C	17.91	1.5045	72.09
O	3.64	0.6259	26.21
Co	0.56	0.7482	0.91
Ru	0.81	0.7642	0.79

4.12 Photophysical Characterisation of Co-MOF

Solid-state UV-vis absorption, spectral and time-resolved photoluminescence (PL and TRPL) tests were carried out on **Co-MOF**. Crystals of the MOF were dispersed in DMF and an identical procedure previously described for the **Ni-MOF** was used to examine and compare the photophysical properties of the **Co-MOF** to $\mathbf{H_4[L_{bpy}\text{-}R_3]^{2+}}$ and **Ni-MOF**.

The UV-vis spectrum of **Co-MOF** (Fig. 4.56) shows that there are no significant differences in the absorption profile between the **Co-MOF** and the **Ni-MOF (**Fig. 4.19), as they both display almost identical absorption spectra. The **Co-MOF** PL emission spectrum (Fig. 4.56) displays a broad emission band centred at 690 nm that is again slightly blue-shifted in comparison to that of $\mathbf{H_4[L_{bpy}\text{-}R_3]^{2+}}$, whilst again highly similar to that obtained for the **Ni-MOF** (Fig. 4.20). A broadening of the emission spectrum is observed and can be attributed to a redistribution of electrons as a result of the bonding between the Ru^{II} polypyridyl complex and the MOFs, consequently affecting the electronic structure of $\mathbf{H_4[L_{bpy}\text{-}R_3]^{2+}}$ in the MOFs. The data obtained demonstrated that the **Co-MOF** retains the same optical and light-harvesting properties as the **Ni-MOF** previously discussed.

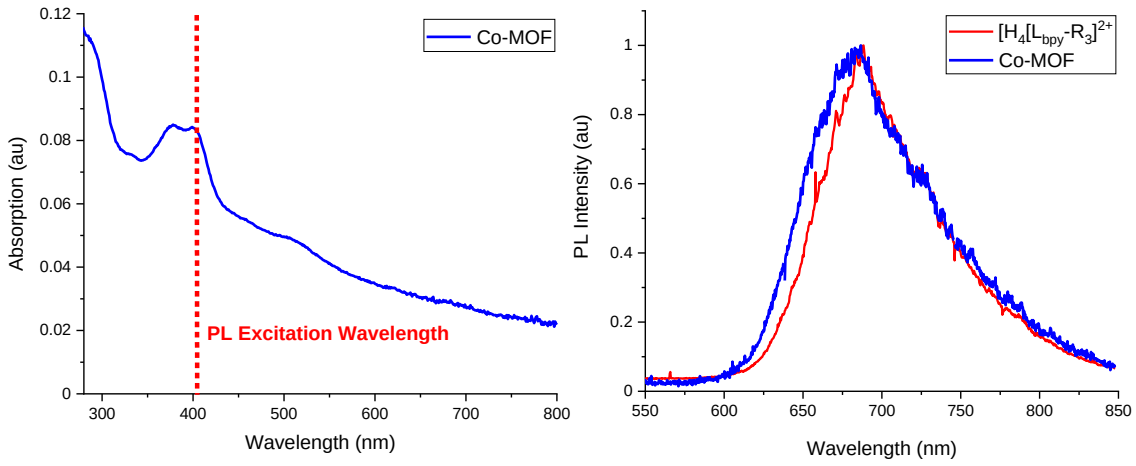

Figure 4.56: Vis-Absorption spectrum of Co-MOF (left) and normalised steady-state photoluminescence (PL) spectra of Co-MOF (blue) and $\mathbf{H_4[L_{bpy}\text{-}R_3]^{2+}}$ (red) (right). Photoluminescence (PL) excitation wavelength of 405 nm is indicated by the dotted line.

TRPL decays were recorded with a 700 nm bandpass filter and a 10 nm full width at half maximum (FWHM) using a 0.2 µW excitation power (Fig. 4.57). The data for **Co-MOF** shows a highly similar excited state lifetime to that calculated for **Ni-MOF** demonstrating that **Co-MOF** also has a considerable quenching impact on the excited state lifetime compared to the uncomplexed $\mathbf{H_4[L_{bpy}\text{-}R_3]^{2+}}$. Additionally, similar to the **Ni-MOF**, a bi-exponential decay was observed for the **Co-MOF,** which is again is in contrast to the uncomplexed $\mathbf{H_4[L_{bpy}\text{-}R_3]^{2+}}$. An intensity-weighted average lifetime, τ_{Avg} (Equation 4.5.3) from the bi-exponential decay for the **Co-MOF** was calculated to be 20.3 ± 0.2 ns.

Spectrally time-resolved photoluminescence decays were recorded using five centre wavelengths across the photoluminescence spectra (650 nm, 750 nm, and 800 nm) and using bandpass filters (FWHM = 10 nm) (Fig. 4.57). The results show that when the metallo-ligand $\mathbf{H_4[L_{bpy}\text{-}R_3]^{2+}}$ is coordinated to Co^{II} ions in the **Co-MOF**, the lifetime of the ^{3}MLCT state of the $\mathbf{H_4[L_{bpy}\text{-}R_3]^{2+}}$ is steadily lowered. This result is consistent with what was previously seen for the **Ni-MOF** (Fig. 4.22).

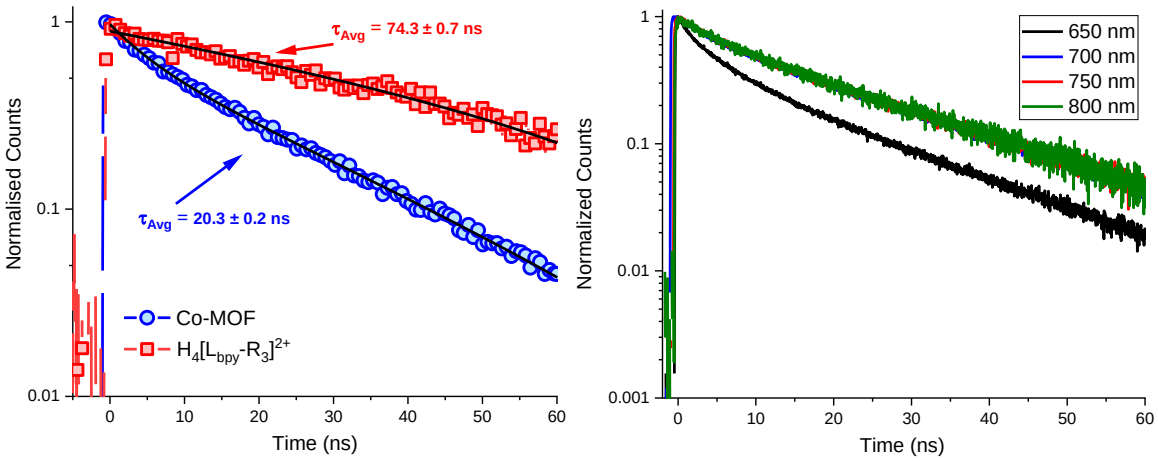

Figure 4.57: Normalised photoluminescence decays of Co-MOF and $\mathbf{H_4[L_{bpy}\text{-}R_3]^{2+}}$ measured in DMF upon excitation at 405 nm using 10 nm bandpass filter centred at 700 nm (left). Normalised time-resolved photoluminescence decays of Co-MOF measured at four central emission wavelengths using 10 nm bandpass filters (λ_{ex} = 405 nm) (right).

Figure 4.58 below shows the average lifetimes obtained for the **Co-MOF** in comparison to the Ru^{II} polypyridine complex $\mathbf{H_4[L_{bpy}\text{-}R_3]^{2+}}$ at centre wavelengths of 650 nm, 700 nm, 750 nm, and 800 nm using bandpass filters (FWHM = 10 nm) and an excitation power of 0.2 µW. According to the findings, longer emission wavelengths result in a slightly longer average lifetime.

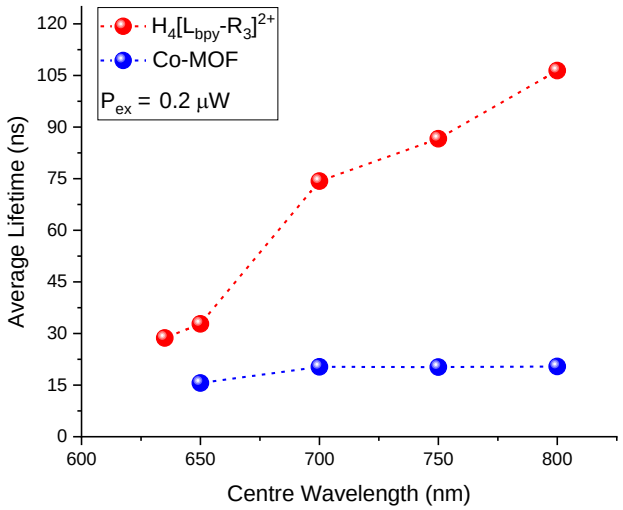

Figure 4.58: Average lifetime measurements in ns at different centre wavelengths of $\mathbf{H_4[L_{bpy}\text{-}R_3]}$ in the Co-MOF (blue) and $\mathbf{H_4[L_{bpy}\text{-}R_3]}$ (red).

Using the previously defined equation (Eq. 4.5.4) for the Quenching Efficiency (%), the data obtained demonstrates that the **Co-MOF** has a Quenching Efficiency of 73.4% when calculated from the decays seen in Figure 4.58 and is comparable to that obtained for **Ni-MOF.** Additionally, the Quenching Efficiency (%) was calculated from the PL decays measured at centre wavelengths of 650 nm, 750 nm, and 800 nm using bandpass filters (FWHM = 10 nm) (Fig. 4.59) to investigate the interaction between $\mathbf{H_4[L_{bpy}\text{-}R_3]^{2+}}$ and the **Co-MOF**. The data shows that the Quenching Efficiency (%) is the lowest at 650 nm as a result of the broadening of the emission spectrum in this region for **Co-MOF** in comparison to $\mathbf{H_4[L_{bpy}\text{-}R_3]^{2+}}$. The Quenching Efficiency (%) is the largest when measured between 700 – 800 nm, where the emission spectrum of **Co-MOF** remained essentially unchanged when compared to $\mathbf{H_4[L_{bpy}\text{-}R_3]^{2+}}$.

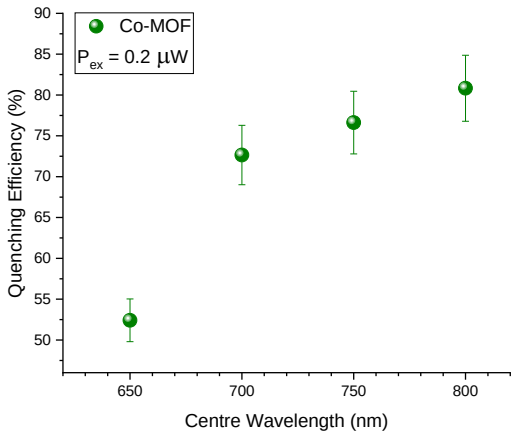

Figure 4.59: Percentage quenching efficiency measured at different centre wavelengths of Co-MOF.

The **Co-MOF** calculated energy band gaps were compared to $\mathbf{H_4[L_{bpy}\text{-}R_3]^{2+}}$ (Fig 3.17) and **Ni-MOF** (Fig 4.28). The results show that **Co-MOF** has improved semiconductor capabilities in comparison to $\mathbf{H_4[L_{bpy}\text{-}R_3]^{2+}}$. The interfacial energy in the **Co-MOF** is lowered due to the charge transfer between $\mathbf{H_4[L_{bpy}\text{-}R_3]^{2+}}$ and the Co^{II} nodes, resulting in a considerable reduction in the energy of all relevant band gaps.[77] This reduction in the energy band gaps is similar to that of **Ni-MOF**, as for both **Ni-MOF** and **Co-MOF,** the LC, MC and MLCT absorption bands are red-shifted to lower energies.

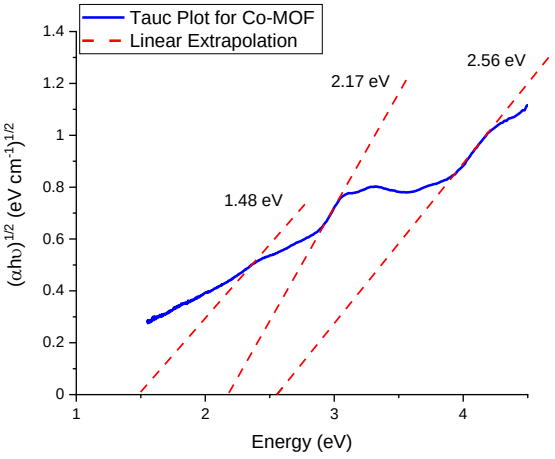

Figure 4.60: Tauc Plot calculated from the UV-Vis absorption spectrum of Co-MOF, indicating the linearly extrapolated MLCT, MC & LC estimated optical band gap energies.

4.13 Cathodic Electrochemical Synthesis and *in-situ* Film Deposition of Co-MOF

Cathodic electrochemical synthesis and *in-situ* film deposition experiments were performed to determine whether **Co-MOF** thin films could be produced. This approach was expected to yield porous thin films of the MOF framework similar to that seen for the **Ni-MOF**, thus, improving the MOFs photo-response characteristics and thereby enhancing its potential for photo-electrocatalytic applications.[98] Hence, the overall aim was to assess the **Co-MOF** processability for photo-electrochemical energy conversion systems and to compare its activity with **Ni-MOF/FTO**.

Co-MOF/FTO fabrication followed the same synthetic procedure as **Ni-MOF/FTO** (Fig 4.29). Within 5 minutes at a potential of −1.5 V (vs $Ag/Ag(cryptand)^+$ in DMF) at ambient temperature, **Co-MOF** was synthesised and deposited from diluted reaction mixtures comprising of millimole quantities of $\mathbf{H_4[L_{bpy}\text{-}R_3]^{2+}}$ and $Co(NO_3)_2{\cdot}6H_2O$, resulting in a homogenous layer on the conductive surface of the FTO electrode (Fig. 4.61). Post-electrochemical deposition, **Co-MOF/FTO** was retrieved from the reaction mixture and washed with fresh DMF to remove any remaining starting material. Finally, to avoid the loss of crystallinity owing to desolvation, the **Co-MOF/FTO**, similar to **Ni-MOF/FTO**, was kept in fresh DMF.

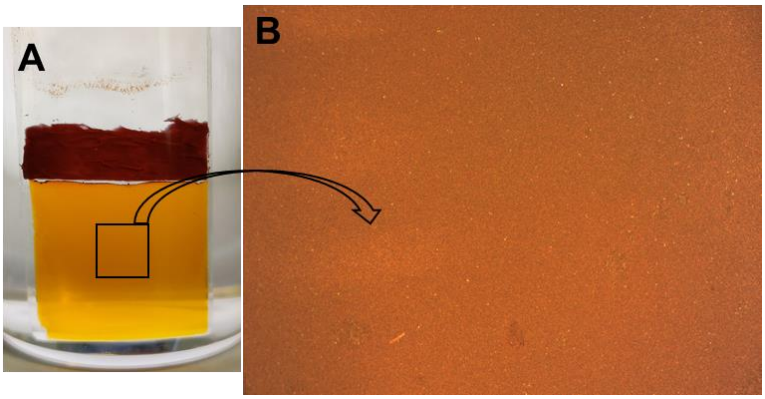

Figure 4.61: Optical image of electrodeposited Co-MOF/FTO (A), 2.5x magnified area of Co-MOF/FTO (B).

Infrared spectroscopy validated the successful cathodic electrochemical synthesis and *in-situ* film deposition of the **Co-MOF** on FTO electrodes. The **Co-MOF/FTO** IR-spectrum below (Fig. 4.62) shows almost identical signals to that of **Co-MOF** (Fig. 4.52). At *ca.* 1558 cm^{-1} and 1420 cm^{-1}, notably matching and particularly characteristic bands of the **Co-MOF** can be clearly observed. These bands can be attributed to the asymmetric

ν_{as}(COO) and symmetric ν_{s}(COO) carboxylate stretches, typical of the carboxylate moieties observed in the framework and earlier discussed in this chapter for both the **Co-MOF** and **Ni-MOF**.

Raman spectroscopy was similarly conducted on the **Co-MOF/FTO**. The Raman spectrum was measured from 200 cm^{-1} to 2500 cm^{-1} and the baseline was corrected using OriginLab 2020 software. The data obtained indicated that the Raman spectra of **Co-MOF** and **Co-MOF/FTO** correlate well showing closely matching signals. In the Raman spectrum (Figure 4.62), the characteristic signal at *ca.* 2218 cm^{-1} can be seen. This signal is derived from the alkyne-moiety vibrations arising from the Ru^{II} polypyridine complex present in the framework of the **Co-MOF**.[63,64] The ν(C=C) vibrations derived from the heteroaromatic moieties are detected at *ca.* 1589 cm^{-1} and 1490 cm^{-1}, whereas ν(C-C) vibrations can be seen at *ca.* 1317 cm^{-1} and 1276 cm^{-1}. The ν(C–H) vibrations that can be attributed to the aromatic rings can be seen at *ca.* 1033 cm^{-1}, 1119 cm^{-1} and 1147 cm^{-1}.[61]

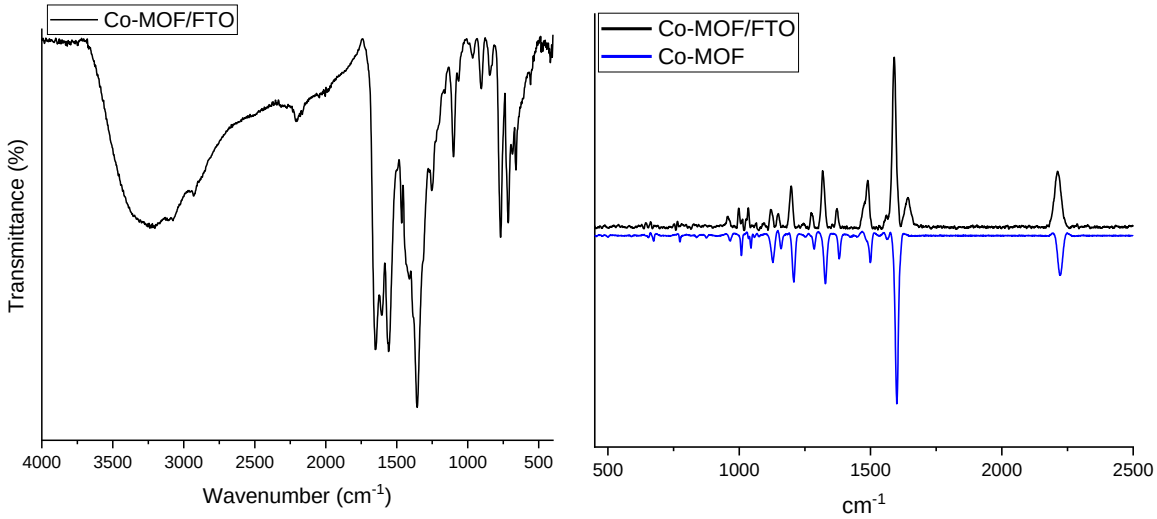

Figure 4.62: FT-IR spectrum (left) of Co-MOF/FTO. Raman spectra (right) of Co-MOF (blue) vs Co-MOF/FTO (black).

On freshly electrochemically deposited **Co-MOF/FTO** electrodes, SEM and EDX studies were conducted. The data obtained verified the constitutional composition and revealed the expected atomic weight (%) ratio of approximately 1:1 for Ru^{II} to Co^{II}, which is in conjunction with the crystal structure data. An SEM image of a homogeneous film of **Co-MOF/FTO** can be seen in Figure 4.63a. Figure 4.63b shows the formation of fractures on the thin film due to the drying effect on the **Co-MOF/FTO** which was also previously seen for the **Ni-MOF/FTO**.

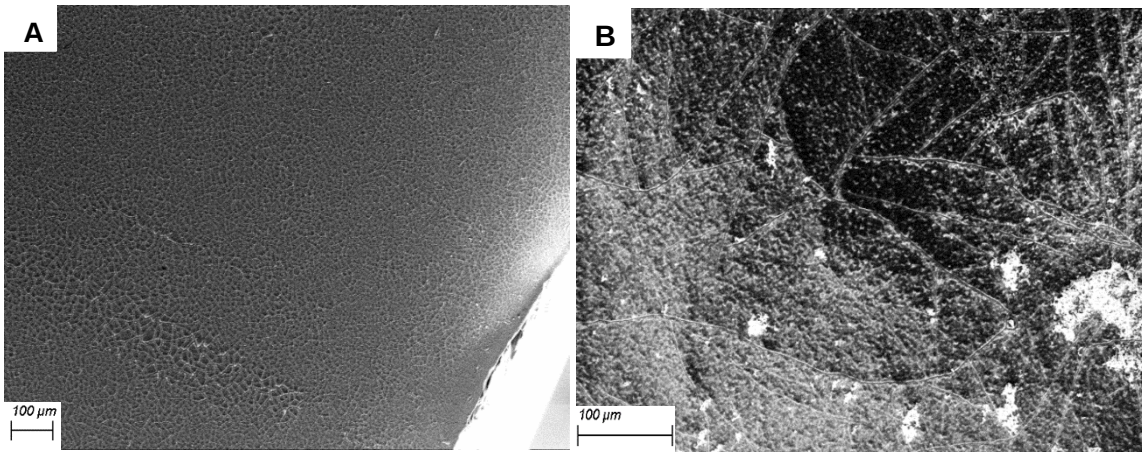

Figure 4.63: SEM images of the Co-MOF/FTO.

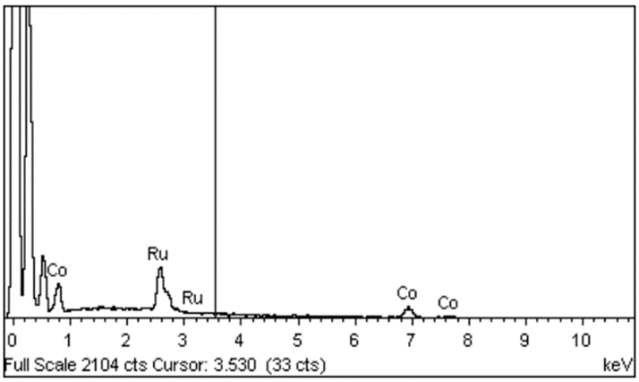

Figure 4.64: EDX analysis for Co-MOF/FTO.

Table 4.10: EDX data obtained for Co-MOF/FTO.

Element	Atomic (%)
Co	54.73
Ru	45.27

4.14 Photo-Electrocatalytic Water Oxidation Studies of Co-MOF/FTO

Photo-electrocatalytic H_2O oxidation studies were carried out to examine the functionality and applicability of the **Co-MOF/FTO** electrodes. The experiments were conducted in MeCN solutions containing specific quantities of H_2O as to ensure the stability of **Co-MOF/FTO** thin films and avoid hydrolytic decompositions. Similar to the photo-electrocatalytic H_2O oxidation experiments carried out with **Ni-MOF/FTO** electrodes, the use of MeCN/H_2O mixtures as the reaction medium, here again, is in line with biomimetic experiments that mimic the dielectric, hydrophobic environment of the membrane protein of photosystem-II which operates using controlled quantities of H_2O.[24]

CV and LSV experiments were conducted in a photoelectrochemical cell (LED 0.149 W, λ = 470 nm) under the same conditions as for the **Ni-MOF/FTO**. A solvent mixture of 5% (v/v) H_2O in MeCN was used to ensure high reaction rates toward oxygen production.[90] Cyclic voltammetry (Fig 4.65) within a potential range of -1.0 V to 1.3 V (vs SCE) in MeCN containing 5-vol-% H_2O was initially measured in dark conditions. The appearance of an oxidative multielectron process attributed to electrocatalytic water oxidation can be seen. At a current density of 0.2 mA, the onset potential appears at *ca.* 1.06 V. Upon blue light irradiation, a strong photo-response is observed in the CV, whereby the onset potential of the electrocatalytic H_2O oxidation is reduced by >95 mV to 0.97 V. At an applied potential of 1.3 V, the catalytic current density was found to increase considerably by 1.2 mA from 2.54 mA in dark conditions to 3.74 mA upon light irradiation. This increase in current density upon light irradiation further demonstrates the photo-capabilities of **Co-MOF/FTO**. Similarly, LSV experiments were further used to characterise the catalytic behaviour in the dark and under light irradiation (Fig. 4.66). The photo-generated oxidative current results in the onset potential shifting significantly. An electrocatalytic onset potential of 1.16 V (vs SCE) was recorded under dark conditions for systems that contain 5-vol-% H_2O, while under light irradiation, the onset potential shifts significantly by 100 mV to 1.06 V (vs SCE).

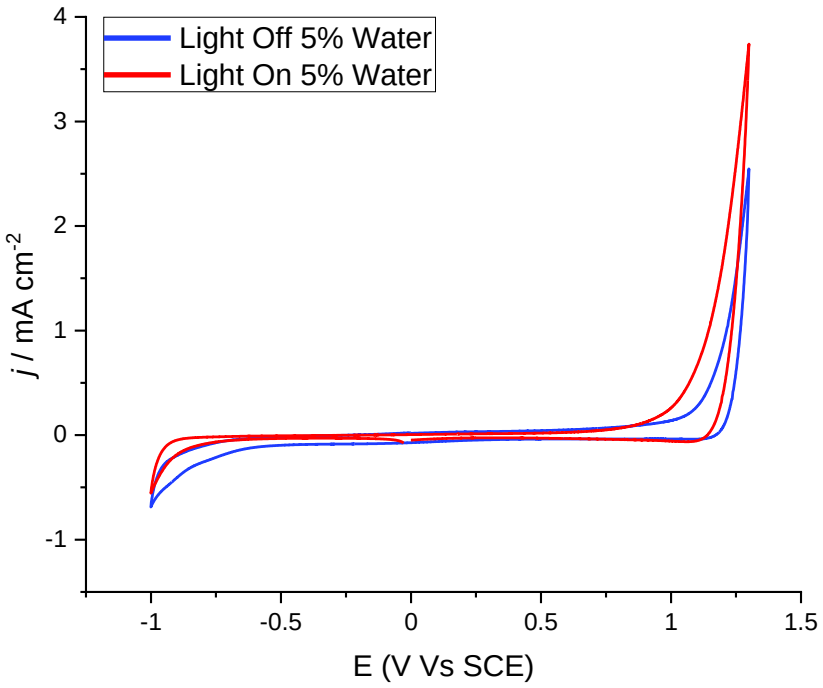

Figure 4.65: CV highlighting the light-influenced water oxidation process in the presence of variable quantities of H_2O; 5% H_2O experiment (red) and 5% H_2O and LED light irradiation (blue).

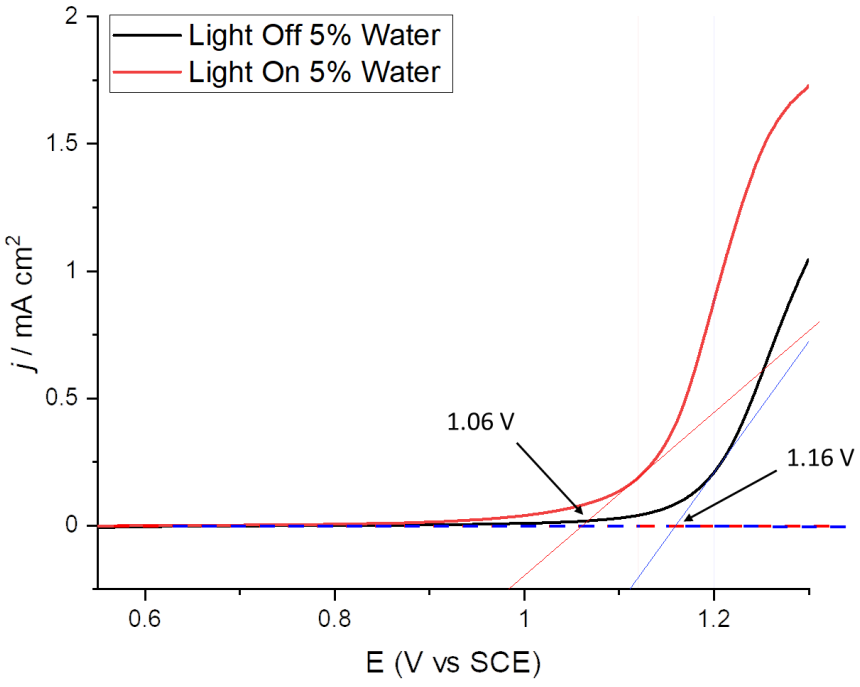

Figure 4.66: LSV in the dark (black) and upon LED light irradiation (red).

Visual inspection of the **Co-MOF/FTO** films after completion of the CV and LSV studies appear stable, revealing no material loss or colour alteration of the deposited MOF (Fig. 4.67). The prepared electrodes are applicable in consecutive catalytic test runs.

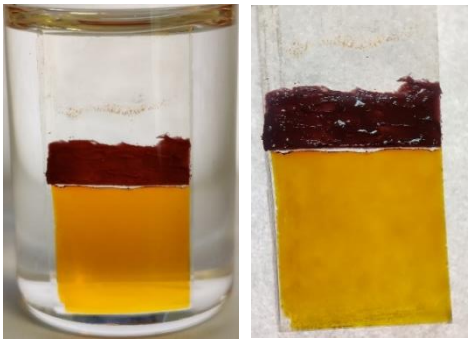

Figure 4.67: Images of Co-MOF/FTO pre-catalysis (left) and post-catalysis (right).

As previously seen for **Ni-MOF/FTO**, the data obtained from the catalytic experiments of **Co-MOF/FTO** demonstrate its ability to facilitate the oxidation of Co^{II} centres and H_2O substrates, which act as electron donors. The data obtained from the catalytic experiments of **Co-MOF/FTO** are comparable to that seen in the literature and the influence of light irradiation on the onset-overpotentials of the H_2O oxidation reaction is widely demonstrated in the literature.[92] A comparative analysis of **Co-MOF/FTO** with **Ni-MOF/FTO** demonstrated an improvement on the onset-overpotential, as well as a significant increase in the current density both with and without light irradiation.

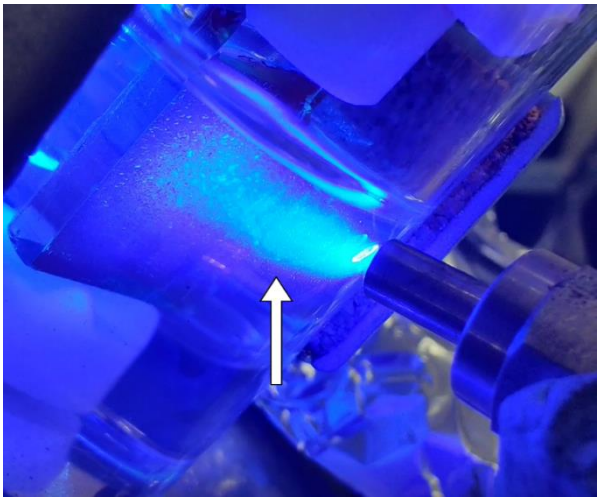

Figure 4.68: LED light irradiation (λ = 470 nm) of the Co-MOF/FTO photoanode. Small O_2 bubbles can be seen evolving at the thin film surface. Arrow pointing at the area where O_2 bubbles can be seen.

After the photo-electrocatalytic water oxidation experiments were completed, **Co-MOF/FTO** post-catalytic characterisation was conducted. The identity and purity of the post-catalytic MOF thin films were determined by FT-IR, Raman, and EDX spectroscopy. Analysis was also carried out to identify whether any decomposition products had formed on the electrodes upon completion of the photo-electrocatalytic experiments. The FT-IR spectrum (Fig. 4.69) obtained for the **Co-MOF/FTO** post-photo-electrocatalytic water oxidation demonstrates indistinguishable characteristic vibrational bands to those previously observed for the freshly prepared **Co-MOF/FTO** thin films. No presence of any significant impurities can be seen in the spectrum. Raman spectroscopy (Fig. 4.69) indicated neither a change in the **Co-MOF/FTO** thin film electrodes nor the formation of metal oxides or other impurities. This again demonstrates that the post-photo-electrocatalytic **Co-MOF/FTO** films are identical to that of pristine, freshly prepared **Co-MOF/FTO** thin films, which were previously discussed in this chapter.

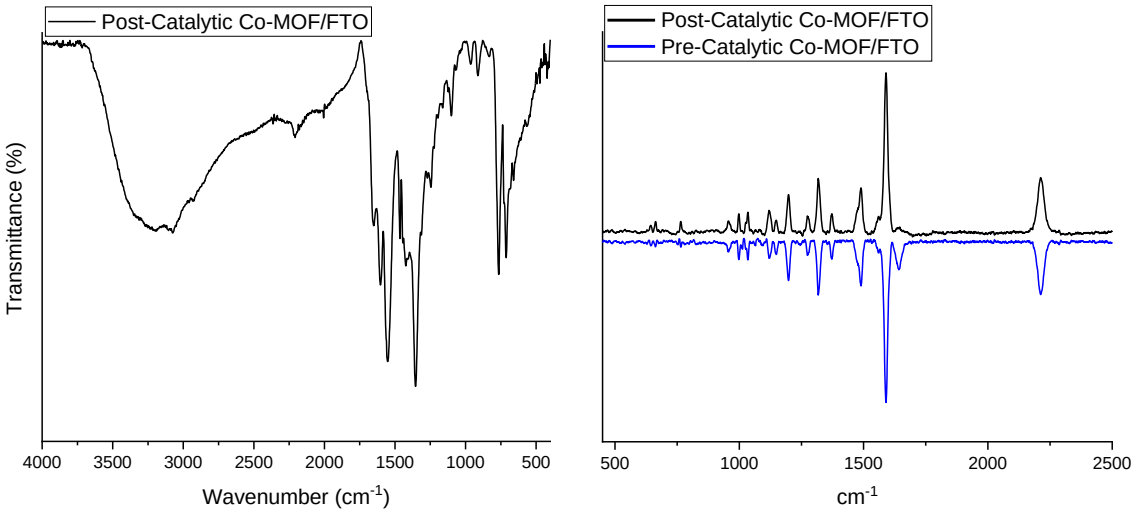

Figure 4.69: FT-IR spectrum (left) of Co-MOF/FTO post-catalysis. Raman spectra (right) of Co-MOF/FTO pre-catalysis (blue) and post-catalysis (black).

SEM and EDX measurements were performed on post-catalytic **Co-MOF/FTO** thin film electrodes. The data demonstrated the expected atomic weight percentage ratio of *ca.* 1:1 of Ru^{II} to Co^{II}, which was previously seen for both the **Co-MOF** and freshly prepared thin films of **Co-MOF/FTO**. Figure 4.70a shows an image obtained under SEM for the post-catalytic **Co-MOF/FTO**, demonstrating retention of the homogenous MOF thin film. Crystal aggregation and the formation of cracks in the thin film caused by a drying effect of **Co-MOF/FTO** upon its removal from the electrolyte solution can be seen in Figure 4.70b.

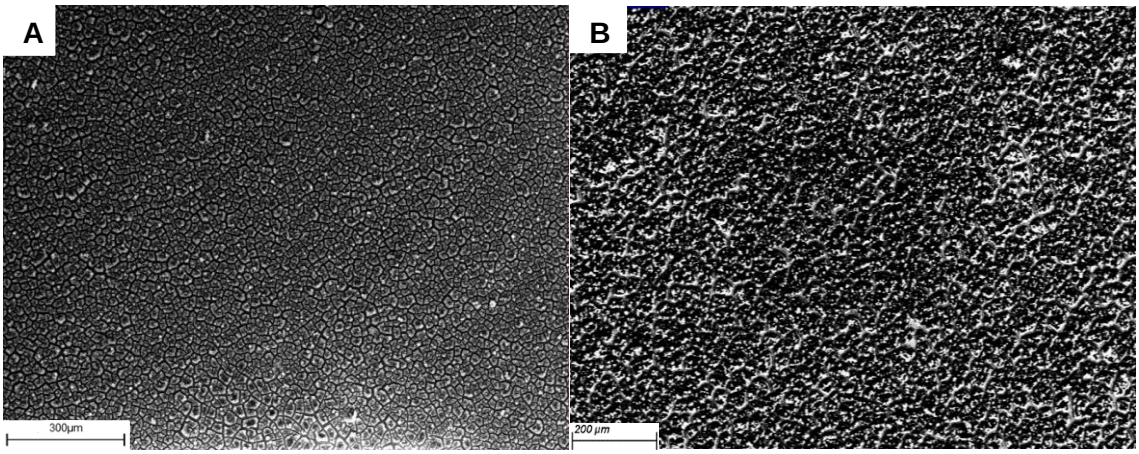

Figure 4.70: SEM images of Co-MOF/FTO post-catalysis at different magnifications.

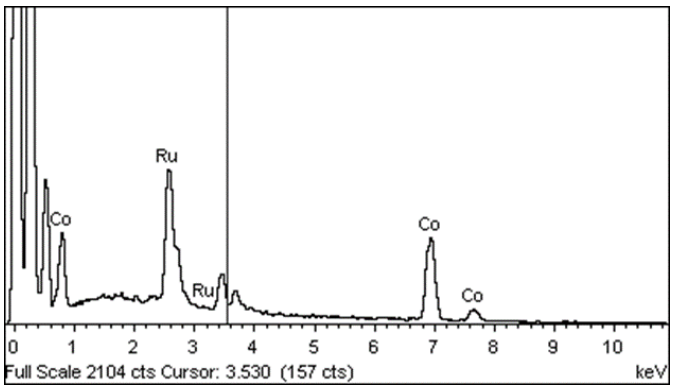

Figure 4.71: EDX analysis for Co-MOF/FTO post-catalysis.

Table 4.11: EDX data obtained for Co-MOF/FTO post-catalysis.

Element	Atomic (%)
Co	56.11
Ru	43.89

4.15 Synthesis and Characterisation of Zn-MOF ($Zn_6(L_{bpy}\text{-}R_3)_{12}(H_2O)_{12}$)

During the reaction between $\mathbf{H_4[L_{bpy}\text{-}R_3]^{2+}}$ and $Zn(NO_3)_2 \cdot 6H_2O$ at a mole ratio of 1:8, red spherical polycrystalline samples of **Zn-MOF** (Fig 4.72) were obtained. The MOF was synthesised using the same procedure as the **Ni-MOF**. However, the **Zn-MOF** crystals obtained were not suitable for single-crystal X-ray diffraction studies due to their polycrystalline nature. Thus, a diffraction pattern and hence a crystal structure could not be obtained.

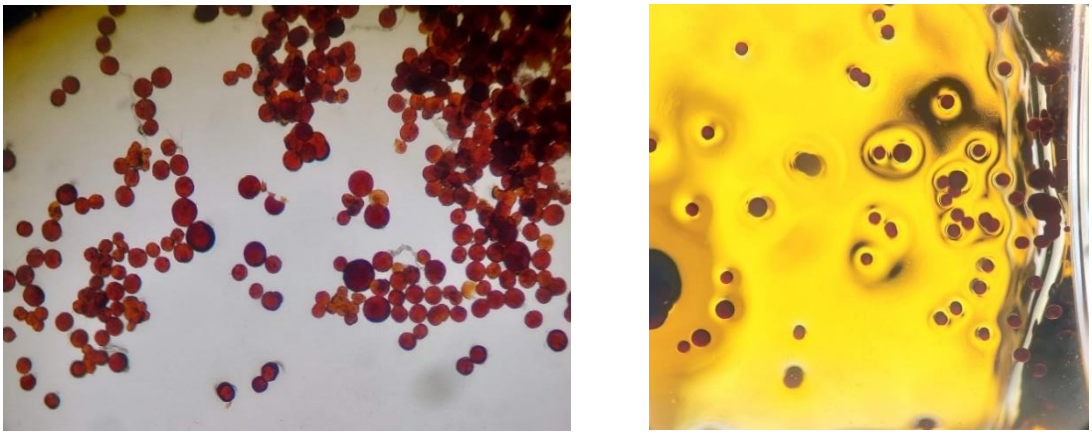

Figure 4.72: Optical microscope images of Zn-MOF crystals.

X-ray powder diffraction experiments of a bulk polycrystalline sample of **Zn-MOF** were conducted in capillaries containing DMF to avoid rapid desolvation and amorphisation of the material. The **Zn-MOF** was found to be isostructural to both the **Ni-MOF** and **Co-MOF** based on the fitting and closely matching signals of the measured X-ray powder diffraction pattern of **Zn-MOF** to the measured X-ray powder diffraction patterns of **Ni-MOF** and **Co-MOF** (Fig 4.73). The obtained experimental pattern of **Zn-MOF** is characterised by signals that appear at 2θ = 5.97°, 7.45°, 8.21°, 9.05° and 11.02°.

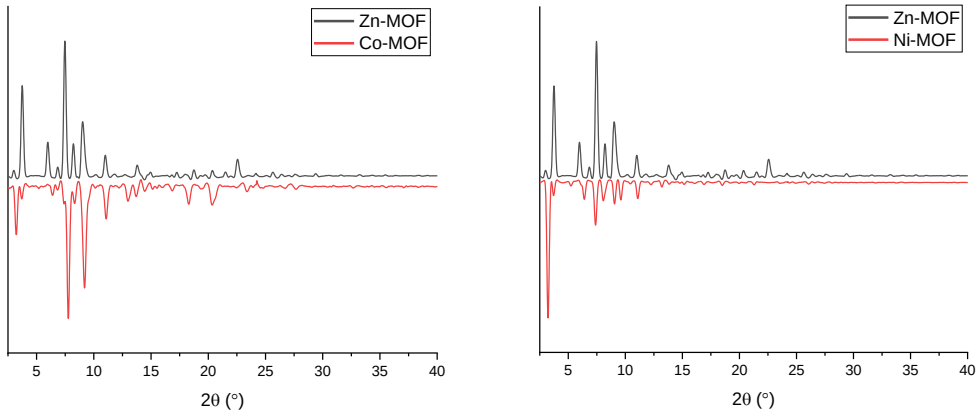

Figure 4.73: Powder X-ray Diffraction patterns for Zn-MOF and Co-MOF (left), Zn-MOF and Ni-MOF (right).

Physicochemical characterisation of **Zn-MOF** was carried out. The FT-IR spectrum (Fig. 4.74a) demonstrated bands at highly similar wavenumbers to those previously obtained for **Ni-MOF** and **Co-MOF**. The broad signal at *ca.* 3420 cm^{-1} can be attributed to ν(O–H) stretching vibrations that derive from solvent molecules within the framework of **Zn-MOF**.[49,50] At 2930 cm^{-1} and 2863 cm^{-1} weak bands that can be attributed to the ν(C-H) vibrations from DMF solvent molecules.[51,52] Asymmetric ν_{as}(COO), and symmetric ν_s(COO) carboxylate stretching vibrations can be seen at 1575 cm^{-1} and 1433 cm^{-1}, respectively.[53,54] Their positions and a Deacon-Phillips value of $\Delta = (\nu_{as}\text{-}\nu_s) = 142$ cm^{-1} are characteristic for *syn*-η^1 carboxylate coordination modes.[55–57] The ν(C=O) stretching vibrations attributed to DMF solvent molecules can be seen at 1652 cm^{-1}.[51,52,58] The bands in the region of 1493 cm^{-1} can be attributed to the ν(C=C) stretching vibrations that derive from the benzene and bipyridine moieties of $\mathbf{H_4[L_{bpy}\text{-}R_3]^{2+}}$.[30,59]

Raman spectroscopy was carried out on a freshly prepared polycrystalline sample of **Zn-MOF**. The Raman spectrum was measured from 200 cm^{-1} to 2500 cm^{-1}, and the baseline was corrected using OriginLab 2020 software. The Raman spectrum (Fig 4.74b) matched closely to the spectra previously obtained for both **Ni-MOF** and **Co-MOF**. The bands between *ca*. 1006 $cm^{-1}$and 1160 cm^{-1} derive from ν(C–H) vibrations.[61] The δ(C–H) bending vibrations can be seen at *ca*. 1207 cm^{-1}.[62] The ν(C–C) single bond vibrations appear at *ca.* 1282 cm^{-1} and 1325 cm^{-1}. The band that appears at *ca.* 1380 cm^{-1} can be attributed to ν_s(C=O) vibrations that derives from the carboxylate groups. The ν(C=C) vibrations can be observed at *ca.* 1498 cm^{-1} and 1599 cm^{-1}. The ν(C≡C) vibration, which is characteristic of the $\mathbf{H_4[L_{bpy}\text{-}R_3]^{2+}}$ metallo-ligand can be seen at 2226 cm^{-1}.

The thermal stability of **Zn-MOF** was examined. A TGA trace (Fig 4.74c) was obtained for a freshly prepared polycrystalline sample of **Zn-MOF** under a constant stream of air and in the temperature range of 30 °C – 600 °C. The data obtained reveals decomposition pathway that follows two steps. The initial step results in a weight loss of *ca.* 31 % and occurs upon heating the sample between *ca.* 30 °C and 120 °C. This weight loss can be attributed to the removal of the constitutional solvent molecules. The second step which can be attributed to the oxidative degradation of the organic ligand moieties, can be seen upon heating the sample above 350 °C. This step results in an approximate weight loss of 40 %.[65–67]

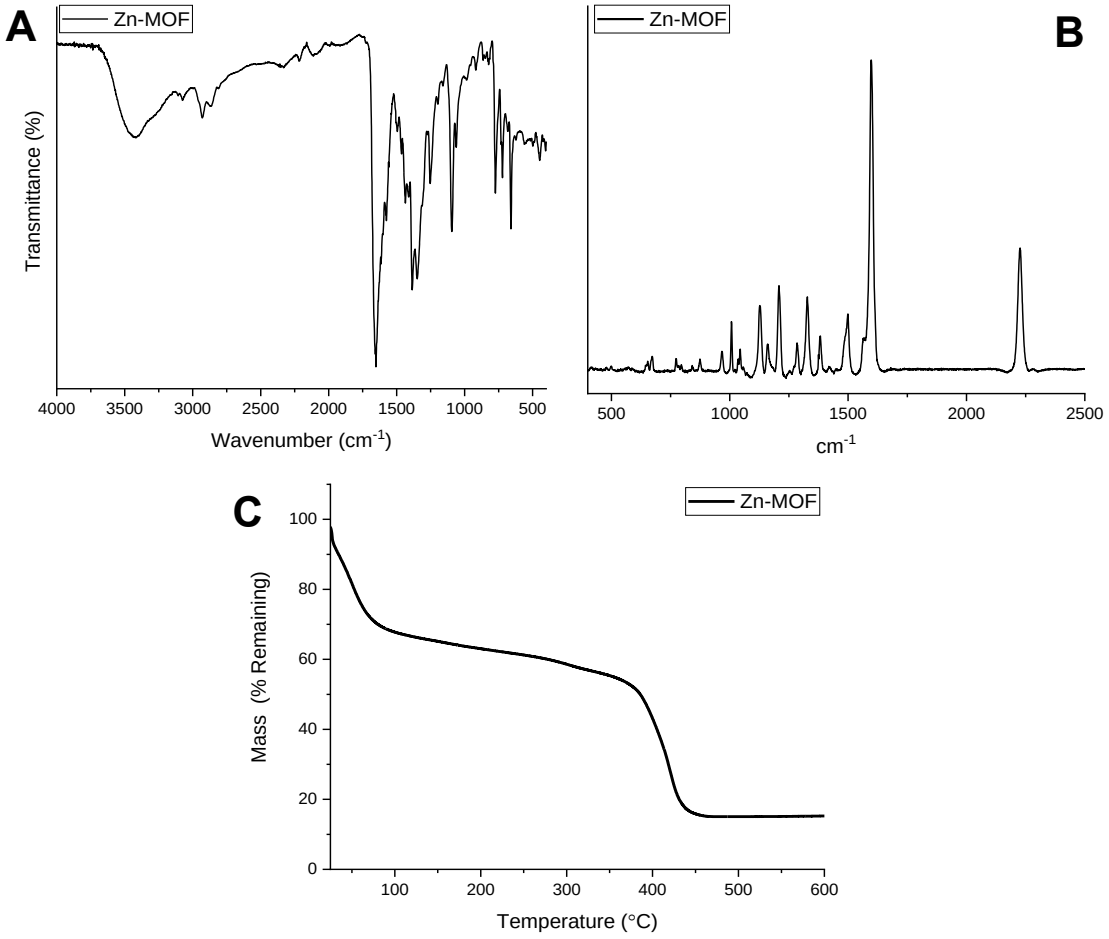

Figure 4.74: FT-IR spectrum (A), Raman spectrum (B) and thermogravimetric analysis measured in an air atmosphere, at a heating rate of 5 °C per minute (C) of Zn-MOF.

4.16 Conclusion and Future Work

In this chapter, the principles of supramolecular chemistry were applied to design a series of MOFs with photoactive capabilities through the use of modified tris(bipyridine)ruthenium(II) ligands. These ligands function as bridging linkers, establish strong coordination bonds to metal ion, provide rigidity to the framework and offer essential light-harvesting characteristics, resulting in stable, permanently porous photoactive MOFs.[4,99,100] Therefore, utilising the novel $\mathbf{H_4[L_{bipy}\text{-}R3]^{2+}}$ metallo-ligand, a series of photoactive, acetylene-extended '3rd-generation' MOFs in which nanoscopic $\{Ni_6\}/\{Co_6\}/\{Zn_6\}$ cages are linked through light-harvesting Ru^{II}-pyridyl metallo-ligands were synthesised.

Single crystals of **Ni-MOF** and **Co-MOF** were formed reproducibly, and polycrystalline material was obtained for the **Zn-MOF**. The MOFs were confirmed to be isostructural *via* single-crystal X-ray diffraction for the **Ni-MOF** and **Co-MOF**, X-ray powder diffraction, FT-IR and Raman spectroscopy. The structures of the **Ni-MOF** and **Co-MOF** were elucidated through single-crystal X-ray diffraction. The MOFs adopt an augmented, cubic **a-fcu** topology that is characterised by large pores and estimated by RASPA[47]. The MOFs are composed of partially hydrated Ni^{II} centres in the **Ni-MOF** and Co^{II} in the **Co-MOF**. These metal centres can potentially facilitate substrate binding and can act as catalytic centres.

Photophysical studies confirm that the optical attributes of the free Ru^{II}-pyridyl metallo-ligands, as indicated from absorption and emission spectra, are maintained in the framework of the MOFs. The coordination of the metallo-ligands to the respective metal ions in each of the MOFs facilitates rapid energy and electron transfer processes throughout the network structures that can be exploited for photo-catalysis and photo-electrochemical studies. Physicochemical characterisation of the MOFs exhibited highly characteristic bands of the free Ru^{II}-pyridyl metallo-ligand and demonstrated the thermal stability of the MOFs.

The nature of the material facilitated electrochemical synthetic studies. Cathodic electrochemical synthesis and *in-situ* film deposition is an alternative synthetic route used in industry to produce MOFs in reduced time compared to solvothermal synthesis methods.[101] Compared to other approaches, successful functionalisation of conductive surfaces through the production of MOF thin films lowers unpredictability by confining

MOF formation to the electrode and allowing for a more controlled synthesis.[102] Thus, **Ni-MOF** and **Co-MOF** were synthesised electrochemically from highly diluted reactant solutions within minutes and deposited on FTO electrodes. Physicochemical characterisation indicated that the thin films formed were consistent with single crystals of their respective MOF. The functionality of the **Ni-MOF/FTO** and **Co-MOF/FTO** systems was demonstrated through photo-electrocatalytic water oxidation studies. CV data demonstrated a reduction of >90 mV to the onset-overpotential upon LED light irradiation of **Ni-MOF/FTO** and **Co-MOF/FTO** electrodes. LSV experiments showed a reduction of 140 mV and 100 mV to the onset-overpotential upon LED light irradiation of **Ni-MOF/FTO** and **Co-MOF/FTO** electrodes, respectively. Post-catalytic characterisation demonstrated identical characteristic bands in the FT-IR and Raman spectra and an expected atomic weight percentage ratio to that of freshly prepared thin films.

Preliminary studies demonstrated the successful doping of **Ni-MOF** single crystals and **Ni-MOF/FTO** with C_{60}. The absorption of C_{60} into the pores of **Ni-MOF** and **Ni-MOF/FTO** resulted in an observable colour change in the crystals and thin films. Physicochemical characterisation demonstrated new bands in the Raman spectra characteristic of C_{60}. This preliminary result demonstrates the MOFs ability to encapsulate guests within its framework, which could be highly beneficial in future catalytic studies.

Future work would involve the improvement of **Ni-MOF/FTO** and **Co-MOF/FTO** photoactivity by optimising the techniques used to obtain the deposited material in order to achieve improved photo-electrocatalytic activity. Further investigation into the PEC stability and methods to improve the system's overall stability. Additionally, the photocatalytic response could be improved by synthesising photoactive MOF networks with a series of different inorganic SBUs and utilising the various metallo-ligands. Areas for future investigations also include further photo-electrocatalytic studies of C_{60} doped **Ni-MOF/FTO** electrodes and research into the quenching of the photoactivity. Additionally, further utilisation of the MOFs ability to absorb various guest molecules and investigation into the respective photocatalytic properties.

4.17 References

1 L. Jiao and H.-L. Jiang, *Chem*, 2019, **5**, 786–804.

2 M. Nemiwal, V. Subbaramaiah, T. C. Zhang and D. Kumar, *Sci. Total Environ.*, 2021, **762**, 144101.

3 H.-C. "Joe" Zhou and S. Kitagawa, *Chem. Soc. Rev.*, 2014, **43**, 5415–5418.

4 O. M. Yaghi, M. O'Keeffe, N. W. Ockwig, H. K. Chae, M. Eddaoudi and J. Kim, *Nature*, 2003, **423**, 705–714.

5 J.-R. Li and H.-C. Zhou, *Nat. Chem.*, 2010, **2**, 893–898.

6 M. J. Kalmutzki, N. Hanikel and O. M. Yaghi, *Sci. Adv.*, 2018, **4**, eaat9180.

7 É. Whelan, F. W. Steuber, T. Gunnlaugsson and W. Schmitt, *Coord. Chem. Rev.*, 2021, **437**, 213757.

8 Y. Lin, C. Kong, Q. Zhang and L. Chen, *Adv. Energy Mater.*, 2017, **7**, 1601296.

9 X. Yu and S. M. Cohen, *Chem. Commun.*, 2015, **51**, 9880–9883.

10 S. Dang, Q.-L. Zhu and Q. Xu, *Nat. Rev. Mater.*, 2018, **3**, 17075.

11 H. Wang, Q.-L. Zhu, R. Zou and Q. Xu, *Chem.*, 2017, **2**, 52–80.

12 C. A. Trickett, A. Helal, B. A. Al-Maythalony, Z. H. Yamani, K. E. Cordova and O. M. Yaghi, *Nat. Rev. Mater.*, 2017, **2**, 17045.

13 H. Furukawa, K. E. Cordova, M. O'Keeffe and O. M. Yaghi, *Science*, 2013, **341**, 1230444.

14 T. Kajiwara, M. Fujii, M. Tsujimoto, K. Kobayashi, M. Higuchi, K. Tanaka and S. Kitagawa, *Angew. Chem. Int. Ed.*, 2016, **55**, 2697–2700.

15 B. An, L. Zeng, M. Jia, Z. Li, Z. Lin, Y. Song, Y. Zhou, J. Cheng, C. Wang and W. Lin, *J. Am. Chem. Soc.*, 2017, **139**, 17747–17750.

16 G. Lan, Z. Li, S. S. Veroneau, Y.-Y. Zhu, Z. Xu, C. Wang and W. Lin, *J. Am. Chem. Soc.*, 2018, **140**, 12369–12373.

17 S. Keskin and S. Kızılel, *Ind. Eng. Chem. Res.*, 2011, **50**, 1799–1812.

18 R. Huang, Y. Peng, C. Wang, Z. Shi and W. Lin, *Eur. J. Inorg. Chem.*, 2016, **2016**, 4358–4362.

19 M. C. So, G. P. Wiederrecht, J. E. Mondloch, J. T. Hupp and O. K. Farha, *Chem. Commun.*, 2015, **51**, 3501–3510.

20 A. S. Munn, R. S. Pillai, S. Biswas, N. Stock, G. Maurin and R. I. Walton, *Dalton Trans.*, 2016, **45**, 4162–4168.

21 H. D. Lawson, S. P. Walton and C. Chan, *ACS Appl. Mater. Interfaces*, 2021, **13**, 7004–7020.

22 S. Subudhi, S. Mansingh, G. Swain, A. Behera, D. Rath and K. Parida, *Inorg. Chem.*, 2019, **58**, 4921–4934.

23 W. Nong, X. Liu, Q. Wang, J. Wu and Y. Guan, *ES Food Agrofor.*, 2020, 11–40.

24 K. N. Ferreira, T. M. Iverson, K. Maghlaoui, J. Barber and S. Iwata, *Science*, 2004, **303**, 1831–1838.

25 S. Styring, *Faraday Discuss.*, 2012, **155**, 357–376.

26 D. M. Arias-Rotondo and J. K. McCusker, *Chem. Soc. Rev.*, 2016, **45**, 5803–5820.

27 S.-N. Zhao, G. Wang, D. Poelman and P. Van Der Voort, *Molecules*, 2018, **23**, 2947.

28 Z. Wu, S. Guo, L.-H. Kong, A.-F. Geng, Y.-J. Wang, P. Wang, S. Yao, K.-K. Chen and Z.-M. Zhang, *Chinese J. Catal.*, 2021, **42**, 1790–1797.

29 A. Santiago-Portillo, H. G. Baldoví, E. Carbonell, S. Navalón, M. Álvaro, H. García and B. Ferrer, *J. Phys. Chem. C*, 2018, **122**, 29190–29199.

30 W. A. Maza, S. R. Ahrenholtz, C. C. Epley, C. S. Day and A. J. Morris, *J. Phys. Chem. C*, 2014, **118**, 14200–14210.

31 C. Bonneau, O. Delgado-Friedrichs, M. O'Keeffe and O. M. Yaghi, *Acta Crystallogr. Sect. A Found. Crystallogr.*, 2003, **59**, 22–27.

32 A. J. Cairns, J. A. Perman, L. Wojtas, V. C. Kravtsov, M. H. Alkordi, M. Eddaoudi and M. J. Zaworotko, *J. Am. Chem. Soc.*, 2008, **130**, 1560–1561.

33 W. Lu, D. Yuan, T. A. Makal, Z. Wei, J.-R. Li and H.-C. Zhou, *Dalton Trans.*, 2013, **42**, 1708–1714.

34 C. S. Diercks, Y. Liu, K. E. Cordova and O. M. Yaghi, *Nat. Mater.*, 2018, **17**, 301–307.

35 M.-N. Collomb, D. V. Morales, C. N. Astudillo, B. Dautreppe and J. Fortage, *Sustain. Energy Fuels*, 2020, **4**, 31–49.

36 M. J. Frisch, G. W. Trucks, H. B. Schlegel, G. E. Scuseria, M. A. Robb, J. R. Cheeseman, G. Scalmani, V. Barone, G. A. Petersson, H. Nakatsuji, X. Li, M. Caricato, A. Marenich, J. Bloino, B. G. Janesko, R. Gomperts, B. Mennucci, H. P. Hratchian, J. V. Ortiz, A. F. Izmaylov, J. L. Sonnenberg, D. Williams-Young, F. Ding, F. Lipparini, F. Egidi, J. Goings, B. Peng, A. Petrone, T. Henderson, D. Ranasinghe, V. G. Zakrzewski, J. Gao, N. Rega, G. Zheng, W. Liang, M. Hada, M. Ehara, K. Toyota, R. Fukuda, J. Hasegawa, M. Ishida, T. Nakajima, Y. Honda, O. Kitao, H. Nakai, T. Vreven, K. Throssell, J. A. Montgomery Jr., J. E. Peralta, F. Ogliaro, M. Bearpark, J. J. Heyd, E. Brothers, K. N. Kudin, V. N. Staroverov, T. Keith, R. Kobayashi, J. Normand, K. Raghavachari, A. Rendell, J. C. Burant, S. S. Iyengar, J. Tomasi, M. Cossi, J. M. Millam, M. Klene, C. Adamo, R. Cammi, J. W. Ochterski, R. L. Martin, K. Morokuma, O. Farkas, J. B. Foresman and D. J. Fox, *Gaussian 09, Revis. A.02*, 2009.

37 C. Adamo and V. Barone, *J. Chem. Phys.*, 1999, **110**, 6158–6170.

38 D. Andrae, U. Häußermann, M. Dolg, H. Stoll and H. Preuß, *Theor. Chim. Acta*, 1990, **77**, 123–141.

39 M. M. Francl, W. J. Pietro, W. J. Hehre, J. S. Binkley, M. S. Gordon, D. J. DeFrees and J. A. Pople, *J. Chem. Phys.*, 1982, **77**, 3654–3665.

40 S. Toyota, *Chem. Rev.*, 2010, **110**, 5398–5424.

41 A. R. Karim, A. Linden, K. K. Baldridge and J. S. Siegel, *Chem. Sci.*, 2010, **1**, 102.

42 S. Bracco, F. Castiglioni, A. Comotti, S. Galli, M. Negroni, A. Maspero and P. Sozzani, *Chem. - A Eur. J.*, 2017, **23**, 11210–11215.

43 P. Martinez-Bulit, A. J. Stirk and S. J. Loeb, *Trends Chem.*, 2019, **1**, 588–600.

44 K. Byrne, M. Zubair, N. Zhu, X.-P. Zhou, D. S. Fox, H. Zhang, B. Twamley, M. J. Lennox, T. Düren and W. Schmitt, *Nat. Commun.*, 2017, **8**, 15268.

45 N. Zhu, M. J. Lennox, T. Düren and W. Schmitt, *Chem. Commun.*, 2014, **50**, 4207–4210.

46 N. Zhu, D. Sensharma, P. Wix, M. J. Lennox, T. Düren, W. Y. Wong and W. Schmitt, *Eur. J. Inorg. Chem.*, 2016, **2016**, 1939–1943.

47 D. Dubbeldam, S. Calero, D. E. Ellis and R. Q. Snurr, *Mol. Simul.*, 2016, **42**, 81–101.

48 O. V. Dolomanov, L. J. Bourhis, R. J. Gildea, J. A. K. Howard and H. Puschmann, *J. Appl. Crystallogr.*, 2009, **42**, 339–341.

49 X. Qin, X. Zhang, M. Wang, Y. Dong, J. Liu, Z. Zhu, M. Li, D. Yang and Y. Shao, *Anal. Chem.*, 2018, **90**, 11622–11628.

50 G. Zhao, Y. Wang, X. Li, X. Dong, H. Wang, B. Du, W. Cao and Q. Wei, *ACS Appl. Mater. Interfaces*, 2018, **10**, 22932–22938.

51 A. Shastri, A. K. Das, S. Krishnakumar, P. J. Singh and B. N. Raja Sekhar, *J. Chem. Phys.*, 2017, **147**, 224305.

52 M. B. Shundalau, P. S. Chybirai, A. I. Komyak, A. P. Zazhogin, M. A. Ksenofontov and D. S. Umreiko, *J. Appl. Spectrosc.*, 2011, **78**, 326–336.

53 S. Alizadeh and D. Nematollahi, *J. Am. Chem. Soc.*, 2017, **139**, 4753–4761.

54 W. A. Maza and A. J. Morris, *J. Phys. Chem. C*, 2014, **118**, 8803–8817.

55 K. Nakamoto, *Infrared and Raman Spectra of Inorganic and Coordination Compounds: Part B: Applications in Coordination, Organometallic, and Bioinorganic Chemistry*, Wiley, New York, 6th Ed., 2008.

56 S. D. Robinson and M. F. Uttley, *J. Chem. Soc. Dalton Trans.*, 1973, 1912.

57 G. Deacon, *Coord. Chem. Rev.*, 1980, **33**, 227–250.

58 K. Ohashi and H. Takeshita, *Spectrochim. Acta Part A Mol. Biomol. Spectrosc.*, 2021, **248**, 119289.

59 W. R. Heinz, I. Agirrezabal-Telleria, R. Junk, J. Berger, J. Wang, D. I. Sharapa, M. Gil-Calvo, I. Luz, M. Soukri, F. Studt, Y. Wang, C. Wöll, H. Bunzen, M. Drees and R. A. Fischer, *ACS Appl. Mater. Interfaces*, 2020, **12**, 40635–40647.

60 A. Shuihab and S. Khalf, *AIP Conf. Proc.*, 2018, **1968**, 020026.

61 D. Lin-Vien, N. B. Colthup, W. G. Fateley and J. G. Grasselli, in *The Handbook of Infrared and Raman Characteristic Frequencies of Organic Molecules*, Elsevier, 1991, pp. 277–306.

62 I. I. Rzeźnicka, H. Horino, N. Kikkawa, S. Sakaguchi, A. Morita, S. Takahashi, T. Komeda, H. Fukumura, T. Yamada and M. Kawai, *Surf. Sci.*, 2013, **617**, 1–9.

63 H. G. M. Edwards, E. Smith and G. Dent., *J. Raman Spectrosc.*, 2005, **36**, 835–835.

64 E. Smith and G. Dent, *Modern Raman Spectroscopy - A Practical Approach*, John Wiley & Sons, Ltd, Chichester, UK, 2004.

65 M. Elcheikh Mahmoud, H. Audi, A. Assoud, T. H. Ghaddar and M. Hmadeh, *J. Am. Chem. Soc.*, 2019, **141**, 7115–7121.

66 D. Micheroni, Z. Lin, Y.-S. Chen and W. Lin, *Inorg. Chem.*, 2019, **58**, 7645–7648.

67 M. Sadakiyo, M. Kon-no, K. Sato, K. Nagaoka, H. Kasai, K. Kato and M. Yamauchi, *Dalton Trans.*, 2014, **43**, 11295–11298.

68 C. Wang, K. E. DeKrafft and W. Lin, *J. Am. Chem. Soc.*, 2012, **134**, 7211–7214.

69 Z.-M. Zhang, T. Zhang, C. Wang, Z. Lin, L.-S. Long and W. Lin, *J. Am. Chem. Soc.*, 2015, **137**, 3197–3200.

70 P. Wu, X. Guo, L. Cheng, C. He, J. Wang and C. Duan, *Inorg. Chem.*, 2016, **55**, 8153–8159.

71 Y. Xiao, Y. Cui, Q. Zheng, S. Xiang, G. Qian and B. Chen, *Chem. Commun.*, 2010, **46**, 5503.

72 E. A. Davis and N. F. Mott, *Philos. Mag.*, 1970, **22**, 0903–0922.

73 J. Tauc, R. Grigorovici and A. Vancu, *Phys. Stat. Sol.*, 1966, **15**, 627–637.

74 N. F. Mott and E. A. Davis, *Electronic processes in non-crystalline materials*, Oxford University, 2012.

75 P. Makuła, M. Pacia and W. Macyk, *J. Phys. Chem. Lett.*, 2018, **9**, 6814–6817.

76 J. Qiu, X. Zhang, Y. Feng, X. Zhang, H. Wang and J. Yao, *Appl. Catal. B Environ.*, 2018, **231**, 317–342.

77 C.-K. Lin, D. Zhao, W.-Y. Gao, Z. Yang, J. Ye, T. Xu, Q. Ge, S. Ma and D.-J. Liu, *Inorg. Chem.*, 2012, **51**, 9039–9044.

78 Y. Zhou, W. Yang, M. Qin and H. Zhao, *Appl. Organomet. Chem.*, 2016, **30**, 188–192.

79 R. Haldar, L. Heinke and C. Wöll, *Adv. Mater.*, 2020, **32**, 1905227.

80 M. Li and M. Dincă, *J. Am. Chem. Soc.*, 2011, **133**, 12926–12929.

81 W.-J. Li, M. Tu, R. Cao and R. A. Fischer, *J. Mater. Chem. A*, 2016, **4**, 12356–12369.

82 D. R. Weinberg, C. J. Gagliardi, J. F. Hull, C. F. Murphy, C. A. Kent, B. C. Westlake, A. Paul, D. H. Ess, D. G. McCafferty and T. J. Meyer, *Chem. Rev.*, 2012, **112**, 4016–4093.

83 O. S. Wenger, *Acc. Chem. Res.*, 2013, **46**, 1517–1526.

84 H. Takeda and O. Ishitani, *Coord. Chem. Rev.*, 2010, **254**, 346–354.

85 D. M. Schultz and T. P. Yoon, *Science*, 2014, **343**, 6174.

86 J. Soriano-López, R. Elliott, A. C. Kathalikkattil, A. M. Ako, M. Mulahmetović, M. Venkatesan and W. Schmitt, *ACS Sustain. Chem. Eng.*, 2020, **8**, 13648–13659.

87 A. M. Ako, A. C. Kathalikkattil, R. Elliott, J. Soriano-López, I. M. McKeogh, M. Zubair, N. Zhu, M. García-Melchor, P. E. Kruger and W. Schmitt, *Inorg. Chem.*, 2020, **59**, 14432–14438.

88 S. Tandon, J. Soriano-López, A. C. Kathalikkattil, G. Jin, P. Wix, M. Venkatesan, R. Lundy, M. A. Morris, G. W. Watson and W. Schmitt, *Sustain. Energy Fuels*, 2020, **4**, 4464–4468.

89 N. Elgrishi, K. J. Rountree, B. D. McCarthy, E. S. Rountree, T. T. Eisenhart and

J. L. Dempsey, *J. Chem. Educ.*, 2018, **95**, 197–206.

90 J. C. Hidalgo-Acosta, M. A. Méndez, M. D. Scanlon, H. Vrubel, V. Amstutz, W. Adamiak, M. Opallo and H. H. Girault, *Chem. Sci.*, 2015, **6**, 1761–1769.

91 R. Ifraemov, R. Shimoni, W. He, G. Peng and I. Hod, *J. Mater. Chem. A*, 2019, **7**, 3046–3053.

92 M. Ali, E. Pervaiz, T. Noor, O. Rabi, R. Zahra and M. Yang, *Int. J. Energy Res.*, 2021, **45**, 1190–1226.

93 S. M. Pratik, L. Gagliardi and C. J. Cramer, *J. Phys. Chem. C*, 2020, **124**, 1878–1887.

94 M. Souto, J. Calbo, S. Mañas-Valero, A. Walsh and G. Mínguez Espallargas, *Beilstein J. Nanotechnol.*, 2019, **10**, 1883–1893.

95 Y. Pan, X. Liu, W. Zhang, Z. Liu, G. Zeng, B. Shao, Q. Liang, Q. He, X. Yuan, D. Huang and M. Chen, *Appl. Catal. B Environ.*, 2020, **265**, 118579.

96 H. Kuzmany, R. Pfeiffer, M. Hulman and C. Kramberger, *Philos. Trans. R. Soc. London. Ser. A Math. Phys. Eng. Sci.*, 2004, **362**, 2375–2406.

97 F. Zhang, C. Yuan, X. Lu, L. Zhang, Q. Che and X. Zhang, *J. Power Sources*, 2012, **203**, 250–256.

98 Z. Zhuang and D. Liu, *Nano-Micro Lett.*, 2020, **12**, 132.

99 T. R. Cook, Y.-R. Zheng and P. J. Stang, *Chem. Rev.*, 2013, **113**, 734–777.

100 K. Wu, K. Li, Y.-J. Hou, M. Pan, L.-Y. Zhang, L. Chen and C.-Y. Su, *Nat. Commun.*, 2016, **7**, 10487.

101 U. Mueller, M. Schubert, F. Teich, H. Puetter, K. Schierle-Arndt and J. Pastré, *J. Mater. Chem.*, 2006, **16**, 626–636.

102 M. Li and M. Dincă, *J. Am. Chem. Soc.*, 2011, **133**, 12926–12929.

Chapter 5

Experimental

5. Experimental

5.1. Materials and Methods

Reagents: All chemicals and solvents were purchased from Sigma-Aldrich, Fisher Scientific Limited., VWR International, Fluorochem Limited, Santa Cruz Biotechnology or Sparks Lab Supplies. Solvents were supplied by internal solvent supplier and used without further purification. Ethanol and methanol were of technical grade quality, while acetonitrile, dichloromethane (DCM) and dimethylformamide (DMF) were of HPLC grade quality except where otherwise stated. Water was deionised except where otherwise noted.

NMR Spectroscopy: ^{1}H and ^{13}C NMR spectra were recorded in suitable deuterated solvents at 293 K on a Bruker Spectrospin DPX- 400 AV AVANCE III and 600 AVANCE II spectrometer operating at 400 MHz and 600 MHz, respectively by Dr. Manuel Rüther and Dr. John O'Brien. Chemical shifts are reported in ppm, with the deuterated solvents acting as an internal reference. Data obtained was analysed *via* Brucker TopSpin 4.0.6 software. Standard abbreviations were used in the analysis of the data: s, singlet; d, doublet; t, triplet; m, multiplet; *J*, coupling constant.

IR Spectroscopy: Infrared spectroscopy was recorded using a PerkinElmer Spectrum One FT-IR spectrometer using a universal attenuated total reflectance (ATR) sampling accessory. Samples were measured with a scan rate of 16 scans per minute with a resolution of 4 cm^{-1} in a spectral range of 4000-400 cm^{-1}. Data was collected and analysed using Spectrum v5.0.1 (2002 PerkinElmer Instrument LLC) and OriginLab 2020 software. Abbreviations used in the analysis of the data are: vs, very strong; s, strong; m, medium; w, weak; br, broad.

Mass Spectrometry: Mass spectrometry was carried out using a Micromass LCT Electrospray mass spectrometer by Dr. Gary Hessman. MALDI spectra were attained using a Waters Maldi-Q-Tof Premier spectrometer in negative mode using DCTB (trans-2-[3-4-tert-butylphenyl)-2-methyl-2-propenylidene]malononitrile) as a MALDI matrix. ESI mass spectra were acquired using a Micromass time of flight (tof) mass spectrometer, interfaced to a Waters 2690 HPLC. All samples were diluted in appropriate HPLC grade solvent. Masses were recorded over the range 100-1000 m/z. The data was obtained and analysed using Masslynx v4.1 software.

Thermogravimetric Analysis: Thermogravimetric Analysis (TGA) was carried out using a Perkin Elmer Pyris-1 thermogravimetric analyser under air atmosphere. Nickel and iron standards were used to calibrate the instrument prior to undergoing measurements. Measurements were carried out between 25 °C and 700 °C at a heating rate of 5 °C per minute in a ceramic crucible. Data were obtained *via* Pyris and analysed *via* OriginLab 2020 software.

Raman Spectroscopy: Raman spectroscopy was performed using a Renishaw inVia Raman microscope. Samples were mounted on glass slides and measured at 50x magnification unless otherwise stated. Samples were treated with a single scan measurement of 10 accumulations at an exposure time of 1 second and a laser power of 100%. The data was obtained using WiRE 3.2 software. The data obtained was analysed *via* OriginLab 2020 software.

Elemental Analysis: Elemental Carbon, Hydrogen and Nitrogen (CHN) analysis was acquired using an Exeter Analytical CE 400 at the Analytical Laboratory, School of Chemistry and Chemical Biology, University College Dublin by Ronan Crowley.

Scanning Electron Microscopy and Energy-Dispersive X-ray Spectroscopy: Scanning Electron Microscopy and Energy-Dispersive X-ray spectroscopy was carried out by Mariah O'Doherty. Data was obtained using a Zeiss Ultra Plus-Scanning Electron Microscope with an imaging resolution of 1 nm, accelerating voltages between 100 V and 30 Kv and EDX elemental analyser. INCA software was used for EDX analysis.

UV-Visible Spectroscopy: Solution-state UV-vis absorption spectroscopy measurements were performed in acetonitrile using matched quartz cuvettes with an optical path length of 1 cm. Absorption spectra were recorded on a Lambda 35 UV-vis spectrometer within a wavelength range of 200 - 700 nm and scan speed of 240 nm/min. Baseline correction measurements using acetonitrile were used for all spectra. Data was obtained *via* UV WINLAB software and analysed *via* OriginLab 2020 software.

Steady State Fluorescence Spectroscopy: Steady state emission spectra were recorded on a Horiba Fluoromax-4P spectrofluorometer with an S detector operating at 950 V high voltage (HV). Measurements were excited at 450 nm within a range of 460 – 825 nm with 5 nm emission and 5 nm excitation slit bandpass (JY monochromator), unless otherwise stated. An integration time of 0.1 seconds and 1 accumulation. Measurements were carried out in acetonitrile using a quartz fluorescence cuvette with an optical path

length of 1 cm. Signal corrections were applied to all measurements. Data was obtained *via* FluorEssence V3.8 powered by Origin 8 software and analysed *via* OriginLab 2020 software.

Time-Resolved Fluorescence Spectroscopy: Fluorescent lifetimes were recorded in acetonitrile using a Horiba Fluorolog-3 Time-Correlated Single Photon Counting (TCSPC) instrument with a single photon counting controller (FluoroHub) and a direct power supply (DPS-1). A repetition rate of 500 KHz was used alongside a sync and coaxial delay of 0 ns. 10,000 counts were collected for each lifetime experiment within the chosen TAC range of 2000 ns. A 372 nm pulsed laser diode was employed with a bandpass of 29.4 nm, unless otherwise stated. A 458 nm pulsed laser diode was used to confirm the results obtained. An excitation wavelength of 450 nm was used, unless otherwise stated. All measurement data was obtained *via* Horiba DataStation v2.4 software. The data was analysed and fitted *via* Horbia Decay Analysis Software v6.3.

Photoluminescence Spectroscopy: Photoluminescence (PL) and absorption spectra were measured using a suspension of material in DMF using a quartz cuvette with an optical path length of 1 cm. Measurements were carried out using a Cary 50 UV-vis spectrophotometer. The excitation power used for the PL measurements was 4 µW. Time-resolved PL (TRPL) measurements in DMF were performed using a PicoQuant Microtime 200 time-resolved confocal microscope system using an excitation of 90 ps pulses at a wavelength of 405 nm with a repetition rate of 10 MHz and an integration time of 4 ms per pixel. The laser spot size was ~430 nm. The materials were drop-casted and dried on quartz slides. The sample was excited through a 40x objective (NA = 0.65) and the PL was collected through the same objective. The excitation power used for the PL measurements was 0.2 µW. All scans were performed over 10 µm x 10 µm square areas.

Fluorescence Lifetime Imaging (FLIM): Lifetime measurements of solid-state samples were measured using a PicoQuant Microtime 200 under the same conditions that were applied for the PL decay measurements. The lifetimes at different spectral locations were measured using bandpass filters with centre wavelengths of 635, 650, 700, 750 and 800 nm, all of which have a full width at half maximum (FWHM) of 10 nm.

Single-Crystal X-Ray Diffraction Analysis: Single crystal X-ray diffraction data were collected by Dr. Nian-Yong Zhu and Dr. Brendan Twamley. Crystals were mounted on a MiTiGen micromount and data for the compounds was collected on a Bruker APEX DUO with graphite-monochromated Mo Kα (λ = 0.71073 Å) or microfocus Cu Kα (λ = 1.54178 Å) radiation. Datasets were collected at 215 - 220 K using an Oxford Cryostream Cobra mounted in a glass capillary with a minute amount of solvent. Bruker APEX2 software[1] was used to collect and reduce the data, determine the space group, solve and refine the structure. Absorption corrections were applied using SADABS.[2] Final refinements were performed with SHELXL.[3] All non-hydrogen atoms were refined anisotropically. All obtained structures contain large void volumes and ordered solvent molecules could not always be accurately located. To account for this, the Platon-SQUEEZE routine was employed to calculate the void volumes of the structures and generate a new reflection file by eliminating the diffraction signals attributed to the solvent molecules that could not be accurately located.

Powder X-Ray Diffraction Analysis: Powder X-ray diffraction patterns were recorded on an APEX II DUO CCD diffractometer using a I μS CuK α X-ray source. Bulk samples were kept in DMF, and ground under solvent to produce micro-crystalline samples and transferred to fill 1-2 cm in height with a pipette into 0.3 - 1.0 mm diameter borosilicate glass or "special glass" capillaries from WJM Glass Müller GmbH. The capillaries were mounted and centred on a goniometer head on a Bruker APEX II diffractometer for data collection. The data were collected upon 360 °φ rotational frames at 2 θ values of 10° and 20° with exposure times of 10 or 20 minutes per frame at a detector distance of 120 mm. Overlapping sections of data were combined and the data was processed using the Bruker APEX2 software routine XRD2-Eval subprogram.[1] Analysis and background corrections were carried out using DIFFRAC.EVA software.

Energy Barrier for Rotation Studies: Density Functional Theory (DFT) calculations were performed, and the MOF was truncated and modelled in a non-periodic environment in vacuum. The calculations were carried out with the cluster code gaussian09[4] using PBE0[5] functional in conjunction with SDDALL[6] basis set with an effective core potential for Ru, 6-31G(2d)[7] basis set for phosphorus, the 6-31G(d)[7] basis set for C and N, and 6-31G(p)[8] basis set for H.

Geometrical Characterisation: To estimate the geometrical properties i.e. helium void fraction, pore volume, surface area and pore size distribution of the materials, the molecular simulation software for adsorption and diffusion in flexible nano porous materials, RASPA, was used.[9]

Solvothermal Synthesis: Solvothermal synthesis was conducted using a Grant QBD4 Dry Block Heating Systems. The reactions were carried out in 1.5 mL sealed micro reaction vials with extra dry solvents except where otherwise stated.

Bulk Electrochemical Deposition: The cathodic electrochemical synthesis and *in-situ* film deposition of MOFs was carried out on a Bio-logic Science Instrument VSP Potentiostat using precut 1 cm^2 fluorine-doped tin oxide (FTO) electrodes. A conventional 3-electrode setup involving a Pt wire counter electrode and an $Ag/Ag(cryptand)^+$/DMF reference electrode in a DMF/H_2O (100/1 v/v) solvent mixture using $(NBu_4)PF_6$ as electrolyte. The synthesis and deposition were achieved from diluted reaction mixtures containing millimolar quantities of material at a potential of –1.5 V for 5 minutes in ambient temperature.

Photo-Electro Catalytic H_2O Oxidation: Photo-Electro Catalytic H_2O Oxidation was carried out on a Bio-logic Science Instrument VSP Potentiostat and conducted in a photoelectrochemical cell with a light emitting diode (LED) with a power of 0.149 W and wavelength (λ) of 470 nm under N_2 flow. A 3-electrode set-up consisting of a FTO working electrode, a Pt-mesh counter electrode and a saturated calomel electrode (SCE) as the reference electrode. Cyclic voltammetry (CV) and linear sweep voltammetry (LSV) within a potential range of -1.0 V to 1.3 V (vs SCE) in dry MeCN was initially used as reference data. All potentials herein are referenced vs SCE unless otherwise stated

5.2 Synthetic Procedures

5.2.1 Synthesis of Methyl 4-((trimethylsilyl)ethynyl)benzoate (TMS-11)

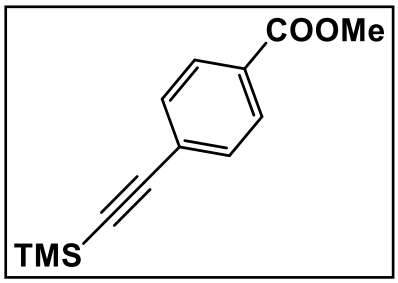

Methyl 4-iodobenzoate (5.7 g, 21.7 mmol) and trimethylsilylacetylene (3.4 mL, 23.9 mmol) were dissolved in a solvent mixture of THF (40 mL) and triethylamine (10 mL) under N_2. The three necked round bottom flask was evacuated and refilled with N_2 multiple times prior to the addition of $Pd(PPh_3)_2Cl_2$ (0.457 g, 0.65 mmol) and CuI (0.496 g, 1.3 mmol). The reaction mixture was stirred for 2 hours at 80 °C prior to cooling to ambient temperature. Following filtration over Celite and washing with diethyl ether the solution was further washed with aqueous NH_4Cl and brine, prior to the organic layer separation. The organic layer was then dried over $MgSO_4$ and the solvent was removed *via* rotary evaporation. The residue was purified by flash chromatography on silica gel eluting with hexane/DCM (4: 1), yielding a white solid product (3.98 g, 79 %). ^{1}H-NMR ($CDCl_3$, 400 MHz); δ_H (ppm) = 0.28 (s, 9H), 3.94 (s, 3H), 7.54 (d, J_1 = 8.47 Hz, 2H), 7.99(d, J_1= 8.56 Hz, 2H).

5.2.2 Synthesis of Methyl 4-ethynylbenzoate (11)

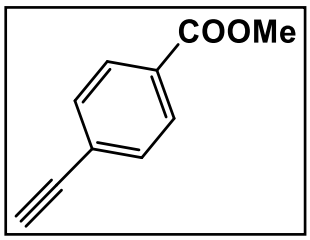

To a pre-evacuated round bottom flask a solvent mixture of methanol (25 mL) and CH_2Cl_2 (50 mL) was added. Methyl 4-((trimethylsilyl)ethynyl)benzoate (2.2g, 9.45 mmol) was added to the solvent mixture, ensuring it was fully dissolved prior to the addition anhydrous K_2CO_3 (2.65g, 19.15 mmol). The reaction mixture was stirred at ambient temperature for an additional 4 hours. The reaction mixture was dried *via* rotary evaporation prior to re-dissolving in DCM and washing with aqueous NH_4Cl and brine. The organic layer was finally separated, dried on $MgSO_4$ and the solvent was removed, yielding the product as crystalline white needles at a quantitative yield. ^{1}H-NMR ($CDCl_3$, 400 MHz); δ_H (ppm) = 3.25 (s, 1H), 3.94 (s, 3H), 7.58 (d, J_1 = 8.62 Hz, 2H), 8.02(d, J_1 = 8.57 Hz, 2H).

5.2.3 Synthesis of Methyl 3-((trimethylsilyl)ethynyl)benzoate (TMS-12)

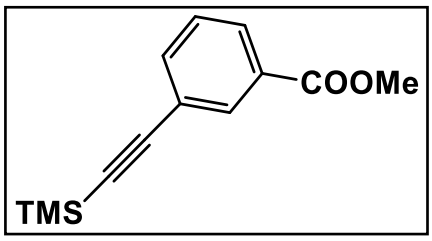

Methyl 3-iodobenzoate (5.7 g, 21.7 mmol) and trimethylsilylacetylene (3.4 mL, 23.9 mmol) were dissolved in a solvent mixture of THF (40 mL) and triethylamine (10 mL) under N2. The three necked round bottom flask was evacuated and refilled with N2 multiple times prior to the addition of $Pd(PPh_3)_2Cl_2$ (0.457 g, 0.65 mmol) and CuI (0.496 g, 1.3 mmol). The reaction mixture was stirred for 2 hours at 80 °C prior to cooling to ambient temperature. Following filtration over Celite and washing with diethyl ether the solution was further washed with aqueous NH_4Cl and brine, prior to the organic layer separation. The organic layer was then dried over $MgSO_4$ and the solvent was removed *via* rotary evaporation. The residue was purified by flash chromatography on silica gel eluting with hexane/DCM (4: 1), yielding a white solid product (3.53 g, 70 %). ^{1}H-NMR ($CDCl_3$, 400 MHz); δ_H (ppm) = 0.27 (s, 9H), 3.93 (s, 3H), 7.39 (t, J_1 = 7.87 Hz, 1H), 7.65 (d, J_1 = 7.61 Hz, 1H), 7.99 (d, J_1 = 7.83 Hz, 1H), 8.15 (s, 1H).

5.2.4 Synthesis of Methyl 3-ethynylbenzoate (12)

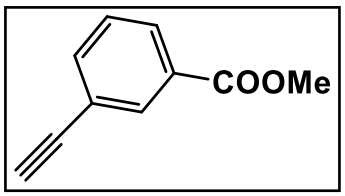

To a pre-evacuated round bottom flask a solvent mixture of methanol (25 mL) and CH_2Cl_2 (50 mL) was added. Methyl 3-((trimethylsilyl)ethynyl)benzoate (2.2 g, 9.45 mmol) was added to the solvent mixture, ensuring it was fully dissolved prior to the addition anhydrous K_2CO_3 (2.65 g, 19.15 mmol). The reaction mixture was stirred at ambient temperature for an additional 3 hours. The reaction mixture was dried *via* rotary evaporation prior to re-dissolving in DCM and washing with aqueous NH_4Cl and brine. The organic layer was finally separated, dried on $MgSO_4$ and the solvent was removed, yielding the product as crystalline white needles at a quantitative yield. ^{1}H-NMR ($CDCl_3$, 400 MHz); δ_H (ppm) = 3.15 (s, 1H), 3.95 (s, 3H), 7.43 (t, J_1 = 7.87 Hz, 1H), 7.69 (d, J_1 = 7.81 Hz, 1H), 8.04 (d, J_1 = 7.96 Hz, 1H), 8.19 (s, 1H) .

5.2.5 Synthesis of Dimethyl 5-(2-(trimethylsilyl)ethynyl)isophtalate (TMS-13)

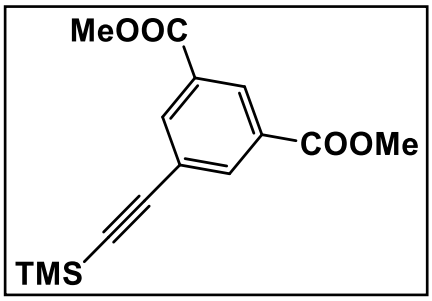

Dimethyl 5-bromoisophtalate (5 g, 18.31 mmol), CuI (0.175 g, 0.915 mmol), and $Pd(PPh_3)_2Cl_2$ (0.64 g, 0.915 mmol) were added to a pre-evacuated round bottomed flask. Following the addition of the reagents the flask was again evacuated and refilled with N_2 multiple times, before trimethylsilylacetylene (3.8 mL, 27.47 mmol), THF (70 mL) and triethylamine (10 mL, 71.81 mmol) were added *via* syringe, consecutively. The reaction solution was stirred under N_2 at ambient temperature for 24 hours, prior to the removal of the volatile. The mixture was re-dissolved in DCM and the organic phase was separated, washed with NH_4Cl, H_2O and brine. The organic solution was dried over $MgSO_4$ and filtered. The solvent was removed prior to purification *via* flash chromatography on silica gel using hexane/DCM (4: 1) as eluent. The product was obtained as an off white crystalline solid. Yield: (4.15 g, 78 %). ^{1}H-NMR ($CDCl_3$, 400 MHz); δ_H (ppm) = 0.29 (s, 9H), 3.98 (s, 6H), 8.32 (d, J_1 = 1.67 Hz, 2H), 8.63 (t, J_1 = 1.70 Hz, 1H).

5.2.6 Synthesis of Dimethyl 5-ethynylisophtalate (13)

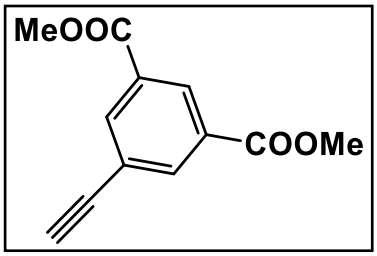

A mixture of dimethyl 5-(2-(trimethylsilyl)ethynyl)-isophtalate (2.5 g, 9.16 mmol), K_2CO_3 (2.5 g, 18.09 mmol) was added to a pre-evacuated round bottomed flask containing mixed solvent of DCM (50 mL) and MeOH (25 mL). The flask was further evacuated and de-gassed with N_2 multiple times prior to stirring for 6 hours at ambient temperature. The reaction solvent was removed by rotary evaporation prior to redissolving in DCM. The filtrate was filtered and the organic phase was washed with H_2O and brine prior to drying over $MgSO_4$. The solution was filtered and the solvent was removed to dryness. The product was obtained as a white crystalline powder at quantitative yield. ^{1}H-NMR ($CDCl_3$, 400 MHz); δ_H (ppm) = 3.20 (s, 1H), 3.98 (s, 6H), 8.34 (d, J_1 = 1.70 Hz, 2H), 8.66 (t, J_1 = 1.69 Hz, 1H).

5.2.7 Synthesis of 2,2'-bipyridine-dihydrobromide (1)

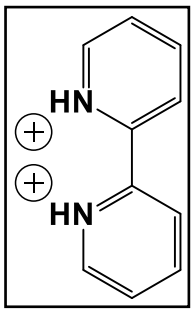

HBr (21.5 mL, 48% wt/wt) was added to a solution of 2,2'-bipyridine (10.0 g, 64.0 mmol) in methanol at 0 °C. Upon addition of the reagents, the cooling bath was removed. The mixture was left stirring at ambient temperature for one hour after which the solvent was removed on a rotary evaporator and allowed to dry under vacuum overnight. A bright yellow powder was collected at a quantitative yield. ^{1}H-NMR ($CDCl_3$, 400 MHz); δ_H (ppm) = 7.78 (s, 2H), 8.3 (s, 4H), 8.7 (s, 2H). MS (ESI): Found *m/z* = 157.07. Calculated *m/z* = 158.08 for [$C_{10}H_{10}N_2$].

5.2.8 Synthesis of 5,5'-dibromo-2,2'-bipyridine (2)

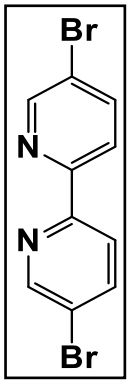

2,2'-bipyridine-dihydrobromide (12.0 g, 37.7 mmol) was ground to a fine powder, upon which a syringe was used to carefully inject bromine (4.00 mL, 2.40 g, 77.6 mmol) into lumps of powder. Care was taken during the slow addition bromine as the powder was continuously grinded until fine, non-fuming orange powder was obtained. The reaction mixture was added to a Teflon bomb and placed into an oven at 185 °C for 72 hours. Upon reaction completion the bomb was then allowed to cool to ambient temperature and its contents were added to a solution of NaOH (200 mL, 1.00 M) slowly. EDTA-tetrasodium salt (10.0 g), Na_2SO_3 (10.0 g), and DCM (200 mL) were added sequentially, and the mixture was allowed to stir at ambient temperature for two hours allowing for the formation of a white precipitate. The precipitate was filtered and washed with boiling H_2O and EtOH respectively. The washed product was allowed to dry overnight yielding a white microcrystalline powder. Yield: (7.34 g, 62 %). ^{1}H-NMR ($CDCl_3$, 400 MHz); δ_H (ppm) = 7.96 (dd, J_1 = 8.65 Hz, J_2 = 2.11 Hz, 2H), 8.31 (d, J_1 = 8.43 Hz, 2H), 8.73 (d, J_1 = 1.87 Hz, 2H). MS (ESI): Found *m/z* = 312.88. Calculated *m/z* = 313.89 for [$C_{10}H_7Br_2N_2$].

5.2.9 Synthesis of 3,8'-dibromo-1,10'-phenanthroline (3)

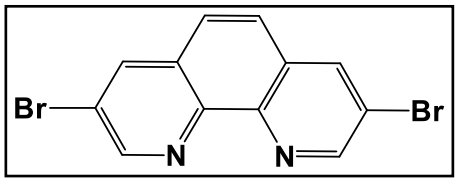

Phenanthroline (5 g, 27.8 mmol), S_2Cl_2 (7.28 ml, 12.3 g, 91.1 mmol), pyridine (7.23 ml, 7.10 g, 89.8 mmol) and Br_2 (4.47 ml, 14 g, 87.6 mmol) was added sequentially to a solution of 1-chlorobutane (200 ml). The reaction solution was allowed to reflux for 12 hours at 78 °C. Upon reaction completion the reaction solution was allowed to cool to ambient temperature prior to the addition of NaOH (excess, 2.0 M) and $CHCl_3$ (100 ml). The organic layer was separated and the crude product was purified *via* flash chromatography on silica gel using $CHCl_3$ as eluent. The solvent was removed *via* rotary evaporation and an analytically pure white crystalline product was obtained by recrystallisation from tetrachloroethane (25 ml). Yield: (5.9 g, 63%). ^{1}H-NMR ($CDCl_3$, 400 MHz); δ_H (ppm) = 7.79 (s, 2H), 8.44 (m, 2H), 9.21 (m, 2H). MS (ESI): Found *m/z* = 335.62. Calculated *m/z* = 337.89 for $[C_{12}H_6Br_2N_2]$.

5.2.10 Synthesis of bis-(2,2'-bipyridine)-ruthenium(II) dichloride (4)

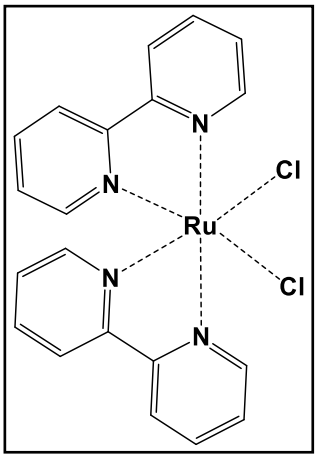

$RuCl_3.xH_2O$ (2.0 g, 8.40 mmol), LiCl (0.40 g, 9.60 mmol) and 2,2'-bipyridine (2.60 g, 8.80 mmol) were added to a pre-evacuated and N_2 flushed 50.0 mL round bottomed flask. DMF (30.0 mL) was further added, and the reaction mixture was evacuated and flushed once more prior to heating to reflux at 160 °C overnight. Upon reaction completion acetone (30.0 mL) was added to the hot solution and the reaction solution was allowed to stir for a further one hour. The purple crystalline precipitate was filtered and washed with cold H_2O until a colourless filtrate was observed. The washed purple microcrystalline material was left to dry prior to collection. Yield: (3.05 g, 75 %). ^{1}H-NMR (d_6-DMSO, 400 MHz); δ_H (ppm) = 7.12 (t, J_1 = 6.20 Hz , 2H), 7.48 (m, 2H) 7.67 (t, J_1 = 7.70 Hz, 2H) 7.78 (t, J_1 = 6.20 Hz, 2H) 8.08 (t, J_1 = 7.77 Hz, 2H) 8.50 (d, J_1 = 7.84 Hz, 2H) 8.65 (d, J_1 = 7.89 Hz, 2H) 9.94 (m, 2H). MS (MALDI-TOF): Found *m/z* = 449.01. Calculated *m/z* = 449.01 for $[C_{20}H_{16}Cl_2N_4Ru]$.

5.2.11 Synthesis of [bis-(2,2'-bipyridine)-ruthenium(II)(5,5'-dibromo-2,2'-bipyridine)]$(PF_6)_2$ (5)

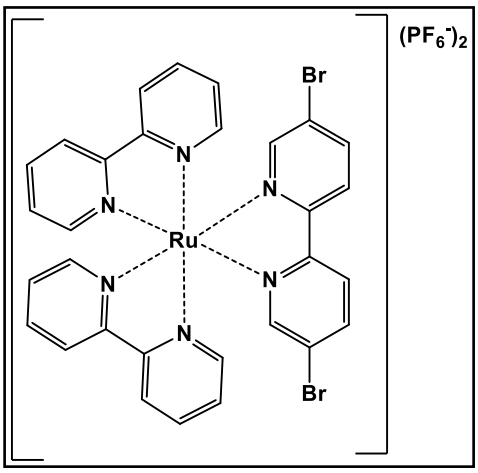

Bis-(2.2'-bipyridine)-ruthenium(II) dichloride (3.84 g, 6.20 mmol) and 5,5'-dibromo-bipyridine (2.58 g, 6.40 mmol) were dissolved in 100.0 mL of an EtOH/H_2O solvent mixture in a 2:1 ratio. The reaction mixture was left to reflux at 120 °C overnight. Upon reaction completion colour change from purple to red was observed. The reaction mixture was allowed to cool to ambient temperature prior to evaporation to dryness on a rotary evaporator. The product was then re-dissolved in deionized water (80.0 mL) and filtered *via* gravity filtration prior to the precipitation of the bright orange solid product by the addition of saturated aqueous solution of NH_4PF_6. The reaction mixture was allowed to stir for 10 minutes, and the product was collected and dried *via* vacuum filtration. Analytically pure crystalline orange needles were obtained by recrystallisation from EtOH/H_2O (2:1). Yield: (5.32 g, 84.4 %). ^{1}H-NMR (d_6-DMSO, 400 MHz); δ_H (ppm) = 7.55 (m, 4H), 7.68 (m, 4H), 7.85 (d, J_1 = 5.23 Hz, 2H), 8.20 (m, 4H), 8.49 (dd, J_1 = 8.75 Hz, J_2 = 2.05 Hz 2H), 8.82 (m, 6H). MS (MALDI-TOF): Found *m/z* = 362.965. Calculated *m/z* = 362.965 for [$C_{30}H_{22}Br_2N_6Ru$].

5.2.12 Synthesis of [bis-(2,2'-bipyridine)-ruthenium(II)(3,8'-dibromo-1,10'-phenanthroline)]$(PF_6)_2$ (6)

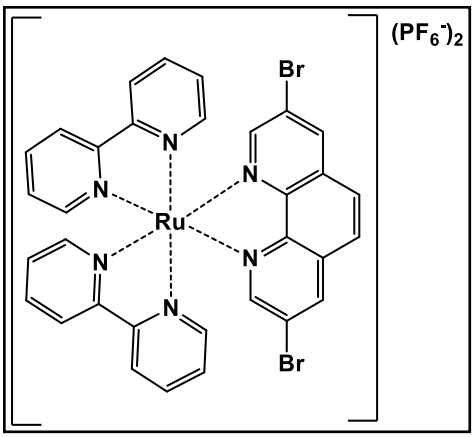

Bis-(2.2'-bipyridine)-ruthenium(II) dichloride (1.92 g, 3.10 mmol) and 3,8'-dibromo-1,10'-phenanthroline (1.4 g, 4.14 mmol) were dissolved in EtOH/H_2O (50 mL) solvent mixture in a 2:1 ratio. The reaction mixture was left to reflux at 105 °C overnight. Upon reaction completion colour change from purple to red was observed. The reaction mixture was allowed to cool to ambient temperature prior to evaporation to dryness on a rotary evaporator. The product was then re-dissolved in deionized water (40.0 mL) and filtered *via* gravity filtration prior

to the precipitation of the bright orange solid product by the addition of saturated aqueous solution of NH_4PF_6. The reaction mixture was allowed to stir for a further 10 minutes and the product was collected and dried *via* vacuum filtration. Analytically pure crystalline red needles were obtained by recrystallisation from $EtOH/H_2O$ (2:1). Yield: (2.13 g, 80 %). ^{1}H-NMR (d_6-DMSO, 400 MHz); δ_H (ppm) = 7.39 (t, J_1 = 6.49 Hz, 3H), 7.60 (t, J_1 = 7.05 Hz, 3H), 7.72 (d, J_1 = 5.36 Hz, 2H), 7.78 (d, J_1 = 5.36 Hz, 2H), 8.14 (t, J_1 = 7.85 2H), 8.22 (t, J_1 = 7. 98 Hz, 2H), 8.32 (m, 4H) 8.42 (s, 2H) 8.50 (s, 2H). MS (MALDI-TOF): Found *m/z* = 374.89. Calculated *m/z* = 375.965 for $[C_{32}H_{22}Br_2N_6Ru]$.

5.2.13 Synthesis of [tris-(5,5'-dibromo-2,2'-bipyridine)-ruthenium(II)]$(PF_6)_2$ (7)

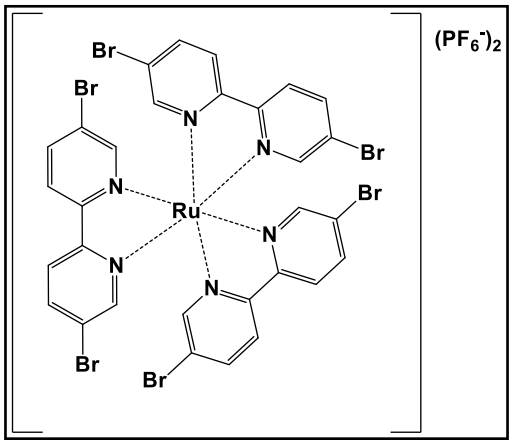

5,5'-dibromo-2,2'-bipyridine (0.5 g, 1.6 mmol) and $[Ru(DMSO)_4Cl_2]$ (0.23 g 0.47 mmol) were allowed to reflux in ethane-1,2-diol (50 ml) at 160 °C for 3 hours. Upon reaction completion the orange-red solution was allowed to cool to ambient temperature prior to the addition of excess saturated aqueous solution of NH_4PF_6. The resulting orange-red precipitate was filtered over Celite and washed with H_2O (3 x 100 ml). The residue was then dissolved in acetonitrile prior to purification *via* column chromatography on silica gel eluting with acetonitrile/H_2O/KNO_3 (14:1:1). Upon collection of the main orange band, an excess aqueous solution of NH_4PF_6 was added and the solvent was reduced by rotary evaporation to yield a fine orange precipitate which was again filtered over Celite and washed with H_2O (2 x 50 ml). Upon washing the precipitate was re-dissolved in acetonitrile and the solvent was removed by rotary evaporation yielding a red crystalline product. Yield: (0.42 g, 62 %). ^{1}H-NMR (d_6-DMSO, 400 MHz); δ_H (ppm) = 7.76 (d, J_1 = 2.01 Hz, 6H), 8.49 (dd, J_1 = 8.79 Hz, J_2 = 2.17 Hz, 6H) 8.75 (d, J_1 = 8.80 Hz, 6H).

5.2.14 Synthesis of [bis-(2,2'-bipyridine)-ruthenium(II)(5,5'-(bis-methyl-4-ethynylbenzoate)-2,2'-bipyridine)]$(PF_6)_2$ (8-R'$_1$)

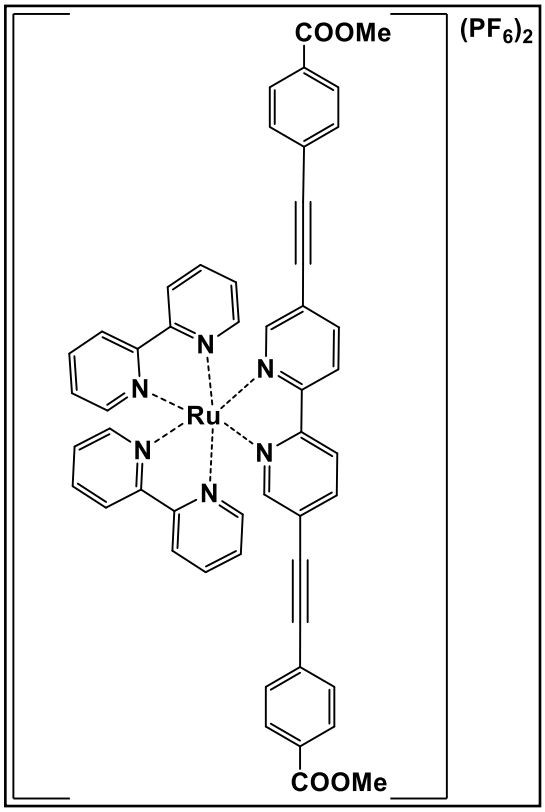

[Bis-(2.2'-bipyridine)-ruthenium(II)(5'5-dibromo-2,2'-bipyridine)]$(PF_6)_2$ (1.8 g, 1.77 mmol) and methyl 4-ethynylbenzoate (2.10 eq.) were dissolved in a pre-degassed round bottom flask containing THF (50 ml) and acetonitrile (19 mL). The reaction mixture was degassed and flushed with N_2 a further three times prior to the addition of DIPA (24 mL), $Pd(PPh_3)_2Cl_2$ (0.07 g, 0.1 mmol) and CuI (0.02 g, 0.1 mmol) respectively under N_2. Prior to refluxing the reaction mixture at 100 °C for 72 hours the flask was evacuated and flushed with N_2 once more. Upon reaction completion the mixture was filtered, and the orange/red precipitate was collected and dried in air for two days. Yield: (1.47 g, 82 %). ^{1}H-NMR (d_6-DMSO, 400 MHz); δ_H (ppm) = 3.87 (s, 6H), 7.56 (m, 4H), 7.65 (m, 4H), 7.71 (m, 2H), 7.87 (m, 4H), 8.01 (m, 4H), 8.20 (m, 4H), 8.42 (m, 2H), 8.84 (m, 4H), 8.96 (m, 2H). MS (MALDI-TOF): Found *m/z* = 442.875. Calculated *m/z* = 443.09 for $[C_{50}H_{36}N_6O_4Ru]$.

5.2.15 Synthesis of [bis-(2,2'-bipyridine)-ruthenium(II)(5,5'-(bis-methyl-3-ethynylbenzoate)-2,2'-bipyridine)]$(PF_6)_2$ (8-R'$_2$)

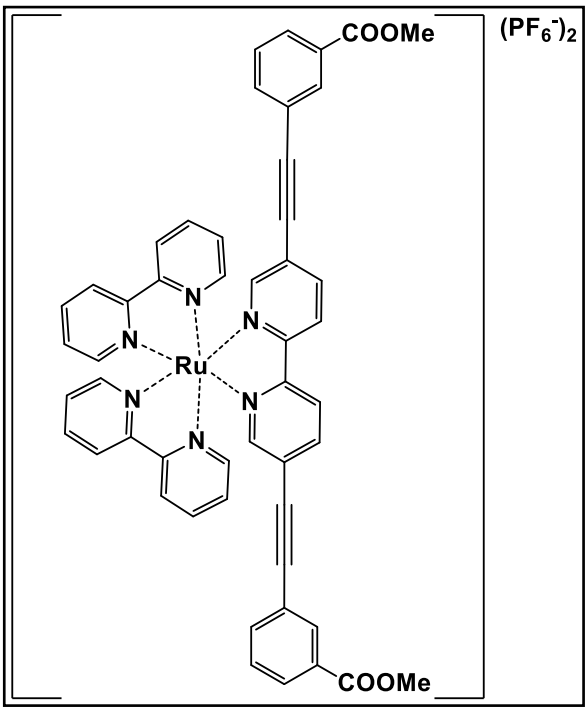

[Bis-(2.2'-bipyridine)-ruthenium(II)(5'5-dibromo-2,2'-bipyridine)]$(PF_6)_2$ (0.476 g, 0.468 mmol) and methyl 3-ethynylbenzoate (2.10 eq.) were dissolved in a pre-degassed round bottom flask containing THF (13 ml) and acetonitrile (5 mL). The reaction mixture was degassed and flushed with N_2 a further three times prior to the addition of DIPA (6 mL), $Pd(PPh_3)_2Cl_2$ (0.0136 g, 0.002 mmol) and CuI (0.0036 g, 0.002 mmol) respectively under N_2. Prior to refluxing the reaction mixture at 100 °C for 72 hours the flask was evacuated and flushed with N_2 once more. Upon reaction completion the mixture was filtered, and the orange/red precipitate was collected and dried in air for two days. Yield: (0.28 g, 59 %). ^{1}H-NMR (d_6-DMSO, 400 MHz); δ_H (ppm) = 3.91 (s, 6H), 7.45 (m, 4H), 7.57 (m, 2H), 7.72 (m, 4H), 7.84 (m, 2H), 7.92 (m, 2H), 8.10 (m, 8H), 8.22 (m, 2H), 8.55 (m, 6H). MS (MALDI-TOF): Found *m/z* = 443.095. Calculated *m/z* = 443.09 for $[C_{50}H_{36}N_6O_4Ru]$.

5.2.16 Synthesis of [bis-(2,2'-bipyridine)-ruthenium(II)(5,5'-(bis-dimethyl-5-ethynylisophtalate)-2,2'-bipyridine)]$(PF_6)_2$ (8-R'$_3$)

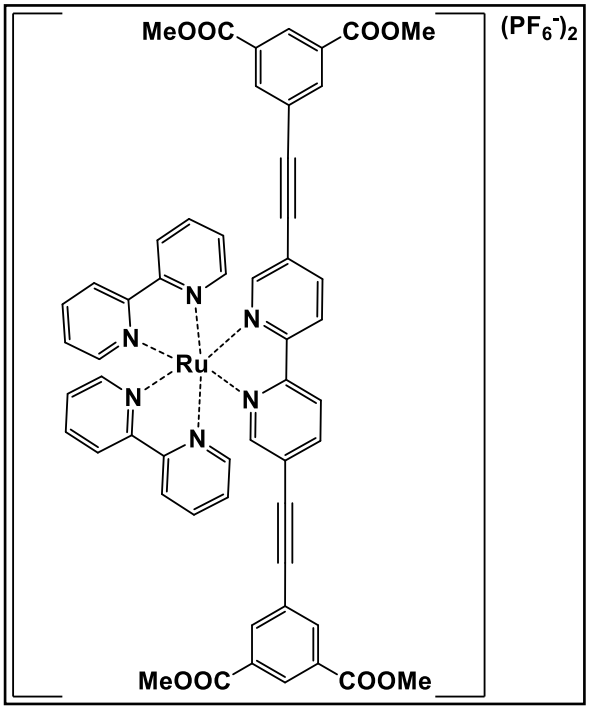

[Bis-(2.2'-bipyridine)-ruthenium(II)(5'5-dibromo-2,2'-bipyridine)]$(PF_6)_2$ (0.9 g, 0.885 mmol) and dimethyl 5-ethynylisophtalate (2.10 eq.) were dissolved in a pre-degassed round bottom flask containing THF (25 ml) and acetonitrile (9.5 mL). The reaction mixture was degassed and flushed with N_2 a further three times prior to the addition of DIPA (12 mL), $Pd(PPh_3)_2Cl_2$ (0.035 g, 0.05 mmol) and CuI (0.01 g, 0.05 mmol) respectively under N_2. Prior to refluxing the reaction mixture at 100 °C for 72 hours the flask was evacuated and flushed with N_2 once more. Upon reaction completion the mixture was filtered, and the orange/red precipitate was collected and dried in air for two days. Yield: 0.8 g, 70 %. ^{1}H-NMR (d_6-DMSO, 400 MHz); δ_H (ppm) = 3.92 (s, 12H), 7.57 (m, 4H), 7.71 (m, 2H), 7.88 (m, 2H), 7.93 (m, 2H), 8.21 (m, 4H), 8.27 (m, 4H), 8.49 (m, 4H), 8.85 (m, 4H) 8.99 (m, 2H). MS (MALDI-TOF): Found *m/z* = 501.095. Calculated *m/z* = 501.095 for $[C_{54}H_{40}N_6O_8Ru]$.

5.2.17 Synthesis of [bis-(2,2'-bipyridine)-ruthenium(II)(3,8'-(bis-dimethyl-5-ethynylisophtalate)-1,10'-phenanthroline)]$(PF_6)_2$ (9)

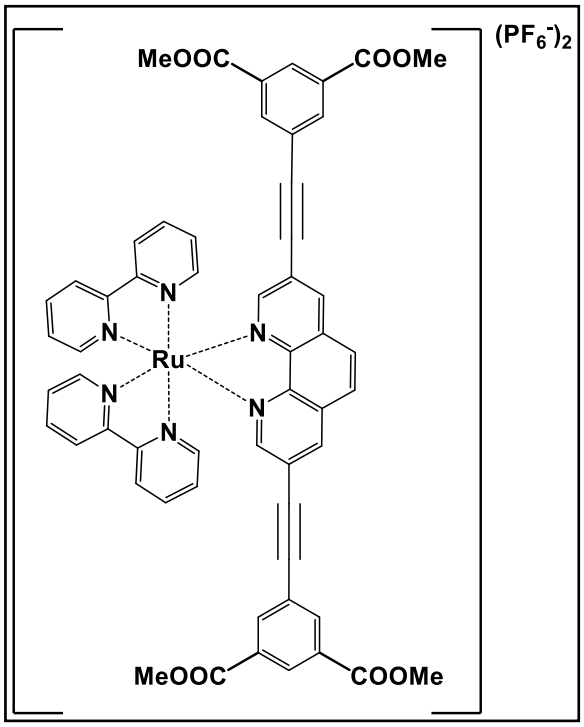

[Bis-(2.2'-bipyridine)-ruthenium(II)(3,8-dibromo-1,10-phenanthroline)]$(PF_6)_2$ (0.352 g, 0.468 mmol) and dimethyl 5-ethynylisophtalate (2.0 eq.) were dissolved in a pre-degassed round bottom flask containing acetonitrile (40.0 mL). The reaction mixture was degassed and flushed with N_2 a further three times prior to the addition of DIPA (10 mL), $Pd(PPh_3)_2Cl_2$ (0.0136 g, 0.002 mmol) and CuI (0.0036 g, 0.002 mmol) respectively under N_2. Prior to refluxing the reaction mixture at 110 °C for 72 hours the flask was evacuated and flushed with N_2 once more. Upon reaction completion the mixture was filtered and excess aqueous NH_4PF_6 was added. The reaction mixture was allowed to stir for 15 minutes, and the dark red precipitate was filtered, collected and allowed to air dry. Yield: 0.247 g, 51 %. ^{1}H-NMR (d_6-DMSO, 400 MHz); δ_H (ppm) = 3.93 (s, 12H), 7.39 (m, 3H), 7.61 (m, 3H), 7.72 (m, 2H), 7.79 (m, 2H), 8.14 (m, 2H), 8.22 (m, 2H), 8.32 (s, 4H), 8.42 (s, 2H), 8.50 (s, 2H), 8.86 (m, 4H), 9.12 (m, 2H). MS (MALDI-TOF): Found *m/z* = 513.145. Calculated *m/z* = 513.1 for $[C_{56}H_{40}N_6O_8Ru]$.

5.2.18 Synthesis of [tris-(5,5'-(bis-dimethyl-5-ethynylisophtalate)-2,2'-bipyridine)-ruthenium(II)]$(PF_6)_2$ (10)

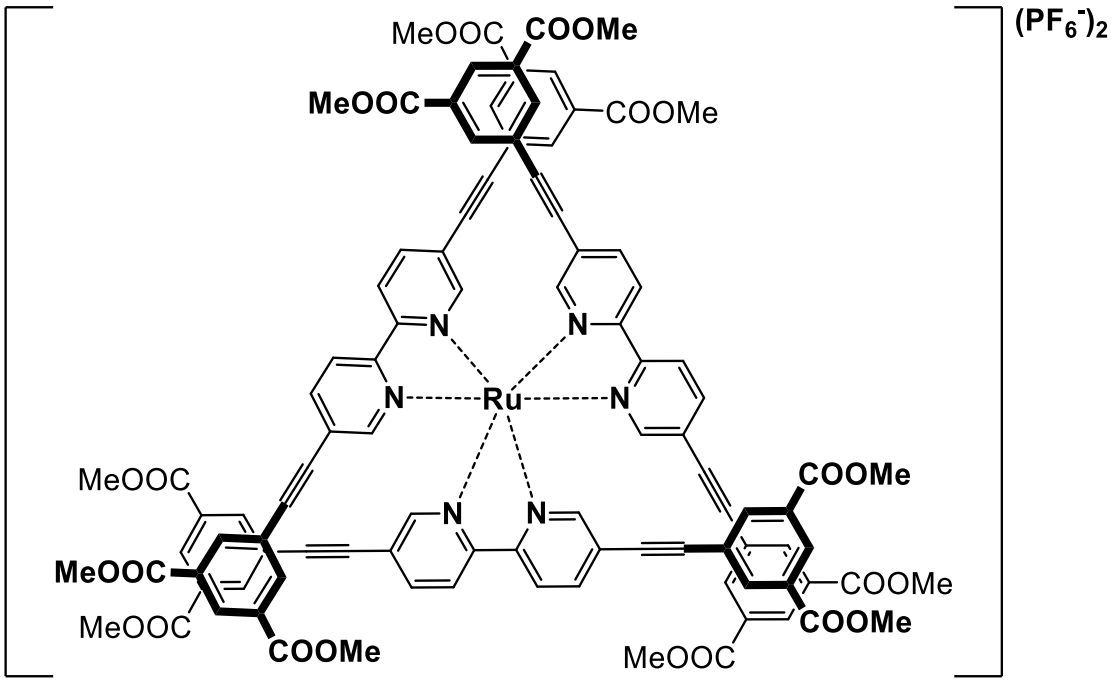

[Tris-(5,5'-dibromo-2,2'-bipyridine)-ruthenium(II)]$(PF_6)_2$ (0.229 g, 0.22 mmol), $Pd(PPh_3)_2Cl_2$ (0.081 g, 0.12 mmol) and CuI (0.022 g, 0.12 mmol) were added to pre-evacuated round bottom flask containing anhydrous DMF (40 ml) and DIPA (8 ml). The reaction mixture was then purged for 45 minutes with N_2 prior to the addition of dimethyl 5-ethynylisophtalate (10.00 eq.) and a colour change of red to black was immediately observed. The reaction mixture was allowed to stir under N_2 at ambient temperature for 24 hours. The reaction mixture was filtered after completion and excess diethyl ether was added to the filtrate and allowed to stir for 15 minutes. The orange precipitate was filtered, dried in air and purified *via* column chromatography on silica gel eluting with acetonitrile/H_2O/$NaNO_3$ (90:9:1). The purified product was concentrated under reduced pressure and an excess aqueous solution of $NaPF_6$ was added to precipitate out the desired brick red product which was filtered and dried in air. Yield: 0.134 g, 42 %. ^{1}H-NMR (d_6-DMSO, 400 MHz); δ_H (ppm) = 3.90 (s, 36H), 8.01 (m, 6H), 8.27 (m, 12H), 8.47 (m, 6H), 8.53 (m, 6H) 9.01 (m, 6H).

5.2.19 Synthesis of [bis-(2,2'-bipyridine)-ruthenium(II)(5,5'-(bis-4-ethynylbenzoic acid)-2,2'-bipyridine)]$(PF_6)_2$ ($H_2[L_{bpy}\text{-}R_1]$)

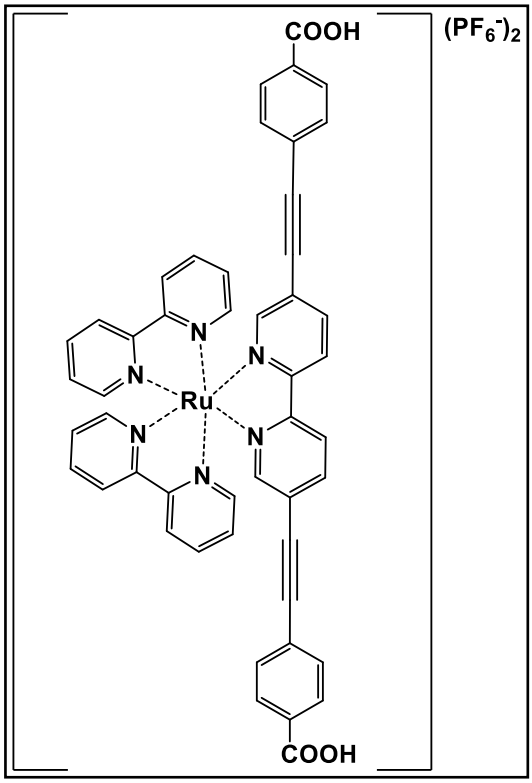

[Bis-(2,2'-bipyridine)-ruthenium(II)(5,5'-(bis-methyl-4-ethynylbenzoate)-2,2'-bipyridine)]$(PF_6)_2$ (0.825 g, 0.824 mmol) and NaOH (0.9 g, 22.5 mmol) were added to a mixture of THF (45 mL) and H_2O (22.5 mL). The mixture was stirred overnight at room temperature prior to the removal of the organic solvent *via* rotary evaporation. The aqueous reaction solution was neutralised by its addition to a stock solution of HPF_6 (20 mL). The mixture was allowed to stir for 30 minutes and a colour change of brown to orange/yellow was observed. The resulting solution was filtered washed with deionised H_2O and dried in air for 2 days prior to collection of the reddish orange solid at a quantitative yield. Yield: 0.7 g 85 %. ^{1}H-NMR (d_6-DMSO, 400 MHz); δ_H (ppm) = 7.58 (m, 8H), 7.72 (m, 2H), 7.83 (m, 2H), 7.88 (m, 2H), 7.97 (m, 4H), 8.20 (m, 4H), 8.42 (m, 2H) 8.95 (m, 6H). ^{13}C NMR (d_6-DMSO, 600 MHz); δ_C (ppm) = 166.9, 157.1, 156.9, 156.1, 153.4, 152.4, 151.7, 140.7, 138.6, 138.5, 132.3, 132.1, 130.2, 128.4, 128.3, 125.4, 125.3, 125.1, 124.9, 123.0, 95.7, 87.5; IR (ATR): ʊ̌ = 3080 (br), 1690 (w), 1602 (w), 1464 (w), 1446 (w), 1240 (w), 1075, (s), 1015 (m), 836 (s), 757 (s), 730 (m), 681 (w), 619 (s), 556 (m), 519 (w), 459 (m), 420 (w); Uv-vis λ_{max}/nm 250 (ε 2.50 x 10^4 M^{-1} cm^{-1}), 285 (ε 5.07 x 10^4 M^{-1} cm^{-1}), 329sh (ε 3.24 x 10^4 M^{-1} cm^{-1}), 363 (ε 4.46 x 10^4 M^{-1} cm^{-1}), 439 (ε 0.70 x 10^4 M^{-1} cm^{-1}), 490 (ε 0.50 x 10^4 M^{-1} cm^{-1}).

5.2.20 Synthesis of [bis-(2,2'-bipyridine)-ruthenium(II)(5,5'-(bis-3-ethynylbenzoic acid)-2,2'-bipyridine)]$(PF_6)_2$ ($H_2[L_{bpy}\text{-}R_2]$)

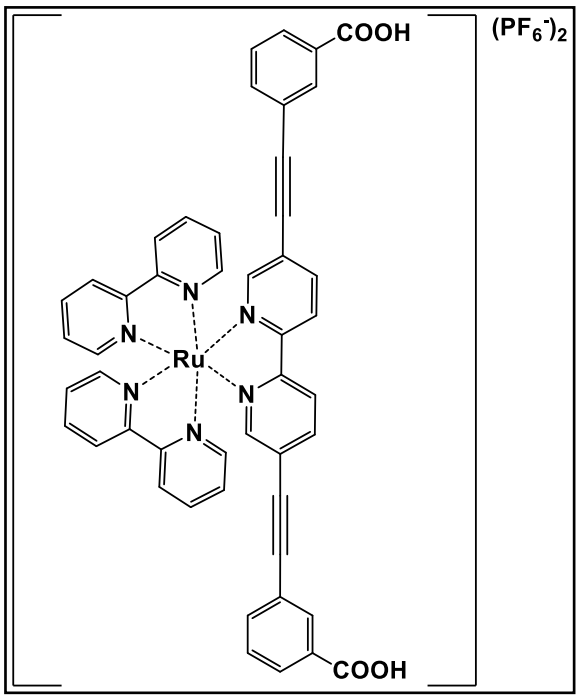

[Bis-(2,2'-bipyridine)-ruthenium(II)(5,5'-(bis methyl-3-ethynylbenzoate)-2,2'-bipyridine)]$(PF_6)_2$ (0.275 g, 0.275 mmol) and NaOH (0.3 g, 7.5 mmol) were added to a mixture of THF (15 mL) and H_2O (7.5 mL). The mixture was stirred overnight at room temperature prior to the removal of the organic solvent *via* rotary evaporation. The aqueous reaction solution was neutralised by its addition to a stock solution of HPF_6 (7.5 mL). The mixture was allowed to stir for 30 minutes and a colour change of brown to orange/yellow was observed. The resulting solution was filtered washed with deionised H_2O and dried in air for 2 days prior to collection of the reddish orange solid at a quantitative yield. Yield: 0.15 g 55 %. ^{1}H-NMR (d_6-DMSO, 400 MHz); δ_H (ppm) = 7.45 (m, 4H), 7.56 (m, 2H), 7.73 (m, 4H), 7.83 (m, 2H), 7.92 (m, 2H), 8.09 (m, 8H), 8.21 (m, 2H), 8.55 (m, 6H). ^{13}C NMR (d_6-DMSO, 600 MHz); δ_C (ppm) = 166.8, 157.1, 157.0, 156.0, 153.3, 152.3, 151.8, 140.7, 138.6, 136.0, 132.8, 132.0, 131.1, 130.0, 128.4, 128.3, 125.2, 125.1, 125.0, 123.1, 121.7, 95.7, 85.9; IR (ATR): ŭ = 3073 (br), 1718 (m), 1602 (w), 1463 (w), 1445 (w), 1375 (w), 1216 (w), 1084 (s), 1045 (s), 912 (w), 833 (s), 756 (s), 730 (m), 713 (w), 681 (w), 648 (w), 619 (s), 556 (m), 522 (w), 488 (w), 470 (w), 426 (w); Uv-vis λ_{max}/nm 254 (ε 2.72 x 10^4 M^{-1} cm^{-1}), 286 (ε 6.11 x 10^4 M^{-1} cm^{-1}), 330sh (ε 3.80 x 10^4 M^{-1} cm^{-1}), 360 (ε 5.11 x 10^4 M^{-1} cm^{-1}), 443 (ε 0.89 x 10^4 M^{-1} cm^{-1}), 497 (ε 0.61 x 10^4 M^{-1} cm^{-1}).

5.2.21 Synthesis of [bis-(2,2'-bipyridine)-ruthenium(II)(5,5'-(bis-5-ethynylisophthalic acid)-2,2'-bipyridine)]$(PF_6)_2$ ($H_4[L_{bpy}\text{-}R_3]$)

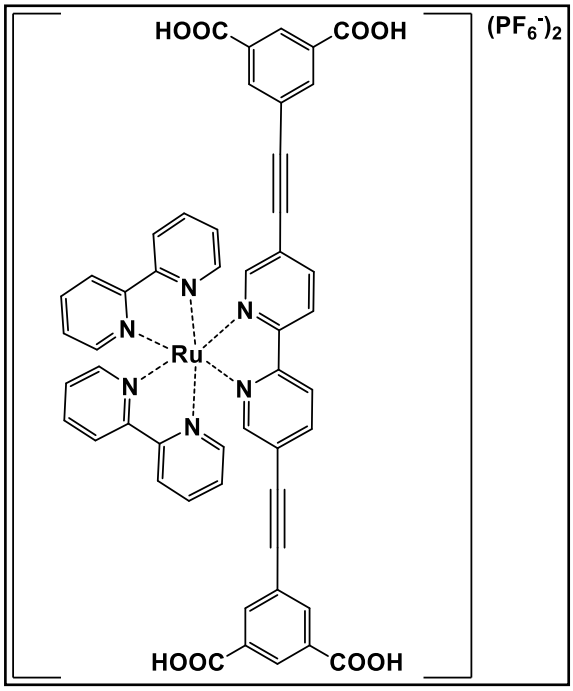

[Bis-(2,2'-bipyridine)-ruthenium(II)(5,5'-(bis-dimethyl-5-ethynylisophtalate)-2,2'-bipyridine)]$(PF_6)_2$ (0.550 g, 0.549 mmol) and NaOH (0.6 g, 15 mmol) were added to a mixture of THF (30 mL) and H_2O (15 mL). The mixture was stirred overnight at room temperature prior to the removal of the organic solvent *via* rotary evaporation. The aqueous reaction solution was neutralised by its addition to a stock solution of HPF_6 (10 mL). The mixture was allowed to stir for 30 minutes and a colour change of brown to orange/yellow was observed. The resulting solution was filtered washed with deionised H_2O and dried in air for 2 days prior to collection of the reddish orange solid at a quantitative yield. Yield: 0.485 g 88 %. ^{1}H-NMR (d_6-DMSO, 400 MHz); δ_H (ppm) = 7.57 (m, 4H), 7.71 (m, 2H), 7.89 (m, 2H), 8.19 (m, 4H), 8.22 (m, 4H), 8.48 (m, 4H), 8.85 (m, 4H), 8.98 (m, 2H). ^{13}C NMR (d_6-DMSO, 600 MHz); δ_C (ppm) = 166.1, 157.0, 156.9, 156.1, 153.4, 152.3, 151.7, 140.9, 138.6, 136.3, 132.7, 131.2, 128.4, 128.3, 125.3, 125.0, 122.9, 122.4, 94.7, 86.7; IR (ATR): ʊ̃ = 3400 (br), 1700, (m), 1640 (m), 1603 (m), 1464 (m), 1444 (m), 1271 (m), 1241 (m), 1179 (w), 1084 (s), 908 (w),837 (w), 760 (s), 730 (w), 716 (w), 671 (m), 620 (s), 609 (m), 561 (w), 526 (w), 494 (w), 476 (w), 451 (w), 424 (w); Uv-vis λ_{max}/nm 252 (ε 2.27 x 10^4 M^{-1} cm^{-1}) 287 (ε 4.70 x 10^4 M^{-1} cm^{-1}), 330sh (ε 3.13 x 10^4 M^{-1} cm^{-1}), 359 (ε 4.22 x 10^4 M^{-1} cm^{-1}), 437 (ε 0.57 x 10^4 M^{-1} cm^{-1}), 493 (ε 0.40 x 10^4 M^{-1} cm^{-1}).

5.2.22 Synthesis of [bis-(2,2'-bipyridine)-ruthenium(II)(3,8'-(bis-5-ethynylisophthalic acid)-1,10'-phenanthroline)]$(PF_6)_2$ ($H_4[L_{phen}\text{-}R_3]$)

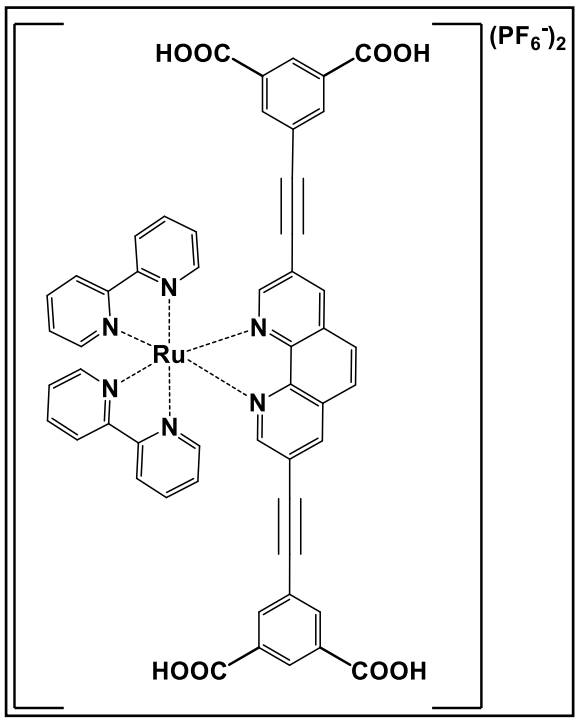

[Bis-(2,2'-bipyridine)-ruthenium(II)(3,8'-(bis-dimethyl-5-ethynylisophtalate)-1,10'-phenanthroline)]$(PF_6)_2$ (0.564 g, 0.549 mmol) and NaOH (0.65 g, 16.25 mmol) were added to a mixture of THF (30 mL) and H_2O (15 mL). The mixture was stirred overnight at room temperature prior to the removal of the organic solvent *via* rotary evaporation. The aqueous reaction solution was neutralised by its addition to a stock solution of HPF_6 (10 mL). The mixture was allowed to stir for 30 minutes and a colour change of brown to orange/yellow was observed. The resulting solution was filtered washed with deionised H_2O and dried in air for 2 days prior to collection of the reddish orange solid at a quantitative yield. ^{1}H-NMR (d_6-DMSO, 400 MHz); δ_H (ppm) = 7.39 (m, 3H), 7.60 (m, 3H), 7.73 (m, 2H), 7.79 (m, 2H), 8.14 (m, 2H), 8.22 (m, 2H), 8.26 (s, 2H) 8.37 (s, 2H), 8.42 (s, 2H), 8.50 (s, 2H), 8.86 (m, 4H), 9.15 (m, 2H). ^{13}C NMR (d_6-DMSO, 600 MHz); δ_C (ppm) = 165.0, 157.3, 157.1, 154.4, 152.6, 151.9, 146.4, 140.3, 138.6, 138.5, 136.5, 131.6, 130.8, 130.7, 130.6, 129.2, 128.2, 125.0, 124.9, 122.9 121.3, 93.3, 87.6, 82.3; IR (ATR): ʊ̃ = 2980 (br), 1718 (s), 1601 (m), 1463 (m), 1445 (m), 1377 (w), 1219 (w), 1156 (w), 1080 (s), 1044 (s), 913 (w), 833 (s), 756 (s), 729 (m), 714 (m), 681 (w), 647 (w), 618 (s), 556 (s), 495 (w), 471 (s), 422 (w); Uv-vis λ_{max}/nm 244 (ε 5.50 x 10^4 M^{-1} cm^{-1}) 285 (ε 9.54 x 10^4 M^{-1} cm^{-1}), 330sh (ε 3.32 x 10^4 M^{-1} cm^{-1}), 355 (ε 4.43 x 10^4 M^{-1} cm^{-1}), 436 (ε 1.06 x 10^4 M^{-1} cm^{-1}), 490 (ε 0.63 x 10^4 M^{-1} cm^{-1}).

5.2.23 Synthesis of [tris-(5,5'-(bis-5-ethynylisophthalic acid)-2,2'-bipyridine)-ruthenium(II)]$(PF_6)_2$ ($H_{12}[L_{tris}\text{-}R_3]$)

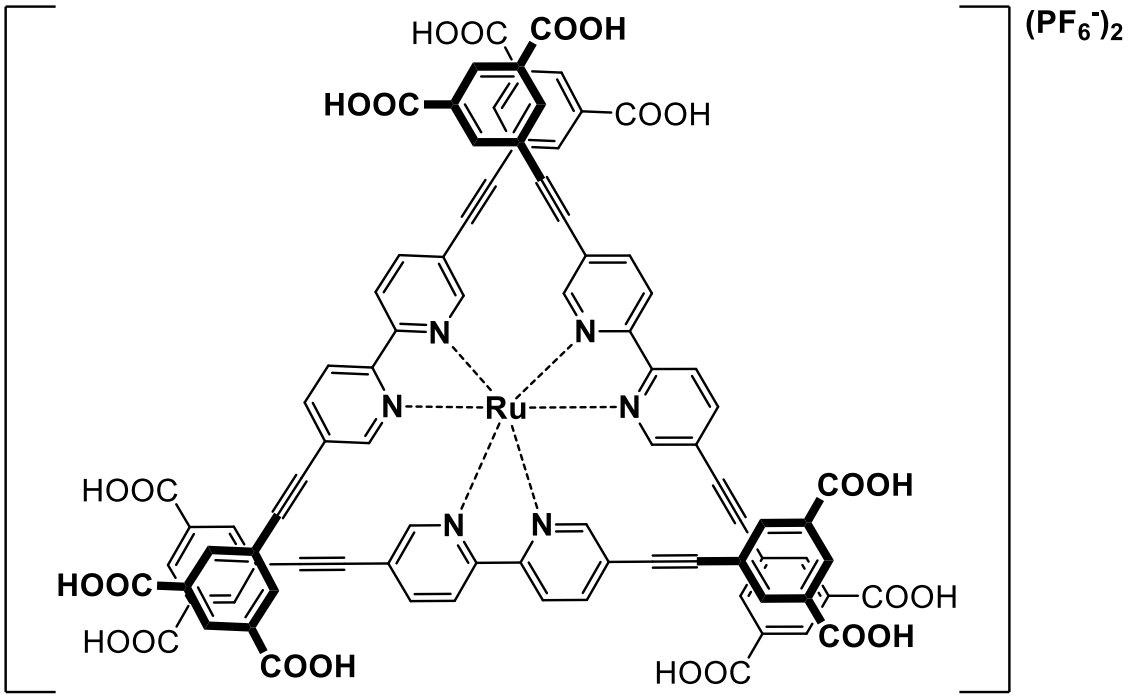

[Tris-(5,5'-(bis-dimethyl-5-ethynylisophtalate)-2,2'-bipyridine)-ruthenium(II)]$(PF_6)_2$ (0.258 g, 0.138 mmol) and NaOH (0.45 g, 11.25 mmol) were added to a mixture of THF (23 mL) and H_2O (12 mL). The mixture was stirred overnight at room temperature prior to the removal of the organic solvent *via* rotary evaporation. The aqueous reaction solution was neutralised by its addition to a stock solution of HPF_6 (9 mL). The mixture was allowed to stir for 30 minutes and a colour change of brown to orange/yellow was observed. The resulting solution was filtered washed with deionised H_2O and dried in air for 2 days prior to collection of the reddish orange solid at a quantitative yield. ^{1}H-NMR (d_6-DMSO, 400 MHz); δ_H (ppm) = 8.06 (m, 6H), 8.28 (m, 12H), 8.47 (m, 6H), 8.53 (m, 6H), 8.99 (m, 6H) IR (ATR): ŭ = 2981 (br), 1718 (s), 1601 (w), 1463 (m), 1445 (w), 1377 (w), 1225 (m), 1157 (w), 1079 (s), 1047 (s), 914 (w), 834 (s), 756 (s), 729 (m), 714 (m), 681 (m), 647 (w), 618, (s), 556 (s), 487 (w), 475 (w), 421 (w).

5.2.24 Synthesis of Ni-MOF

$H_4[L_{bpy}\text{-}R_3][2PF_6]$ (9 mg, 0.008 mmol) and $Ni(NO_3)_2\ 6H_2O$ (17.5 mg, 0.060 mmol) were dissolved in DMF (0.7 mL) and added to a 1.5 mL glass vial. The mixture was sonicated for 10 minutes and rapidly shaken to ensure a homogenous mixture. The vial was then placed in an aluminium heating block at 85 °C for 24 hours. Red octahedral crystals spheres were obtained. The crystals were washed with DMF. Yield: 6.5 mg. CHN analysis of dried material per formula ($C_{50}H_{32}N_6NiO_{10}Ru$) calcd. C 57.93 % H 3.11 % N 8.11 %; found C 56.86 % H 2.97 % N 8.22 %. IR (ATR): ŭ = 3408 (br), 2929 (w), 2213 (w), 1659 (s), 1564 (m), 1498 (w), 1466 (w), 1415 (m), 1364 (s), 1252 (m), 1198 (w), 1163 (w), 1094 (s), 1063 (m), 917 (w), 849 (w), 778 (s), 722 (s), 660 (s), 557 (w), 488 (w), 446 (w); Uv-vis: λ_{max}/nm = 295, 378, 405, 510.

5.2.25 Synthesis of Co-MOF

$H_4[L_{bpy}\text{-}R_3][2PF_6]$ (8 mg, 0.007 mmol) and $Co(NO_3)_2\ 6H_2O$ (17.5 mg, 0.060 mmol) were dissolved in DMF (0.7 mL) and added to a 1.5 mL glass vial. The mixture was sonicated for 15 minutes and rapidly shaken to ensure a homogenous mixture. The vial was then placed in an aluminium heating block at 65 °C for 72 hours. Red octahedral crystals were obtained. The crystals were washed with fresh DMF. Yield: 5.5 mg. CHN analysis of dried material per formula ($C_{50}H_{32}N_6NiO_{10}Ru$) calcd. C 57.92 % H 3.11 % N 8.11 %; found C 57.21 % H 3.32 % N 7.98 %. IR (ATR): ŭ = 3406 (br), 2928 (w), 2210 (w), 1655 (s), 1569 (m), 1498 (w), 1464 (w), 1419 (m), 1356 (s), 1252 (m), 1198 (w), 1156 (w), 1095 (s), 1060 (m), 914 (w), 844 (w), 774 (s), 714 (s), 659 (s), 557 (w), 483 (w), 444 (w); Uv-vis: λ_{max}/nm = 290, 376, 405, 512.

5.2.26 Synthesis of Zn-MOF

$H_4[L_{bpy}\text{-}R_3][2PF_6]$ (8 mg, 0.007 mmol) and $Zn(NO_3)_2\ 6H_2O$ (17.5 mg, 0.058 mmol) were dissolved in DMF (0.7 mL) and added to a 1.5 mL glass vial. The mixture was sonicated for 15 minutes and rapidly shaken to ensure a homogenous mixture. The vial was then placed in an aluminium heating block at 85 °C for 72 hours. Deep red polycrystalline spheres were obtained. The crystals were washed with DMF. Yield: 5 mg. CHN analysis of dried material per formula ($C_{50}H_{32}N_6NiO_{10}Ru$) calcd. C 57.56 % H 3.09 % N 8.06 %; found C 56.91 % H 3.02 % N 8.24 %. IR (ATR): ŭ = 3417 (br), 2928 (w), 2213 (w), 1652 (s), 1575 (m), 1496 (w), 1464 (w), 1430 (m), 1385 (s), 1347 (s), 1253 (m), 1196 (w), 1158 (w), 1093 (s), 1060 (m), 920 (w), 863 (w), 773 (s), 720 (s), 659 (s), 560 (w), 497 (w), 448 (w).

5.3 References

1 A. V. Bruker, *Bruker AXS Inc., Madison, Wisconsin, USA*.

2 S. Bruker, *Bruker AXS Inc., Madison, Wisconsin, USA*.

3 G. M. Sheldrick, *Acta Crystallogr. Sect. A Found. Crystallogr.*, 2015, A71, 3.

4 M. J. Frisch, G. W. Trucks, H. B. Schlegel, G. E. Scuseria, M. A. Robb, J. R. Cheeseman, G. Scalmani, V. Barone, G. A. Petersson, H. Nakatsuji, X. Li, M. Caricato, A. Marenich, J. Bloino, B. G. Janesko, R. Gomperts, B. Mennucci, H. P. Hratchian, J. V. Ortiz, A. F. Izmaylov, J. L. Sonnenberg, D. Williams-Young, F. Ding, F. Lipparini, F. Egidi, J. Goings, B. Peng, A. Petrone, T. Henderson, D. Ranasinghe, V. G. Zakrzewski, J. Gao, N. Rega, G. Zheng, W. Liang, M. Hada, M. Ehara, K. Toyota, R. Fukuda, J. Hasegawa, M. Ishida, T. Nakajima, Y. Honda, O. Kitao, H. Nakai, T. Vreven, K. Throssell, J. A. Montgomery Jr., J. E. Peralta, F. Ogliaro, M. Bearpark, J. J. Heyd, E. Brothers, K. N. Kudin, V. N. Staroverov, T. Keith, R. Kobayashi, J. Normand, K. Raghavachari, A. Rendell, J. C. Burant, S. S. Iyengar, J. Tomasi, M. Cossi, J. M. Millam, M. Klene, C. Adamo, R. Cammi, J. W. Ochterski, R. L. Martin, K. Morokuma, O. Farkas, J. B. Foresman and D. J. Fox, *Gaussian 09, Revis. A.02*, 2009.

5 C. Adamo and V. Barone, *J. Chem. Phys.*, 1999, **110**, 6158–6170.

6 D. Andrae, U. Häußermann, M. Dolg, H. Stoll and H. Preuß, *Theor. Chim. Acta*, 1990, **77**, 123–141.

7 M. J. Frisch, J. A. Pople and J. S. Binkley, *J. Chem. Phys.*, 1984, **80**, 3265–3269.

8 M. M. Francl, W. J. Pietro, W. J. Hehre, J. S. Binkley, M. S. Gordon, D. J. DeFrees and J. A. Pople, *J. Chem. Phys.*, 1982, **77**, 3654–3665.

9 D. Dubbeldam, S. Calero, D. E. Ellis and R. Q. Snurr, *Mol. Simul.*, 2016, **42**, 81–101.

Chapter 6

Conclusion and Future Outlook

6. Conclusion and Future Outlook

In summary, the overall aim of this research project was to design and synthesise a series of novel, porous, photoactive 3rd generation MOFs that could be used in light-driven chemical transformations and other related applications. A further aim was to design and develop homogeneous MOF thin films *via* bulk electrochemical deposition and to exploit their photoactive capabilities in photo- and electro-catalytic H_2O oxidation studies.

These aims were achieved with the design and synthesis of five acetylene-extended, light-harvesting Ru^{II}-bipyridyl metallo-ligands **$H_2[L_{bpy}\text{-}R_1]^{2+}$**, **$H_2[L_{bpy}\text{-}R_2]^{2+}$**, **$H_4[L_{bpy}\text{-}R_3]^{2+}$**, **$H_4[L_{phen}\text{-}R_3]^{2+}$** and **$H_{12}[L_{tris}\text{-}R_3]^{2+}$**. Their identities and purities were initially investigated prior to examining their photophysical, photochemical and electrochemical properties. The Ru^{II}-based heteroleptic metallo-ligand **$H_4[L_{bpy}\text{-}R_3]^{2+}$** was subsequently used in combination with Ni^{II}, Co^{II} and Zn^{II}-based building units to synthesise the isostructural MOFs **Ni-MOF**, **Co-MOF** and **Zn-MOF**. Their structures were elucidated and their physicochemical and photophysical properties were investigated. Following this, an experimental procedure to produce MOF thin films, was developed. The **Ni-MOF/FTO** and the **Co-MOF/FTO** were electrochemically synthesised on conductive fluorine doped tin oxide (FTO) glass electrodes using a technique termed cathodic electrochemical synthesis and *in-situ* film deposition. Physicochemical characterisation was carried out to demonstrate successful deposition and to examine the purity of the MOF thin films. Following this, an experimental setup was developed to test and validate the applicability of both the **Ni-MOF/FTO** and the **Co-MOF/FTO** as photocatalysts for photo-electrocatalytic H_2O oxidation studies.

Following is a brief overview of the work discussed in each chapter of this thesis:

In chapter 2, an efficient synthetic strategy which enabled the synthesis of the desired complexes was designed and carried out. Additionally, modification of literature work-up procedures afforded greater purity and scalability of the five acetylene-extended Ru^{II} polypyridyl complexes **$H_2[L_{bpy}\text{-}R_1]^{2+}$**, **$H_2[L_{bpy}\text{-}R_2]^{2+}$**, **$H_4[L_{bpy}\text{-}R_3]^{2+}$**, **$H_4[L_{phen}\text{-}R_3]^{2+}$** and **$H_{12}[L_{tris}\text{-}R_3]^{2+}$**. Single crystals suitable for single crystal x-ray diffraction studies were obtained for the **$H_2[L_{bpy}\text{-}R_1]^{2+}$**, **$H_2[L_{bpy}\text{-}R_2]^{2+}$**, **$H_4[L_{bpy}\text{-}R_3]^{2+}$**, and **$H_4[L_{phen}\text{-}R_3]^{2+}$** metallo-ligands. The extended $[Ru(bpy)_3]^{2+}$ derivatives offer various functionalities which can be utilised for MOF synthesis. The presence of O- donors allow the metallo-ligands to coordinate to various main group and transition metal ions *via* a variety of

binding modes. Similarly, high levels of aromaticity present within the metallo-ligands, as seen from their respective crystal structures, increases the occurrence of strong π – π stacking interactions. These interactions have the potential to enhances the stability of supramolecular assemblies prepared using these metallo-ligands. Furthermore, post-synthetic characterisation demonstrated both the physicochemical properties of the Ru^{II}-based metallo-ligands and the similarities between the novel metallo-ligands and $[Ru(bpy)_3]^{2+}$. Future work may include the synthesis of other extended metallo-ligands that include softer N-donors in addition to the present O-donors. This functionalisation is envisaged to provide a metallo-ligand with the ability to bind to various hard and soft mix metals through various coordination modes, allowing for the production of mix metal MOFs.

Having obtained highly pure samples of the novel metallo-ligands, the photophysical, photochemical and electrochemical properties of $\mathbf{H_2[L_{bpy}\text{-}R_1]^{2+}}$, $\mathbf{H_2[L_{bpy}\text{-}R_2]^{2+}}$, $\mathbf{H_4[L_{bpy}\text{-}R_3]^{2+}}$, and $\mathbf{H_4[L_{phen}\text{-}R_3]^{2+}}$ were subsequently examined in chapter 3. A comparative analysis between the metallo-ligands and $[Ru(bpy)_3]^{2+}$ was carried out. The novel Ru^{II}-based metallo-ligands retained the distinctive characteristic properties of $[Ru(bpy)_3]^{2+}$, as shown by the obtained UV-Vis absorption and steady-state emission spectra. The characteristic Ru^{II} polypyridyl transitions were identified to be slightly red-shifted as a result of the increased conjugation present in the metallo-ligand systems when compared to $[Ru(bpy)_3]^{2+}$. A reduction in the estimated band gap energies for the metallo-ligands in comparison to $[Ru(bpy)_3]^{2+}$ demonstrated the metallo-ligands enhanced capacity for photon absorption and conduction. Therefore, this highlighted that the metallo-ligands could act as chromophores in the framework of MOFs and be utilised in a variety of photo/electro-catalytic applications. Similarly, the extended fluorescent lifetimes of the metallo-ligands post-bis-alkynyl functionalisation when compared to $[Ru(bpy)_3]^{2+}$, again emphasised the applicability of these complexes for the synthesis of photoactive MOFs. Finally, the retention of the distinctive characteristic properties of $[Ru(bpy)_3]^{2+}$ was again demonstrated by solution-phase cyclic voltammetry, whereby the reversible redox nature and especially the characteristic redox pair Ru^{III}/Ru^{II} is maintained within the novel metallo-ligands. Future work would involve an additional improvement in the metallo-ligands fluorescent lifetimes and an investigation into the various factors which influence these lifetimes. Additionally, future investigations would include the synthesis of other light-harvesting ligands along with a comparative analysis

with the synthesised Ru^{II}-based metallo-ligands in order to identify the major strucutral features which influence the photophysical and photochemical properties.

In chapter 4, the design, synthesis, and characterisation of a series of acetylene-extended '3rd-generation' MOFs with photoactive capabilities was described. The MOFs [X(**L_{bpy}-R3**)$(H_2O)_2$] (X = Ni/Co/Zn) were identified to consist of nanoscopic {Ni_6}/{Co_6}/{Zn_6} cages that are linked through light-harvesting Ru^{II}-pyridyl **$H_4[L_{bipy}$-R3$]^{2+}$** metallo-ligands. Various spectroscopic techniques along with single-crystal X-ray diffraction and X-ray powder diffraction elucidated the structure, purity and characteristics of the MOFs. The crystal structure of **Ni-MOF** and **Co-MOF** was described in detail, highlighting that the MOFs adopt an augmented, cubic **a-fcu** topology that is characterised by large pores which were estimated by RASPA. Subsequently, photophysical studies of the **Ni-MOF** and the **Co-MOF** were discussed. It was identified that the optical attributes of the free Ru^{II}-pyridyl metallo-ligands, as indicated from the absorption and emission spectra, are maintained in the framework of the MOFs. The photoluminescence data demonstrated that the coordination of the metallo-ligands to the corresponding metal ions in the MOFs facilitates rapid energy and electron transfer processes throughout the network structures.

After establishing the standard solvothermal synthetic process for the synthesis of **Ni-MOF** and **Co-MOF**, efforts proceeded to investigate other, optimised methods of producing the MOFs in larger quantities at a reduced time and cost, along with the objective of emulating industrial synthetic processes. Cathodic electrochemical synthesis and *in-situ* film deposition was used to produce thin films of **Ni-MOF** and **Co-MOF** on a conductive FTO glass electrodes in less than 5 minutes. An electrolyte solution containing the **$H_4[L_{bipy}$-R3$]^{2+}$** metallo-ligand and either Ni^{II} or Co^{II} ions, in combination with a -1.5 V potential, was used to self-assemble thin films of **Ni-MOF** and **Co-MOF**, respectively. Physicochemical characterisation along with a comparative analysis of the thin films with single crystals of their respective MOF strongly indicated the successful functionalisation of the conductive surfaces and identified and confirmed the thin films as **Ni-MOF/FTO** and **Co-MOF/FTO**, respectively.

With these characteristics in mind, it was decided to investigate the applicability of both the **Ni-MOF/FTO** and **Co-MOF/FTO** as heterogeneous WOC in organic media under photo-electrochemical conditions. CV data demonstrated a reduction of more than 90 mV

to the onset-overpotential upon LED light irradiation of **Ni-MOF/FTO** and **Co-MOF/FTO** electrodes. The LSV experiments revealed that LED light irradiation of **Ni-MOF/FTO** and **Co-MOF/FT**O electrodes reduced the onset-overpotential by 140 mV and 100 mV, respectively. Furthermore, visual inspection and post-catalytic characterisation indicated neither loss of material nor the formation of decomposition products, such as metal oxides. Comparative data analysis of post-catalytic films with pre-catalytic films demonstrated closely matching characteristic bands along with highly similar atomic weight percentage ratios. Future work would involve an extended photophysical analysis of the thin films along with the optimisation of the deposited material in order to achieve enhanced photoactivity. Additionally, further investigation into the PEC stability and identification and design of novel methods to improve the system's overall stability. The synthesis of various other photoactive MOF networks composed of different inorganic SBUs, as well as an investigation into their applicability for water oxidation catalysis and other photocatalytic applications, are areas for future research.